Modelisation et simulation de l'interaction onde de choc/couche limite turbulente en écoulement interne avec effets de coins

Corentin Roussel

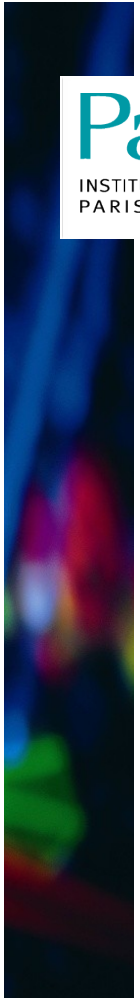

ParisTech
INSTITUT DES SCIENCES ET TECHNOLOGIES
PARIS INSTITUTE OF TECHNOLOGY

ARTS ET MÉTIERS ParisTech

2016-ENAM-0025

École doctorale n° 432 : Sciences des métiers de l'ingénieur

Doctorat ParisTech

T H È S E

pour obtenir le grade de docteur délivré par

l'École Nationale Supérieure d'Arts et Métiers

Spécialité " mécanique et matériaux"

présentée et soutenue publiquement par

Corentin ROUSSEL

le 22 Juin 2016

Modélisation et simulation de l'interaction onde de choc – couche limite turbulente en écoulement interne avec effets de coins

Directeur de thèse : **Francesco GRASSO**
Co-encadrement de la thèse : **Frédéric ALIZARD**

Jury

M. Sergio PIROZZOLI, Professeur, Dipartimento di Ingegneria Meccanica e Aerospaziale, La Sapienza	Président
M. Abdellah HADJADJ, Professeur, INSA Rouen, Université de Normandie	Rapporteur
M. Holger BABINSKY, Professeur, Fluids Group, Cambridge University	Rapporteur
M. Lionel LARCHÊVEQUE, MCF, IUSTI, Université d'Aix-Marseille	Examinateur
M. Christophe NOTTIN, Docteur-ingénieur, Département aérodynamique et performances, MBDA	Examinateur
M. Frédéric ALIZARD, MCF, Dynfluid, Conservatoire National des Arts et Métiers	Examinateur
M. Francesco GRASSO, Professeur, Dynfluid, Conservatoire National des Arts et Métiers	Examinateur

T H È S E

Arts et Métiers ParisTech - Centre de Paris
Laboratoire Dynfluid - EA 92

Remerciements (Acknowledgement)

This section regards personal acknowledgement and is written in French. Formal acknowledgement are located after the conclusions.

Je tiens à remercier mes directeurs de thèse Frédérique Alizard et Francesco Grasso. La réalisation d'une thèse n'est ni un travail solitaire, ni une chose facile et le travail rendu est le plus souvent le résultat d'une équipe. Je souhaite ainsi remercier Frédérique Alizard d'avoir partagé ses conseils, son expérience personnelle, et de m'avoir laissé une grande liberté lors de cette thèse. Je remercie Francesco Grasso pour son investissement personnel, ses remarques et conseils qui m'aideront à améliorer la qualité de mes documents. Malgré les difficultés initiales, ils ont fait le choix de m'accompagner jusqu'à la fin de ma thèse et je les en remercie.

Je voudrais ensuite remercier les rapporteurs Abdellah HADJADJ et Holger BABINSKY pour l'intérêt et les remarques apportés au manuscrit, Sergio PIROZZOLI pour avoir accepté d'être le président du jury, Lionel LARCHÊVEQUE pour la qualité de ses remarques et l'ensemble des membres du jury pour avoir accepté d'être présents le jour J. Je remercie en particulier Christophe Nottin, qui a suivi la thèse en tant que représentant de MBDA, mais surtout, Christophe m'a apporté des conseils de qualités (avec gentillesse) tout au long de la thèse.

Je remercie bien entendu l'ensemble des membres du laboratoire Alain, Cédric, Damien, Jean-Christophe, Paola, Simon, Stephania, Virginie, Xavier, Xavier (un deuxième), ... Tous ont contribué à cette expérience et se devaient d'être remerciés dans ce manuscrit. Je ne rentre pas trop dans le détail, et pourtant le temps que certains ont pris pour m'expliquer l'organisation, le traitement et post-traitement des données sur calculateur, la prise en compte de mon emploi du temps pour l'enseignement... Pour toutes ces choses et d'autres, je vous remercie. Fait exceptionnel, Damien et Jean-Christophe ont survécu à plusieurs dizaines de Vendredi en tant que co-bureau. Félicitations !

Mes remerciements vont également aux doctorants des plus anciens, Karim, Pierre-Yves, Jean-Christophe (Grand Maître Bizu), Leslie, Florian, Ronan, Matthieu (Maitre Bizu), Wouter, aux plus jeunes, Miloud, Lucas, Elio, Alessandro (Ale), Mirko, Francesco (Chicho), Amandine, Loris ... Bien sur je n'oublie pas mes compagnons des JDD, Grégoire (surnom censuré), Elie (Le Zizi). Je remercie aussi les intermittents de la recherche, Andrea (Italian stud) et Chloe (juste Chloe). Alors que le labo se vide et que les ventilateurs ronronnent, vous êtes encore présents (avec Ale) pour partager un café ou un repas sur un coin de table mais aussi un ping-pong sur un coin de table, ou encore une mousse sur un coin de table... Toutes ces activités qui musclent les bras et usent les tables.

Je remercie mes amis et tous ceux qui m'ont prodigué leurs conseils ou tout simplement de l'écoute, en commençant par mon ancien coloc Dr. Courbin, Nathalie (peut-être futur Dr. Courbin aussi ;)), Sebastien Deck, You Ren, Alix Tantet, la famille Gueudry, et plus largement tous mes amis.

Pour finir avec le meilleur, mes remerciements vont à ma famille. Je remercie ma grand mère Gisèle, ma soeur, ma mère et celle qui partage ma vie, Charlotte (Cha). Sans elle j'aurais probablement eut les regrets que je n'aurai pas. Je vous remercie pour tout.

"Voilà voilà" ... En tout cas merci tout le monde! J'espère ne pas avoir oublié quelqu'un... ou *"quelque chose"*.

Contents

1 State of the art **13**
- 1.1 Introduction . . . 13
- 1.2 Shock-wave turbulent boundary layer interaction: issues and general properties . 17
  - 1.2.1 Detached and attached interactions, inviscid and viscous theoretical approach 17
  - 1.2.2 Mean flow and broadband unsteadiness in supersonic detached interactions 19
  - 1.2.3 Transonic interactions . . . 23
- 1.3 Shock-wave boundary layer with side walls effects . . . 25
  - 1.3.1 Supersonic interactions: experimental and numerical observations . . . 25
  - 1.3.2 Experiment in transonic interactions, confinement effects . . . 26
  - 1.3.3 Shock-trains and pseudo-shock system . . . 28

2 Numerical Methods **33**
- 2.1 Governing equations . . . 33
- 2.2 Filtered equations . . . 34
- 2.3 Spatial and temporal discretization . . . 35
  - 2.3.1 Spatial discretization of the Euler equations . . . 35
  - 2.3.2 Spatial discretization of the viscous terms . . . 36
  - 2.3.3 Scheme for the temporal integration: 4^{th} Runge-Kutta . . . 37
- 2.4 Explicit filter . . . 37
- 2.5 Sub-grid stress: explicit and implicit modeling . . . 37
  - 2.5.1 Subgrid explicit modeling: Dynamic Smagorinsky . . . 38
- 2.6 Boundary conditions . . . 40

3 Turbulence initialisation **43**
- 3.1 Turbulent boundary layer: a priori properties . . . 43
  - 3.1.1 Streamwise distribution of the boundary layer thickness . . . 44
  - 3.1.2 Estimation of the inner length scale for an incompressible flow . . . 44
  - 3.1.3 Estimation of the inner length scale for a **compressible** flow . . . 46
- 3.2 Generation of turbulent inflow . . . 49
  - 3.2.1 Recycling/rescaling on a single wall . . . 49
  - 3.2.2 Multi-wall recycling/rescaling . . . 50

4 Validations **52**
- 4.1 Supersonic turbulent boundary layer . . . 52
  - 4.1.1 Mesh and resolution . . . 53
  - 4.1.2 Skin friction coefficient and boundary layer thicknesses . . . 53
  - 4.1.3 Mean flow and turbulence statistics . . . 55
  - 4.1.4 Turbulent Kinetic Energy budget . . . 56
- 4.2 Transonic shock-wave turbulent boundary layer interaction . . . 57
  - 4.2.1 Scaling parameters . . . 57
  - 4.2.2 Mesh and resolution . . . 58
  - 4.2.3 Wall statistics . . . 58
  - 4.2.4 Boundary layer thickness trough the shock . . . 60
  - 4.2.5 Pressure gradient and velocity profile . . . 61

4.2.6 Fluctuations and turbulent kinetic energy budget . . . 62
4.2.7 Qualitative visualisation . . . 63
4.3 Supersonic turbulent boundary layer in a rectangular duct . . . 64
4.3.1 Analysis along the wall bisector ($z = L_z/2$) . . . 66
4.3.2 Analysis in the transverse plane . . . 67

5 Side walls effect on shock-train 74
5.1 Parameters of the study . . . 74
5.2 Centreline flow properties ($z = L_z/2$) . . . 76
5.2.1 Boundary layer scales and wall pressure signature . . . 77
5.2.2 Influence of the aspect ratio on the mean flow and turbulence statistical properties . . . 83
5.3 Skin frictions patterns . . . 101
5.4 Flow organization . . . 105

6 Unsteady analysis of shock-train interactions 109
6.1 Wall pressure dynamics . . . 109
6.2 Dynamic Mode Decomposition . . . 113
6.2.1 Description of the method . . . 113
6.2.2 Flow analysis . . . 115

7 Conclusions and Future Work 121
7.1 Future Work . . . 122
7.2 Acknowledgement . . . 122

I Appendix 123

A Uncommented results 124
A.1 Contours of the static pressure in the longitudinal midplane (z=Lz/2) . . . 124
A.2 Instantaneous visualization of the density gradient magnitude . . . 126
A.3 Low-frequency DMD mode . . . 127

B Details on the post-process 128
B.1 Measurable budget of the turbulent Kinetic energy equation for LES . . . 128
B.1.1 LES momentum equation . . . 128
B.1.2 Kinetic energy . . . 129

List of Figures

1.1 (a) Picture of a MIG-29K aircraft. Two squared air intakes can be observed under the aircraft. Retrieved from Wikipedia. (b) Schematic of the generation and propagation of shock-waves in supersonic aircraft engine. The shock-waves are drawn in red. . . . 14

1.2 Experimental Schlieren visualization of the different categories of SWBLI: (a), a transonic interaction over a bump [34]; (b), an oblique shock-wave boundary layer interaction [34]; (c), a compression corner interaction [37]; (d), a shock-wave boundary layer interaction in an over expanded diffuser [14]; (e), an oblique shock induced by the separation in front of a forward-facing step [55] . . . 16

1.3 Typical wall pressure distributions for SWBLI. Reprinted from Délery and Dussauge [27]. . . . 17

1.4 The interaction flow multi-layer structure or triple deck [27] . . . 18

1.5 Diagrammatic representation of the different mechanisms involved in quasi two-dimensional SWBLI. Reprinted from Dussauge [34] . . . 20

1.6 Visualisation of the streamwise velocity fluctuations in the plane $y = 0.01\delta_0$. Reprinted from Touber and Sandham [101]. . . . 21

1.7 Isocontour of the spanwise averaged pre-multiplied PSD of the wall pressure (arbitrary scale) with $x^* = (x-x_0)/L$ the streamwise position defined as the distance to the shock rescaled by the interaction length and St_L the Strouhal number based on the interaction length. (a) Large eddy simulation of a oblique shock-wave boundary layer interaction. The shock impact the wall with an angle of 30.8 degree in Mach 2.15 flow. The blue line indicate a Strouhal number of 0.03 ($St_L = 0.03$). Reprinted from [4]. (b) Direct numerical simulation of a shock-wave–turbulent boundary layer interaction generated by 24 degree compression ramp in Mach 2.9 flow. Adapted from [81] . . . 22

1.8 Power spectral density of the wall pressure fluctuations and the streamwise momentum fluctuations measured with hot wire anemometry (HWA). Date are obtained at the mean location of the foot shock for different angles of deflection of the initial impinging shock. Reprinted from Dupont et al. [33] . . . 23

1.9 Schematic of the flow induced by a normal SWBLIs without separation. Reprinted from Babinsky and Harvey [5] . . . 23

1.10 Schematic of the flow induced by a normal SWBLIs with separation. Reprinted from Babinsky and Harvey [5] . . . 24

1.11 Instantaneous streamwise velocity fluctuations u' at $y^+ = 10.8$ of an incipient transonic interaction. Reprinted from Pirozzoli et al. [76] . . . 24

1.12 (a) Oil flow measurements and (b) surface flow sketch for a oblique shock-wave boundary layer interaction at $M_\infty = 3$ from [13]. The flow is from bottom to top. An important spanwise velocity component is observed that sweep flow from the centerline towards the side walls. . . . 25

1.13 Distortion of the main shock-waves is illustrated with contours of the time- averaged streamwise density gradient for a moderately separated oblique shock-wave/boundary-layer interaction at $M_\infty = 2.7$ in a rectangular duct with an aspect ratio of 2. (a) Show shock-waves above the interaction region, with shock structures from five different x–z planes (at y = 49, 40, 30, 20 and 10 mm) superimposed. (b) Show the shock structures on the x–z plane at y = 6 mm, *i.e.* close to the location where the shock impinges on the apex of the recirculation bubble. Reprinted from Wang et al. [108] 26
1.14 Experimental data for attached (open symbols) and separated (filled symbols) transonic SWBLIs. Reprinted from Bruce et al. [17] 27
1.15 Oil flow patterns on the tunnel floor and sidewalls for a $M_\infty = 1.4$ shock. Only the bottom half of the tunnel side walls are shown. Reprinted from Bruce et al. [17] 28
1.16 Experimental data for attached (open symbols) and separated (filled symbols) transonic SBLIs, plotted against the variable δ^*/w. Reprinted from [17] 29
1.17 Babinsky *et al* [6] proposed variation of separation lengths (along wind tunnel floor centerline) as a function of wind tunnel 'inverse viscous aspect ratio'. Reprinted from Babinsky et al. [6] 29
1.18 Schematic sketch of normal shock-wave/turbulent boundary layer interaction in a constant area duct. Reprinted from Matsuo et al. [66] 30
1.19 Schematic static pressure distribution along duct centerline and wall surface in constant-area duct for condition wherein a "normal" shock is present. Reprinted from Matsuo et al. [66]. 31

2.1 Spectrum of homogeneous turbulence with an ideal spectral filter cut-off at k_c that separates large scales from smaller mostly dissipative scales. Backscattering is (by hypothesis) neglected. 39
2.2 Schematic of the computational domain. 40

3.1 Block diagram describing the algorithm used to estimate the initial skin friction coefficient. 45
3.2 Time-averaged incompressible velocity profile $\overline{u}(y)$ 45
3.3 Schematic of the extraction and rescaling of a quantity ϕ [12]. (a) Extraction of turbulent quantity ϕ in the duct cross section at the recycling location. The walls are numbered from 1 to 4; (b) Rescaling along each wall. The quantity ϕ rescaled in the direction normal to the n^{th} wall becomes the rescaled quantity ϕ_n. 51

4.1 Incompressible skin friction coefficient (see table 4.1 for nomenclature). 54
4.2 Mean incompressible shape factor H_i with H_{th} defined in (4.1). See table 4.1 for nomenclature. 54
4.3 Favre-averaged van Driest velocity profile $\overline{u}_{vd}$ in inner scaling 55
4.4 $u_{i_{rms}}$ and $u''v''$ in inner scaling. (see table 4.1 for nomenclature) 56
4.5 Turbulent kinetic energy budget in the TBL (see table 4.1 for nomenclature) . . 57
4.6 Evolution in the streamwise direction of the streamwise spacing in wall units. . . 58
4.7 Wall pressure distribution along the streamwise direction (x) 59
4.8 "Isentropic" wall Mach number 59
4.9 Skin friction coefficient 60
4.10 Boundary layer thickness 60
4.11 Shape factors for the NSBLI 61
4.12 Mach number at the edge of the vorticity boundary thickness 61
4.13 Velocity profile normalized by local boundary-layer thickness 62
4.14 Reynolds stresses for the NSBLI 62
4.15 TKE budget for the NSBLI 63
4.16 Q criterion 63
4.17 Q criterion, zoom on the interaction area. 64
4.18 Schematic of the rectangular duct geometry. 65

4.19 Undisturbed flow simulation. Sensitivity to mean inflow conditions. Distribution of the van Driest mean velocity u^+_{vd} (left panel) and of the normal Reynolds stress components $(\widetilde{\rho u_i' u_i'}/(\rho_w u_\tau^2))^{1/2}$ in inner unit. Dashed line, Case A ($x/\delta_{in} = 25$, $Re_\theta = 1880$); solid line, Case B ($x/\delta_{in} = 25$, $Re_\theta = 2610$); ▲ LES of Morgan [67]. 66
4.20 Undisturbed flow simulation. Sensitivity to mean inflow conditions. Distribution of the van Driest mean velocity u^+_{vd} (left panel) and of the normal Reynolds stress components $(\widetilde{\rho u_i' u_i'}/(\rho_w u_\tau^2))^{1/2}$ in inner unit. Dashed line, Case A ($x/\delta_{in} = 63$, $Re_\tau = 380$); solid line, Case B ($x/\delta_{in} = 56$, $Re_\tau = 380$). 66
4.21 Distribution of the displacement δ^*, and momentum θ thicknesses normalized by δ_{in} (left panel) and of the skin friction coefficient (right panel) as a function of x/δ_{in}. Dashed line, Case A; solid line, Case B. 67
4.22 Eleven evenly spaced contours of the velocity components in the transverse plane, $x/\delta_{in} = 60$. Dashed line, Case A; solid line and the background iso-contour, Case B. (a) $\widetilde{u}/u_\infty$ from 0 to 1; (b) $\widetilde{v}/u_\infty$ from -0.02 to 0.02; (c) $\widetilde{w}/u_\infty$ from -0.02 to 0.02. 68
4.23 Fifteen evenly spaced contours the mean streamwise vorticity $(\widetilde{\omega_x}\delta/u_\infty)$ from -2 to 2 at $x/\delta_{in} = 25$ (left panel) and $x/\delta_{in} = 60$ (right panel). Dashed line, Case A; solid line and background iso-contours, Case B. 69
4.24 Eleven evenly spaced contours of $\left[\left(\frac{\partial^2}{\partial y^2} - \frac{\partial^2}{\partial z^2}\right)(-\widetilde{v'w'})\right]\delta^2/u_\infty^2$ from -1.75 to 1.75 at $x/\delta_{in} = 25$ (left panel) and $x/\delta_{in} = 60$ (right panel). Dashed line, Case A; solid line and background iso-contours, Case B. 69
4.25 Eleven evenly spaced contours of $\widetilde{u'u'}^{1/2}/u_\infty$ from 0 to 0.14 at $x/\delta_{in} = 25$ (left panel) and $x/\delta_{in} = 60$ (right panel). Dashed line, Case A; solid line and background iso-contours, Case B. 70
4.26 Eleven evenly spaced contours of $\widetilde{v'v'}^{1/2}/u_\infty$ from 0 to 0.07 at $x/\delta_{in} = 25$ (left panel) and $x/\delta_{in} = 60$ (right panel). Dashed line, Case A; solid line and background iso-contours, Case B. 70
4.27 Eleven evenly spaced contours of $\widetilde{w'w'}^{1/2}/u_\infty$ from 0 to 0.07 at $x/\delta_{in} = 25$ (left panel) and $x/\delta_{in} = 60$ (right panel). Dashed line, Case A; solid line and background iso-contours, Case B. 71
4.28 Eleven evenly spaced contours of $\widetilde{v'w'}/u_\infty^2$ from -0.0005 to 0.0005 at $x/\delta_{in} = 25$ (left panel) and $x/\delta_{in} = 60$ (right panel). Dashed line, Case A; solid line and background iso-contours, Case B. 71
4.29 Eleven evenly spaced contours of $\widetilde{u'v'}/u_\infty^2$ from -0.002 to 0.002 at $x/\delta_{in} = 25$ (left panel) and $x/\delta_{in} = 60$ (right panel). Dashed line, Case A; solid line and background iso-contours, Case B. 72
4.30 Eleven evenly spaced contours of $\widetilde{w'u'}/u_\infty^2$ from -0.002 to 0.002 at $x/\delta_{in} = 25$ (left panel) and $x/\delta_{in} = 60$ (right panel). Dashed line, Case A; solid line and background iso-contours, Case B. 72

5.1 Schematic of the duct geometry. Subscript 1 and 2 indicate, respectively, the location where the confinement (δ/h) is equal to 0.32 and the beginning of the interaction (the location where the pressure starts to rise). 75
5.2 Contours of the density gradient magnitude between 0 (white) and 1.5 (black). (a) periodic boundary conditions in the spanwise direction (AR=∞); (b) AR=5; (c) AR=2.257; (d) AR=1.5 77
5.3 Streamwise distribution of the characteristic boundary layer scales for various aspect ratios evaluated at the centerline ($z = Lz/2$). (a) boundary layer thickness scaled by the duct height; (b) incompressible shape factor; (c) displacement thickness scaled by the duct height; (d) momentum thickness scaled by the duct height; (e) displacement thickness scaled by its value at the beginning of the interaction; (f) momentum thickness scaled by its value at the beginning of the interaction. ——— , AR=∞ current simulation; – – –, AR=5 current simulation; —×—, AR=∞ LES Ref. [68]; •, exp. Ref. [21], AR=2.257. 80

5.4 Streamwise distribution of the characteristic boundary layer scales for various aspect ratios evaluated at the centerline ($z = Lz/2$). (a) boundary layer thickness scaled by the duct height; (b) incompressible shape factor; (c) displacement thickness scaled by the duct height; (d) momentum thickness scaled by the duct height; (e) displacement thickness scaled by its value at the beginning of the interaction; (f) momentum thickness scaled by its value at the beginning of the interaction. ——— , AR=2.257 current simulation; – – –, AR=1.5 current simulation; —×—, AR=2.257 LES Ref. [68]; •, exp. Ref. [21], AR=2.257. 81
5.5 Wall pressure distribution along the centerline ($z = L_z/2$) scaled by the wall pressure at the beginning of the interaction p_2 for various shock-train configurations. (a) ——— , AR=∞ current simulation; – – –, AR=5 current simulation; —×—, AR=∞ LES Ref. [68]; (b) ——— , AR=2.257 current simulation; – – –, AR=1.5 current simulation; —×—, AR=2.257 LES Ref. [68]; •, exp. Ref. [21], AR=2.257. 82
5.6 Streamwise distribution of the skin friction coefficient evaluated at the centerline ($z = L_z/2$) for various shock-train configurations. Panel a, ——— , AR=∞ current simulation; – – –, AR=5 current simulation; —×—, AR=∞ LES Ref. [68]; Panel b, ——— , AR=2.257 current simulation; – – –, AR=1.5 current simulation; —×—, AR=2.257 LES Ref. [68]; •, exp. Ref. [21], AR=2.257. 82
5.7 Contours of the streamwise mean velocity component in the longitudinal midplane ($z = Lz/2$). Eleven evenly spaced contours from 0 to 1. Color contours, current simulation; black contour lines, LES data of [68] for the same aspect ratio. Panel a, AR=∞; panel b, AR=5; panel c, AR=2.257; panel d, AR=1.5 84
5.8 Contours of the mean velocity component in the wall-normal direction (y) in the longitudinal midplane ($z = Lz/2$). Eleven evenly spaced contours from -0.1 to 0.1. Color contours, current simulation; black contour lines, LES data of [68] for the same aspect ratio. Panel a, AR=∞; panel b, AR=5; panel c, AR=2.257; panel d, AR=1.5 85
5.9 Distribution of u/u_∞ in the wall-normal direction (y) at twelve streamwise locations in the longitudinal midplane ($z = Lz/2$). ——— , AR=∞ current simulation; – – –, AR=5 current simulation; —×—, AR=∞ LES Ref. [68] 86
5.10 Distribution of u/u_∞ in the wall-normal direction (y) at twelve streamwise locations in the longitudinal midplane ($z = Lz/2$). ——— , AR=2.257 current simulation; – – –, AR=1.5 current simulation; —×—, AR=2.257 LES Ref. [68] 86
5.11 Distribution of v/u_∞ in the wall-normal direction (y) at twelve streamwise locations in the longitudinal midplane ($z = Lz/2$). ——— , AR=∞ current simulation; – – –, AR=5 current simulation; —×—, AR=∞ LES Ref. [68] 87
5.12 Distribution of v/u_∞ in the wall-normal direction (y) at twelve streamwise locations in the longitudinal midplane ($z = Lz/2$). ——— , AR=2.257 current simulation; – – –, AR=1.5 current simulation; —×—, AR=2.257 LES Ref. [68] 87
5.13 Contours of the local Mach number in the longitudinal midplane ($z = Lz/2$). Eleven evenly spaced contours from 0 to 1.61. (a) AR=∞; (b) AR=5; (c) AR=2.257; (d) AR=1.5 88
5.14 Contours of the total pressure in the longitudinal midplane ($z = Lz/2$). Eleven evenly spaced contours from 0.8 to 4.8. (a) AR=∞; (b) AR=5; (c) AR=2.257; (d) AR=1.5 89
5.15 Streamwise distribution of the total pressure at various aspect ratios evaluated at the mid-plane ($z = Lz/2$) and at the duct centerline ($y = Ly/2$). 90
5.16 Contours of the Reynolds stress $\widetilde{u''u''}/u_\infty^2$ in the longitudinal midplane ($z = Lz/2$). Eleven evenly spaced contours from 0 to 0.016. Color contours, current simulation; black contour lines, LES data of Morgan et al. [68] for the same aspect ratio. (a) AR=∞; (b) AR=5; (c) AR=2.257; (d) AR=1.5 91
5.17 Contours of the Reynolds stress $\widetilde{v''v''}/u_\infty^2$ in the longitudinal midplane ($z = Lz/2$). Eleven evenly spaced contours from 0 to 0.08. Color contours, current simulation; black contour lines, LES data of Morgan et al. [68] for the same aspect ratio. (a) AR=∞; (b) AR=5; (c) AR=2.257; (d) AR=1.5 92

5.18 Contours of the Reynolds stress $\widetilde{w''w''}/u_\infty^2$ in the longitudinal midplane ($z = Lz/2$). Eleven evenly spaced contours from 0 to 0.08. Color contours, current simulation; black contour lines, LES data of Morgan et al. [68] for the same aspect ratio. (a) AR=∞; (b) AR=5; (c) AR=2.257; (d) AR=1.5 93
5.19 Contours of the Reynolds stress $\widetilde{u''v''}/u_\infty^2$ in the longitudinal midplane ($z = Lz/2$). Eleven evenly spaced contours from $-4.0\,10^{-3}$ to $4.0\,10^{-3}$. Color contours, current simulation; black contour lines, LES data of Morgan et al. [68] for the same aspect ratio. (a) AR=∞; (b) AR=5; (c) AR=2.257; (d) AR=1.5 94
5.20 Contours of the turbulent kinetic energy k/u_∞^2 in the longitudinal midplane ($z = Lz/2$). Eleven evenly spaced contours from 0 to 0.018. Color contours, current simulation; black contour lines, LES data of Morgan et al. [68] for the same aspect ratio. (a) AR=∞; (b) AR=5; (c) AR=2.257; (d) AR=1.5 95
5.21 Distribution of $\widetilde{u''u''}/u_\infty^2$ in the wall-normal direction (y) at twelve streamwise locations in the longitudinal midplane ($z = Lz/2$). ——— , AR=∞ current simulation; – – –, AR=5 current simulation; —×—, AR=∞ LES Ref. [68] . . . 96
5.22 Distribution of $\widetilde{u''u''}/u_\infty^2$ in the wall-normal direction (y) at twelve streamwise locations in the longitudinal midplane ($z = Lz/2$). ——— , AR=2.257 current simulation; – – –, AR=1.5 current simulation; —×—, AR=2.257 LES Ref. [68] 96
5.23 Distribution of $\widetilde{v''v''}/u_\infty^2$ in the wall-normal direction (y) at twelve streamwise locations in the longitudinal midplane ($z = Lz/2$). ——— , AR=∞ current simulation; – – –, AR=5 current simulation; —×—, AR=∞ LES Ref. [68] . . . 97
5.24 Distribution of $\widetilde{v''v''}/u_\infty^2$ in the wall-normal direction (y) at twelve streamwise locations in the longitudinal midplane ($z = Lz/2$). ——— , AR=2.257 current simulation; – – –, AR=1.5 current simulation; —×—, AR=2.257 LES Ref. [68] 97
5.25 Distribution of $\widetilde{w''w''}/u_\infty^2$ in the wall-normal direction (y) at twelve streamwise locations in the longitudinal midplane ($z = Lz/2$). ——— , AR=∞ current simulation; – – –, AR=5 current simulation; —×—, AR=∞ LES Ref. [68] . . . 98
5.26 Distribution of $\widetilde{w''w''}/u_\infty^2$ in the wall-normal direction (y) at twelve streamwise locations in the longitudinal midplane ($z = Lz/2$). ——— , AR=2.257 current simulation; – – –, AR=1.5 current simulation; —×—, AR=2.257 LES Ref. [68] 98
5.27 Distribution of $\widetilde{u''v''}/u_\infty^2$ in the wall-normal direction (y) at twelve streamwise locations in the longitudinal midplane ($z = Lz/2$). ——— , AR=∞ current simulation; – – –, AR=5 current simulation; —×—, AR=∞ LES Ref. [68] . . . 99
5.28 Distribution of $\widetilde{u''v''}/u_\infty^2$ in the wall-normal direction (y) at twelve streamwise locations in the longitudinal midplane ($z = Lz/2$). ——— , AR=2.257 current simulation; – – –, AR=1.5 current simulation; —×—, AR=2.257 LES Ref. [68] 99
5.29 Distribution of k/u_∞^2 in the wall-normal direction (y) at twelve streamwise locations in the longitudinal midplane ($z = Lz/2$). ——— , AR=∞ current simulation; – – –, AR=5 current simulation; —×—, AR=∞ LES Ref. [68] 100
5.30 Distribution of $k/\rho_\infty u_\infty^2$ in the wall-normal direction (y) at twelve streamwise locations in the longitudinal midplane ($z = Lz/2$). ——— , AR=2.257 current simulation; – – –, AR=1.5 current simulation; —×—, AR=2.257 LES Ref. [68] 100
5.31 Contours of the skin friction coefficient in the plane $y = Ly$ between -0.1 to 3.7 ($\times 10^-3$) overlay with 8 isocontours of the wall pressure scaled by $p2$ (black contour lines) from 1 to 1.7. (a) AR=∞; (b) AR=5; (c) AR=2.257; (d) AR=1.5 102
5.32 Skin friction lines overlay with 8 contours of the wall pressure rescaled by the wall pressure at the beginning of the interaction p_2 (red contour lines) from 1 to 1.7. (a) AR=∞; (b) AR=5; (c) AR=2.257; (d) AR=1.5; (e) AR=2.257, Oil flow visualization Ref. [21] 103
5.33 Contours of $\partial w/\partial y$ for various shock-train configurations overlay with 8 isocontours of the wall pressure scaled by $p2$ (black contour lines) from 1 to 1.7. (a) AR=∞; (b) AR=5; (c) AR=2.257; (d) AR=1.5 104
5.34 Instantaneous contours of the density gradient at various aspect ratios at the $y = Ly/2$ plane as a function of the normalized streamwise variable $x^* = (x - x_2)/\delta_1$. (a) AR=∞. (b) AR=5.0. (c) AR=2.257. (d) AR=1.5 106

5.35 Instantaneous contours of the density gradient at various aspect ratios at the $z = Lz/2$ plane as a function of the normalized streamwise variable $x^* = (x - x_2)/\delta_1$. (a) AR=∞. (b) AR=5.0. (c) AR=2.257. (d) AR=1.5 107

6.1 Contour of the power spectral density of the wall pressure (PSD(p_w)) on the upper wall $y = L_y$ (a) at a distance of 2 wall units from the lateral wall ($z^+ = 2$); (b) at the mid-plane ($z = Lz/2$). x^* being the rescaled streamwise variable $(x - x_2)/L$ and $St_L = fL/u_\infty$. 110
6.2 Contour of the power spectral density of the wall pressure (PSD(p_w)) on the upper wall $y = L_y$ (a) at a distance of 2 wall units from the lateral wall ($z^+ = 2$); (b) at the mid-plane ($z = Lz/2$). x^* being the rescaled streamwise variable $(x - x_2)/L$ and $St_{\delta_2} = f\delta_2/u_\infty$. Red lines indicate the first four tones given by equation 6.3. 111
6.3 Distribution of the amplitude of the wall pressure power spectral density at $St_{\delta_2} = 0.71$ as a function of the normalized streamwise variable $x^* = (x-x_2)/L$ at various spanwise locations and at the upper wall ($y = L_y$). (a) z/δ_1 =0; 0.05; 0.2. (b) z/δ_1 =1; 2; 3. (c) z/δ_1 =3.5; 5; 7. 112
6.4 Distribution of the amplitude of the wall pressure power spectral density at $St_{\delta_2} = 0.142$ as a function of the normalized streamwise variable $x^* = (x - x_2)/L$ at various spanwise locations and at the upper wall ($y = L_y$). (a) z/δ_1 =0; 0.05; 0.2. (b) z/δ_1 =1; 2; 3. (c) z/δ_1 =3.5; 5; 7. 113
6.5 Ritz eigenvalues of the DMD modes where λ_r and λ_i are the real and imaginary parts, respectively. Green diamond symbols indicate that the corresponding modes are plotted. 116
6.6 Amplitude of the modes as a function of the reduced frequency ($St_{\delta_2} = fu_\infty/\delta_2$). Red lines indicate the resonant frequencies and dashed blue lines correspond to the resolvability limits of the DMD (assuming 5 points per wavelength). Green diamond symbols indicate the two modes flanking the first resonant tone. (a) Resolved modes (b) zoom between $St_{\delta_2} = 0.06$ and 0.08. 116
6.7 Contours of the modal quantities to left of the first resonant mode tone ($St_{\delta_2} = 7.04.10^{-2}$; $St_L = 0.478$) (a) Modal streamwise velocity at mid-plane ($z = Lz/2$). (b) Modal pressure at the upper wall. (c) Modal y-velocity component at $x^* = 0.5$. (d) Modal z-velocity component at $x^* = 0.5$. 117
6.8 Contours of the modal quantities to right of the first resonant mode tone ($St_{\delta_2} = 7.16.10^{-2}$; $St_L = 0.486$) (a) Modal streamwise velocity at mid-plane ($z = Lz/2$). (b) Modal pressure at the upper wall. (c) Modal y-velocity component at $x^* = 0.5$. (d) Modal z-velocity component at $x^* = 0.5$. 118
6.9 (a) Streamwise distribution and (b) PSD in the streamwise direction of the two pressure modes flanking the resolved first acoustic tone 119
6.10 Contours of the modal y- and z-velocity components associated with the mean flow (the zero-frequency dynamic mode) at $x^* = 0.5$. (a) y-velocity component (b) z-velocity component 119

A.1 Contours of static pressure divided by the wall pressure at x_2 in the longitudinal midplane ($z = Lz/2$). Eleven evenly spaced contours from 0.9 to 2.4. (a) AR=∞; (b) AR=5; (c) AR=2.257; (d) AR=1.5 125
A.2 Density gradient magnitude for the case AR=2.257. 126
A.3 Contours of the modal quantities to right of the first resonant mode tone ($St_{\delta_2} = 7.4.10^{-3}$; $St_L = 0.05$) (a) Modal streamwise velocity at mid-plane ($z = Lz/2$). (b) Modal pressure at the upper wall. (c) Modal y-velocity component at $x^* = 0.5$. (d) Modal z-velocity component at $x^* = 0.5$. 127

List of Tables

4.1 Mach and Reynolds number at a reference station for our LES and the DNS of Pirozzoli and Bernardini [74] and Schlatter and Örlü [93]. Two simulations have been carried out one with a Smagorinksy sub-grid model (LES SMD) and one without sub-grid model (ILES). 53

4.2 Boundary layer and flow properties at the origin of the interaction (subscript 0). 57

5.1 Confinement parameters for the current LES of periodic shock-train and LES of shock-trains in ducts of various aspect-ratio, and, for the two LES of Morgan et al. [68] that consist of a periodic shock-train and a shock-train with an aspect ratio of 2.257; and for the experiment of Carroll and Dutton [21]. 75

5.2 Mesh parameters for the current LES of periodic shock-train and LES of shock-trains in ducts of various aspect-ratio, and, for the two LES of Morgan et al. [68] that consist of a periodic shock-train and a shock-train with an aspect ratio of 2.257. For our simulations the spacing is given in inner unit at the location x_2. Region of stretching are indicated with a dash. 76

5.3 Time-integration parameters for the statistics of the current LES, where t_0 is the initial time at which data is collected for statistics and T is the period of integration. (a) time is normalized by δ_1/u_∞; (b) time is normalized in throughput time ($\sqrt{\gamma}M_\infty.Lx/u_\infty$). 76

Chapter 1

State of the art

Contents

1.1 Introduction 13
1.2 Shock-wave turbulent boundary layer interaction: issues and general properties 17
1.2.1 Detached and attached interactions, inviscid and viscous theoretical approach 17
1.2.2 Mean flow and broadband unsteadiness in supersonic detached interactions 19
1.2.3 Transonic interactions 23
1.3 Shock-wave boundary layer with side walls effects 25
1.3.1 Supersonic interactions: experimental and numerical observations . . . 25
1.3.2 Experiment in transonic interactions, confinement effects 26
1.3.3 Shock-trains and pseudo-shock system 28

1.1 Introduction

Context

In 1945, on board of the Bell X-1, Chuck Yeager became the first human to break the sound barrier even though the knowledge of the flight mechanics and aircraft control in transonic flight regime was limited at that time. Since then, intense efforts within the aerospace community have been devoted to improve the understanding of the underlying flow physics. In particular, significant advances have been made regarding the aircraft design leading to more reliable and safer high speed vehicles.

Interactions between shock-waves and turbulent boundary layers are one of the most common and often unavoidable feature of high speed flights (transonic, supersonic or hypersonic). For more than 70 years, their role in limiting the aerodynamic performances have been widely investigated in both internal and external flow systems such as transonic wings, air intakes and supersonics diffusers. In all cases, the interaction between the turbulent boundary layer and the shock-wave produces intense aerodynamic and thermal loads that may lead to structural damages.

Focusing in particular on internal flows, the physical phenomena associated with shock-wave turbulent boundary layer interactions (SWBLI) play an essential role in catastrophic failure modes such as engine unstart. These interactions appear in a wide variety of internal systems, including ducts or supersonic inlets of aircraft engines. They produce complex flow structures which may involve multiple oblique or normal shock-waves depending, for example, on the engine's shape,

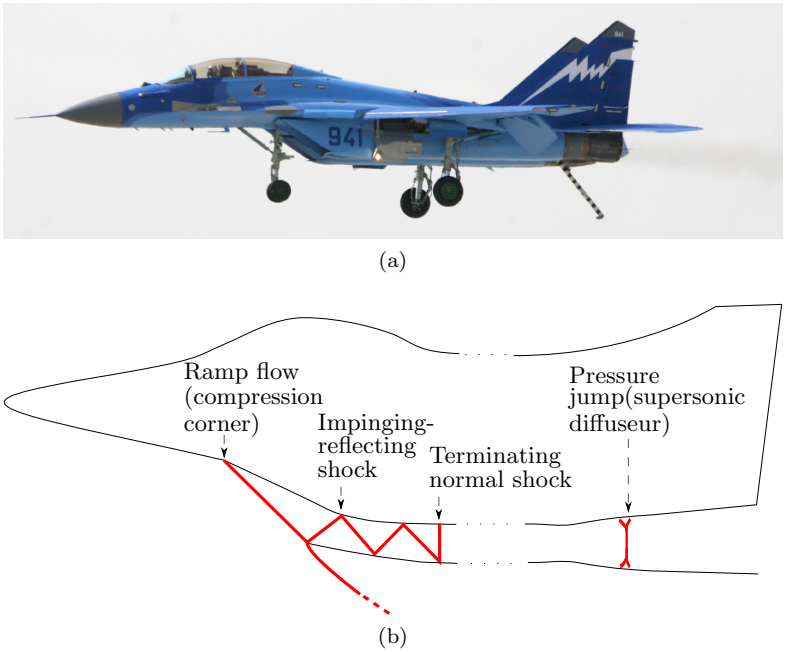

Figure 1.1: (a) Picture of a MIG-29K aircraft. Two squared air intakes can be observed under the aircraft. Retrieved from Wikipedia. (b) Schematic of the generation and propagation of shock-waves in supersonic aircraft engine. The shock-waves are drawn in red.

the upstream and downstream pressure conditions, the state of the upstream boundary layer, etc.

A simplified illustration of SWBLI occurring in supersonic air intakes is shown in figure 1.1. Due to the geometry constraints, the flow is first deflected though the formation of an oblique shock (in red), leading to a pressure rise and to a variation of the flow properties. Then, inside the air intake, a series of incident and reflected shocks form that produce a decrease of the Mach number and an increase of the pressure. Depending on the Mach number and on the Reynolds number of the flow (which have an influence on the properties of the boundary layer that develops along the air intake walls), as well as on the aspect ratio of the air intake (the ratio of the width over the height), either an oblique or normal shock-train forms [66].

In the present work we focus our attention on the so-called transonic interactions resulting from normal shock-train interacting with a turbulent boundary layer (ST) While significant advances have been made, especially regarding the 2.5D steady features of these interactions in the transonic regime, many aspects concerning the unsteady properties and their three-dimensional character of have not yet been fully explored [23, 29]. In particular, in order to reduce structural damages and dynamic loads, an accurate estimation of the temporal evolution of the wall pressure signature is of fundamental importance. Similarly, the unsteadiness and three-dimensionality of the flow and its topology are also strongly affected by the occurrence of secondary flows associated with corner effects typical of rectangular supersonic diffuser.

These phenomena being characterized by large disparate scales (both temporal ans spatial), the use of high-fidelity calculations including Direct Numerical Simulations or Large Eddy Simulations (referenced hereafter as DNS and LES, respectively) are essential for their physical understanding. A first preliminary attempt of high fidelity simulations of internal transonic shock-wave/turbulent boundary layer interaction has recently been conducted only by Morgan *et al* [67] in a rectangular duct, successfully exhibiting the most important flow features as observed in a realistic configuration.

The major challenge of transonic interactions in comparison with supersonic ones from the strong

sensitivity to the downstream subsonic flow conditions. Moreover, experiments are usually made at higher Reynolds numbers than the numerical simulations (high Reynolds number simulations [99] are still unaffordable). In addition, many questions remain open regarding the influence of the confinement and of the aspect ratio on the unsteady features. This thesis investigates three-dimensional aspects and unsteady features of transonic shock-wave/boundary layer interactions in a rectangular duct by means of wall resolved LES aiming to provide some insight into the full range of turbulence flow scales, wall pressure signature and corner flow effects.

The literature on shock-wave boundary layer interaction in internal flows is much less abundant than external configurations. For this reason, the first part of the state of the art is dedicated to the presentation of other types of interactions that have encountered much more interest these last decades and that share many similarities with the thesis subject. In order to illustrate the physical mechanisms involved in shock-wave turbulent boundary layer interactions in a duct, we first introduce the most widely seen SWBLI configurations. In an attempt to summarize the main properties of those configurations, we then expose the two main states of SWBLI (with or without a detached boundary layer) and its main unsteady characteristics. After this introduction to some of the general key aspects of SWBLI, a description of transonic interaction is given and the effects of side walls are detailed. Finally we conclude with the specificities of shock-trains which are a case of multiple shock-wave boundary layer interaction in duct flows.

SWBLI: first experiments and the need of classification

The first visual evidence of a shock-wave, provided by Mach [3] in 1887, has stimulated many researchers to investigate in more details shock-related phenomena. More than 50 years after Mach's pioneer work, the first[1] published experiment on SWBLI is presented by Ferri [40]. Shortly after Ferri's work [40], many published results are about the understanding of the main issues of SWBLI (see for instance, [30, 39, 62]... and [95] for more detailed list). However, the first configurations used by the previous authors involved too many factors to insure a clear understanding of the main mechanisms involved in SWBLI.

Since the 1950's[95] and until now, in order to clarify the role of the phenomena involved in SWBLI, simplified geometries and configurations are designed. Five main categories are defined that best describe and gather the most current elemental configurations of SWBLI [5, 27]. Experimental Schlieren visualisation of the instantaneous flow field for the five configurations are shown in figure 1.2. The differences between canonical flow configurations are mainly driven by the way the shock-waves are formed, either by a deflected surface, an external shock generator or an imposed pressure gradient. These configurations regard quasi two-dimensional flows (*i.e.* the flow is assumed to be periodic in the spanwise direction) and their descriptions are given below:

a) Normal shock
A normal shock is generated by an increased back pressure. Downstream of the shock the flow is subsonic and the incoming flow is supersonic so the interaction is transonic. One peculiarity is that all perturbations downstream of the shock may influence the interaction whereas in supersonic interactions, only a near-wall zone is subsonic.

b) Impinging-reflecting oblique shock
An oblique shock is generated upstream of the interaction and impacts the boundary layer. The shock-induced pressure gradient thickens the boundary layer upstream of the impinging point. The thickening of the boundary layer deflects the flow and produces a reflected shock.

c) Ramp flows
The flow trajectory is modified caused by a bending of the wall (a compression corners). The bending angle may be sufficiently small to keep the boundary layer attached but the deflection of the flow produces a shock-wave. The incoming boundary layer is thickened by

[1] According to Adamson and Messiter [2] and Dolling [29]

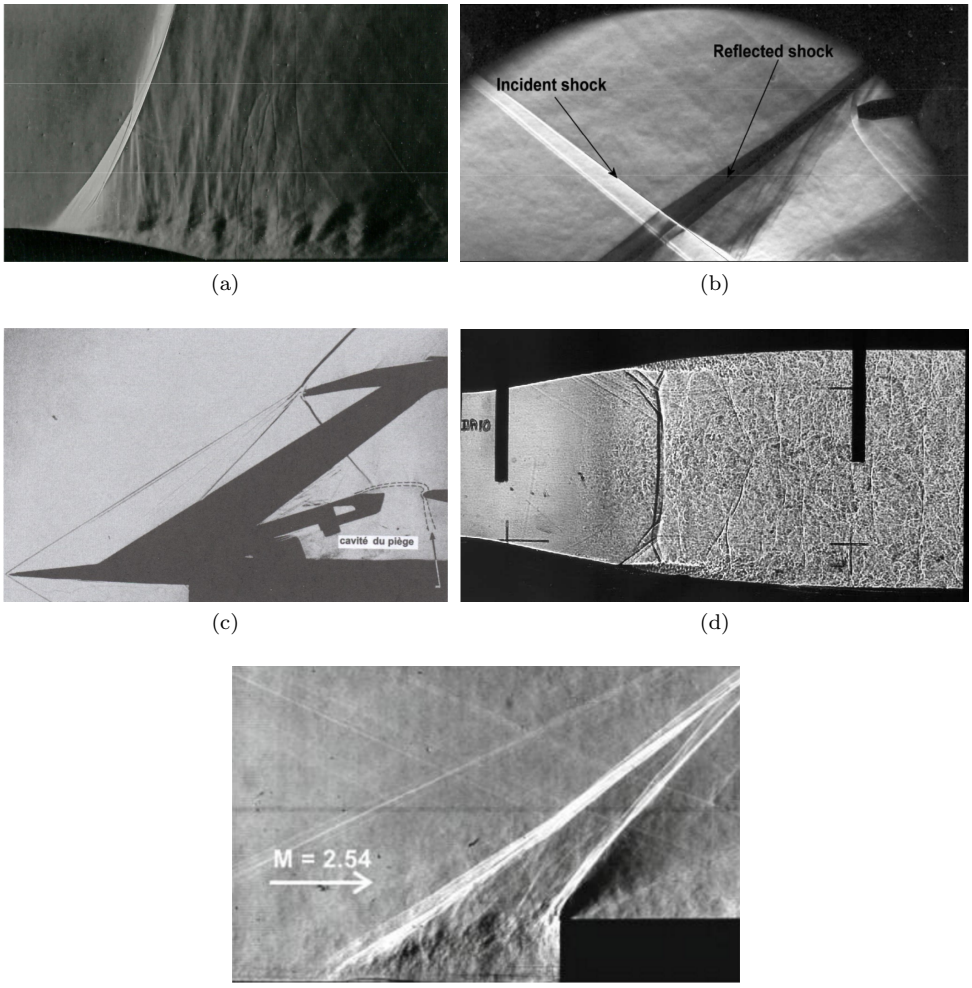

(a) (b) (c) (d) (e)

Figure 1.2: Experimental Schlieren visualization of the different categories of SWBLI: (a), a transonic interaction over a bump [34]; (b), an oblique shock-wave boundary layer interaction [34]; (c), a compression corner interaction [37]; (d), a shock-wave boundary layer interaction in an over expanded diffuser [14]; (e), an oblique shock induced by the separation in front of a forward-facing step [55]

the shock-wave induced pressure gradient. The compression are moved downstream of the corner, where the boundary layer thicken.

d) Imposed pressure jump
An imposed pressure jump modifies the trajectory of the flow leading to the production of an oblique shock. This case is characteristic of supersonic diffuser.

e) Oblique shock induced by a forward-facing step
The shock encounters an obstacle that produces a separation upstream of the flow. The upstream separation deflects the flow and generates an oblique shock. The oblique shock interacts with the incoming boundary layer.

These configurations share general features as underlined by Délery and Dussauge [27]. In particular, the mean flow properties, the scaling laws and the flow unsteadiness are strongly governed by the presence or absence of a detached boundary layer. Thus in the following we first summarize some of the main characteristics of attached and detached interactions that are most likely common between any SWBLI (including the interactions studied in this document).

1.2 Shock-wave turbulent boundary layer interaction: issues and general properties

1.2.1 Detached and attached interactions, inviscid and viscous theoretical approach

A common aspect of SWBLI is the occurrence of a separated area when the pressure gradient induced by the presence of the shock is strong enough. In figure 1.3, we show a comparison of the wall pressure distribution between an inviscid theory and an analysis that incorporates the viscous effects. On the left, the wall pressure distribution for an attached SWBLI (i.e without separation) or also called a "weak" interaction is shown. The word "weak" is used to indicate that the solution is *"weakly affected by the viscous effect"* [5]. The main difference between the viscous and inviscid wall pressure distribution is that in the viscous case, the origin of the interaction is moved slightly upstream due to the presence of a subsonic zone in the boundary layer that produces an upstream (with respect to the nominal shock position) propagation of pressure disturbances associated with the pressure jump across the shock. The boundary layer remains attached through out the whole interaction.

For strong interaction i.e the boundary layer is detached from the wall (see figure 1.3b), the wall pressure distribution exhibits a plateau (no such a characteristic is observed for attached flows) between the separation point of the boundary layer (S) and its reattachment (R). Separation of the boundary layer occurs in the vicinity of the first pressure increase while a second pressure rise is observed during the reattachment of the flow.

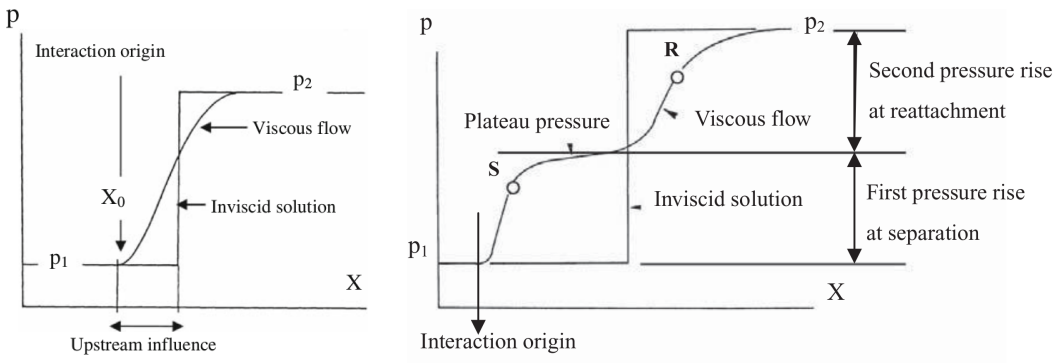

(a) attached flows (b) separated flows

Figure 1.3: Typical wall pressure distributions for SWBLI. Reprinted from Délery and Dussauge [27].

For both laminar and turbulent regimes, a theory that relies on a multiple-deck analysis emerged in the middle of 20^{th} century to model mean flow properties of shock-wave boundary layer interaction. As proposed by Lighthill [63], the structure of the boundary can be divided into multiple sub-layers. In figure 1.4, an illustration of the triple deck structure is shown: 1) the outer part of the boundary layer is mostly potential and irrotational; 2) the middle deck is rotational and inviscid; and 3) the inner deck is viscous and rotational. While the viscous time and length scale are greater than the flow characteristic scales, this approach remains valid. When the boundary layer is submitted to an adverse pressure gradient imposed by the shock, it undergoes modification over a time and length scale that are shorter than the viscous ones, except in the viscous layer where viscous effects are dominant ([5, 27]). The shock is modelled as a forcing function that is applied on the outer deck system of equations. The disturbed system of equations is simplified, keeping only the leading order scales (see [5] for more details).

While for a wide range of two dimensional configurations an attached flow can be approximated with such an analysis, the separated interaction remains a hard task since viscous scales dominate

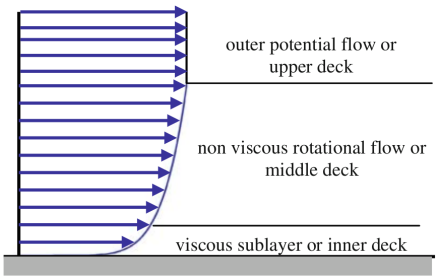

Figure 1.4: The interaction flow multi-layer structure or triple deck [27]

and the assumption of minor viscous effect is not valid. In that respect, the determination of critical parameters that induce the flow separation and the separation extent or separation length L have been the topic of many theoretical investigations.

A major reference to determine the onset of separation, based on the triple deck approach, is the work of Stewartson and Williams [100], and is approach. This theory, usually called "the free interaction theory" (name proposed by Chapman *et al* [22]), assumes that *"the pressure rise at separation and the extent of the first part of the interaction depend only on the flow properties at the separation onset and not on the downstream condition"* [27]. This property is well verified experimentally for quasi two-dimensional flow (3D flow with mean properties homogeneous in the spanwise direction, also noted 2.5D flow).

Apart from the critical parameters associated with the onset of flow separation, the knowledge of the interaction extent, is also of fundamental interest due to the strong effect of the SWBLI unsteadiness on the wall pressure loads. Using the free interaction theory, the interaction length L is proportional to $L \propto \delta_0^*.C_{f_0}^{-1/2}.(M_0^2-1)^{-1/4}$ [5], where the boundary displacement thickness (δ_0^*), the skin friction coefficient (C_{f_0}), the Mach number (M_0) are evaluated at the origin of the interaction. Upstream of the interaction the flow is undisturbed by the shock and the skin friction can be related to the Reynolds number. Thus, the interaction length scales with the Reynolds number, the boundary layer displacement thickness and the Mach number upstream of the interaction. For the case of transonic interactions, Delery & Marvin [28] show that $L \sim 70\delta_0^*(H_{i_0}-1)$, where H_{i_0} denotes the incompressible shape factor (defined as the ratio of the incompressible displacement thickness δ_i^* over the incompressible momentum thickness θ_i). To summarize, the main parameters [5] that are likely to influence the interaction length are:

- Mach number
- Shock intensity parameter (ramp angle, angle of flow deflection...)
- Boundary layer thickness
- The Shape factor H_{i_0}
- Local Reynolds number

The first two parameters are a measure of the strength of the "inviscid disturbance", and; the last three parameters characterize the state of the boundary layer and its ability to resist separation [23].

Despite the valuable informations provided by the free interaction theory, data scattering between analytical and experimental approaches and the impossibility for analytical approaches to describe three-dimensional aspects and unsteadiness of SWBLI motivate the use of both experimental approach and simulations to increase the understanding of SWBLI. Regarding the numerical simulation issues, the absence or presence of boundary layer separation, conditions the choice of the numerical model. For example, the averaged solutions obtained by means of the Reynolds-averaged Navier-Stokes (RANS) equations may produce acceptable results as long as the boundary layer remains attached through the whole interaction. Nonetheless, to close the RANS system of equations a model is required, and as soon as the boundary layer is detached

no general modelling has been been proposed that makes it possible to predict the SWBLI flow properties with an acceptable error [29, 58]. Moreover, RANS only provides a stationary flow field. To increase our understanding of SWBLI via simulation tools, other mathematical/numerical models have to be used. In particular, due to change of the interaction dynamics and scales, high-fidelity models are needed to simulate interaction with separated flows.

The increase of the available computational power and development of improved compressible numerical schemes have made possible to simulate SWBLI either by DNS or by LES. Due to their expensive computational costs, direct and large-eddy simulations are often restricted to cases with Reynolds number values lower than the experimental ones. Since 1990's, both methods have shown to be able to forecast most of the SWBLI properties with or without separation of the boundary layer[2] [1, 45, 53, 91, 103] We now details some general aspects of the mean and unsteady properties of SWBLI based on experiments and numerical simulations.

1.2.2 Mean flow and broadband unsteadiness in supersonic detached interactions

Most of the recent numerical work on the SWBLIs focus on the study of impinging-reflecting shock and ramp flow. In these cases, the outer flow (*i.e.* outside the boundary layer) remains supersonic through out the SWBLI. This subsection presents briefly the findings on supersonic interactions.

If the pressure jump across the shock is sufficiently large, the resulting pressure gradient may lead to the separation of the incoming boundary layer. For ramp flow configuration [81, 82], the deflection of the flow leads to the generation of compression waves, upstream of the ramp, that coalesce to generate an oblique compression shock. If the ramp angle is large enough, the resulting separated flow at the foot of the shock exhibits complex flow features, with different characteristics length scales such as the incoming boundary layer thickness, the separation length, the mixing layer thickness, and, velocity scales such as the friction and convection velocity.

In the case of impinging shock-wave/supersonic boundary layer interaction [16, 27, 49, 69, 71, 77, 101], the boundary layer separates if the pressure jump across the shock is strong enough. The interaction thus leads to compression waves behind the bubble that coalesce producing the separation shock. The mean flow exhibits similar phenomena as in the compression ramp interaction.

[2] More precisely, Hunt and Nixon [53] in 1995 and Urbin et al. [103] in 2000 have simulated the first VLES (very large eddy simulation) and LES of a SWBLI over compression ramp, the first published LES of an impinging shock-wave and of a transonic interaction are made by Garnier et al. [45] in 2002 and by Sandham et al. [91] in 2003, respectively. The first DNS of a SWBLI over a compression ramp is published by Adams [1] in 2000.

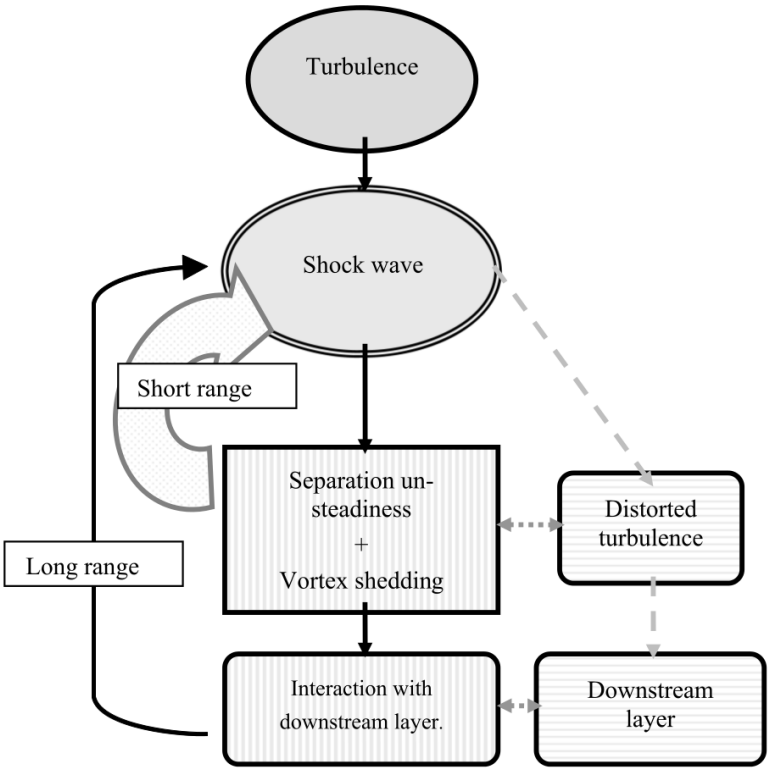

Figure 1.5: Diagrammatic representation of the different mechanisms involved in quasi two-dimensional SWBLI. Reprinted from Dussauge [34]

Regarding the unsteadiness, multiple phenomena may interact inside the SWBLI as noted by Dussauge [34]: "the amplification of incident turbulence through the shock, the properties of the separated bubbles, [...] the response of the shock-wave to these excitations, the vortex shedding of large scale structure into the reattached layer, and finally the merging of these vortices into a new boundary layer relaxing to a new equilibrium." (illustrated in figure 1.5).

Based on the previous mean flow considerations, if we assume that the flow coherent motion are driven by characteristic length and velocity scales, the different flow cases may exhibit similar characteristic unsteadiness, when using an appropriate scaling Dussauge [34]. In particular, both numerical simulations and experiments have shed some light on the broadband activity of the SWBLI. In that respect, the power spectra exhibits a broadband bump in the mixing layer region of the order $O(0.1u_\infty/\delta)$ as well as characteristics high frequencies ($O(u_\infty/\delta)$) associated with near wall turbulent boundary layer region [81]. Furthermore, in addition to mean flow separation developing with increasing interaction strength, an unsteadiness appears at frequencies ($O(0.01u_\infty/\delta)$) much lower than the characteristic frequency of the energetic eddies in the incoming boundary layer [81]. To illustrate this comment, in figure 1.6 we report the fluctuations of the streamwise velocity component for the oblique SWBLI of [101]. The figure shows that the flow is dominated by near wall streaks structures upstream of the incident shock while downstream of the shock it is populated by larger scale motions associated with the eddies along the shear layer.

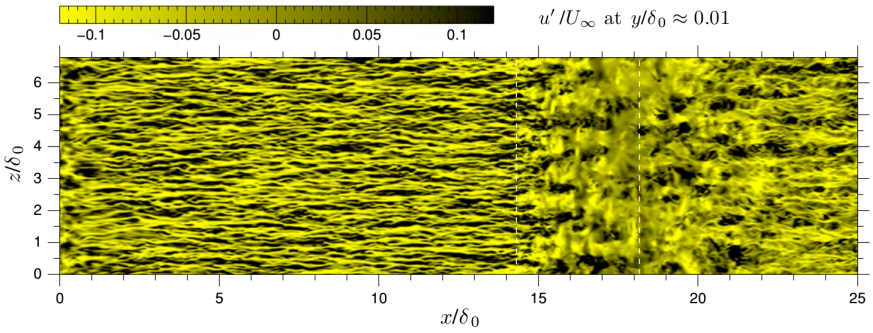

Figure 1.6: Visualisation of the streamwise velocity fluctuations in the plane $y = 0.01\delta_0$. Reprinted from Touber and Sandham [101].

While the high and medium frequencies are well understood, the physical origin of the low-frequency shock motion is still not fully explained. Previous works have correlated the low-frequency shock motion with fluctuations in the incoming boundary layer (upstream influence of superstructures $O(10\delta)$ associated with the turbulent boundary layer [41, 42]) or with the eddies developing along the separated flow leading to a low frequency breathing of the bubble [23, 71]. Different conclusions have been drawn as to whether the shock motion is caused by a low-frequency mechanism in the upstream or downstream flow.

When considering an equilibrium state corresponding to a mean flow, a linear behaviour of the dynamical system based on a global intrinsic phenomenon is sometime observed (i.e. emergence of a global mode). The low-frequency unsteadiness has been suggested to be a global response to an external forcing perturbation [48, 92]. Nonetheless, no global mode clearly emerged from those analysis. Consistent with the findings of Plotkin [78], Touber and Sandham [102] recently proposed a low order model that shows that the dynamical system, composed of the shock foot and the upstream turbulent boundary layer, behaves as a low-pass filter. In their approach, the physical mechanism at the origin of the external perturbations (which trigger the low-frequency unsteadiness) is not specified.

Independently of the scenario, as initially suggested [3] by Dussauge [34], these low-frequency unsteadiness scales with the upstream velocity u_∞ and the interaction length scale L. Hence introducing a Strouhal number $St_L = f.L/u_\infty$, three main sources of unsteadiness are observed and associated with: the upstream turbulence of the boundary layer of relatively high frequency $St_L \sim O(10^0)$; "medium" frequencies in the range $0.1 \leq St_L \leq 0.5$ characteristic of the shear layer (associated with Kelvin-Helmholtz instability for fully separated flow); and the displacement of the shock foot whose frequency is generally spanning the range $0.02 \leq St_L \leq 0.05$ [33].

In figure 1.8 we report the LES results of Ref [4] for impinging shock interaction (panel a) and the DNS results of Ref [81] (panel b) for a compression ramp SWBLI. In figure 1.8 we report the experimental results of Ref [33] for impinging shock interaction with different shock angles. The figure shows that the Strouhal number St_L associated with the low-frequency motion of the shock is similar.

[3] "independently of the geometry of the particular configurations, these situations seem to share some common properties, like frequency of the shock system motion conveniently normalized" [34].

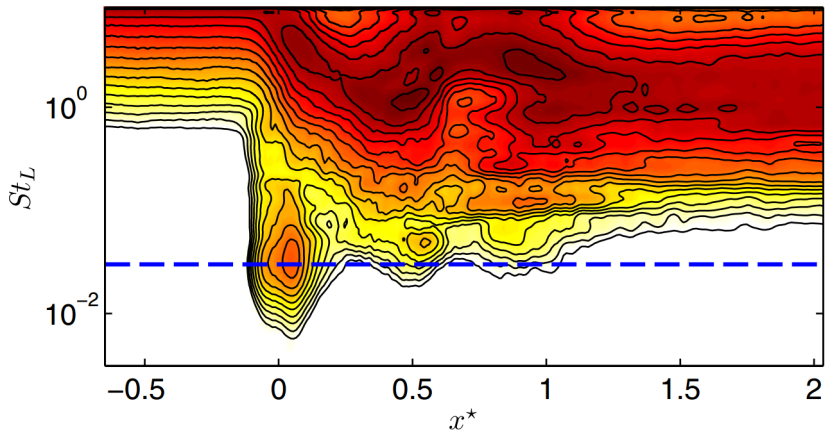

(a)

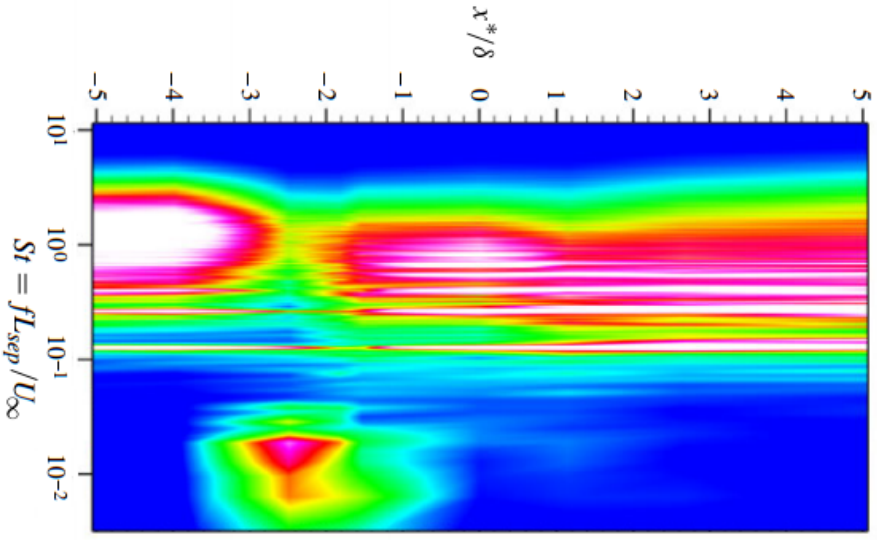

(b)

Figure 1.7: Isocontour of the spanwise averaged pre-multiplied PSD of the wall pressure (arbitrary scale) with $x^* = (x - x_0)/L$ the streamwise position defined as the distance to the shock rescaled by the interaction length and St_L the Strouhal number based on the interaction length. (a) Large eddy simulation of a oblique shock-wave boundary layer interaction. The shock impact the wall with an angle of 30.8 degree in Mach 2.15 flow. The blue line indicate a Strouhal number of 0.03 ($St_L = 0.03$). Reprinted from [4]. (b) Direct numerical simulation of a shock-wave–turbulent boundary layer interaction generated by 24 degree compression ramp in Mach 2.9 flow. Adapted from [81]

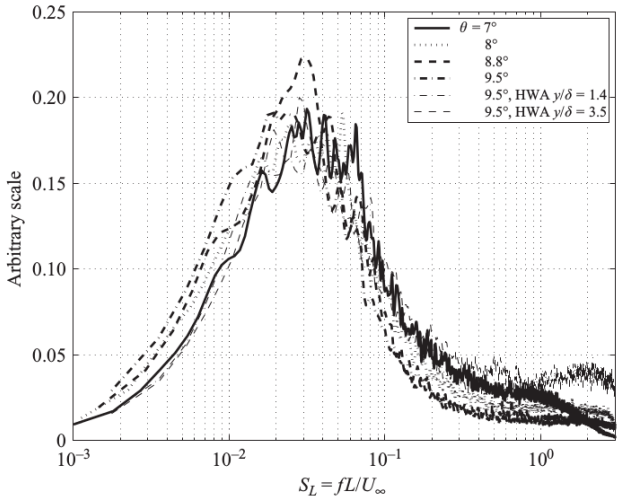

Figure 1.8: Power spectral density of the wall pressure fluctuations and the streamwise momentum fluctuations measured with hot wire anemometry (HWA). Date are obtained at the mean location of the foot shock for different angles of deflection of the initial impinging shock. Reprinted from Dupont et al. [33]

1.2.3 Transonic interactions

In the following, the case of transonic interactions are detailed.

Shown in figure 1.9 is a sketch of the normal SWBLI (without separation) is drawn. Outside the boundary layer, the upstream supersonic flow becomes subsonic as it goes through the shock. Closer to the boundary layer edge the shock is slightly curved and as it enters the upper part of the boundary layer it gives rise to compression waves that progressively compress the flow. As a consequence, the flow passing through the "shock foot" undergoes a near-isentropic compression over a finite streamwise extent. Since the boundary layer is submitted to an adverse pressure gradient, it thickens and the flow is deflected from the wall.

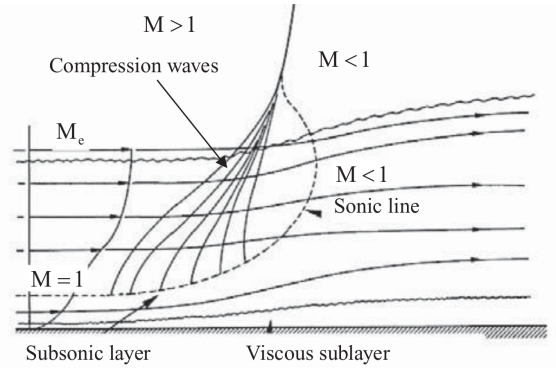

Figure 1.9: Schematic of the flow induced by a normal SWBLIs without separation. Reprinted from Babinsky and Harvey [5]

In the case of a transonic interaction with separation (figure 1.10) a lambda λ shock structure forms. The normal shock $C3$ bifurcates above the boundary layer into two shock-waves: $C1$ and $C2$. The shock $C1$ the so-called separation shock resulting from the coalescence of the compression waves, while the shock $C2$ is the so-called reattachment shock. Downstream of $C2$ the flow can be either subsonic or supersonic with Mach number close to unity. When the flow Mach number is supersonic, the flow undergoes an almost isentropic compression attaining

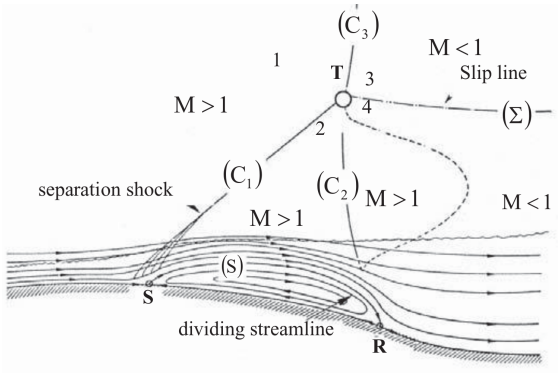

Figure 1.10: Schematic of the flow induced by a normal SWBLIs with separation. Reprinted from Babinsky and Harvey [5]

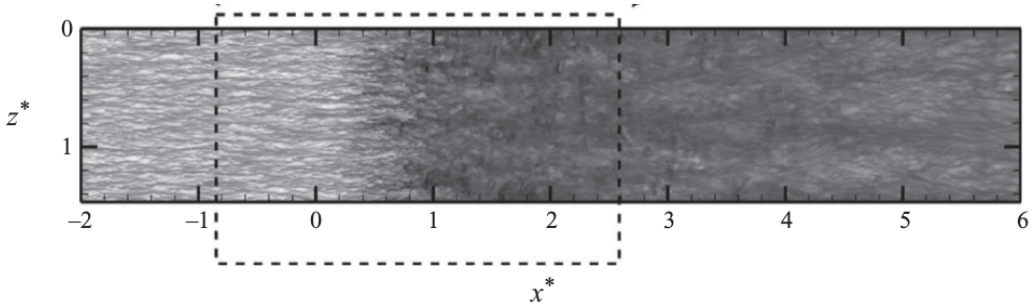

Figure 1.11: Instantaneous streamwise velocity fluctuations u' at $y^+ = 10.8$ of an incipient transonic interaction. Reprinted from Pirozzoli et al. [76]

subsonic conditions. In this case, the region comprised by C2 and the sonic line is called the "supersonic tongue"[5].

The λ-pattern of the shock is composed of four states: State 1 corresponds to the upstream flow state; State 2 is the state corresponding to the Rankine-Hugoniot (RH) jump conditions across the oblique shock C1; State 3 is the solution of the RH jump conditions across the normal shock C3; State 4 is the solution of the RH jump conditions connecting state 2 and 4; and in general differs from state 3; as a consequence, a slip line (Σ) forms. The point "T" is the "triple point".

While the above mean flow properties and shock structures of the interaction are specific to the transonic interaction, global properties are shared with other interactions. For instance, regarding the evolution of the structure in the inner region of the boundary layer, figure 1.11 shows that before and after the shock the flow exhibits similarities with the supersonic case (figure 1.6) *i.e.* the flow is dominated by near wall streaky structures upstream the incident shock while downstream of the shock it is populated by larger scale motion associated with the eddies along the shear layer.

Although the flow shares many similarities with supersonic interactions, for transonic flow, the subsonic region downstream of the shock may also propagates information and influences the shock motion. As a consequence, the question of a common mechanism that may produces low-frequency unsteadiness is unanswered.

In fact, for the buffet case, a feedback mechanism between the edge of the wing profile and the shock might be observed. Slow acoustic waves propagating against the external flow can influence the unsteadiness of the system [83, 84].

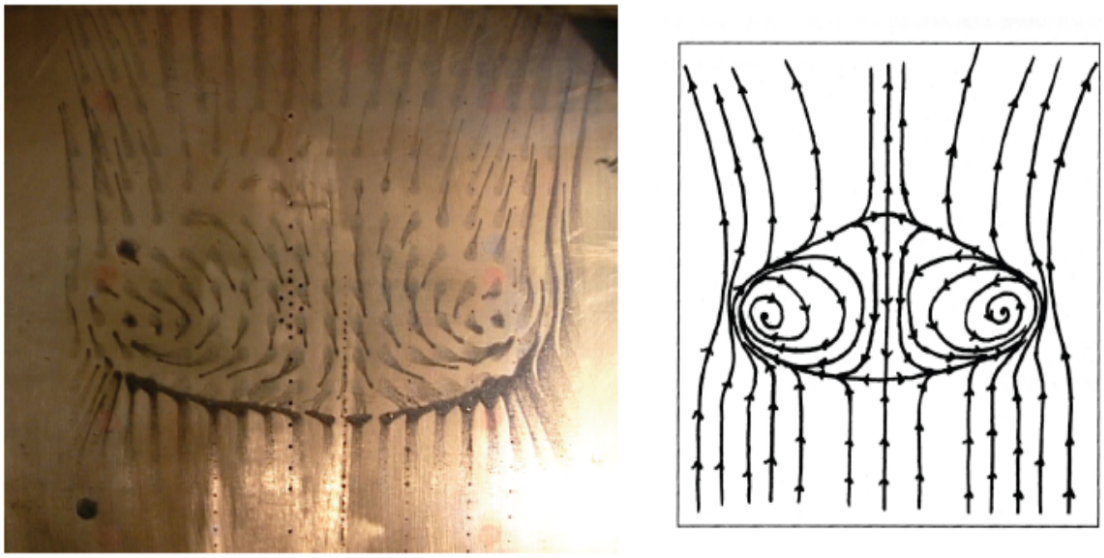

Figure 1.12: (a) Oil flow measurements and (b) surface flow sketch for a oblique shock-wave boundary layer interaction at $M_\infty = 3$ from [13]. The flow is from bottom to top. An important spanwise velocity component is observed that sweep flow from the centerline towards the side walls.

1.3 Shock-wave boundary layer with side walls effects

For practical reasons, most of the supersonic experiments are carried out in wind tunnels of finite span where side walls effects are inevitable and estimating the influence of side walls is a major issue. Furthermore, in the presence of lateral walls the confinement of the flow modifies the evolution of pressure and velocity outside the boundary layer. In addition, turbulent boundary layers and secondary flow motions (as identified by Prandtl [15, 80]) introduce new sources of turbulence and unsteadiness. Side walls also play an important role in determining the size and shape of the recirculation bubble, which in turn may influence the characteristics of the interaction dynamics including low-frequency motion.

1.3.1 Supersonic interactions: experimental and numerical observations

In figure 1.12, we report the oil flow visualization (panel a) and a sketch of the skin friction lines (panel b) of SWBLI in the presence of side walls. The figure show that the friction lines are curved in the presence of side walls while in quasi two-dimensional interaction they remain straight during the interaction. Two counter-rotating vortices (associated with the three-dimensionality of the interaction) forms. They produce an additional spanwise velocity component inside the recirculation bubble and modify the dynamics of the interaction. Moreover, the interaction length vary in the spanwise direction.

The modification of the interaction topology is often coupled with a modification of the shock structure. The latter is modified as it interacts with the side walls boundaries as shown in the experiments of Helmer et al. [51] and Wang et al. [107], and in the simulations of Bermejo-Moreno et al. [7] and Wang et al. [108].

The latter authors have also analysed the influence of the aspect ratio and find that for a width over height ratio of 4, the flow field in the central plane is close to that of a corresponding quasi-2D case. As the aspect ratio of the duct is decreased, they observe that the separation and

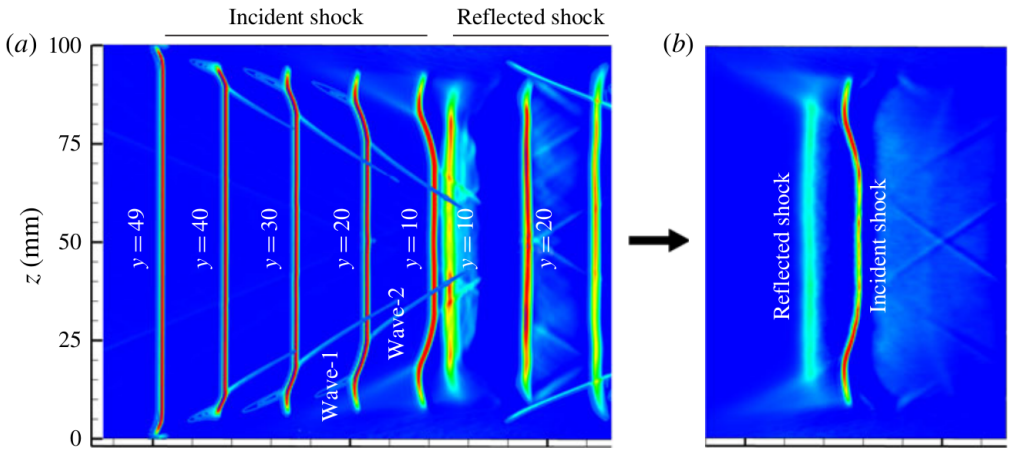

Figure 1.13: Distortion of the main shock-waves is illustrated with contours of the time- averaged streamwise density gradient for a moderately separated oblique shock-wave/boundary-layer interaction at $M_\infty = 2.7$ in a rectangular duct with an aspect ratio of 2. (a) Show shock-waves above the interaction region, with shock structures from five different x–z planes (at y = 49, 40, 30, 20 and 10 mm) superimposed. (b) Show the shock structures on the x–z plane at y = 6 mm, *i.e.* close to the location where the shock impinges on the apex of the recirculation bubble. Reprinted from Wang et al. [108]

reattachment points on the central plane move upstream simultaneously, while the bubble extent initially increases and then stabilizes with a length 30 times larger than the quasi-2D case. For their cases with an aspect ratio smaller than 4, the incident shock on the central plane is found to be curved and strengthened even before the interaction (figure 1.13, left panel).On the spanwise edge of the shock, progressive compression waves are visible and look similar to the "λ" pattern observed in transonic interaction. The impinging shock that interact with the boundary layer on the duct floor is curved (figure 1.13, right panel) whereas for a two-dimensional interaction the shock is straight.

Evidence of the influence of corner flows are also found in the experiments by Dupont et al. [33] who use vorticity detectors placed at different heights to infer the presence of two counter-rotating vortices near the corners. The rotation frequency of these corner vortices is found to be of the same order as the low-frequency motion of the reflected shock, suggesting that there is also a direct link between the two.

To close this subsection, one can remark that studies on the impact of the corner flow on the unsteadiness of the SWBLI are limited in numbers. A few recent numerical studies have attempted to show the influence of side walls [45, 108] but no wall-resolved LES or DNS have been performed that assess the effect on the wall pressure signature. The WMLES of Bermejo-Moreno et al. [7] shows that the frequencies at which these low-frequency motions occur are consistent with the range found in prior studies in the literature but no clear conclusion can be drawn. And yet, according to [33, 35], the three-dimensionality in separated SWBLI field has the potential to contribute to the flow unsteadiness. Recent work [6, 16, 17, 19] shows that the corner effects may strongly influence the structure of the SWBLI.

1.3.2 Experiment in transonic interactions, confinement effects

As the experimental tools become more precise and quantitative (progress in PIV, LDV ...) criteria on the minimum aspect ratio required to obtain a centerline 2D flow has changed, the understanding of the influence of aspect ratio is progressing. A recent experimental work [104, 105] on a fully developed turbulent incompressible boundary layer in a duct flow (considering two boundary layers from opposite walls spatially developed and are merged) has investigated

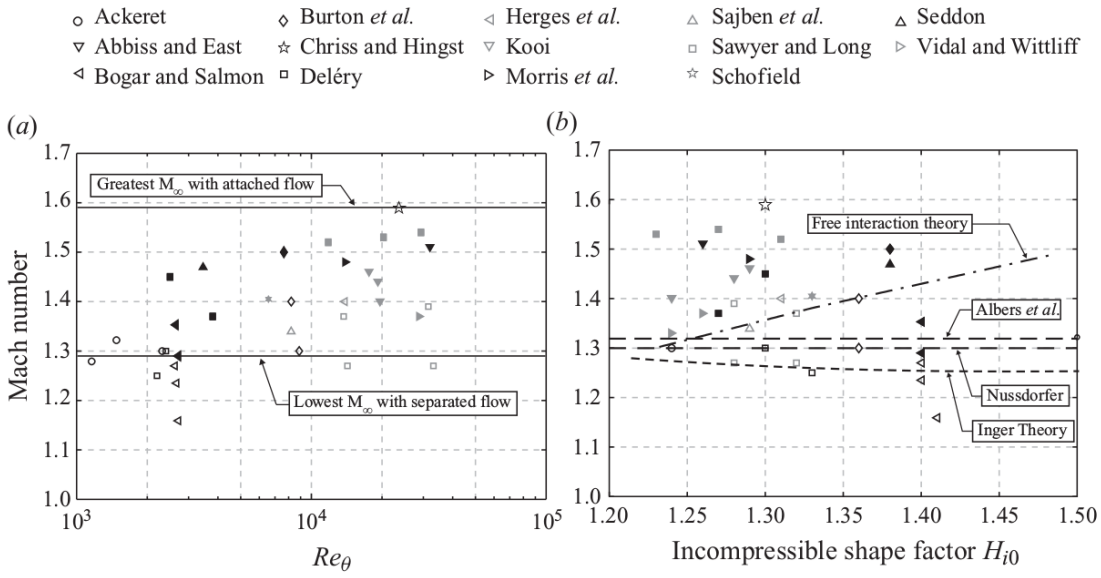

Figure 1.14: Experimental data for attached (open symbols) and separated (filled symbols) transonic SWBLIs. Reprinted from Bruce et al. [17]

the influence of AR at moderate Reynolds number ($Re_\tau \in [200\,;900]$). Comparison with a quasi-two-dimensional DNS show that side walls effects are always observed. Those authors conclude that "*the conditions observed in the homogeneous region of a high-aspect-ratio turbulent duct flow do not match the exact ones found in a spanwise-periodic channel*". In this context, it is possible that some experimental SWBLI are influenced by the presence of side walls, whereas the interaction was originally assumed to be quasi-two-dimensional.

In figure 1.14, we report data from Ref. [17] that analysed transonic SWBLI experiments originally collected by Sajben et al. [90] and classified as being nominally two dimensional (*i.e.* 2.5D). In the figure, open and full symbols indicate, respectively, attached and separated flow. In panel a, data is reported as a function of $Re_\theta$and in panel b data is reported as a function of H_{i_0}. As observed by Bruce et al. [17], the data is rather scattered and no clear indication of separation criteria can be identified when using these parameters introduced to characterize "classical" SWBLI (*i.e.* without considering the influence of side walls).

Recent works [6, 16, 17, 19] show that side walls effects associated with the interaction between secondary flows induced produced by the corners and separation (see figure 1.15), may explain some of the data scattering observed in figure 1.14. To account for the confinement and/or 3D effects, Bruce *et al*[17] introduce the "effective aspect ratio" δ^*/W, where δ^* is a displacement thickness and W is the wind tunnel width. Plotting the data reported in figure 1.14 versus the upstream Mach number and the effective aspect ratio, a better data reduction is obtained. Two distinct regions are clearly identified (figure 1.16): a region where a fully developed centerline mean separation is observed from a region where the separation is either intermittent or non-existent. Furthermore, the free interaction theoretical limit of quasi-two-dimensional-separation occurring at Mach 1.31 is recovered (which is not the case using the scaling of figure 1.14) The data are organized in two distinct regions (except for one case out of thirty-two), that has fully-developed-centerline separation but is located in the attached-boundary-layer region. This "suggests that geometrical differences between experimental facilities are a significant factor that can affect the onset of separation" [17].

In the presence of corner flows, the velocity profile is less "full". As a consequence the boundary layer in the vicinity of the corner is more prone to separation when subjects to strong adverse pressure gradient [17]. This causes more extended separation (than the centerline separation) that can spread upstream and downstream of the zone of the APG. Figure 1.16 shows that

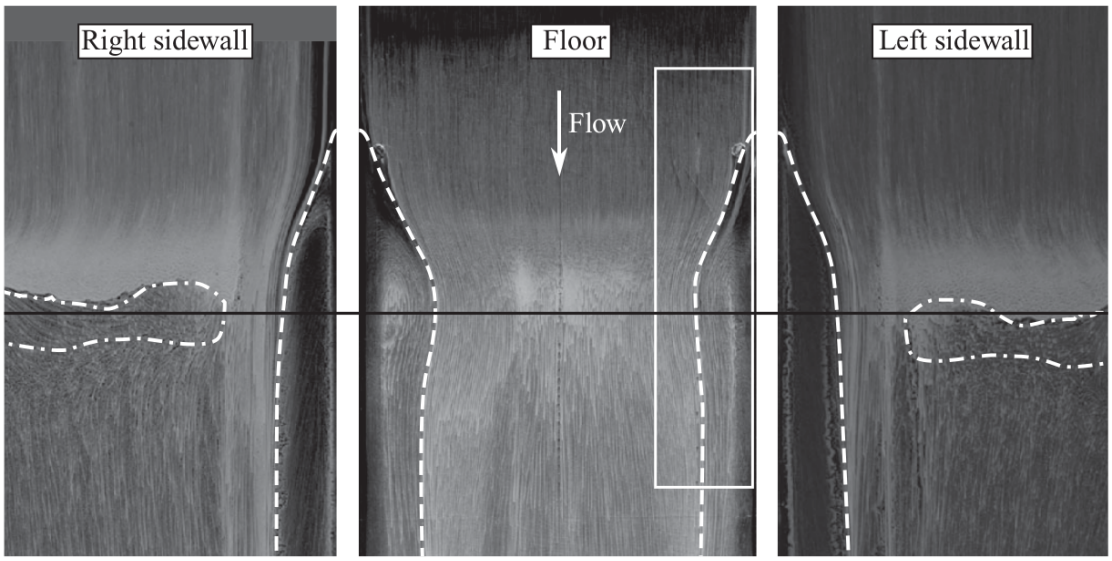

Figure 1.15: Oil flow patterns on the tunnel floor and sidewalls for a $M_\infty = 1.4$ shock. Only the bottom half of the tunnel side walls are shown. Reprinted from Bruce et al. [17]

confinement seems to reduce the likelihood of centerline separation.

From this observation Bruce *et al* [17] propose two scenario: the first one assumes that the blockage effect generated by the corner flows may be sufficient to decelerate the flow in the supersonic region and/or to accelerate the flow in the post-shock subsonic region. Thus an "aerodynamic nozzle" is produced that may smear the adverse pressure gradient imposed by the normal shock-wave. The other one takes into account the production of compression waves associated with corner separation (see figure 1.17). When the boundary layer is submitted to an adverse pressure gradient (APG) it thickens, and in the vicinity of the corner, compression waves upstream of the centerline interaction are produced. If the shock is sufficiently strong a large three-dimensional bifurcation of the shock-wave structure can be observed and depending on the effective aspect ratio the compression waves may cross before or after the shock (figure 1.17). When the compression waves, originating from the corner cross after the shock-wave it is expected that the interaction length increases [6]. On the contrary, when corner waves cross upstream of the shock, it is unclear whether or not the corner waves may be sufficiently strong to trigger the separation.

1.3.3 Shock-trains and pseudo-shock system

As mentioned above, SWBLI in internal flow are modified and affected by the confinement. When the confinement effects are sufficiently strong a shock-train forms. At low supersonic Mach number and with a low confinement parameter (δ/W), a single straight and normal shock forms (figure 1.18 (a)). As the Mach number is increased, the normal shock begins to curve (panel b). If the adverse pressure gradient (APG) imposed by the shock is sufficiently strong the thickening of the boundary layer upstream of the shock induces a deflection of the flow that generates compression waves that coalesce and modify the topology of the normal shock producing a bifurcated shock (panel c). Under stronger APG (panel d), the thickening of the boundary layer and the local shock curvature produce an "aerodynamic nozzle effect"[50]. Through this nozzle the flow is accelerated and expansion waves are observed. The core flow becomes supersonic again. If the triple point distance from the wall is greater than the duct half-height, the leading oblique shock-waves of each opposite walls cross producing an oblique shock-train. The normal part of the shock (C3 in figure 1.10) disappears.

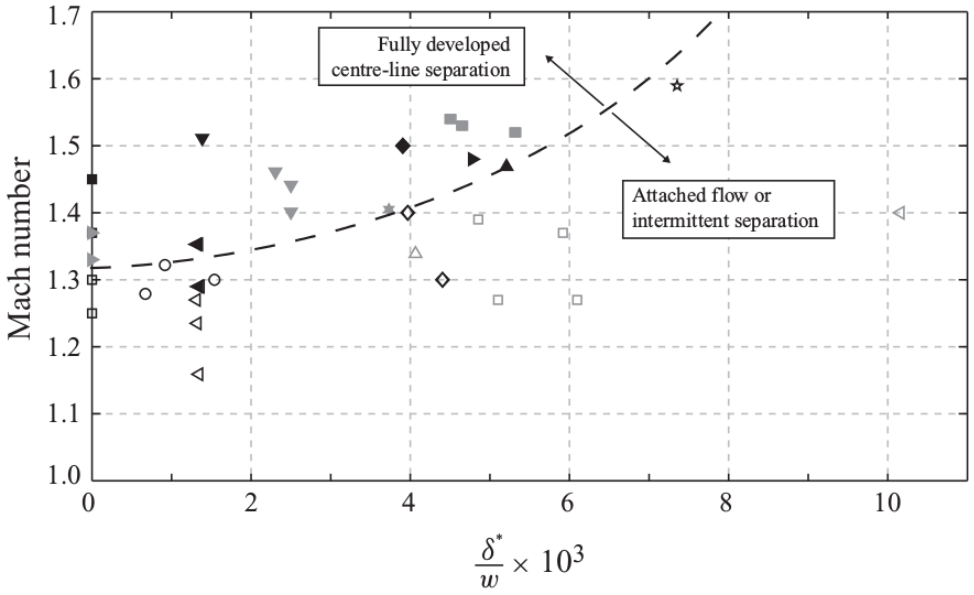

Figure 1.16: Experimental data for attached (open symbols) and separated (filled symbols) transonic SBLIs, plotted against the variable δ^*/w. Reprinted from [17]

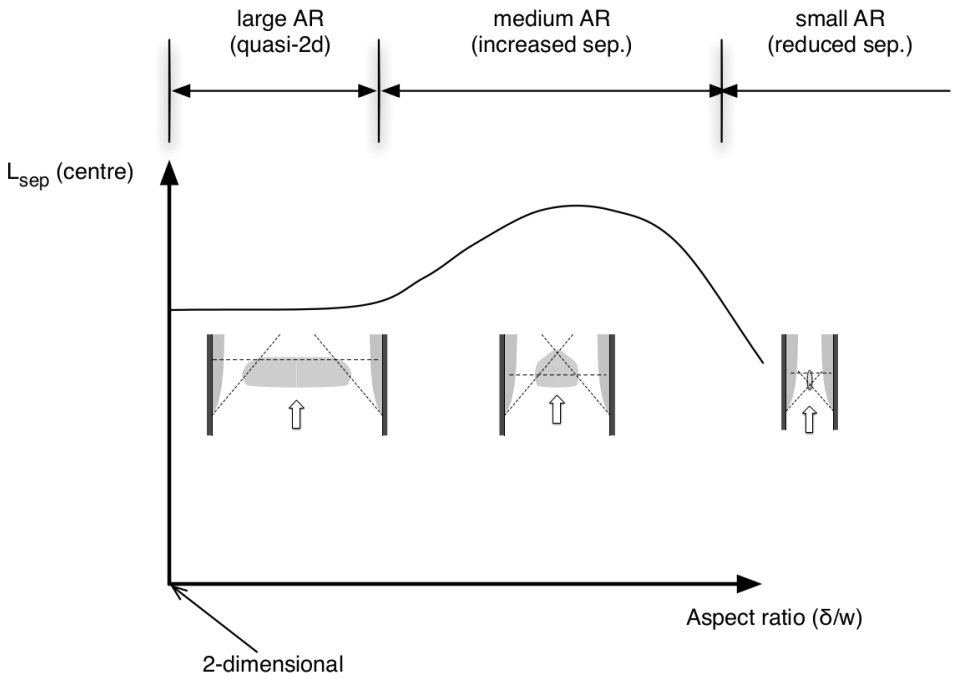

Figure 1.17: Babinsky *et al* [6] proposed variation of separation lengths (along wind tunnel floor centerline) as a function of wind tunnel 'inverse viscous aspect ratio'. Reprinted from Babinsky et al. [6]

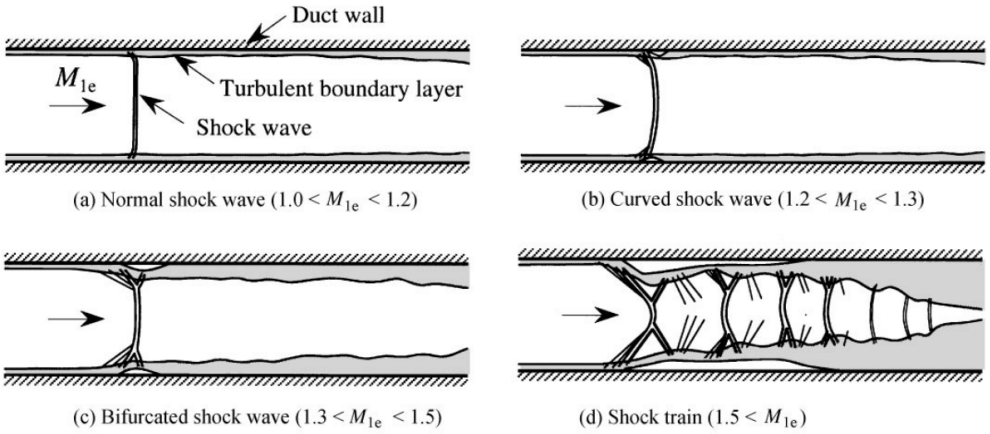

Figure 1.18: Schematic sketch of normal shock-wave/turbulent boundary layer interaction in a constant area duct. Reprinted from Matsuo et al. [66]

For the case (d) of figure 1.18, an example of wall pressure distribution is reported in figure 1.19. The multiple shock pattern that forms is called a shock-train. It comprised between the position where pressure starts to rise (point 1) and the position of the final downstream shock (point j). After the shock-train the flow may undergo a further compression in the mixing region. The region between point 1 and point 2 is the so-called pseudo-shock. Due to viscous effects, the pressure decreases downstream of point 2.

A few experimental and numerical studies dealing with shock-trains have been published in the literature. We recall the LES of a Mach 5 inlet-isolator system of Koo and Raman [59], the LES of the HyShot combustor system of Ingenito et al. [54], the detached-eddy simulation (DES) of a supersonic combustor with an isolator shock-train of Cocks et al. [24], the WMLES of an oblique shock propagating inside a duct of Bermejo-Moreno et al. [7], and, the wall-resolved LES of a transonic shock-train of Morgan et al. [68].

The latter study is of utmost importance as it is the first wall-resolved LES of a normal shock-train in a constant area rectangular duct with fully resolved boundary layers. The geometry and the selected flow conditions correspond to the experiment of Carroll and Dutton [21] In the experiment, the duct is slightly diverging (divergence angle of both upper and lower section wall is 0.13 deg) while Ref. [68] assumes a constant area duct. In addition, to ensure adequate mesh resolution, Morgan et al. choose a Reynolds number of ($Re_\delta \sim 16200$) approximately one order of magnitude less than the experiment. We point out that performing high fidelity simulations at the same Reynolds number than the experiment is still not affordable. As a consequence, the comparison of the numerical results with the experimental ones may be biased by the differences in the Reynolds number effects. In order to maintain the first shock at a location where the confinement ratio is equal to 0.32, as in the experiment, they set the outflow pressure is at a value different than the experiment.

We observe that several issues remain concerning the shock-train interaction both in providing accurate flow statistics and in understanding the emergence of coherent motions as well as their spatial and temporal scales. In the present work we will then focus on the analysis of the statistical properties of the flow, and on the unsteady characteristics of shock-train simulation (in particular on low and medium frequencies).

The present document is organized as follow. First, we detail the methods and tools used for the simulations. Then a chapter is devoted to validation. The latter consists of three test cases that are representative of the inherent difficulties that arise when one deals with the simulation of a shock train interactions in a rectangular duct. Chapters 4 and 5 discuss on the large eddy simulations of a shock-train interactions in rectangular duct, focusing on the influence of various aspect ratios (chapter 4) and on the unsteady analysis for a given aspect ratio (chapter 5).

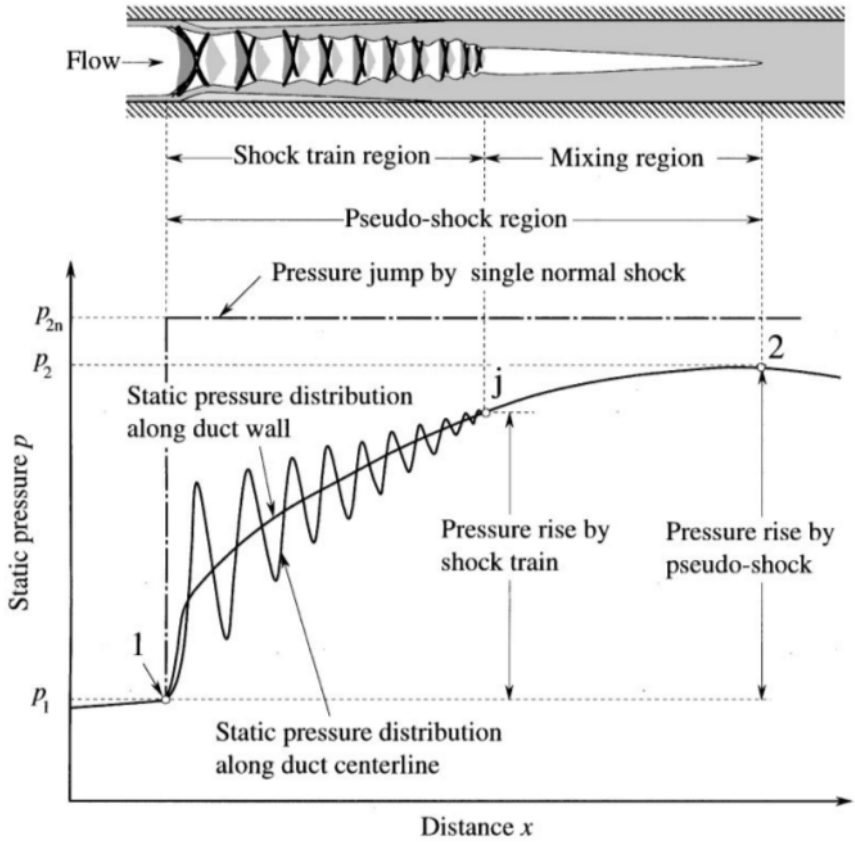

Figure 1.19: Schematic static pressure distribution along duct centerline and wall surface in constant-area duct for condition wherein a "normal" shock is present. Reprinted from Matsuo et al. [66].

Finally, in Chapter 6 some conclusions are given.

Chapter Summary

- Shock-wave boundary layer interactions occur in external and internal flows and impact various devices
- Different classifications of SWBLI are possible
  - Depending on the mechanism that generates the shock
    - Descriptive approach restricted to canonical configurations.
    - No clear separation of the underlying physic.
  - Based on the state of the boundary layer: separated or attached interaction.
    - Separation of the dominant scales of the flow: weak interactions (*i.e.* where viscous effects are weak) and strong interactions.
    - Different unsteadiness are observed: low-frequency unsteadiness seems specific to detached interaction.
- Side walls influence strongly the centerline flow
  - The separation onset of the boundary layer can be estimated for quasi-two dimensional flow only.
  - Experiments are usually done inside duct of finite span and theoretical approaches fail to predict the separation onset.
  - The "effective aspect ratio", defined as the displacement thickness over the width of the duct (δ^*/W), accurately estimates the limit of the separation onset.
- Side walls and confinement effects modified the SWBLI topology
  - In internal flow, the shock in transonic interaction changes from normal to bifurcated as the confinement and Mach number increase. For higher confinement, secondary shocks appear and the interaction is called a shock-train.
  - The confinement is expressed as the boundary layer thickness divided by the duct half-height: δ/h.
  - The duct width and height both impact the shock-train.
  - Most results on that type of interaction are experimental.
- One experiment on shock-train have been reproduced numerically by means of wall-resolved large eddy simulation.
  - The experimental and numerical database consist of mean and turbulent statistics.
  - High fidelity simulations of transonic interactions are less abundant.
- The current thesis analysed shock-train interaction and contains the following results:
  - Four LES with different aspect ratios are carried out and compared.
  - For two aspect ratios, comparisons with the LES Morgan et al. [68] and the experimental results of Carroll and Dutton [21] are provided.
  - Analysis of the shock-train unsteadiness for one aspect ratio.

Chapter 2

Numerical Methods

Contents

2.1 Governing equations 33
2.2 Filtered equations 34
2.3 Spatial and temporal discretization 35
2.3.1 Spatial discretization of the Euler equations 35
2.3.2 Spatial discretization of the viscous terms 36
2.3.3 Scheme for the temporal integration: 4^{th} Runge-Kutta 37
2.4 Explicit filter 37
2.5 Sub-grid stress: explicit and implicit modeling 37
2.5.1 Subgrid explicit modeling: Dynamic Smagorinsky 38
2.6 Boundary conditions 40

2.1 Governing equations

We solve the three-dimensional Navier–Stokes equations for a perfect compressible gas

$$\frac{\partial \rho}{\partial t} + \frac{\partial \rho\, u_i}{\partial x_i} = 0 \tag{2.1}$$

$$\frac{\partial \rho\, u_i}{\partial t} + \frac{\partial \rho\, u_i u_j}{\partial x_j} + \frac{\partial p}{\partial x_j} - \frac{\partial \sigma_{ij}}{\partial x_j} = 0 \tag{2.2}$$

$$\frac{\partial \rho\, E}{\partial t} + \frac{\partial (\rho\, E + p) u_j}{\partial x_j} - \frac{\partial (\sigma_{ij}\, u_j - q_j)}{\partial x_j} = 0 \tag{2.3}$$

where ρ is the density, u_i a component of the velocity vector ($i \in \{1, 2, 3\}$), and the total energy E is

$$\rho E = \frac{p}{\gamma - 1} + \frac{\rho u_i u_i}{2} \tag{2.4}$$

Considering a Newtonian fluid we obtain under the Stokes hypothesis:

$$\sigma_{ij} = 2\mu S_{ij} - \frac{2}{3}\mu S_{kk}\delta_{ij} \tag{2.5}$$

$$S_{ij} = \frac{1}{2}\left(\frac{\partial u_i}{\partial x_j} + \frac{\partial u_j}{\partial x_i}\right) \tag{2.6}$$

Where S_{ij} is the strain-rate tensor and with the heat flux q_j (Fourier model):

$$q_j = -\lambda \frac{\partial T}{\partial x_j} \qquad \lambda = \frac{c_p \mu}{Pr} \tag{2.7}$$

Where $Pr = 0,72$ is the molecular Prandlt number and λ is the thermal constant. This system is closed by the perfect gaz equation.

2.2 Filtered equations

The direct resolution of the Navier-Stokes equations (eq 2.1 to 2.3) up-to the finest scales of turbulence is prohibitive [99]. To limit the cost, generally expressed in computational hours, we do not solve directly these equations, instead, we choose to solve solely the "largest eddies". Large Eddy Simulation (LES) has been previously used with shock-wave boundary layer interactions with [43, 68, 108] and without side walls effects [38, 95, 101]. It introduces a separation between the various scales of turbulence: the "small" scales are modelled while the "large" scales are resolved. "Small" and "large" are relative to a reference value mostly defined by the mesh. The grid and the property of the numerical scheme define the resolvability limits and act as a first implicit filter: eddies too small to be evaluated on the computational grid are modelled. Between the fully resolved scales and those modelled, some scales are partially evaluated on the grid and are corrupted by the discretization and numerical errors. A (sharp) explicit filter may be used to remove the partially resolved scales. An other approach is to use a subgrid model. More information on LES is accessible in [44, 88].

To remove the smallest unresolved eddies we introduce a spatial filter, for this section, the spatial filtering operator is noted $\bar{(\cdot)}$. It transforms any quantity ϕ in its filtered counterpart $\bar{\phi}$. For compressible flows, to account for the additional density related terms that appear when one uses a spatial filtering, a "Favre filter" is classically used. This operator transforms $\overline{\rho\phi}$ into $\bar{\rho}\tilde{\phi}$ where $\tilde{\phi}$ is a Favre filtered quantity. Moreover, in the following, we assume that the filtering operator commutes with derivatives. Note that these notations are valid solely for this chapter.

Applying the Favre-filtering operator to the continuity equation we obtain:

$$\frac{\partial \bar{\rho}}{\partial t} + \frac{\partial \bar{\rho}\tilde{u}_i}{\partial x_i} = 0 \tag{2.8}$$

Doing the same for the continuity equation:

$$\frac{\partial \bar{\rho}\tilde{u}_i}{\partial t} + \frac{\partial \bar{\rho}\tilde{u}_i\tilde{u}_j}{\partial x_j} + \frac{\partial \bar{p}}{\partial x_i} = \frac{\partial \tau_{ij}}{\partial x_j} + \frac{\partial \widetilde{\sigma_{ij}}}{\partial x_j} \tag{2.9}$$

Where τ_{ij} are the subgrid scale (SGS) terms:

$$\tau_{ij} = \widetilde{u_i u_j} - \tilde{u}_i\tilde{u}_j \tag{2.10}$$

The quantity $\widetilde{u_i u_i}$ contains unknown quantities (thus it can't be computed). As a consequence, filtering the total energy (equation 2.4) leads to an equation that is not computable without further hypotheses. Following Vreman et al. [106], we note the total computable energy

$$\bar{\rho}\check{E} = \frac{\bar{p}}{\gamma - 1} + \frac{1}{2}\bar{\rho}\tilde{u}_i\tilde{u}_i$$

Where $\check{(\cdot)}$ represents a computable quantity. The computable energy equation is:

$$\frac{\partial \check{E}}{\partial t} + \frac{\partial (\check{E} + \bar{p})\widetilde{u_j}}{\partial x_j} + \frac{\partial \bar{p}}{\partial x_j} - \frac{\partial (\check{\sigma}_{ij}\,\widetilde{u_j} - \check{q_j})}{\partial x_j} = B \tag{2.11}$$

Where B corresponds to the subgrid scale terms as exposed in reference [44].

These equations are similar to the Navier-Stokes equations except for a new term, τ_{ij}, in the momentum equation and B in the computable energy equation. In the current work, the SGS terms are either modelled through an explicit Smagorinsky dynamic model, or through the numerical scheme (implicit LES, abbreviated ILES).

2.3 Spatial and temporal discretization

The Navier-Stokes filtered equations are discretized on a Cartesian mesh by means of a conservative finite-difference approach. The flow solver relies on central eight-order discretization of the convective terms of the Navier-Stokes equations cast in fully split form[57, 72] whereas a seventh-order weighted essentially non-oscillatory (WENO) reconstruction [56] is activated near shocklets to inhibit spurious Gibbs oscillations. To distinguish smooth zones from shocked ones, a switch based on the Ducros [76] sensor is used.

The diffusive terms in the Navier-Stokes equations are cast in Laplacian form for improved numerical stability Pirozzoli [73], and approximated with forth-order central difference formulas.

The resulting semi-discrete system of equations is advanced in time by means of a standard, fully explicit fourth-order Runge-Kutta algorithm.

An explicit 8^{th} order filter is applied every 10 iterations during the time integration of the statistics.

2.3.1 Spatial discretization of the Euler equations

Kennedy-Gruber skew-symmetric splitting [72]: smooth zones discretization

Standard central differencing schemes are unstable. Due to the non-dissipative property of those schemes, aliasing errors are not damped and are cumulated during the time integration. The growth of those mesh-to-mesh oscillations generally leads to an unstable solver except if a correction is applied to the central scheme or if it is combined with a stabilizing tool (filtering, artificial viscosity...).

The chosen approach relies on a splitting of the derivatives [57, 72]. As shown by Ducros *et al* [32], the splitting of the convective derivative have stabilizing properties. This result was confirmed by Pirozzoli [72] who also proposed an efficient formulation using a discrete local averaging operator.

From splitting of the convective derivative [57] we have:

$$\begin{aligned}\frac{\partial \rho u_i \phi}{\partial x_i} = \alpha \frac{\partial \rho u_i \phi}{\partial x_i} + \beta \left(u_i \frac{\partial \rho \phi}{\partial x_i} + \rho \frac{\partial u_i \phi}{\partial x_i} + \phi \frac{\partial \rho u_i}{\partial x_i} \right) \\ +(1-\alpha-\beta) \left(\rho u_i \frac{\partial \phi}{\partial x_i} + \rho \phi \frac{\partial u_i}{\partial x_i} + \phi u_i \frac{\partial \rho}{\partial x_i} \right)\end{aligned} \tag{2.12}$$

where ϕ is a generic transported scalar quantity.

This expression formally requires the computation of 6 additional derivatives. To decrease the computational cost, the above formulation is modified [72]. A locally conservative approximation is obtained from the previous skew-symmetric form (with $\alpha = \beta = 1/4$):

$$f_{j+1/2} = 2 \sum_{l=1}^{L} a_l \sum_{m=0}^{l-1} \widetilde{(\rho, u, \phi)}_{j-l;l} \tag{2.13}$$

Where a_l are coefficients that maximize the formal order of accuracy and the operator $\widetilde{(f, g, h)}_{j;l}$ is the three-variable discrete averaging operator that is defined as:

$$\widetilde{(f, g, h)}_{j;l} = \frac{1}{8}(f_j + f_{j+l})(g_j + g_{j+l})(h_j + h_{j+l}). \tag{2.14}$$

This formulation yields semi-discrete preservation of kinetic energy when applied to both the continuity and momentum equations Pirozzoli [72].

WENO scheme [56]: discontinuous zones discretization

WENO schemes consist of a polynomial combination between multiple numerical flux. Those flux are computed using a low order flux splitting scheme, called the "building block". The building block scheme dictates how the flux is (re)-constructed. It gives some of its properties to the WENO scheme. Once all the low-order flux in the characteristic area are computed a WENO polynomial reconstruction procedure can be applied to obtained the smoothest solution. This is done through a weighted sum of the flux over the candidate stencils:

$$f_{i+1/2}^{(r)} = \sum_{r=0}^{k-1} C_l^r f_{i-r+l} \tag{2.15}$$

where $f_{i+1/2}^{(r)}$ are the reconstructed flux and C_l^r are the polynomial coefficients.

WENO scheme have been introduced by Liu et al. [64], and then generalized by Jiang and Shu [56]. The first one uses Roe [85] flux splitting scheme as a building block and the second one uses the Lax-Friedrich flux splitting.

Ducros sensor: coupling two discretizations

The Ducros sensor [31] consists of a ratio between a quantity that is higher in region of strong velocity gradient, such as shocks, divided by a second quantity that is higher in turbulent region or in vortex-like structures. The sensor, noted Θ, tends to 1 in region where pressure gradient dominates (for instance in shocks and acoustic waves) and 0 otherwise.

$$\Theta = \frac{(\nabla \cdot U)^2}{(\nabla \cdot U)^2 + (\nabla \times U)^2 + \varepsilon} \tag{2.16}$$

It can be checked that $0 \leq \Theta \leq 1$, with ε a constant to avoid invalid floating point operations.

2.3.2 Spatial discretization of the viscous terms

To improve the numerical stability, viscosity flux are cast in a Laplacian form [73, 74]. To be more precise, the quantity :

$$\frac{\partial \sigma_{ij}}{\partial x_j} = \frac{\partial}{\partial x_j}\left[\mu\left(\frac{\partial u_i}{\partial x_j} + \frac{\partial u_j}{\partial x_i} - \frac{2}{3}\frac{\partial u_k}{\partial x_k}\delta_{ij}\right)\right] \tag{2.17}$$

can be rewritten as:

$$\frac{\partial \sigma_{ij}}{\partial x_j} = \left(\frac{\partial u_i}{\partial x_j} + \frac{\partial u_j}{\partial x_i} - \frac{2}{3}\frac{\partial u_k}{\partial x_k}\delta_{ij}\right)\frac{\partial \mu}{\partial x_j} + \mu\left[\frac{\partial}{\partial x_j}\left(\frac{\partial u_i}{\partial x_j} + \frac{\partial u_j}{\partial x_i} - \frac{2}{3}\frac{\partial u_k}{\partial x_k}\delta_{ij}\right)\right]$$

Let $A = \frac{\partial}{\partial x_j}\left(\frac{\partial u_i}{\partial x_j} + \frac{\partial u_j}{\partial x_i} - \frac{2}{3}\frac{\partial u_k}{\partial x_k}\delta_{ij}\right)$
Then

$$A = \frac{\partial^2 u_i}{\partial x_j^2} + \frac{\partial^2 u_j}{\partial x_i x_j} - \frac{2}{3}\frac{\partial^2 u_k}{\partial x_k x_i}\delta_{ij}$$

$$A = \frac{\partial^2 u_i}{\partial x_j^2} + \frac{\partial^2 u_j}{\partial x_i x_j} - \frac{2}{3}\frac{\partial^2 u_j}{\partial x_j x_i}\delta_{ij}$$

$$A = \frac{\partial^2 u_i}{\partial x_j^2} + \frac{1}{3}\frac{\partial^2 u_j}{\partial x_j x_i}\delta_{ij}$$

Finally, the diffusive terms are expanded in the form:

$$\frac{\partial \sigma_{ij}}{\partial x_j} = \left(\frac{\partial u_i}{\partial x_j} + \frac{\partial u_j}{\partial x_i} - \frac{2}{3}\frac{\partial u_k}{\partial x_k}\right)\frac{\partial \mu}{\partial x_j} + \mu\frac{\partial^2 u_i}{\partial x_j^2} + \mu\left(\frac{1}{3}\frac{\partial^2 u_j}{\partial x_j x_i}\right) \tag{2.18}$$

2.3.3 Scheme for the temporal integration: 4^{th} Runge-Kutta

A Runge-Kutta scheme with p sub-steps to solve the Cauchy's problem (on Φ) defined by the equation $\partial\Phi/\partial t = F(\Phi, t)$ and by an initial condition (Φ_0), can be written as:

$$\begin{aligned} \Phi^{n+1} &= \Phi^n + \Delta t \sum_{i=1}^{p} b_i k^i \quad \text{with} \quad k^i = F\left(\Phi^n + \sum_{j=1}^{i-1} a_{ij} k^j, t^n + c_i \Delta t\right) \\ \Phi^0 &= \Phi_0 \end{aligned}$$

where $c_i = \sum_{j=1}^{i-1} a_{ij}$ for $i = 1, ...p$. For any standard Runge-Kutta scheme, coefficients are obtained thanks to the Taylor series expansion of Φ.

The 4^{th} Runge-Kutta scheme is used in all of our simulations:

$$\Phi^{n+1} = \Phi^n + \Delta t \left[\frac{1}{6}\left(k_1 + 2k_2 + 2k_3 + k_4\right)\right]$$

$$\begin{cases} k_1 = & F(\Phi, t) \\ k_2 = & F(\Phi + \frac{h}{2}, t + \frac{h}{2} k_1) \\ k_3 = & F(\Phi + \frac{h}{2}, t + \frac{h}{2} k_2) \\ k_4 = & F(\Phi + h, t + h k_3) \end{cases}$$

2.4 Explicit filter

Filters are commonly used to damp the aliasing errors (thus stabilizing the spatial scheme) or as an implicit model. Many filters are found in the literature: compact ones [60], explicit filters with standard or modified coefficients (for instance DRP schemes [9]), non-linear selective filters (for example, the Adaptive Nonlinear Selective Filtering or ANSF [10, 11]) ... In our simulation, the solver is stable without the need for an additional dissipation. The filter is solely used to remove weak mesh-to-mesh oscillations of finite amplitude increase the noise during the visualization of gradient related quantities. Thus, it was checked that the filter can be removed with no consequence on the total (measurable) dissipation.

A $2N + 1$ points stencil filter applied to variable u on a uniform mesh gives:

$$\hat{u}(x) = u(x) - \sigma D_u(x) \qquad \text{with} \qquad D_u(x) = \sum_{j=-N}^{N} c_j u(x + j\Delta_x) \tag{2.19}$$

where the symbol $\hat{.}$ indicates the obtained filtered quantity, $0 \leq \sigma \leq 1$ is a parameter to control the amplitude of the filter, and $c_j = c_{-j}$ are coefficients:

c_j	c_0	c_1	c_2	c_3	c_4
value	35/128	-7/32	7/64	-1/32	1/256

2.5 Sub-grid stress: explicit and implicit modeling

"The problem of subgrid modeling consists in taking the interaction with the fluctuating field into account in the evolution equation of the filtered field"[44]. Two approaches for modeling the subgrid terms are used [88]:

- functional modeling

- structural modeling

Structural modeling focuses on making the best approximation of a given quantity. Functional modeling intents to reproduce the effects, *i.e.* to mimic different physical properties and behaviors on a given quantity. This second type of modeling does not constraint the underlying mathematical structure of the model (*i.e.* the structure of the phenomena and of the modeled may be different). These models are constructed with the following assumptions [88]:

- energy transfer between resolved scale and subgrid scale is sufficient to describe the action of the subgrid scale. As a consequence, the action of the subgrid scales on the resolved is mostly energetic,
- a total separation between resolved scale and sub-grid scale exist,
- The Boussinesq hypothesis is assumed. The energy transfer from resolved scales to the sub-grid scales is similar to a molecular mechanism (diffusion). This effect can be modeled through the addition of a subgrid viscosity ν_t. In Smagorinsky models, under Boussinesq hypothesis, the deviatoric part of the subgrid tensor τ_{ij}^d is defined as:

$$\tau_{ij}^d = \tau_{ij} - \frac{1}{3}\delta_{ij}\tau_{kk} = -2\overline{\rho}\nu_t\left(\tilde{S}_{ij} - \frac{1}{3}\delta_{ij}\tilde{S}_{kk}\right) \tag{2.20}$$

- the flow is in constant spectral equilibrium so there is no accumulation of energy at any frequency and the energy spectrum remains invariant with time.

The Dynamic Smagorinsky model (SMD) belongs to the family of the functional modeling whereas the implicit modeling belongs to the structural modeling. In the following two Smagorinsky models are briefly introduced. The numerical scheme used for the implicit modeling are detailed in previous section.

2.5.1 Subgrid explicit modeling: Dynamic Smagorinsky

Smagorinsky [96] model (SM)

For the Smagorinsky model, the smallest scales are assumed to be isotropic. In the figure 2.1, a spectrum of homogeneous turbulence (THI) is drawn. This sketch shows the different hypothesis require to use a Smagorinsky model: the THI spectrum is not modified by the presence of the filter, so, the resolved and modeled scales are solely linked through energetic transfer. The production of energy is achieved by the resolved scales and spectral equilibrium is maintained by energy transfer to the modeled scales (there is no backscattering). Those scales are supposed to be isotropic, mostly dissipative and are not in the inertial range.

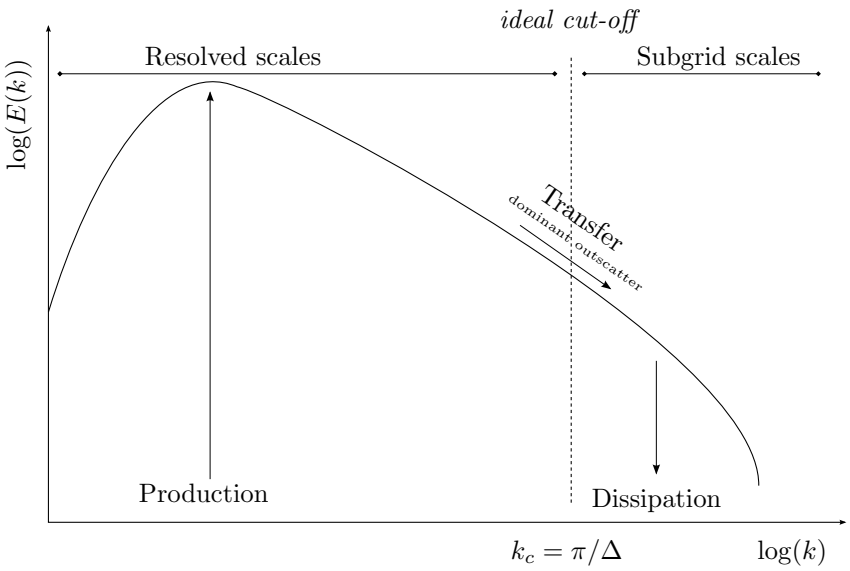

Figure 2.1: Spectrum of homogeneous turbulence with an ideal spectral filter cut-off at k_c that separates large scales from smaller mostly dissipative scales. Backscattering is (by hypothesis) neglected.

In Smagorinsky [96] model, the eddy viscosity is obtained by assuming that the small scales are in equilibrium. The consequence is that the eddy viscosity ν_t is approximate by:

$$\nu_t = C_s^2 \overline{\Delta}^2 (2\tilde{S}_{ij}\tilde{S}_{ij})^{1/2} \tag{2.21}$$

Where C_s is the Smagorinsky constant, $\overline{\Delta}$ is the filter width, and $(2\tilde{S}_{ij}\tilde{S}_{ij})$ is the magnitude of the (resolved) large-scales strain-rate tensor:

$$\widetilde{S_{ij}} = \frac{1}{2}\left(\frac{\partial \tilde{u}_i}{\partial x_j} + \frac{\partial \tilde{u}_j}{\partial x_i}\right) \tag{2.22}$$

Dynamic Smagorinsky model (DSM)

The Germano et al. [46] Dynamic Smagorinsky model is a modified Smagorinsky [96] model where the Smagorinsky constant C_s is locally evaluated. In order to defined a local constant that best approximates the effect of the unresolved scales at a given coordinate, we need to obtain further information on the local properties of the flow. One approach consists of extracting information from the smallest resolved scales and to use this information to approximate the unresolved scales. To do so, a test filter is applied on the resolved scales.

Let $\widehat{\cdot}$ be the test filter operator that transformed a quantity $\rho\phi$ into $\widehat{\rho}\widehat{\phi}$. The sub-grid stress $\tau_{ij} = \widetilde{u_i u_j} - \tilde{u}_i\tilde{u}_j$ becomes:

$$T_{ij} = \widehat{\widetilde{u_i u_j}} - \left(\widehat{\tilde{u}_i}\widehat{\tilde{u}_j}\right) \tag{2.23}$$

The resolved turbulent stresses are defined as[46]:

$$\mathcal{L}_{ij} = \widehat{\widetilde{u}_i\widetilde{u}_j} - \widehat{\tilde{u}}_i\widehat{\tilde{u}}_j \tag{2.24}$$

And

$$\mathcal{L}_{ij} = T_{ij} - \hat{\tau}_{ij} \tag{2.25}$$

We can write:

$$\tau_{ij}^d = -2\overline{\rho}C_d\overline{\Delta}^2 \left|\widetilde{S}_{ij}\right| \widetilde{S}_{ij}^d \tag{2.26}$$

$$T_{ij} = -2\overline{\rho}C_d\hat{\Delta}^2\left|\widehat{\widetilde{S}_{ij}}\right|\widehat{\widetilde{S}^d_{ij}} \tag{2.27}$$

A least square procedure is applied:

$$C_d = \frac{\langle\left(\mathcal{L}_{ij} - \frac{1}{3}\mathcal{L}_{ij}\delta_{ij}\right)\mathcal{M}_{ij}\rangle}{\langle\mathcal{M}_{pq}\mathcal{M}_{pq}\rangle} \tag{2.28}$$

$$C_I = \frac{\langle\mathcal{L}_{ij}\rangle}{\langle 2\hat{\Delta}\hat{\overline{\rho}}\left|\hat{\tilde{S}}\right|^2 - 2\overline{\Delta}\widehat{\overline{\rho}\left|\tilde{S}\right|^2}\rangle} \tag{2.29}$$

$$\mathrm{Pr}_t = C\frac{\langle N_i N_i\rangle}{\langle -K_j N_j\rangle} \tag{2.30}$$

The value of $\hat{\Delta} = (\hat{\Delta}_1\hat{\Delta}_2\hat{\Delta}_3)^{1/3}$ is set to $2\overline{\Delta}$, $\mathcal{L}_{ij}$ and:

$$\mathcal{M}_{ij} = -2\hat{\Delta}^2\hat{\overline{\rho}}\left|\hat{\tilde{S}}\right|\left(\hat{\tilde{S}}_{ij} - \tfrac{1}{3}\hat{\tilde{S}}_{kk}\delta_{ij}\right) + 2\overline{\Delta}^2\left[\overline{\rho}\left|\tilde{S}\right|\left(\tilde{S}_{ij} - \tfrac{1}{3}\tilde{S}_{kk}\delta_{ij}\right)\right]^{\wedge} \tag{2.31}$$

$$N_i = \hat{\Delta}^2\hat{\overline{\rho}}\left|\hat{\tilde{S}}\right|\frac{\partial\hat{\tilde{T}}}{\partial x_i} - \overline{\Delta}^2\left[\overline{\rho}\left|\tilde{S}\right|\frac{\partial\tilde{T}}{\partial x_i}\right]^{\wedge} \tag{2.32}$$

$$K_i = \widehat{\overline{\rho}\widetilde{u}_i\tilde{T}} - \left(1/\hat{\overline{\rho}}\right)\widehat{\overline{\rho}\widetilde{u}_i}\widehat{\overline{\rho}\tilde{T}} \tag{2.33}$$

2.6 Boundary conditions

In all simulations the computational domain consists of a rectangular box as shown in figure 2.2.

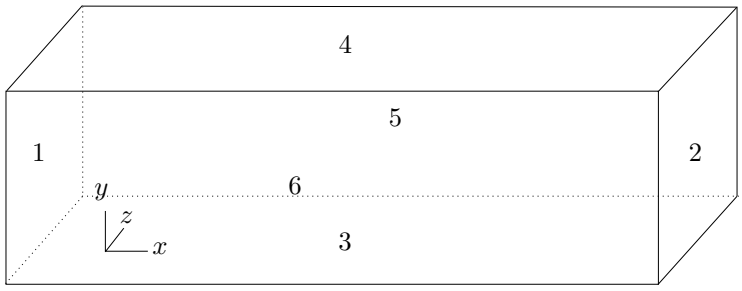

Figure 2.2: Schematic of the computational domain.

The boundary conditions are numbered from 1 to 6.

At the inflow plane (1), a turbulent inflow condition is applied. The recycling-rescaling methods used to produce the turbulent inflow condition are described in section 3.2.1

At the outflow plane (2), a non-reflecting subsonic or supersonic outflow [79] boundary condition is imposed. For the simulations of shock-trains, the pressure is forced to relax to a given value.

In all simulations at the plane $y = 0$ (3), a non-slip adiabatic wall boundary condition corrected to be perfectly reflecting [79] is enforced. This boundary condition is enforced by prescribing zero wall-normal gradient for temperature, and homogeneous Dirichlet boundary conditions for all velocity components.

For external flow simulations at the plane $y = Ly$ (4), a non-reflecting supersonic outflow boundary condition is prescribed. For internal flow simulations at the plane $y = Ly$ (4), a non-slip adiabatic wall boundary condition corrected to be perfectly reflecting [79] is enforced.

At the plane (5) and (6), for all simulations except those with side walls, a periodic boundary condition is applied. Otherwise a non-slip adiabatic wall boundary condition corrected to be perfectly reflecting [79] is applied.

Simulation of internal flows: inlet body force

In internal flow, in order to minimize and to prevent the leading edge shock from interacting with the boundary layer, a body force (F) is added to the right-hand side of the Navier-Stokes equations as suggested by Morgan *et al* [68].

$$F = \xi(x, y, z) \begin{bmatrix} \rho_\infty - \rho \\ \rho_\infty u_\infty - \rho u \\ \rho_\infty v_\infty - \rho v \\ \rho_\infty v_\infty - \rho w \\ \rho_\infty E_\infty - \rho E \end{bmatrix} \tag{2.34}$$

Where $\xi(x/\delta_{in}, y/\delta_{in}, z/\delta_{in})$ is defined as 0 if $y/\delta_{in} \notin [2\delta_{in}, L_y/\delta_{in} - 2\delta_{in}]$ otherwise:

$$\begin{aligned}
\xi(x/\delta_{in}, y/\delta_{in}, z/\delta_{in}) &= \xi_0 \times \xi_1(x/\delta_{in}) \times \xi_2(y/\delta_{in}) \times \xi_3(z/\delta_{in}) \\
\text{where} \quad \xi_0 &= 1.0e^{-5} \\
\xi_1(x/\delta_{in}) &= \frac{1 - \tanh(x/\delta_{in} - x_{rec}/\delta_{in} + 3\delta_{in})}{2} \\
\xi_2(y/\delta_{in}) &= \left(\frac{(y/\delta_{in} - 2\delta_{in})(L_y/\delta_{in} - y/\delta_{in} - 2\delta_{in})}{L_y/\delta_{in}/2 - 2\delta_{in}} \right)^4 \\
\xi_3(z/\delta_{in}) &= \left(\frac{\tanh 2(z/\delta_{in} - 2\delta_{in}) + \tanh 2(L_z/\delta_{in} - z/\delta_{in} - 2\delta_{in})}{2} \right)^2
\end{aligned}$$

Chapter Summary

- We numerically solve the Navier-Stokes equations for compressible flows
  - These equations are filtered and only the largest eddies are resolved.
  - The filtering of the Navier-Stokes equations produces additional terms, the subgrid terms.
  - Subgrid terms are modeled:
    - by a dynamic Smagorinsky (explicit modeling).
    - by the numerical scheme: no explicit model is used.
- To solve the filtered Navier-Stokes equations a finite-difference solver is used
  - For the spatial discretization:
    - 8^{th}-order central discretization of the convective terms cast in fully split form [72].
    - 7^{th}-order weighted essentially non-oscillatory (WENO) reconstruction near shocks and shocklets.
    - To distinguish smooth zones from shocked ones, a switch based on the Ducros sensor is used.
    - A 8^{th}-order filter may be used to remove small finite amplitude mesh-to-mesh oscillations.
  - For the temporal time integration:
    - A 4^{th}-order Runge-Kutta scheme is used.
- The boundary conditions are given on the computational domain.

Chapter 3

Turbulence initialisation

Contents

3.1 Turbulent boundary layer: a priori properties 43
3.1.1 Streamwise distribution of the boundary layer thickness 44
3.1.2 Estimation of the inner length scale for an incompressible flow 44
3.1.3 Estimation of the inner length scale for a **compressible** flow 46
3.2 Generation of turbulent inflow 49
3.2.1 Recycling/rescaling on a single wall 49
3.2.2 Multi-wall recycling/rescaling 50

3.1 Turbulent boundary layer: a priori properties

At the beginning of the simulation, $t = 0$, we solely know the upstream inflow quantities such as the static pressure, T_∞; the Mach number, M_∞; and the Reynolds number, here expressed at the inflow of the computational domain based on the boundary layer thickness, $Re_{\delta_{in}}$ (the boundary layer thickness being defined as the wall-distance where the velocity reaches 99% of u_∞). In order to generate an initial solution and/or an initial mesh, the characteristic length scales of the turbulent boundary layer have to be estimated. Since no direct equation relates at a chosen Reynolds number the inner length scales of the turbulent boundary layer with the outer ones, an iterative process is proposed hereafter to obtain such relation. This iterative process is stopped when the skin friction coefficient reaches a constant value. The skin friction coefficient is by definition:

$$c_f = \frac{\tau_w}{\frac{1}{2}\rho u_\infty^2} \tag{3.1}$$

where τ_w is the tangential stress at the wall. We also define the friction velocity, $u_\tau = \sqrt{\tau_w/\rho}$, and the wall unit that is $l_\nu = \nu_w/u_\tau$. We then proceed in the following steps:

1. We estimate the distribution of the boundary layer thickness on the flat plate $\delta(x)$, where x is the streamwise distance from the inflow of the computational domain.
2. Knowing $Re_{\delta_{in}}$, the inflow Reynolds number based on the boundary layer thickness, we determine for each value of the streamwise position x a local Reynolds number $Re_{\delta(x)} = (Re_{\delta_{in}}/\delta_{in}).\delta(x)$
3. At a given value of x, using $\delta(x)$ and $Re_{\delta(x)}$, we estimate the inner length scale of the turbulent boundary layer l_ν via an iterative process.
4. The relation between the inner and outer length scales being estimated, a first mesh and solution may be computed.

In the following we first describe the method for incompressible cases. Then, the method is generalized and detailed for compressible flows.

3.1.1 Streamwise distribution of the boundary layer thickness

Considering a viscous flow over a flat plate, a boundary layer spatially develops from the leading edge of the plate. The distance from the leading edge is noted X_0. Our computational domain is a rectangular box whose inflow plane is located at a virtual length X_0 from the origin of the boundary layer. At the inflow plane (subscript "in"), the Reynolds number based on the boundary layer thickness is equal to a targeted value, noted $Re_{\delta_{in}}$, where δ_{in} is the boundary layer thickness.

The value of X_0 is usually unknown. In order to estimate it, we assume that the velocity is approximated by a power law profile, $u/u_\infty = (y/\delta)^{1/n}$. We use the following relations[1]:

$$X_0/\delta_{in} = \frac{1}{0.16}\left(Re_{X_0}\right)^{1/7} \tag{3.2}$$

$$X_0/\delta_{in} = \frac{1}{0.16}\left(\frac{X_0}{\delta_{in}}Re_{\delta_{in}}\right)^{1/7} \tag{3.3}$$

We then estimate $\delta(x)/\delta_{in}$ with the equation:

$$\frac{X_0+x}{X_0} = \left(\frac{\delta(x)}{\delta_{in}}\right)^{7/6} \tag{3.4}$$

Where we remind that $\delta(x)$ is the boundary layer at a distance x from the inflow (*i.e* the boundary layer at a virtual length $X_0 + x$ from the origin of the boundary layer).

We deduce an approximation of $\delta(x)$

$$\delta(x)/\delta_{in} = (1 + x/X_0)^{6/7} \tag{3.5}$$

We obtain for each value of x a value of δ, knowing the value of $Re_{\delta_{in}}$ we thus have $Re_\delta = \delta.Re_{\delta_{in}}/\delta_{in}$.

3.1.2 Estimation of the inner length scale for an incompressible flow

An iterative approach is used to approximate the skin friction coefficient (c_f). The approach is initialized with an empirical value $c_f^{(0)}$. From this value we compute the inner length scales of the boundary layer. The boundary layer thickness (obtained previously) and the inner length scales of the boundary layer are then used to produce a mean (empirical) velocity profile. Then, we compute the boundary layer thicknesses (including the momentum thickness θ) associated with this velocity profile. Thus, we obtain an estimation of the Reynolds number based on the momentum thickness Re_θ. The latter value is used to estimate the skin friction coefficient c_f by applying the Karman-Schoenherr correlation [2]. This process is applied until convergence occurs on the skin friction coefficients (see figure 3.1).

[1] See Prandtl, 1961, vol II, pp 620-626 or White, *Viscous Fluid Flow*, pp 430 equation (6-70)

[2] This correlation is classically used. See for instance [52]

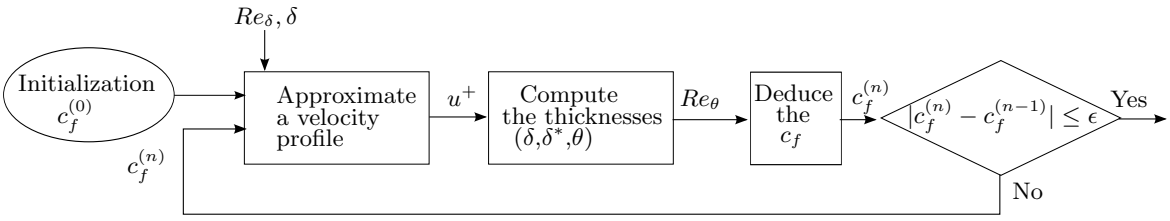

Figure 3.1: Block diagram describing the algorithm used to estimate the initial skin friction coefficient.

Step 1: mean velocity profile estimation for a chosen Reynolds number

The initial value of the skin friction coefficient is unknown, we assume an initial value either guessed or from the literature. This value is usually order of $O(10^{-4})$. By definition we have for an incompressible flow:

$$u_\tau = u_\infty \sqrt{c_f^{(0)}/2} \tag{3.6}$$

The density is constant and fixed ($\rho = \rho_\infty$) and we suppose, in a first approach, a constant pressure for the whole domain $p(x, y, z) = p_\infty$.

The turbulent boundary layer consists of an inner and outer layer [25]. For an incompressible turbulent boundary layer a mean velocity profile is shown in figure 3.2 (the wall-normal direction being y).

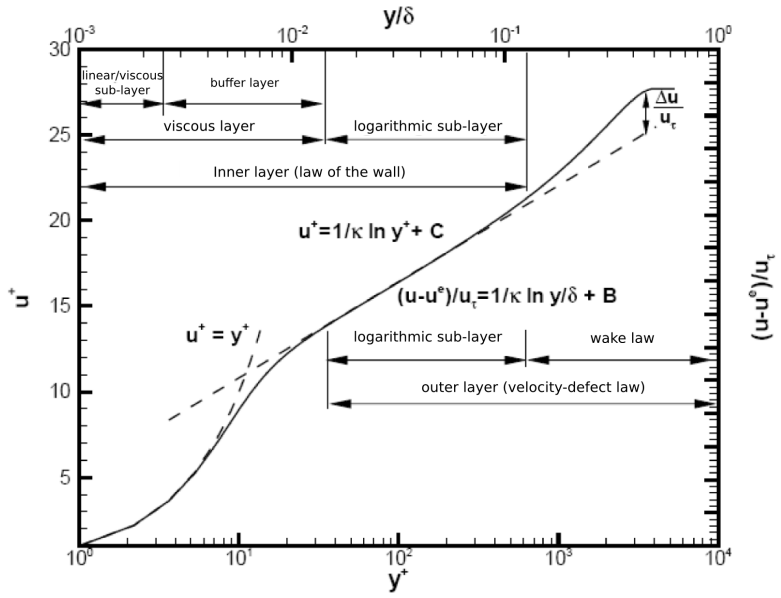

Figure 3.2: Time-averaged incompressible velocity profile $\overline{u}(y)$. Translated from [26]

.

The estimation of the velocity profile is composed of an inner layer (where we use the laws of Reichardt and Finley) and an outer layer split in a logarithmique sub-layer and a wake law. Let $\eta = y/\delta(x)$ and $y^+ = y/(u_\tau/\nu)$ be the normalized-wall distance expressed in outer and inner scaling , we have for the mean velocity:

$$\begin{cases} u^+ = & 1/\kappa \log(1+\kappa y^+) & \\ & + c_1(1-\exp(-y^+/c_2) - y^+/c_2 \exp(-by^+)) & \\ & + 2k_p/\kappa(\sin(\frac{\pi}{2}\eta))^2 & \eta < 1 \\ u^+ = & u_\infty/u_\tau & \eta > 1 \end{cases} \tag{3.7}$$

where $\kappa = 0.41$ is the von Karman coefficient, $c_1 = -1/\kappa.\log(\kappa) + c$, $b = 0.33$, $c_2 = 11.0$ and $c = 5.2$ are constant, and for each value of x we define the coefficient k_p at $y = \delta$ as

$$k_p = \kappa k_{p_0}/2 \tag{3.8}$$

$$k_{p_0} = \frac{u_\infty}{u_\tau} - \frac{1}{\kappa}\log(1+\kappa y^+) - c_1(1-\exp(-\frac{y^+}{c_2}) - \frac{y^+}{c_2}\exp(-by^+)) \tag{3.9}$$

We have obtained an estimation of $u(x,y)^+$ from an initial value of the skin friction coefficient. We now check the validity of the initial skin friction coefficient.

Step 2: computation of the integral boundary layer thicknesses

From the mean velocity profile, we compute the boundary layer thicknesses δ, δ^*, θ.

For the sake of completeness, we remind the definition of boundary layer thicknesses and of the incompressible shape factor for an incompressible flow:

$$\delta_i^* = \int_0^\delta \left(1 - \frac{u}{u_e}\right) dy \tag{3.10}$$

$$\theta_i = \int_0^\delta \frac{u}{u_e}\left(1 - \frac{u}{u_e}\right) dy \tag{3.11}$$

$$H_i = \delta_i^*/\theta_i \tag{3.12}$$

where subscript "i" indicates the incompressible definition a given quantity. Where δ is the δ_{99} boundary layer thickness (wall-distance where $u_e = 0.99u_\infty$), δ_i^* is the incompressible displacement thickness, θ_i is the incompressible momentum thickness, and, H_i is the incompressible shape factor. u_e, ρ_e correspond to the velocity and, respectively, the density at the edge of the boundary layer.

From the mean velocity profile we now have an estimate of $\theta_i(x)$

Step 3 and 4: validation of the initial value for the skin friction coefficient and stopping criterion

From these thicknesses, an empirical equation relates the skin friction coefficient to the Reynolds number based on the momentum thickness.

$$c_f^{(1)} = 1./(17.08\left[\log_{10}(Re_{\theta_i})\right]^2 + 25.11\log_{10}(Re_{\theta_i}) + 6.012) \tag{3.13}$$

We recognize in the previous equation the Karman–Schoenherr correlation for an incompressible boundary layer without pressure gradient. If the initial guess for the skin friction coefficient is far from the one obtain through the Karman–Schoenherr correlation, the initial value is modified: $c_f^{(0)} \leftarrow c_f^{(1)}$. The procedure is applied again until convergence of the skin friction coefficient is reached.

3.1.3 Estimation of the inner length scale for a compressible flow

In this subsection we generalize the previous method for compressible flows. Let us assume that the density fluctuations and their derivative are weak. So, the effects of compressibility are mostly due to a change in the mean density profile. This hypothesis is similar to the Morkovin hypothesis [97] and is well verified for low supersonic number (*i.e* Mach number lower than 3). As a consequence, using an appropriate scaling and transformation, the previous approach is easily generalized for compressible flow.

Step 1: mean velocity and mean temperature profile estimation for a chosen Reynolds number

Different time-averaged and scaling are used for compressible flows and are introduced hereafter. For a quantity $\phi(t)$ the time-averaged between t_0 and t_1, is defined as:

$$\overline{\phi} = \int_{t_0}^{t_1} \phi(t)dt$$

For compressible flows, the time-averaged operator is replaced by the Favre-averaged operator:

$$\widetilde{\phi} = \frac{\int_{t_0}^{t_1} \rho\phi(t)dt}{\int_{t_0}^{t_1} \rho dt} = \frac{\overline{\rho\phi}}{\overline{\rho}}$$

For a turbulent boundary layer in a $M_\infty < 3$ flow, the compressible velocity profile can be obtained from an incompressible one, via a van Driest transformation.

$$u_{vd} = \int_0^{\tilde{u}} \left(\frac{\rho}{\rho_w}\right)^{1/2} du \tag{3.14}$$

where u_{vd} is the van Driest transformation of $\widetilde{u}$ (Favre-averaged value of u).

An inverse van Driest transformation exist to convert a incompressible quantity into a compressible one. The incompressible velocity profile defined in subsection 3.1.2 is then transformed into a compressible velocity profile. In addition, the wall temperature and wall density remain unknown and should be defined. Two equations are used to estimate the wall temperature (including the Crocco-Buseman equation [25]):

$$r = Pr^{1/3} \tag{3.15}$$

$$T_w = T_\infty + \frac{u_\infty^2}{2c_p} r \tag{3.16}$$

Where c_p is the heat capacity at constant pressure, r is the recovery factor for a turbulent boundary layer and $Pr \sim 0.72$ is the Prandtl number. If we suppose that the pressure is constant inside the boundary layer, $p(x, y, z) = p_\infty$, then the wall density is defined as: $\rho_w = p_\infty / RT_w$ which is set constant for the whole flat plate.

The value of the skin friction coefficient is unknown – this is similar to the incompressible case. We initialize the skin friction coefficient with a theoretical or empirical value, for instance, $c_f^{(0)} = 5 \times 10^{-4}$. For each streamwise position we have:

$$u_\tau = u_\infty \sqrt{c_f^{(0)}/2} \sqrt{\rho_\infty/\rho_w} \tag{3.17}$$

As in the incompressible case, for each streamwise position we define a coefficient k_p, at $y = \delta$ we have,

$$k_{p_0} = \frac{u_{vd_\infty}}{u_\tau} - \frac{1}{\kappa}\log(1 + \kappa y^+) - c_1(1 - \exp(-\frac{y^+}{c_2}) - \frac{y^+}{c_2}\exp(-by^+)) \tag{3.18}$$

$$k_p = \kappa k_{p_0}/2 \tag{3.19}$$

We apply the van Driest transformation on the mean incompressible velocity profile: u becomes u_{vd}. The same layers and constants are used to define the current velocity profile than the one used previously (see equation 3.7). The streamwise evolution of the temperature and density at the wall are neglected. We now have an estimate of the van Direst velocity, in inner unit $u_{vd}(x, y)^+$, obtained from the initial value of the skin friction coefficient $c_f^{(0)}$. We end the procedure by checking the initial value of the skin friction coefficient.

Step 2: computation of the integral boundary layer thicknesses

We use the inverse van Driest transformation to obtain the mean velocity profile $\widetilde{u}(x, y, z)$.

$$a_{vd} = \sqrt{T_w/T_\infty - 1} \tag{3.20}$$
$$\widetilde{u} = \frac{u_\infty}{a_{vd}} \sin(a_{vd}.u_{vd}(x, y)/u_\infty) \tag{3.21}$$
$$\tag{3.22}$$

From the velocity profile we compute the boundary layer thicknesses: δ, δ^*, θ. For the sake of completeness, we remind the definition of boundary layer thicknesses for a compressible flow.

$$\delta = y|_{u=0.99u_\infty} \tag{3.23}$$
$$\delta^* = \int_0^\delta \left(1 - \frac{\rho}{\rho_e}\frac{u}{u_e}\right) dy \tag{3.24}$$
$$\theta = \int_0^\delta \frac{\rho}{\rho_e}\frac{u}{u_e}\left(1 - \frac{u}{u_e}\right) dy \tag{3.25}$$
$$H = \delta^*/\theta \tag{3.26}$$

Where δ^* is the displacement thickness, θ is the momentum thickness, and, H is the shape factor. Setting the density ratio ρ/ρ_e equal to unity, one obtains the incompressible definitions.

Step 3 and 4: validation of the initial value for the skin friction coefficient and stopping criterion

As in the previous subsection, we use an empirical equation that relates the skin friction coefficient to the Reynolds number based on the momentum thickness. This equation being valid solely for incompressible turbulent boundary layer, to apply it, we need to convert the compressible quantities into incompressible ones.

The incompressible value for the skin friction coefficient is approximated and need to be transformed into a compressible one in order to compare the current approximation with the initial guess. To avoid confusion between quantities obtained using incompressible definitions (such as θ_i for instance) and compressible quantities modified by van Driest transformation, the subscript "*inc*" denotes transformation compressible quantity whereas the "*i*" subscript denotes quantities defined using incompressible definitions. For the skin friction coefficient c_f, we use the van Driest II transformed:

$$c_f = c_{finc}/F_c \tag{3.27}$$
$$F_c = \frac{\overline{T_w}/T_\infty - 1}{\arcsin^2 \alpha} \tag{3.28}$$
$$\alpha = \frac{\overline{T_w}/T_\infty - 1}{\sqrt{\overline{T_w}/T_\infty \left(\overline{T_w}/T_\infty - 1\right)}} \tag{3.29}$$

Using the Karman-Schoenherr correlation, we have:

$$f = \mu_\infty/\mu_w \tag{3.30}$$
$$Re_{\theta_{inc}} = f.Re_\theta \tag{3.31}$$
$$c_{f_{inc}} = 1./(17.08\left[\log_{10}(Re_{\theta_{inc}})\right]^2 + 25.11\log_{10}(Re_{\theta_{inc}}) + 6.012) \tag{3.32}$$

As long as the initial skin friction coefficient $c_f^{(0)}$ is not close from the estimated value c_f, the initial value is replaced $c_f^{(0)} \leftarrow c_f$ and the previous procedure is applied again (until convergence is reached). The stopping criterion is such that for a chosen arbitrary value ϵ we should have $\epsilon \geq ||c_f^{(0)} - c_f||$ Compressible turbulent flows are deeply described in reference [97].

Density and pressure profile

From the previous velocity profile, using the Crocco-Buseman equation [25], the density profile can be computed $\rho(x, y)$. Under boundary layer assumptions, the pressure is constant inside the turbulent boundary layer and it is set to p_∞.

$$T = T_w - \frac{\widetilde{u_\infty^2}}{2c_p} r \tag{3.33}$$

$$\rho(x, y) = p_\infty / RT \tag{3.34}$$

3.2 Generation of turbulent inflow

3.2.1 Recycling/rescaling on a single wall

The recycling-rescaling method used in the present work relies on the one developed by Pirozzoli *et al* [76] that is based on the approach of Lund *et al* [65], and Xu *et al* [109]. At the rescaling plane, which coincides with the inlet plane, the fluctuations, extracted at x_{rec}, are injected at the inlet plane (*i.e.* they are added to the mean flow component) to produce a realistic turbulence inflow boundary condition.

At the inflow (x_{in}) we then impose:

$$\begin{array}{lcccl} \rho(x_{in}, y, z, t) & = & \bar{\rho}(y) & + & \rho'_{recy}(y, z, t) \\ u(x_{in}, y, z, t) & = & \bar{u}(y) & + & u'_{recy}(y, z, t) \\ v(x_{in}, y, z, t) & = & \bar{v}(y) & + & v'_{recy}(y, z, t) \\ w(x_{in}, y, z, t) & = & & & w'_{recy}(y, z, t) \\ p(x_{in}, y, z, t) & = & p_\infty & & \end{array} \tag{3.35}$$

where the subscript "recy" indicates the value of any variable rescaled from the recycling plane.

To avoid numerical "drift" phenomena (Sagaut *et al* [89]), the mean field at the inflow is kept constant, and only density and velocity fluctuations are reintroduced to the inflow. The rescaling procedure is applied by dividing the boundary layer into two sub-layers: 1) the inner layer (subscript 'inn') where velocity is assumed to scale in wall coordinatesand 2) the outer layer (subscript 'out') where flow properties scale in outer units. The fluctuation of a generic quantity (ϕ) is assumed to be a weighted combination of the inner- and outer-layer fluctuations where the weight function $W(\eta)$ is defined as[65]:

$$W(\eta) = \frac{1}{2}\left\{1 + \frac{\tanh\left[\frac{\alpha.(\eta - b)}{(1-2b)\eta + b}\right]}{\tanh(\alpha)}\right\} \tag{3.36}$$

with $\alpha = 4$ and $b = 0.2$.
The inflow density and velocity fluctuations in each sub-layer are rescaled from the recycling station x_{rec} according to:

$$\begin{array}{lcccl} \rho'_{inn}(x_{in}, y^+, z, t) & = & & & \rho'(x_{rec}, y^+, z, t) \\ \rho'_{out}(x_{in}, \eta\ \ , z, t) & = & & & \rho'(x_{rec}, \eta\ \ , z, t) \\ u'_{i,inn}(x_{in}, y^+, z, t) & = & \gamma & & u'_i(x_{rec}, y^+, z, t) \\ u'_{i,out}(x_{in}, \eta\ \ , z, t) & = & \gamma & & u'_i(x_{rec}, \eta\ \ , z, t) \end{array} \tag{3.37}$$

where γ is the rescaling parameter:

$$\gamma = \frac{u_{\tau,in}}{u_{\tau,rec}} \sqrt{\frac{\rho_{w,in}}{\rho_{w,rec}}} \tag{3.38}$$

The whole flow field is initialized at $t = 0$ by assuming a mean turbulent boundary layer as described in the previous section and with superposed deterministic perturbations mimicking inner- and outer-layer coherent structures (Li & Coleman[61], Pirozzoli *et al* [75]), and the rescaling parameters at the recycled station $(u_{\tau,rec}, \delta_{v,rec}, \delta_{rec})$ are defined using analytical laws:

$$\frac{\delta_{rec}}{\delta_{in}} = \left[1 + \left(\frac{x_{rec} - x_{in}}{\delta_{in}}\right) 0.27^{\frac{6}{5}} Re_{\delta_{in}}^{-\frac{1}{5}}\right]^{5/6} \tag{3.39}$$

$$\frac{u_{\tau,rec}}{u_{\tau,in}} = \left(\frac{\delta_{rec}}{\delta_{in}}\right)^{1/10} \tag{3.40}$$

3.2.2 Multi-wall recycling/rescaling

Extension of RR methods to multiple walls

Following Boles *et al* [12], we assume that the boundary layers evolving along each wall are independent of each other. We can apply the rescaling separately along each wall. For any turbulent quantity ϕ we obtain $nwalls$ rescaled quantities ϕ_n ($nwalls$ being the number of walls and ϕ_n the quantity rescaled along the n^{th} wall). The method is illustrated in 3.3 where we assume four turbulent boundary layers developing inside a rectangular duct. The turbulent quantities at a given streamwise plane x (illustrated in subfigure (a)) are rescaled along each wall. This produces four rescaled planes, ϕ_n, that are each a rescaling of the original flow in one direction as shown in 3.3 (b).

Then, in order to reconstruct ϕ at the inlet, the rescaled quantity ϕ_n are summed

$$\phi = \sum_{n=1}^{nwalls} W_n.\phi_n \tag{3.41}$$

where W_n is a weighting function based on the inverse squared wall distance (d) to ensure the coupling and is given by:

$$W_n = \frac{1}{d_n^2} \left(\sum_{m=1}^{nwalls} \frac{1}{d_m^2}\right)^{-1} \tag{3.42}$$

Modification of the mean flow at the recycled plane

Regarding the mean flow at the recycling plane, we assume that the flow exhibits a quadrant symmetry in the transverse plane. A time and quadrant averaging procedure is used to force the mean flow to be symmetric (see also [12, 67]).

Mean flow conditions at the inflow

At the inflow plane, the mean flow that is estimated during the initialization is used, unless otherwise specified. Its computation in presence of multiple-walls have not been detailed yet. It consists of two steps: in a first step, each wall is treated separately and n mean flows are computed using the method given in section 3.1; in a second step, the mean flows are merged according to equations 3.41 and 3.42 where ϕ is a mean quantity and ϕ_n is the mean flow along the n^{th} wall.

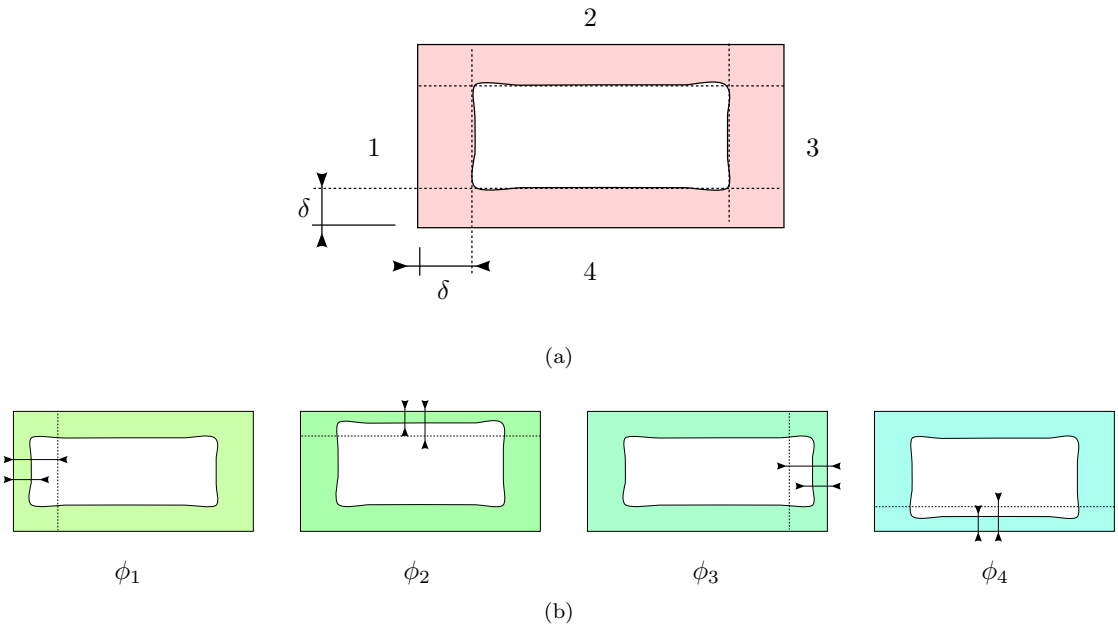

Figure 3.3: Schematic of the extraction and rescaling of a quantity ϕ [12]. (a) Extraction of turbulent quantity ϕ in the duct cross section at the recycling location. The walls are numbered from 1 to 4; (b) Rescaling along each wall. The quantity ϕ rescaled in the direction normal to the n^{th} wall becomes the rescaled quantity ϕ_n.

Chapter Summary

- The method used to initialized the mean flow is detailed
  - The boundary layer inner and outer length scales are estimated using an iterative approach
  - A composite empirical velocity profile is computed in the process
  - The approach is described for incompressible and compressible flows
- The method used to produce the turbulence at the inflow ($x = 0$) is described
  - For external flow, it consists of a recycling-rescaling inflow method generalized for compressible flow
  - For internal flow, the external recycling-rescaling approach is generalized to multiple-walls

Chapter 4

Validations

Contents

4.1 Supersonic turbulent boundary layer 52
4.1.1 Mesh and resolution 53
4.1.2 Skin friction coefficient and boundary layer thicknesses 53
4.1.3 Mean flow and turbulence statistics 55
4.1.4 Turbulent Kinetic Energy budget 56
4.2 Transonic shock-wave turbulent boundary layer interaction 57
4.2.1 Scaling parameters 57
4.2.2 Mesh and resolution 58
4.2.3 Wall statistics 58
4.2.4 Boundary layer thickness trough the shock 60
4.2.5 Pressure gradient and velocity profile 61
4.2.6 Fluctuations and turbulent kinetic energy budget 62
4.2.7 Qualitative visualisation 63
4.3 Supersonic turbulent boundary layer in a rectangular duct 64
4.3.1 Analysis along the wall bisector ($z = L_z/2$) 66
4.3.2 Analysis in the transverse plane 67

This thesis concerns the interaction of a supersonic turbulent boundary layer with normal shock-waves inside a rectangular duct (with corner flows). The validation consists of large eddy simulations of three test cases: first, simulations of a Mach-two-adiabatic-turbulent-boundary-layer are carried out with and without an explicit sub-grid model; then, LES of transonic interaction in an Mach 1.3 external flow are carried out; and finally, a sensitivity analysis on the effects of the mean inflow condition onto the corner flows is investigated. The latter point has been detailed during an AIAA conference [86]. For the sake of clarity and conciseness only the main results are exposed hereafter, mesh convergence, assessments of the boundary conditions ... are not shown.

4.1 Supersonic turbulent boundary layer

As explained by Smits and Dussauge [97], obtaining accurate statistics in experiments of supersonic flows is a difficult task. A standard approach is to compare supersonic compressible results with incompressible results under the assumption that the Morkovin's hypothesis [70] hold. Two large eddy simulations of an adiabatic Mach-two-turbulent-boundary-layer have been carried out, one with a Dynamic Smagorinksy sub-grid model (LES SMD) and one without sub-grid model (ILES). Our results are compared with the DNS data of Pirozzoli and Bernardini [74] that has

been done in a similar configuration, and, with the incompressible DNS data of Schlatter and Örlü [93]. The comparison of our results with these two databases are done at a reference station where we have similar Reynolds numbers. Information on the boundary layer at this reference station is given in table 4.1.

Case	$Mach$	$Re_{\theta i}$	Re_τ	Legend
DNS of Pirozzoli and Bernardini [74]	2.0	1327	447	$\triangle$
DNS of Schlatter and Örlü [93]	$\times$	1420	492	$\diamond$
LES SMD	2.0	1212	450	back curve
ILES	2.0	1200	450	coloured curve

Table 4.1: Mach and Reynolds number at a reference station for our LES and the DNS of Pirozzoli and Bernardini [74] and Schlatter and Örlü [93]. Two simulations have been carried out one with a Smagorinksy sub-grid model (LES SMD) and one without sub-grid model (ILES).

4.1.1 Mesh and resolution

For the LES SMD and ILES simulations the same mesh have been used. A convergence study was previously done. In the wall-normal direction (y) the mesh is stretched whereas in the streamwise (x) and spanwise (z) directions a constant grid-spacing is used. It was shown that the current resolution is sufficiently fine to resolve a turbulent boundary layer (with the current numerical schemes and models). The current LES resolution is $\Delta_x^+ \times \Delta_{y_w}^+ \times \Delta_z^+ = 30 \times 1.1 \times 15$ and the computational domain extent is $L_x \times L_y \times L_z = 100\delta_{in} \times 10\delta_{in} \times 5\delta_{in}$, where δ_{in} is the boundary layer thickness at the inflow. The resolution and extent for the DNS of reference[74] are $\Delta_x^+ \times \Delta_{y_w}^+ \times \Delta_z^+ \simeq 5 \times 0.7 \times 5$ and $L_x \times L_y \times L_z = 106\delta_{in} \times 8.3\delta_{in} \times 9.6\delta_{in}$, respectively.

For both cases an 8^{th} order finite difference scheme is used to compute the Eulerian flux and standard 4^{th} order finite difference scheme is used for the viscous flux. A 8^{th} order standard explicit filter is applied every 5 interations with an amplitude coefficient of 0.4 in x and 0.05 in y. Time integration is obtained by a 4^{th} order standard Runge-Kutta scheme in time with a CFL equals to 0.9. The numerical tools have been described with more details in chapter 2.

4.1.2 Skin friction coefficient and boundary layer thicknesses

The van Driest transformation and the Kármán-Schoenherr correlation have been introduced in the previous chapter. In order for the compressible data to collapse on the incompressible ones, we use the van Driest transformation (as usually done [67, 74, 98]...). In figure 4.1, the skin friction coefficient is compared with the Blasius and Kármán-Schoenherr correlation. Evolution of the skin friction coefficient is given in function of the streamwise station x/δ_{in} and $Re_{\theta_{inc}} = \rho_e u_e \theta / \mu_w$.

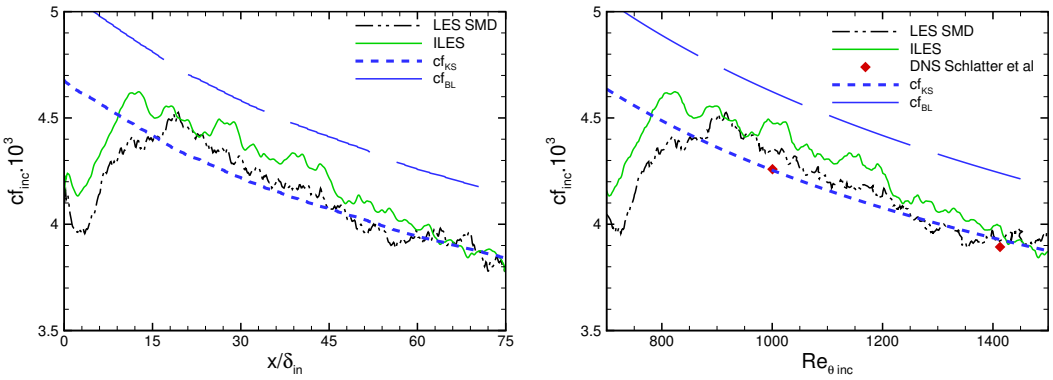

(a) c_{finc} streamwise evolution

(b) c_{finc} evolution related with $Re_{\theta_{inc}}$

Figure 4.1: Incompressible skin friction coefficient (see table 4.1 for nomenclature).

In figure 4.2, we compare the incompressible shape factor obtained by LES with the two DNS [74, 93] and an empirical correlation. Our data lays between Schlatter and Örlü [93] DNS data and an incompressible empirical correlation that holds for an incompressible equilibrium turbulent boundary layer [25]:

$$H_{th} = \frac{1}{1 - G\left(\frac{c_f}{2}\right)^{1/2}} \tag{4.1}$$

where $G = 6.3$ is the Clauser shape factor.

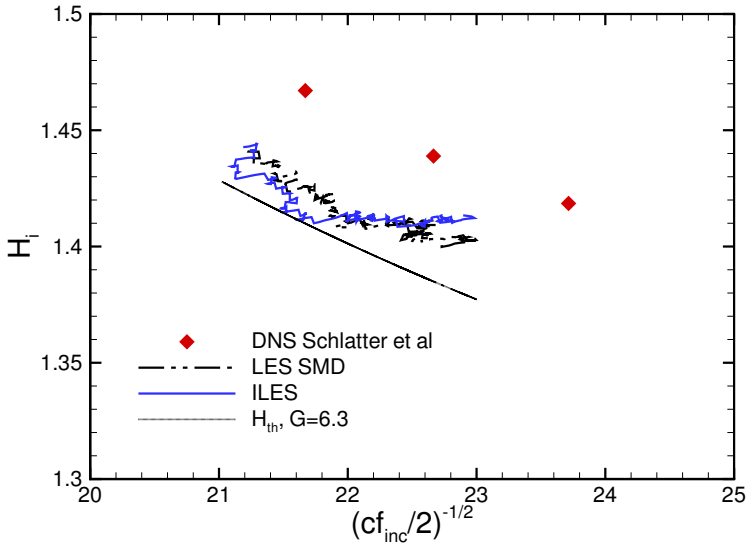

Figure 4.2: Mean incompressible shape factor H_i with H_{th} defined in (4.1). See table 4.1 for nomenclature.

.

4.1.3 Mean flow and turbulence statistics

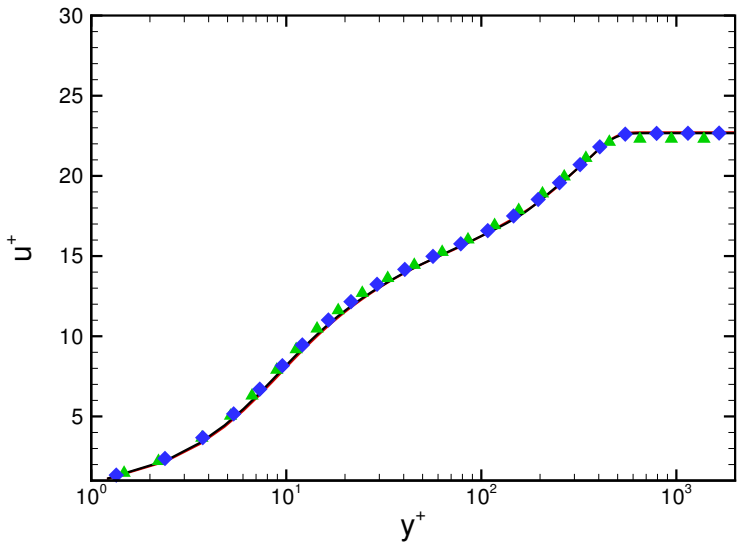

Figure 4.3: Favre-averaged van Driest velocity profile $\overline{u}_{vd}$ in inner scaling: $u^+ = \overline{u}_{vd}/u_\tau$ and $y^+ = yu_\tau/\nu$ (see table 4.1 for nomenclature)

In figure 4.3, the van Driest transformation of the velocity in the streamwise direction is plotted. This transformation accounts for compressibility effects and thus allowing compressible and incompressible velocity data to match (see section 5.2c). A similar scaling is provided for the fluctuating quantities (figure 4.4). Time-averaged root mean square is replaced with density weighted Favre-averaged root-mean square

$$\phi_{rms} = \sqrt{\overline{\phi''\phi''}} \quad \rightarrow \quad \widetilde{\phi_{rms}} = \sqrt{\frac{\overline{\rho}}{\overline{\rho}_w}}\sqrt{\widetilde{\phi''\phi''}}$$

We observe that the current LES results are mostly in the interval define by the two DNS references.

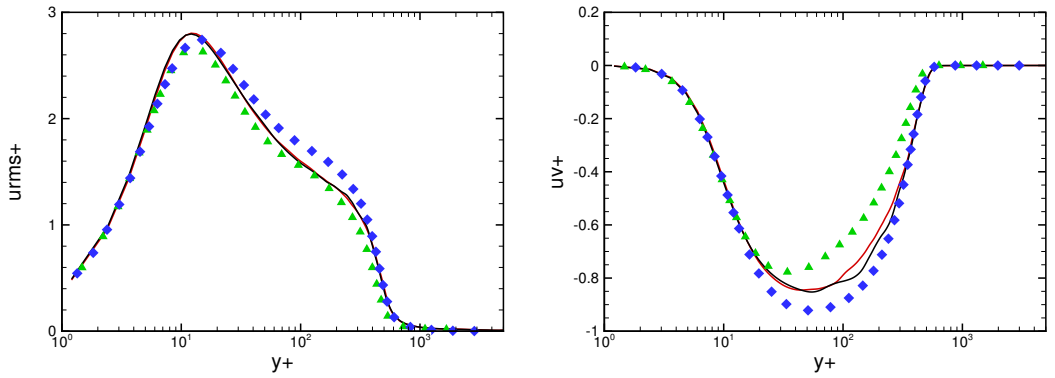

(a) $\sqrt{\frac{\bar{\rho}}{\bar{\rho}_w}}\sqrt{\widetilde{u''u''}/u_\tau^2}$

(b) $\frac{\bar{\rho}}{\bar{\rho}_w}\widetilde{u''v''}/u_\tau^2$

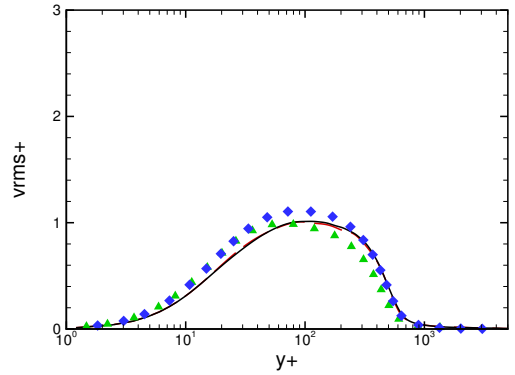

(c) $\sqrt{\frac{\bar{\rho}}{\bar{\rho}_w}}\sqrt{\widetilde{v''v''}/u_\tau^2}$

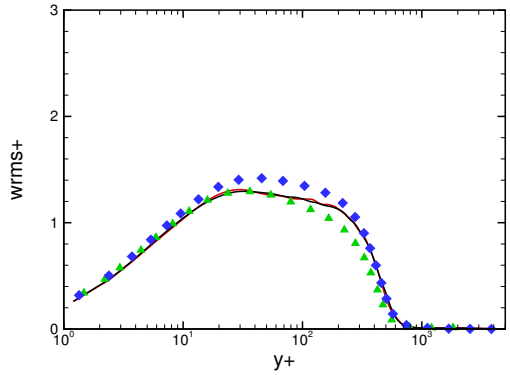

(d) $\sqrt{\frac{\bar{\rho}}{\bar{\rho}_w}}\sqrt{\widetilde{w''w''}/u_\tau^2}$

Figure 4.4: $u_{i_{rms}}$ and $u''v''$ in inner scaling. (see table 4.1 for nomenclature)

4.1.4 Turbulent Kinetic Energy budget

In figure 4.5, we compare the density scaled TKE budget terms with those of Schlatter and Örlü [93]. The terms T,P,V, and D reported in figure 4.5, represent the different contributions to the turbulence kinetic energy budget.

$$C = \frac{\partial \bar{\rho}\widetilde{u_j}k}{\partial x_j} \tag{4.2}$$

$$T = -\frac{\partial}{\partial x_j}\left[\frac{1}{2}\bar{\rho}\widetilde{u_i''u_i''u_j''} + \overline{p'u_j''}\right] \tag{4.3}$$

$$P = -\bar{\rho}\widetilde{u_i''u_j''}\frac{\partial \tilde{u}_i}{\partial x_j} \tag{4.4}$$

$$V = \frac{\partial \overline{\sigma_{ij}'u_i''}}{\partial x_j}$$

$$D = \overline{\sigma_{ij}'\frac{\partial u_i''}{\partial x_j}} + F + M \tag{4.5}$$

Where F and M are the explicit filter and the sub-grid model contribution to the dissipation. We observe a good collapse of our data indicating that the compressibility effects are weak when we account for the density variation effects (as mentioned by Pirozzoli and Bernardini [74]).

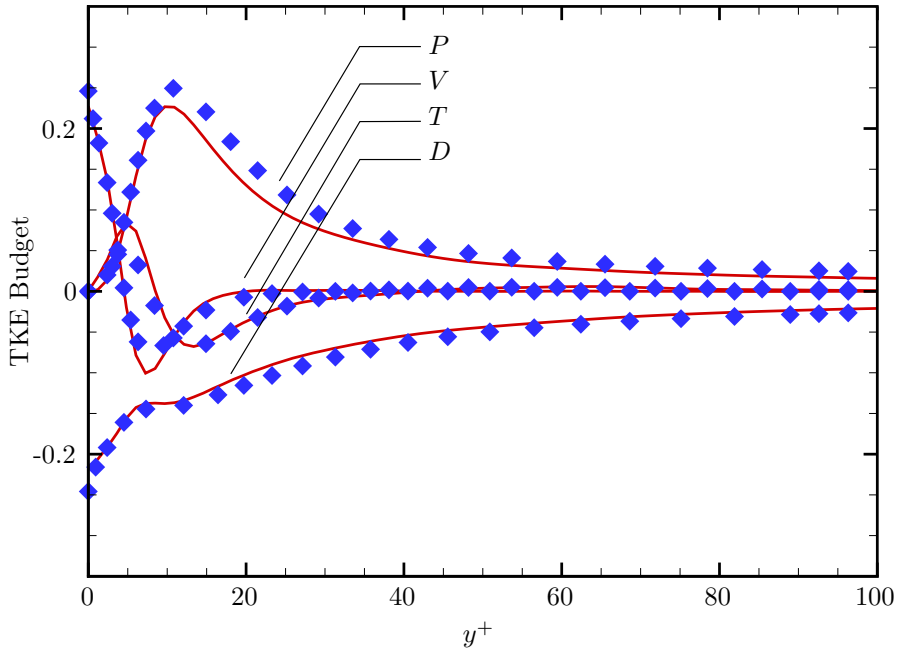

Figure 4.5: Turbulent kinetic energy budget in the TBL (see table 4.1 for nomenclature)

4.2 Transonic shock-wave turbulent boundary layer interaction

To check the validity of our approach for the simulation of an incipient transonic interaction, we carry out an LES under the conditions corresponding to the DNS of Pirozzoli et al. [76]. The parameters of the simulation are given in table 4.2.

Case	$Mach$	$Re_{\theta i}$	H_{i_0}	legend
DNS of Pirozzoli et al. [76]	1.3	1215	1.44	dash-dot
Exp. of Delery and Marvin [28]	1.3	7526	1.30	circle
Current LES	1.3	1300	1.43	line

Table 4.2: Boundary layer and flow properties at the origin of the interaction (subscript 0).

4.2.1 Scaling parameters

Let L_{int} be the interaction length scale, it is defined as the distance between the sonic point location (where the isentropic wall Mach number equal one, $M_w = 1$) and the origin of the interaction. The origin of the interaction is defined as the point where the pressure "starts to rise and attains $p_w = 1.005 p_\infty$"[76].

In order to account for the variation of the pressure upstream of the shock due to the pressure interaction effects (a leading edge followed by expansion waves), we take for p_∞ the value of the wall-pressure at a distance of the leading edge of $15\delta_{in}$. L_{int} is then use to scale the streamwise coordinate $x^* = (x - x_0)/L_{int}$.

For the zero-pressure-gradient boundary layer a useful length scale is the boundary layer thickness defined as the distance from the wall where the velocity is 99% of the undisturbed upstream

velocity. This length scale is not well defined if the velocity at the edge of the boundary layer (u_e) vary in x. In the DNS used for the comparison [76], the edge of the boundary layer is defined as the wall-normal (y) station where the vorticity is equal to $0.005u_\infty/\delta_{in}$. For the purpose of doing meaningful comparisons, we use this definition hereafter.

4.2.2 Mesh and resolution

We report in figure 4.6 the grid spacing in the streamwise direction scales in wall units . One can see that the mesh is stretched before and after the shock to decrease the computational cost. The streamwise grid spacing is near or lower than 30 wall units in the undisturbed turbulent boundary layer ($\Delta_x^+ \simeq 30$) and reaches 10 wall units around the shock location ($\Delta_x^+ \lesssim 10$). It remains lower than 25 past the interaction region. The current LES resolution is $\Delta_x^+ \times \Delta_{y_w}^+ \times \Delta_z^+ \simeq 30-10-25\times 1.0\times 15$ and the computational domain extent is $Lx\times Ly\times Lz = 110\delta_{in}\times 350\delta_{in}\times 7/\delta_{in}$, where δ_{in} is the boundary layer thickness at the inflow.

Indeed, previous computation with a coarser resolution ($\Delta_x^+ \simeq 20$ around the shock) were not perfectly collapsing with the DNS dataset. In order to validate our code and to remove any possible doubt, we decide to compute the solution on a finer mesh (in x) and the results are shown in the section. Solely a slight difference has been observed with the mesh whose resolution is $\Delta_x^+ \simeq 20$.

For the DNS, the resolution and computational domain extent are $\Delta_x^+ \times \Delta_{y_w}^+ \times \Delta_z^+ \simeq 4.5-7.5\times 1.1\times 5$ and $Lx\times Ly\times Lz = 106.8\delta_{in}\times 427\delta_{in}\times 12.8\delta_{in}$, respectively.

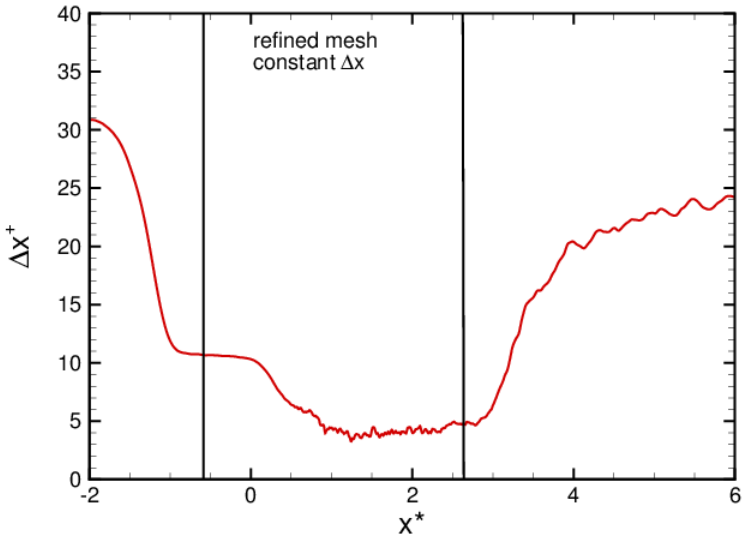

Figure 4.6: Evolution in the streamwise direction of the streamwise spacing in wall units.

4.2.3 Wall statistics

An excellent collapse with the DNS dataset of Pirozzoli and Bernardini [74] is obtained on "isentropic" wall Mach number[1] (figure 4.8), mean wall pressure (figure 4.7) distribution and skin friction coefficient (figure 4.9).

[1]Mach number related to the mean wall pressure through isentropic relation

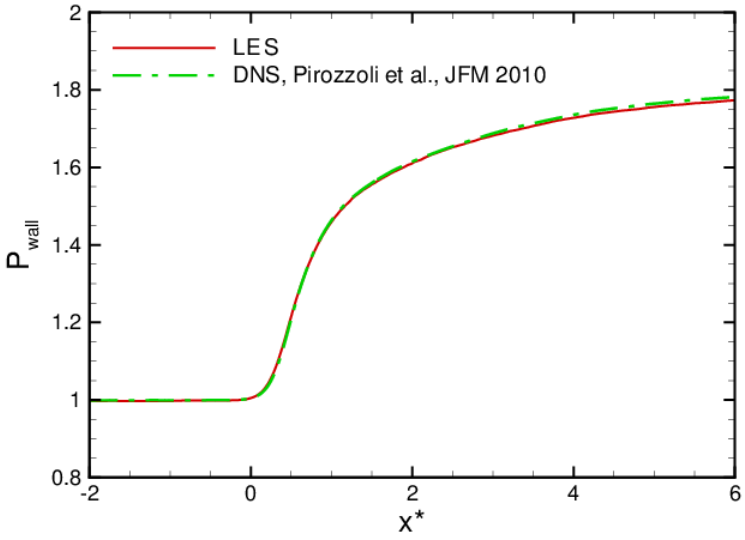

Figure 4.7: Wall pressure distribution along the streamwise direction (x) for the transonic shock-wave turbulent boundary layer interaction at $M_\infty = 1.3$ and $Re_{\theta in} = 750$.

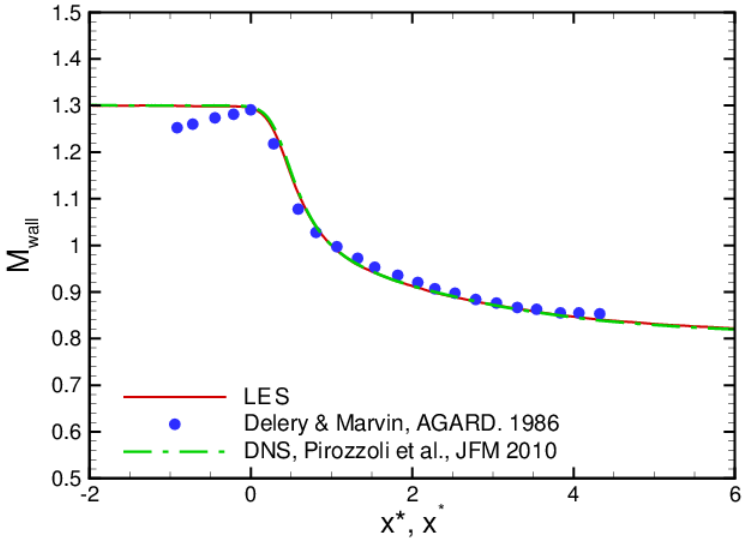

Figure 4.8: Isentropic wall Mach number for the transonic shock-wave turbulent boundary layer interaction at $M_\infty = 1.3$ and $Re_{\theta in} = 750$.

As we can see in figure 4.9, between $x^* \in [-2; -1]$ the present LES skin friction increases and approaches the DNS result. Looking at figure 4.6, it seems that an increase in resolution is the cause of this phenomenon (our turbulent inflow being done with a coarser mesh to reduce the computational cost.) Finally, considering that the present LES Reynolds number is slightly different at the reference station (we have $Re_{\theta i} = 1300$ against $Re_{\theta i} = 1215$ for the DNS of reference of Pirozzoli et al. [76]), this explains the small difference in the skin friction at the reference station. The figure confirms that our resolution is sufficiently fine in the interaction area to reproduce the skin friction since our results are matching the one of the DNS of reference in the area downstream of $x^* = 0$.

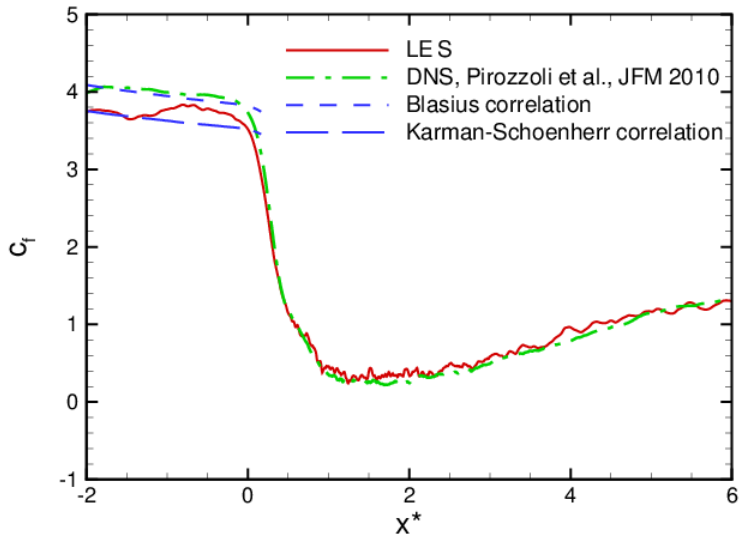

Figure 4.9: Skin friction coefficient for the transonic shock-wave turbulent boundary layer interaction at $M_\infty = 1.3$ and $Re_{\theta in} = 750$.

4.2.4 Boundary layer thickness trough the shock

In figure 4.10, we plot the boundary layer displacement and momentum thickness divided by their respective values at the beginning of the interaction. Results are almost collapsing with the DNS results in both amplitude and behaviour. The vertical lines show the location of the refined mesh in x where a constant spacing of $\Delta_x^+ = 10$ is applied (see figure 4.6).

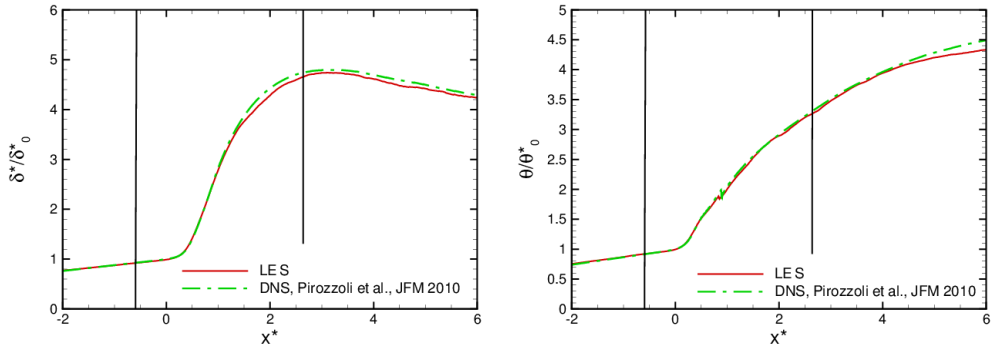

(a) (b)

Figure 4.10: Boundary layer thickness for the transonic shock-wave turbulent boundary layer interaction at $M_\infty = 1.3$ and $Re_{\theta in} = 750$.

The small differences in the shape factors are likely due to differences in the inflow boundary layer thickness.

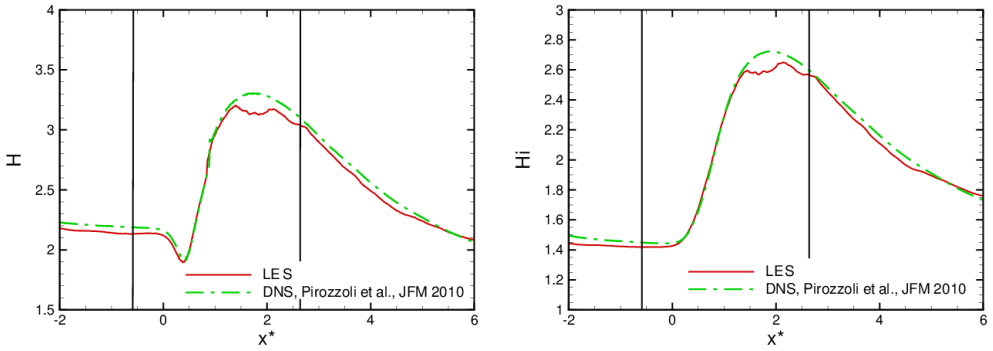

(a) (b)

Figure 4.11: Shape factors for the transonic shock-wave turbulent boundary layer interaction at $M_\infty = 1.3$ and $Re_{\theta in} = 750$.

4.2.5 Pressure gradient and velocity profile

The streamwise distribution of the velocity profile at the edge of the vorticity boundary layer is the same. This is illustrated in figure 4.12.

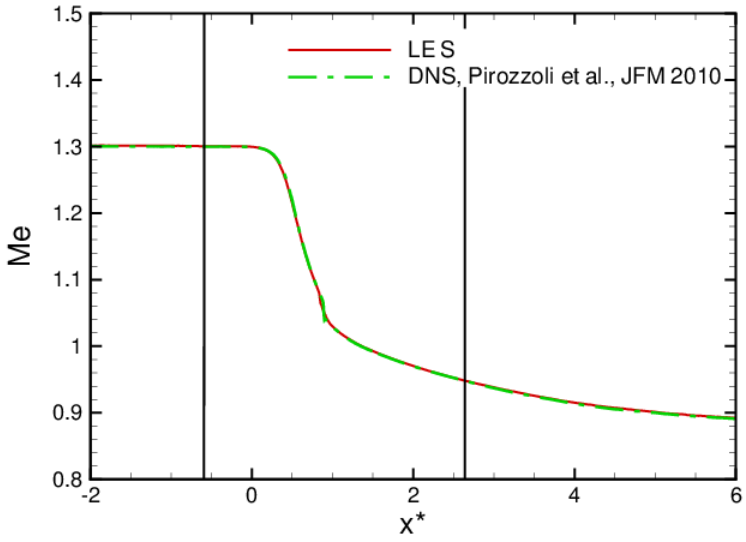

Figure 4.12: Mach number at the edge of the vorticity boundary thickness for the transonic shock-wave turbulent boundary layer interaction at $M_\infty = 1.3$ and $Re_{\theta in} = 750$.

In figure 4.13, we compare the velocity profile at two streamwise positions x_1 (upstream of the interaction, $x^* = -0.2$) and x_5 (downstream of the interaction, $x^* = 1.69$). The results shows that the LES results collapse with the DNS ones.

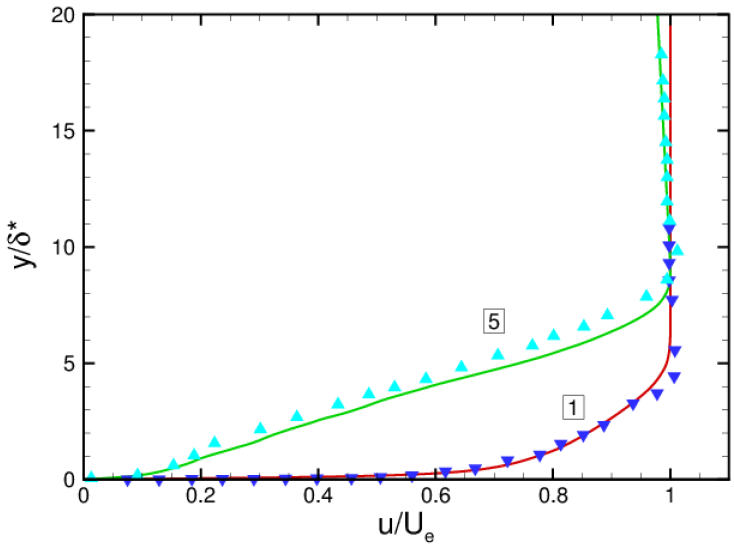

Figure 4.13: Velocity profile normalized by local boundary-layer thickness and local mean external velocity at $x_1 = -0.2$ and $x_5 = 1.69$ for the transonic shock-wave turbulent boundary layer interaction at $M_\infty = 1.3$ and $Re_{\theta in} = 750$. Lines, current LES; symbols, DNS of Ref. [76]

4.2.6 Fluctuations and turbulent kinetic energy budget

In this section we compare the turbulent statistics beginning with the Reynolds stresses at x_1 and x_5. In order to underline the streamwise evolution of the Reynolds stresses $R_{ij} = -\widetilde{u_i'' u_j''}$ and TKE, the reference inner velocity length scale is taken at the reference station ($x^* = 0$, subscript "ref"). In Figures 4.14 and 4.15, all terms are scaled by the density ratio $\rho/\rho_{w,ref}$ and non-dimensionalised by $u_{\tau,ref}$.

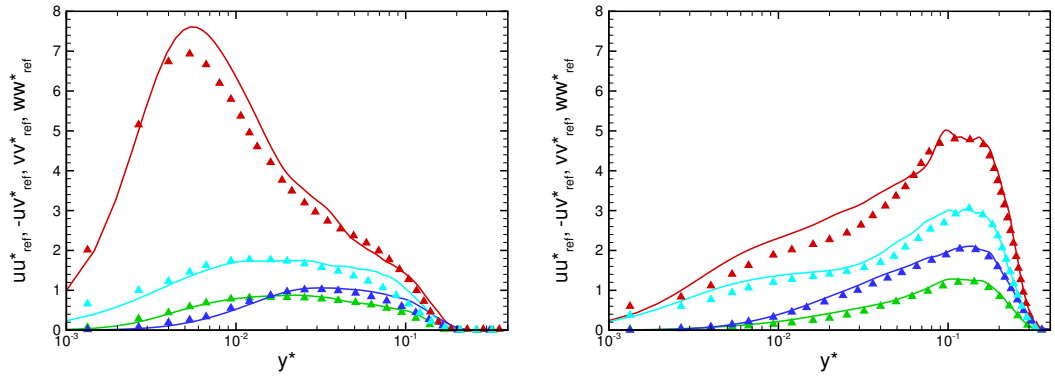

(a) x_1 (b) x_5

Figure 4.14: Reynolds stresses for the transonic shock-wave turbulent boundary layer interaction at $M_\infty = 1.3$ and $Re_{\theta in} = 750$. Red curve, uu^*, blue curve vv^*, cyan curve ww^* and green curve uv^*. Lines, current LES; symbols, DNS of Ref. [76]

The terms C,T,P,V, and D reported in figure 4.15, represent the different contributions to the turbulence kinetic energy budget. Upstream of the interaction, the LES collapses with the DNS while downstream of the interaction figure 4.14b, the differences are likely to be due to differences in the streamwise evolution of the skin friction velocity.

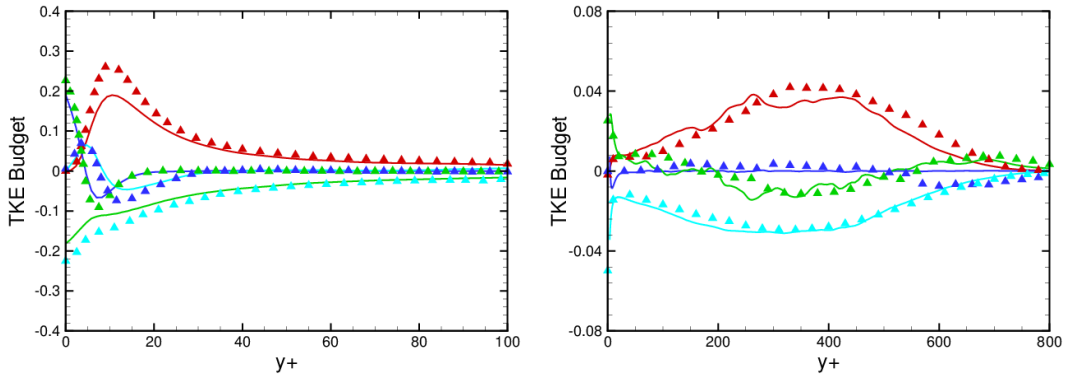

(a) x_1 (advection is not shown)

(b) x_5 (viscous diffusion is not shown)

Figure 4.15: TKE budget for the transonic shock-wave turbulent boundary layer interaction at $M_\infty = 1.3$ and $Re_{\theta in} = 750$. Red curve, production, blue curve, turbulent transport, cyan curve, dissipation, green curve, diffusion and brown curve, advection. Lines, current LES; symbols, DNS of Ref. [76]

4.2.7 Qualitative visualisation

A more complete representation of the flow is reported in the following figures where the isosurface of Q criterion is represented.

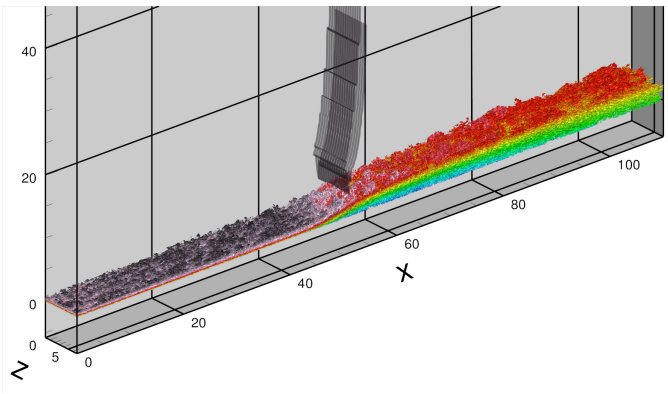

Figure 4.16: Q criterion ($Q = -0,15(U_\infty/\delta_0)^2$), coloured with the local Mach number ($M = [0\,;1.0]$ blue to red, $M = [1.0\,;1.3[$ white to black, $M = 1.0$ is in white). Shock position is shown in black with an isosurface of the streamwise velocity derivative.

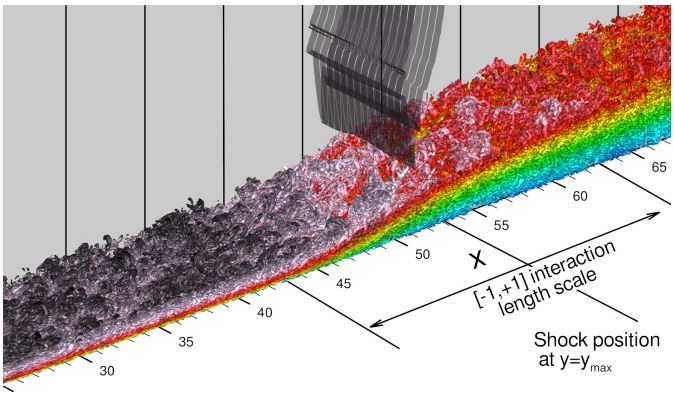

Figure 4.17: Zoom on the interaction area. Q criterion ($Q = -0,15(U_\infty/\delta_0)^2$), coloured with the local Mach number ($M = [0\,;1.0[$ blue to red, $M = [1.0\,;1.3]$ white to black, $M = 1.0$ is in white). Shock position is shown in black with an isosurface of the streamwise velocity derivative.

4.3 Supersonic turbulent boundary layer in a rectangular duct: influence of the mean inflow conditions on the wall bisector and the corner flows

This last validation case has lead to a presentation at the AIAA conference. In the following, we consider the undisturbed flow in a rectangular duct at $M = 1.61$. The geometry and the selected inflow conditions correspond to the case of the experiment of Carroll and Dutton [21] and of the wall-resolved LES of Morgan *et al* [67, 68]. To inhibit the formation of shocks, (supersonic) non reflecting outflow conditions are imposed at the exit plane. The length (L_x) of the duct (of interest for the analysis) is 400mm; the width (L_z) and the height ($L_y = 2h$) are, respectively, 76.2mm and 33.75mm.

The simulations have been carried out on a Cartesian non uniform grid consisting of $1402 \times 279 \times 515$ points. The streamwise extent (L_x), the spanwise length (L_z) and the duct height (L_y), expressed in δ_{in} units, are, 109.3, 9.2 and 20.7 respectively; the mesh resolution in wall units is $\Delta_x^+ \simeq 20$, and Δ_y^+ and Δ_z^+ vary between 1 and 15.

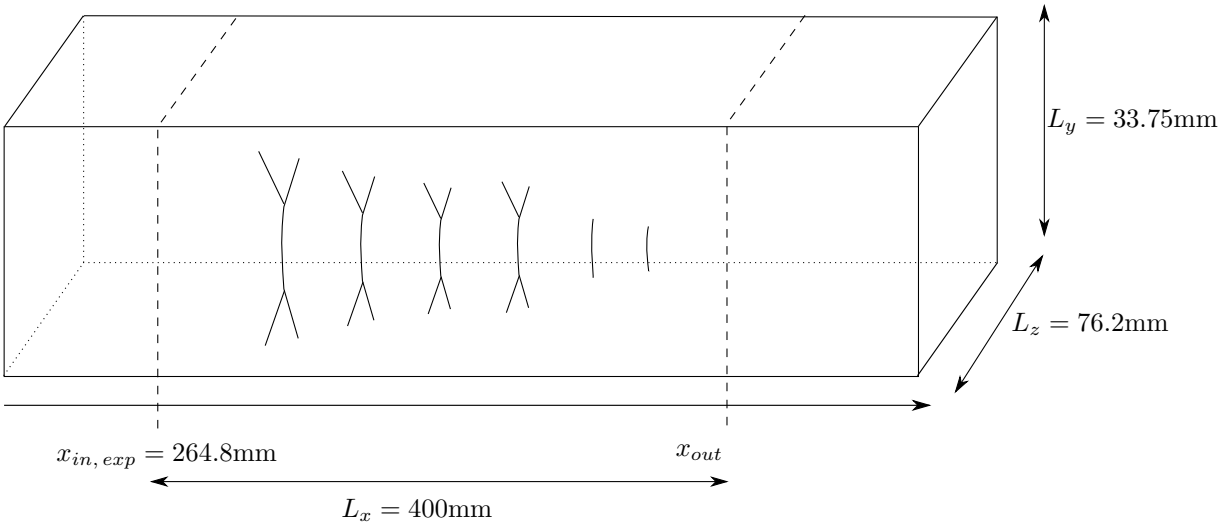

Figure 4.18: Schematic of the rectangular duct geometry.

The present work deals with supersonic flow in a rectangular duct, and focuses on the use of a RR strategy and on the sensitivity of the flow topology upon the turbulence properties at the inflow by considering two different mean inflow conditions. One (Case A) is based on the assumption that the boundary layers developing along adjacent walls are loosely coupled. The other (Case B) is based on a strategy that accounts for near-corner effects by injecting at the inlet the rescaled mean flow extracted at the recycling station, as is done for the turbulence inflow generation.

Case A:

At the inflow, the van Driest transformation mean velocity distribution is computed assuming a turbulent flat plate boundary layer profile. For the wall-binormal direction y we have:

$$u_{vd}^{+} = \begin{cases} \dfrac{1}{\kappa}\log(1+\kappa y^{+}) + C_1\left(1-\exp(-\dfrac{y^{+}}{\eta_1}) - \dfrac{y^{+}}{\eta_1}\exp(-by^{+})\right) + k_0 \sin\left(\dfrac{\pi}{2}y/\delta_{in}\right)^2 & (y<\delta) \\ u_{vd_\infty}/u_\tau & (y \geq \delta) \end{cases} \tag{4.6}$$

where $b = 0.33$, $C_1 = -\frac{1}{\kappa}\log(\kappa) + C$, $C = 5.2$, $\eta_1 = 11$, $\kappa = 0.41$ is von Karman constant and $k_0 = u_{vd_\infty}/u_\tau - \frac{1}{\kappa}\log(1+\kappa\delta/\delta_\nu) + C_1\left(1-\exp(-\frac{\delta/\delta_\nu}{\eta_1}) - \frac{\delta/\delta_\nu}{\eta_1}\exp(-b\delta/\delta_\nu)\right)$.

The mean velocity along the wall-binormal direction y is then obtained by the inverse van Driest transformation. Similar distributions are used for the other wall-binormal directions. The coupling between adjacent walls is then enforced through a weighting function based on the inverse squared wall distances. The pressure is assumed to be uniform and the mean density is determined from the Crocco-Busemann integral.

Case B:

In Case B we account for near-corner secondary flow by redistributing at the inlet the "Case A" mean variables extracted at the recycling plane and rescaled in the units of the inflow plane, as done for the generation of the fluctuating field. This treatment is similar to the one described by Morgan *et al*[67] where the mean flow component is recycled and imposed as an inflow condition.

To highlight the influence of the mean inflow component, we analyze the flow properties at the centerline ($z = L_z/2$), and in two transverse planes located, respectively, at $x/\delta_{in} = 25$ and $x/\delta_{in} = 60$. For all cases, the recycling station is fixed at $x_{rec} = 18.5\delta_{in}$.

4.3.1 Analysis along the wall bisector ($z = L_z/2$)

In figures 4.19 and 4.20 we report the distribution of the van Driest mean velocity component (in wall unit, left panel) and the normal Reynolds stress (in outer unit, right panel) at various distances from the inlet; in figure 4.19 we also report the results of the undisturbed flow analysis of Morgan [67]. At a given location ($x/\delta_{in} = 25$) we observe that the mean inflow conditions have some influence on the evolution of the boundary layer, as inferred both from the differences in the velocity and Reynolds stress distributions reported in figure 4.19. The figure also shows that Case B results compare most favorably with the LES reference of Morgan[67]. At a distance from the inlet where the Re_τ is the same both for Case A and Case B the dependence on the mean inflow conditions is weak (see figure 4.20).

In figure 4.21 we report the distributions of the displacement and momentum thicknesses (normalized by δ_{in}, left panel) and of the skin friction coefficient (right panel) at the mid-longitudinal plane as a function of the streamwise coordinate (x) scaled by the inflow boundary layer thickness. The figure shows that the growth rate of the boundary layer thicknesses and the skin friction coefficient are weakly dependent of the mean inflow conditions.

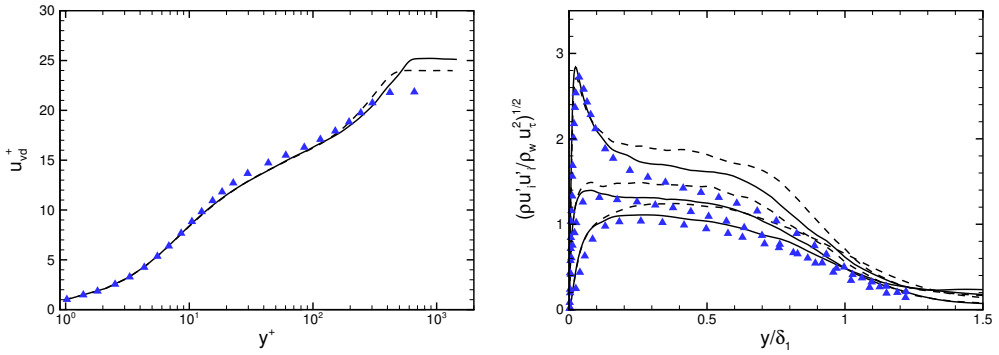

Figure 4.19: Undisturbed flow simulation. Sensitivity to mean inflow conditions. Distribution of the van Driest mean velocity u^+_{vd} (left panel) and of the normal Reynolds stress components $(\rho\widetilde{u'_i u'_i}/(\rho_w u_\tau^2))^{1/2}$ in inner unit. Dashed line, Case A ($x/\delta_{in} = 25$, $Re_\theta = 1880$); solid line, Case B ($x/\delta_{in} = 25$, $Re_\theta = 2610$); ▲ LES of Morgan [67].

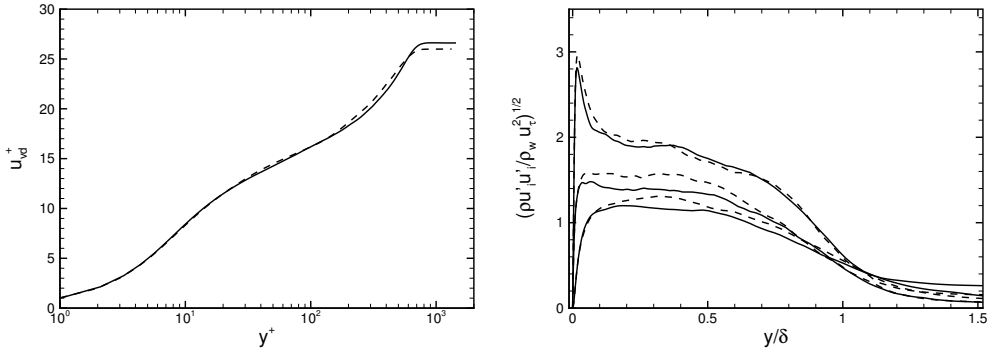

Figure 4.20: Undisturbed flow simulation. Sensitivity to mean inflow conditions. Distribution of the van Driest mean velocity u^+_{vd} (left panel) and of the normal Reynolds stress components $(\rho\widetilde{u'_i u'_i}/(\rho_w u_\tau^2))^{1/2}$ in inner unit. Dashed line, Case A ($x/\delta_{in} = 63$, $Re_\tau = 380$); solid line, Case B ($x/\delta_{in} = 56$, $Re_\tau = 380$).

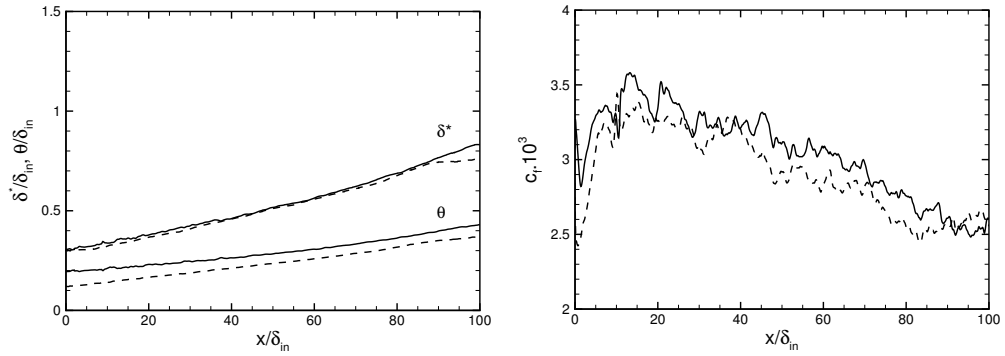

Figure 4.21: Distribution of the displacement δ^*, and momentum θ thicknesses normalized by δ_{in} (left panel) and of the skin friction coefficient (right panel) as a function of x/δ_{in}. Dashed line, Case A; solid line, Case B.

4.3.2 Analysis in the transverse plane

Turbulent flows in non circular ducts (either squared or rectangular) are characterized by secondary motions where fluid elements possess an angular velocity in the streamwise flow direction. Secondary flows are associated with non-zero streamwise vorticity component that exists only if the transverse velocity components are non zero. The main streamwise flow determines transverse turbulence components and correlations, while the streamwise vorticity is the result of convection, diffusion due to molecular effects, vortex stretching, baroclinic torque (associated with the pressure gradient and density variations) and stress-induced mechanism due to turbulence.

In order to further elucidate the influence of the near-corner secondary flow and the dependence upon the mean inflow condition, we analyze the distribution of the Reynolds stress components (both the normal and the off-diagonal ones) and the mean streamwise vorticity component in the transverse plane. For the analysis, as proposed by Morgan [67], all quantities are time and quadrant averaged.

In figure 4.22 we report the mean streamwise velocity component $\tilde{u}$ (panel (a)), the mean transverse velocity components $\tilde{v}$ (panel (b)) and $\tilde{w}$ (panel (c)) at $x/\delta_{in} = 60$. The figure shows that $\tilde{u}$ varies along the corner bisector and that secondary flows due to corner effects induce transverse flow parallel to each wall, and consequently,$\tilde{v}$ and $\tilde{w}$ are non-zero. As observed by Brundrett and Baines[18] and also found by Morgan[67], near-corner secondary flow produces two counter rotating vortices per quadrant, which are fed by the induced motion of fluid elements that move toward the corner in the bisector direction and divert around the corner in the directions parallel to the walls.

The mechanism of streamwise vorticity generation is of primary importance for the establishment of secondary flows. The Mach number of the simulation being rather low, the compressibility effects are negligible[67] and the streamwise vorticity budget[18] reduces to

$$\bar{\rho}\bar{v}\frac{\partial\overline{\omega_x}}{\partial y} + \bar{\rho}\bar{w}\frac{\partial\overline{\omega_x}}{\partial z} = \frac{\partial^2\overline{\rho}(\overline{w'^2} - \overline{v'^2})}{\partial y\partial z} - \left(\frac{\partial^2}{\partial y^2} - \frac{\partial^2}{\partial z^2}\right)\overline{\rho v'w'} + \mu\left(\frac{\partial^2\overline{\omega_x}}{\partial y^2} + \frac{\partial^2\overline{\omega_x}}{\partial z^2}\right) \tag{4.7}$$

where we have assumed that μ is constant. The equation shows that the streamwise vorticity budget depends on the transverse motion (mean velocity components and their gradient on the transverse plane) and on the effects of the turbulent stresses (the stress-induced generation) as well as on viscous effects.

Figures 4.23 and 4.24 show, respectively, the iso-contours of the streamwise vorticity and the stress-induced generation at two transverse planes ($x/\delta_{in} = 25$ and $x/\delta_{in} = 60$). The figures show that the flow pockets (the near-corner counter-rotating vortices) are associated with the

region where the streamwise vorticity is largest due to the dominant effect of the stress-induced contribution, and confirms that the flow topology is weakly affected by the mean inflow conditions.

The Reynolds stress tensor (whose components are reported in figures 4.25–4.30) is anisotropic. From the figures, it can be seen that there is a reduction of the streamwise normal component $\widetilde{u'u'}$ close to the corner. Secondary flows induce a motion parallel to each wall, and both normal stress components $\widetilde{v'v'}$ and $\widetilde{w'w'}$ increase along each wall on a scale $o(\delta)$ from the corner. The off-diagonal components $\widetilde{u'v'}$, and $\widetilde{u'w'}$ vary in the wall bisector direction and increase near the corner. The $\widetilde{v'w'}$ component is one order of magnitude smaller; and it varies along the corner bisector direction and exhibits a peak in the vicinity of the corner. Despite some differences in the local friction Reynolds number at $x/\delta_{in} = 60$ (Case A: $Re_\tau = 362$, Case B: $Re_\tau = 395$), the topology of the transverse flow is not significantly affected by the inflow conditions when scaled in outer units.

Further analysis on the dynamic of the secondary flows in the corner are not carried out. We remind that the inflow used for case b is based on the results obtained for case a. We can assume that one of the reason why case a and case b flows are similar is caused by the mean flow at the inflow that are somehow correlated. This correlation biased the comparison and prevents us from doing a deeper analysis. In order to continue the analysis, the two mean flow should be uncorrelated and for instance obtained through RANS simulation with a linear eddy viscosity and a non-linear one (in order to obtain secondary flows).

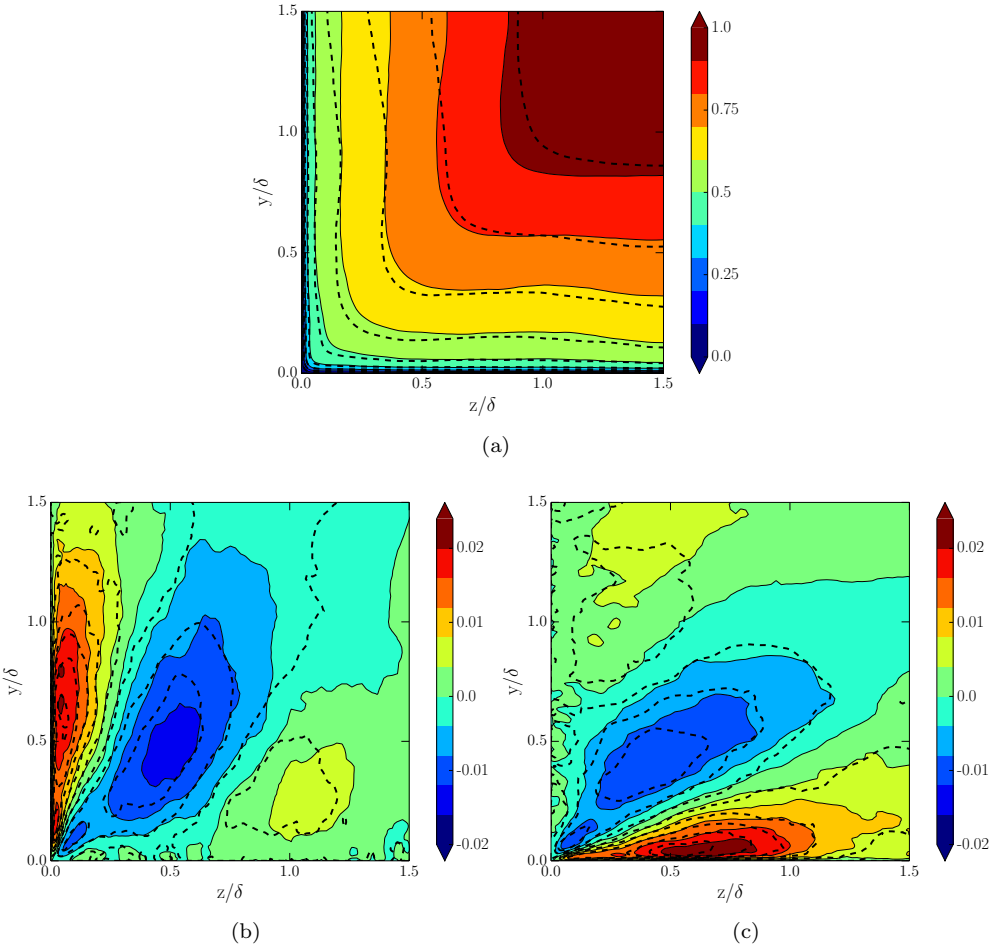

Figure 4.22: Eleven evenly spaced contours of the velocity components in the transverse plane, $x/\delta_{in} = 60$. Dashed line, Case A; solid line and the background iso-contour, Case B. (a) $\widetilde{u}/u_\infty$ from 0 to 1; (b) $\widetilde{v}/u_\infty$ from -0.02 to 0.02; (c) $\widetilde{w}/u_\infty$ from -0.02 to 0.02.

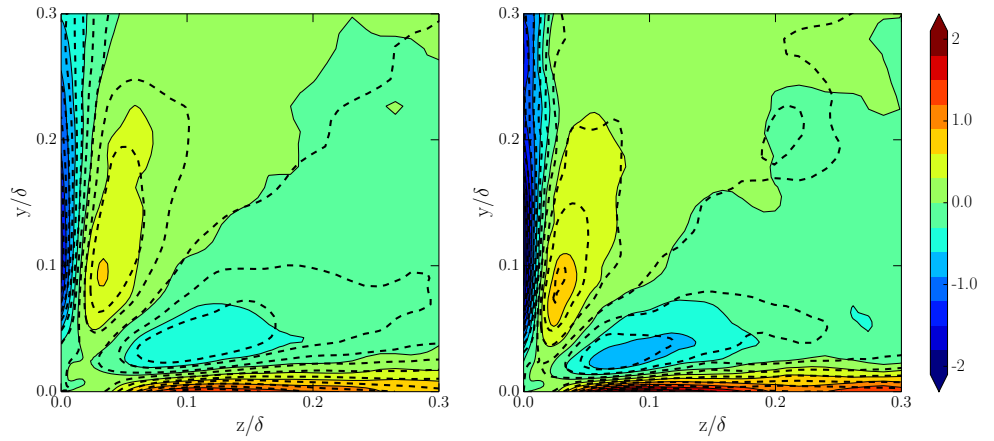

Figure 4.23: Fifteen evenly spaced contours the mean streamwise vorticity ($\widetilde{\omega_x}\delta/u_\infty$) from -2 to 2 at $x/\delta_{in} = 25$ (left panel) and $x/\delta_{in} = 60$ (right panel). Dashed line, Case A; solid line and background iso-contours, Case B.

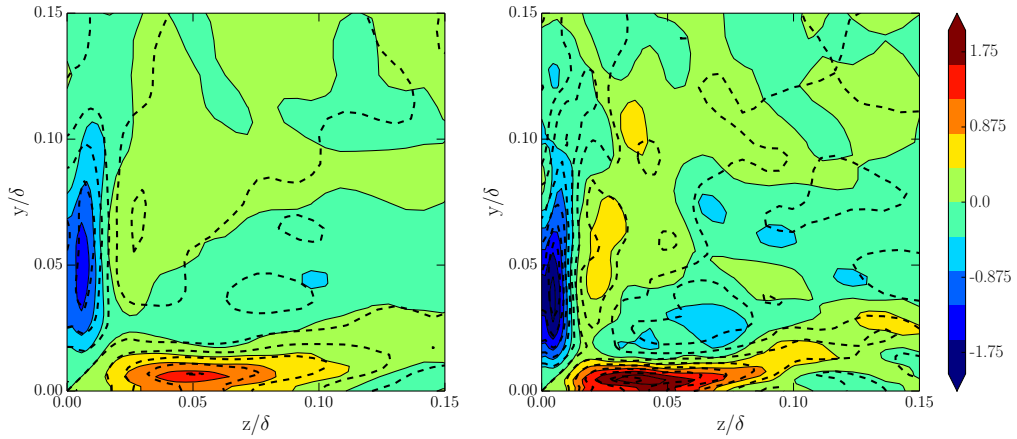

Figure 4.24: Eleven evenly spaced contours of $\left[\left(\frac{\partial^2}{\partial y^2} - \frac{\partial^2}{\partial z^2}\right)\left(-\widetilde{v'w'}\right)\right]\delta^2/u_\infty^2$ from -1.75 to 1.75 at $x/\delta_{in} = 25$ (left panel) and $x/\delta_{in} = 60$ (right panel). Dashed line, Case A; solid line and background iso-contours, Case B.

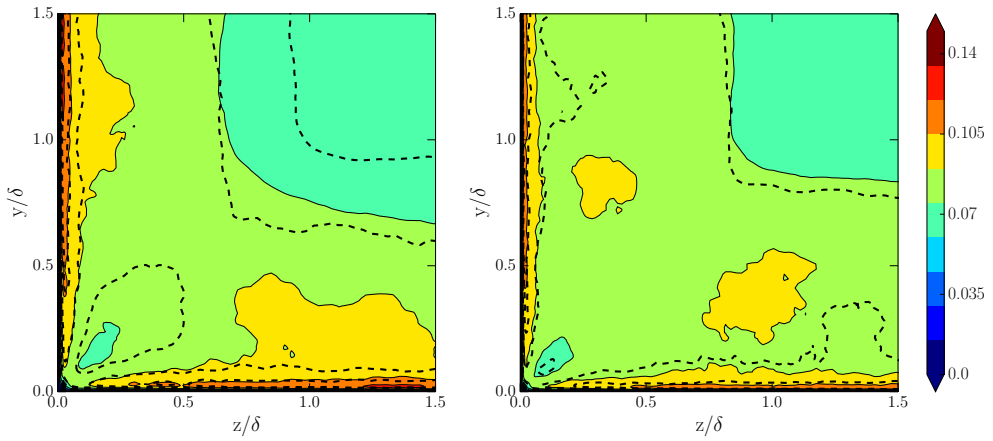

Figure 4.25: Eleven evenly spaced contours of $\widetilde{u'u'}^{1/2}/u_\infty$ from 0 to 0.14 at $x/\delta_{in} = 25$ (left panel) and $x/\delta_{in} = 60$ (right panel). Dashed line, Case A; solid line and background iso-contours, Case B.

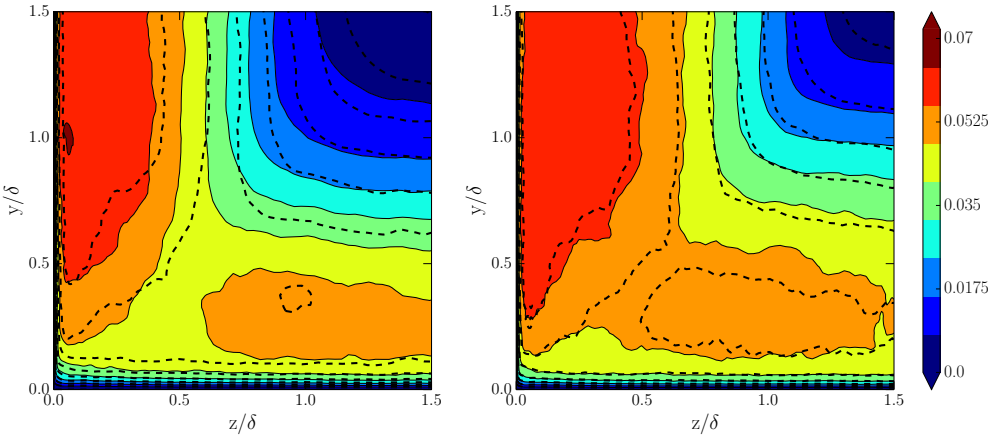

Figure 4.26: Eleven evenly spaced contours of $\widetilde{v'v'}^{1/2}/u_\infty$ from 0 to 0.07 at $x/\delta_{in} = 25$ (left panel) and $x/\delta_{in} = 60$ (right panel). Dashed line, Case A; solid line and background iso-contours, Case B.

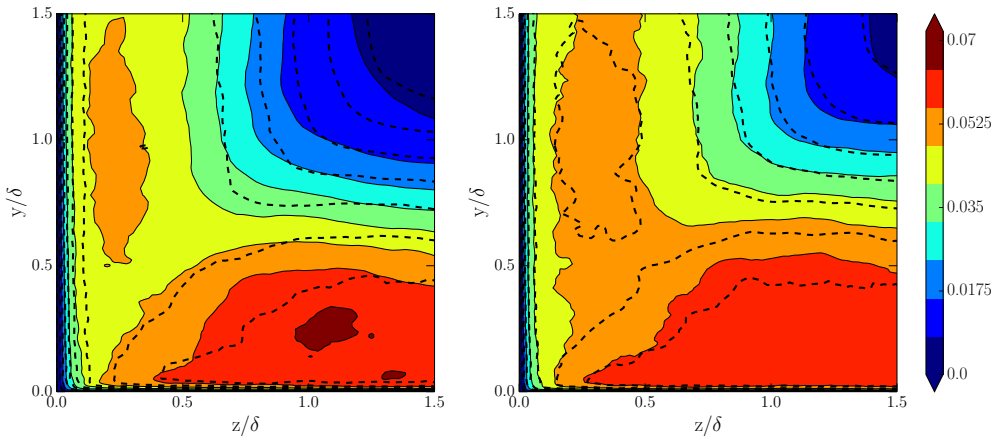

Figure 4.27: Eleven evenly spaced contours of $\widetilde{w'w'}^{1/2}/u_\infty$ from 0 to 0.07 at $x/\delta_{in} = 25$ (left panel) and $x/\delta_{in} = 60$ (right panel). Dashed line, Case A; solid line and background iso-contours, Case B.

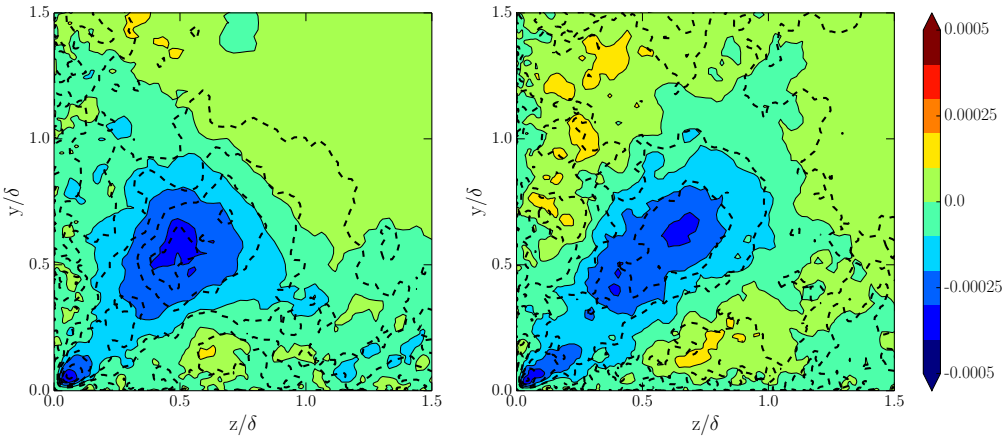

Figure 4.28: Eleven evenly spaced contours of $\widetilde{v'w'}/u_\infty^2$ from -0.0005 to 0.0005 at $x/\delta_{in} = 25$ (left panel) and $x/\delta_{in} = 60$ (right panel). Dashed line, Case A; solid line and background iso-contours, Case B.

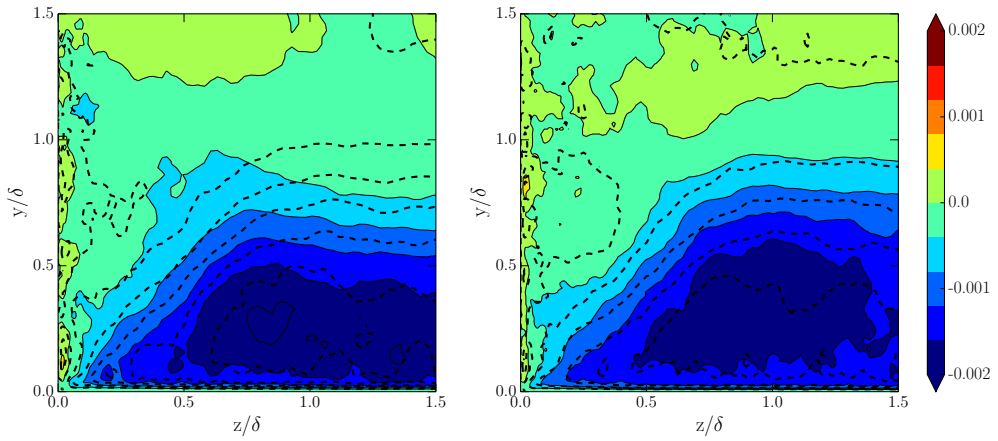

Figure 4.29: Eleven evenly spaced contours of $\widetilde{u'v'}/u_\infty^2$ from -0.002 to 0.002 at $x/\delta_{in} = 25$ (left panel) and $x/\delta_{in} = 60$ (right panel). Dashed line, Case A; solid line and background iso-contours, Case B.

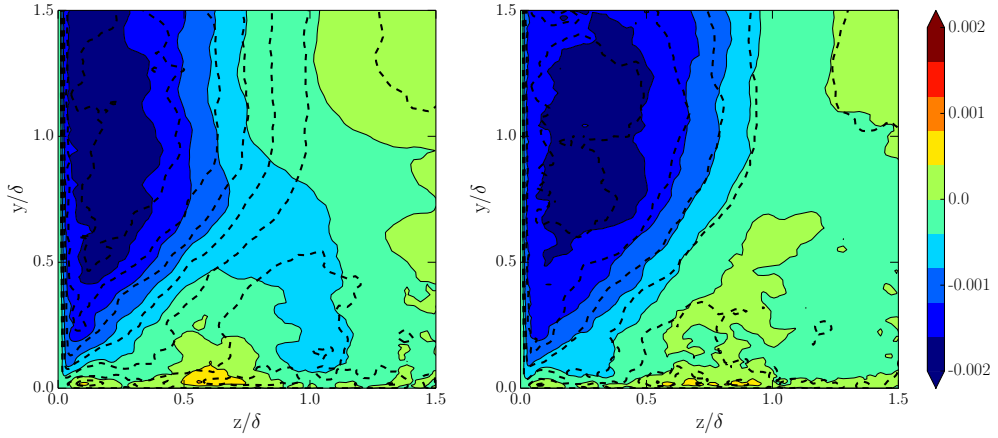

Figure 4.30: Eleven evenly spaced contours of $\widetilde{w'u'}/u_\infty^2$ from -0.002 to 0.002 at $x/\delta_{in} = 25$ (left panel) and $x/\delta_{in} = 60$ (right panel). Dashed line, Case A; solid line and background iso-contours, Case B.

Chapter Summary

- Multiples Large-Eddy-Simulations have been carried out to validate the numerical tools on three test cases.
  1) LES of a Mach-two-adiabatic-turbulent-boundary-layer
     - The effect of the subgrid model is assessed: ILES is efficient and precise.
     - The results match the reference compressible DNS and incompressible DNS, where appropriate.
     - Using the van Driest transformation compressible results collapse on the incompressible ones
  2) LES of transonic interaction in a Mach 1.3 external flow
     - The case is designed to test the outflow boundary condition that impose the outflow pressure
     - A DNS of a transonic interaction is successfully reproduced in LES with a coarser mesh
  3) LES of boundary layers spatially developing inside a rectangular duct
     - Similar results are observed with two different mean inflow conditions
     - The turbulent inflow boundary condition gives satisfying results
- The results of those LES have shown our capacity to carried out LES of turbulent wall-bounded flow: 1) without shock on a flat plate, 2) with a normal shock and 3) inside a diffuser without shock.

→ all the required ingredients have been tested.

Chapter 5

Side walls effect on shock-train

Contents

5.1 Parameters of the study 74
5.2 Centreline flow properties ($z = L_z/2$) 76
5.2.1 Boundary layer scales and wall pressure signature 77
5.2.2 Influence of the aspect ratio on the mean flow and turbulence statistical properties 83
5.3 Skin frictions patterns 101
5.4 Flow organization 105

In this chapter, we discuss large eddy simulations of a Mach 1.61 shock-train in constant rectangular ducts at various aspect ratios (AR=W/H), W and H being the spanwise extent and the height respectively. Four aspect ratios are considered AR=∞; 5; 2.257; 1.5 (The AR=∞ case corresponds to a simulation where periodic boundary conditions are imposed in the spanwise direction). Simulations are carried out without sub-grid model corresponding to the approach previously called ILES. Results are compared with the simulations of Morgan et al. [68] and with the experiment of Carroll and Dutton [21], where appropriate.

5.1 Parameters of the study

In the present thesis we focus on the experiment of Carroll and Dutton [21] of a Mach 1.61 shock-train in a slightly diverging rectangular duct. The divergence angle of both inner and upper walls being very small (0.13° for each wall), as in Ref. [68], we assume a constant rectangular duct whose length, height and width ($Lx \times Ly \times Lz$) are set equal to 400mm×33.75mm×76.2mm. Similarly, to ensure adequate mesh resolution, the Reynolds number based on the boundary layer thickness at the beginning of the interaction is set one order of magnitude less than the experimental value ($Re_\delta \sim 15000$, that is approximately the same value than in Morgan et al. [68]). As described in section 3.2.2, we use a recycling-rescaling method for the turbulence generation at the inflow according to the approach proposed by Boles et al. [12] and used by Morgan et al. [68]. The latter introduces a separate mesh to simulate the undisturbed boundary layers developing on the wall to generate the inflow turbulence on the so-called interaction mesh (*i.e.* the one used for the shock-train simulation). By doing-so, the effect of the leading edge shock on the inflow turbulence are weakened.

A confinement parameter is defined as the ratio of the boundary layer thickness at the beginning of the interaction δ_2 divided by the half-height h. In order to match the confinement parameter of Ref. [21], as done by Morgan et al. [68], we have varied the outflow pressure so as to match the location of the initial shock ($AR = 2.257$ and $AR = 1.5$). For the higher aspect ratio cases (AR=5; ∞), we have let the shock-train system adapt to the outflow conditions that are

unchanged with respect to the experiment. The parameters of the study are reported in table 5.1 including the values of Morgan et al. [68] and Carroll and Dutton [21]; observe that subscript 1 and 2 indicate, respectively, the location where the confinement is equal to 0.32 and the beginning of the interaction where the pressure starts to rise. A schematic summarized the main parameter in figure 5.1.

Between the various AR cases we observe that the Reynolds number and the ratio δ_2/h are not equal between all cases. Differences in the Reynolds number at the beginning of the interaction are small and are assumed to be negligible. The variation of the parameter δ_2/h has been studied experimentally by Dutton and Carroll [36] and may modify the shock-train (length, recovery pressure ...). Nonetheless, due to the fact that the width variation is one order of magnitude higher than the variation of δ_2/h, we may assume that the dominant effect is the variation of the width. For $AR = 1.5$ and $AR = 2.257$ the parameter δ_2/h is constant and for cases $AR = 5$ and $AR = \infty$ it varies less than 10%.

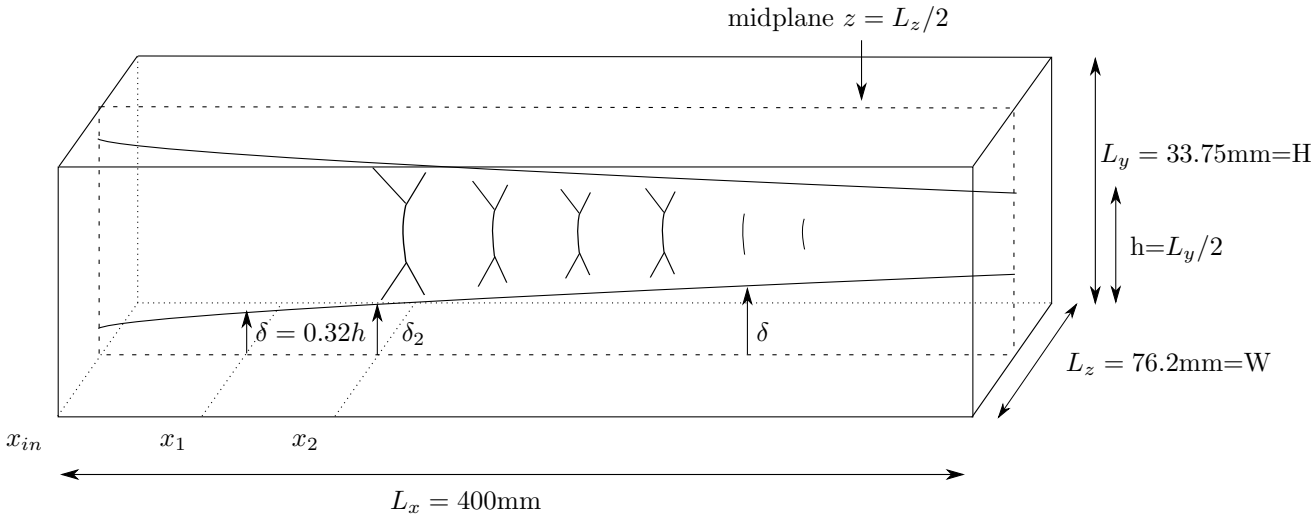

Figure 5.1: Schematic of the duct geometry. Subscript 1 and 2 indicate, respectively, the location where the confinement (δ/h) is equal to 0.32 and the beginning of the interaction (the location where the pressure starts to rise).

The mesh parameters (number of nodes Nx, Ny and Nz, mesh extent Lx, Ly and Lz normalized by the boundary layer thickness at x_1, and grid-spacing in wall units at the beginning of the interaction) are given in table 5.2. In table 5.3 we report the initial time (t_0) at which data is collected for statistics and the period of integration (T) both in the boundary layer outer units δ_1/u_∞ and in throughput time units $\sqrt{\gamma}M_\infty.Lx/u_\infty$.

AR	x_1/δ_1	x_2/δ_1	δ_{in}/h	δ_1/h	δ_2/h	Re_{δ_2}	p_{out}/p_{in}
∞	14.2	25.3	0.24	0.32	0.39	19000	2.23170
5.0	14.0	19.0	0.24	0.32	0.35	16400	2.23102
2.257	14.0	14.0	0.24	0.32	0.32	15300	2.04967
1.5	12.9	12.0	0.24	0.32	0.31	15000	1.93472
∞, case 'L3' of Ref [68]	9.96	18.9	0.27	0.32	0.36	18200	2.23085
2.257, case 'L2' of Ref [68]	6.15	6.15	0.27	0.32	0.32	16200	2.04623
2.257, experiment of [21]	0	0	0.32	0.32	0.32	$O(10^6)$	2.23085

Table 5.1: Confinement parameters for the current LES of periodic shock-train and LES of shock-trains in ducts of various aspect-ratio, and, for the two LES of Morgan et al. [68] that consist of a periodic shock-train and a shock-train with an aspect ratio of 2.257; and for the experiment of Carroll and Dutton [21].

For comparison, all data are reported in the rescaled coordinate $(x - x_2)/\delta_1$. The LES being highly resolved, to meet storage constraints, only data at the spanwise mid-plane $z = Lz/2$ and at the upper walls are stored at all times at a sampling rate of $0.19\delta_1/u_\infty$. We observe that for the case AR=5, the period over which the data are collected is rather short (due to shortage on computational time), hence, an 8^{th} order filter is applied to the data for post-treatment. A similar filter is applied for the post-treatment of the wall normal derivatives used to draw the friction lines (see the following section).

AR	Nx	Ny	Nz	Lx/δ_1	Ly/δ_1	Lz/δ_1	Δ_x^+	Δ_y^+	Δ_z^+	Points ($\times 10^6$)
∞	1402	279	188	74	6.25	6.45	21	0.9-13-0.9	13	73.5
5.0	1402	279	1023	74	6.25	31.25	21	0.9-13-0.9	0.9-13-0.9	400.1
2.257	1402	279	515	74	6.25	14.1	21	0.9-13-0.9	0.9-13-0.9	201.4
1.5	1402	279	375	74	6.25	9.39	21	0.9-13-0.9	0.9-13-0.9	146.7
∞, Ref [68]	1601	401	131	74	6.25	3.0	20	1-10-1	10	85.4
2.257, Ref [68]	1072	289	515	74	6.25	14.1	30	1-15-1	1-15-1	159.6

Table 5.2: Mesh parameters for the current LES of periodic shock-train and LES of shock-trains in ducts of various aspect-ratio, and, for the two LES of Morgan et al. [68] that consist of a periodic shock-train and a shock-train with an aspect ratio of 2.257. For our simulations the spacing is given in inner unit at the location x_2. Region of stretching are indicated with a dash.

AR	1.5	2.257	5.0	∞
T	104	300	52	300
t_0	1242	867	660	760

(a)

AR	1.5	2.257	5.0	∞
T	0.8	2.2	0.4	2.2
t_0	8.8	6.1	4.7	5.4

(b)

Table 5.3: Time-integration parameters for the statistics of the current LES, where t_0 is the initial time at which data is collected for statistics and T is the period of integration. (a) time is normalized by δ_1/u_∞; (b) time is normalized in throughput time ($\sqrt{\gamma}M_\infty.Lx/u_\infty$).

5.2 Centreline flow properties ($z = L_z/2$)

In figure 5.2 we report the contours of the mean gradient density magnitude at various aspect ratios (AR=∞, panel a; AR=5, panel b; AR=2.257, panel c; AR=1.5, panel d)

For all cases, the flow is propagating from left to right and an initial shock, which is curved, is located between $(x - x_2)/\delta_1 = 3$ and 4. The flow is compressed by a second and a third shocks located between $(x - x_2)/\delta_1 = 8$ and 9, and around $(x - x_2)/\delta_1 = 13$, respectively. Along the bottom and top walls ($y = 0$ and $y = 6.25$)the boundary layers thicken just after x_2, where oblique compression waves are progressively imposing an adverse pressure gradient, and secondary shocks become weaker and are straighter in the streamwise direction. During the compression, the thickening of the boundary layers reduces the effective section. This reduction acts as an aerodynamic nozzle making the flow to accelerate.

Careful examination reveals evidence of slip lines close to the core of the flow (at wall distance where the compression waves and the initial shock merge). Weaker secondary shocks are visible, increasing of number as the aspect ratio is decreased (for AR=1.5 secondary shocks can be seen until at least $(x - x_2)/\delta_1 \sim 40$). In the case AR=1.5, the shocks are stronger. As observed by Morgan et al. [68], the farther the initial shock is located downstream, the weaker is the second shock and the confinement ratio δ/h is higher. We observe that the secondary shock of the AR=2.257 case is slightly stronger than the cases with larger aspect ratio (however, those cases have higher confinement parameter). The AR=1.5 case has the same confinement than the AR=2.257 case, and it exhibits stronger secondary and tertiary shocks.

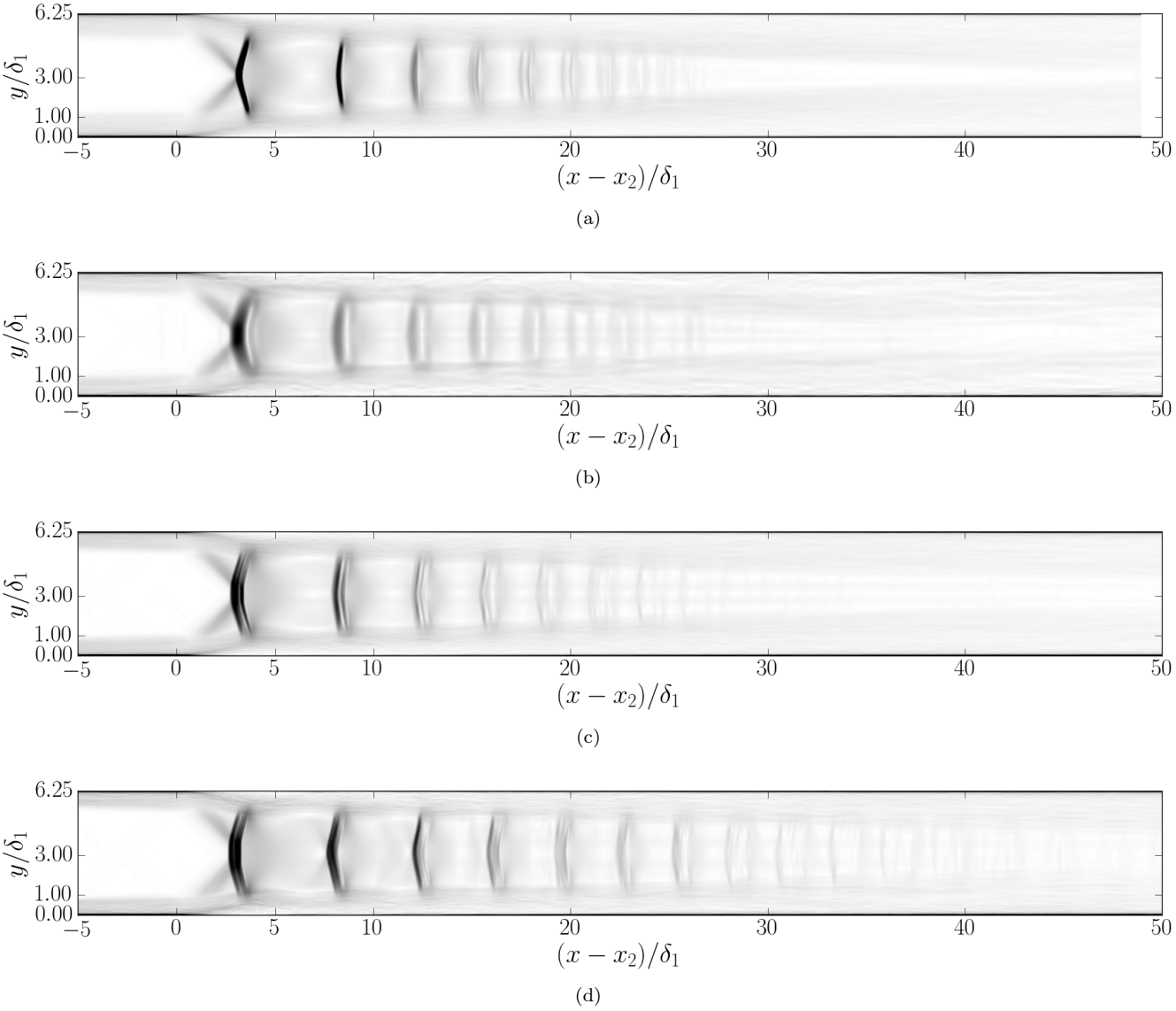

Figure 5.2: Contours of the density gradient magnitude between 0 (white) and 1.5 (black). (a) periodic boundary conditions in the spanwise direction (AR=∞); (b) AR=5; (c) AR=2.257; (d) AR=1.5

5.2.1 Boundary layer scales and wall pressure signature

In this subsection we compare the different boundary layer scales with the experimental results of Carroll and Dutton [21] and the LES results of Morgan et al. [68].

Various definitions of the boundary layer thickness can be found in the literature. In the previous chapter, we have used two of those definitions: for the supersonic boundary layer, the boundary layer thickness is usually defined as the wall distance where the velocity reaches the value of 99% of u_∞; for the transonic case, it is defined as the wall distance where the vorticity magnitude reaches 0.005. In this section, the boundary layer thickness δ is defined as the wall-distance where the velocity reaches 99% of the velocity at the center of the duct, noted $u_c(x)$, and the momentum and displacement thicknesses are computed through equations 3.10 and 3.11 that

become

$$\delta^*(x,z) = \int_0^\delta \left(1 - \frac{u(x,y,z)}{u_c(x)}\right) dy \tag{5.1}$$

$$\theta(x,z) = \int_0^\delta \left(1 - \frac{u(x,y,z)}{u_c(x)}\right) \frac{u(x,y,z)}{u_c(x)} dy \tag{5.2}$$

The streamwise distribution of the characteristic boundary layer scales are reported in figure 5.3 (AR=∞ and AR=5 cases) and in figure 5.4 (AR=2.257 and AR=1.5 cases). The results are compared with the simulation of Morgan et al. [68] and the experiment of Carroll and Dutton [21]. The quantities are normalized by the duct height (panels a,c,d) and by the corresponding value at the origin of the interaction (panels e,f). From the experimental distribution we observe that: 1) the boundary layer thickness is continuously increasing; 2) the displacement thickness is maximum close to the initial shock location and then continuously decreases; and 3) the momentum thickness is still growing downstream of the initial shock until a location $(x - x_2)/\delta_1 \sim 30$. The results show that higher aspect ratios geometries tend to have thicker boundary layer downstream of the shock-train than cases with smaller aspect ratios. The boundary layer scales have an oscillatory behaviour through the shock-train and a rather smooth distribution downstream. Three local minimum are observed at the location of the primary, secondary and tertiary shock ($(x - x_2)\delta_1 \sim 3.5$; ~ 5; ~ 13, respectively).

A possible explanation for this behaviour is that the boundary layers developing along each wall are submitted to successive variations of the pressure gradient, and multiple compressions and expansions lead to oscillations of the boundary layer thicknesses. During compressions, the boundary layer is thickened by the adverse pressure gradient, while in the expansion, the favorable pressure gradient makes it thinner. Nonetheless, the shocks seem to be localized close to the local minima of the boundary layer thicknesses. This is probably caused by the use of the centreline velocity in the definition of the boundary layer thicknesses (equations 5.1 and 5.2). Curvatures of the shocks are minimum at the centre of the duct. This induces a local minimum in the velocity profile at the centre of the duct[1] and consequently for these minima in the boundary layer thicknesses. The minima of the first oscillations are located just downstream of the first shocks or at the end of strong compression waves.

We can see that the position of the end of the first shock is the same for all cases. Nonetheless, a progressive lag appears in the position of the downstream compressions. This may be due to the use of δ_1 for the normalization which is a fixed value ($\delta_1 = 0.32h$) independent of the physics of the flow.

The distributions of the incompressible displacement and momentum thicknesses show some discrepancies with respect to the experimental results and those of Morgan et al. [68] (panel c and d of figures 5.3 and 5.4). When rescaling δ_i^* and θ_i by their values at the beginning of the interaction, a better agreement with the experiment is observed (panel e and f of figures 5.3 and 5.4). In particular, this result seems to indicate that the half-height of the duct is not the appropriate length to scale the boundary layer thicknesses. The displacement and momentum thicknesses of AR=2.257 case nearly matches the experimental values of Carroll and Dutton [21]. The case AR=5 exhibits an oscillation at the end of the computational domain that is likely caused by the short time of integration of the statistics.

For all cases, the incompressible shape factor (panel b of figures 5.3 and 5.4) exhibits a first peak at $(x-x_2)\delta_1 \sim 5$ with an amplitude $\sim 2.5-2.8$. After this peak, it decreases with different slopes depending on the value of the aspect ratio. Cases with higher aspect ratio tend to have an higher incompressible shape factor past the first shock. The collapsing of the data tends to indicate that the incompressible shape factor downstream of the initial shock may not be strongly influenced by the initial Reynolds number, at least for the lower AR cases (panel b figure 5.4).

Morgan et al. [68] point out that the observed discrepancies with respect to the experimental results may be ascribed either to differences in the geometry (constant section versus diverging)

[1] This is observed in the next subsection in subfigures 5.9 (e) and 5.10 (e)

and/or in the assumed Reynolds number of the simulation. The better matching of the present simulations with the experimental data seems to indicate that this conclusion has to be taken with caution and that other factors may be at the origin of the discrepancies.

In figure 5.5 we report the mean wall pressure distribution (panel a, AR=∞ and AR=5 cases; and panel b, AR=2.257 and AR=1.5 cases) as a function of the rescaled variable $(x - x_2)/\delta_1$ at the centerline plane ($z = Lz/2$). We observe that due to differences in the outflow pressure, the mean wall pressure relaxes to a value lower than the experimental one (figure 5.5). However, the pressure increase across the initial shock-train well compares with the experiment. For the higher AR cases, having imposed the same outflow pressure condition, the mean wall pressure distribution is very close to the periodic shock-train simulation of Morgan et al. [68]. Figure 5.5 (b) shows that mean wall pressure distribution is lower than in the simulation of Morgan et al. [68] The AR=2.257 case exhibits a mean wall pressure distribution lower than the one reported by Morgan et al. [68]. The distance between the inflow plane and the beginning of the interaction being greater than in Ref. [68] and the side wall effects being greater for AR=2.257 and AR=1.5 may explain such difference. However, the extent of the shock-train is of the same order as the one of Ref. [68]. As predicted in the case of an axisymmetric shock-train by Billig [8], our results indicate that the pseudo-shock is affected by the aspect ratio. In particular, it decreases as the aspect ratio decreases (varying between $(x - x_2)/\delta_1 \simeq 35$ and 50).

Shown in figure 5.6 is the distribution of the skin friction as a function of $(x - x_2)/\delta_1$ at the centerline plane ($z = Lz/2$). The minimum value of C_f attained across the initial shock is equal to the value of Ref. [21] and does not depend on the aspect ratio. This result may be partially biased by the fact that the vertical confinement between the cases is slightly different. Past the initial shock, the skin friction coefficient reaches higher values as the aspect ratio is reduced.

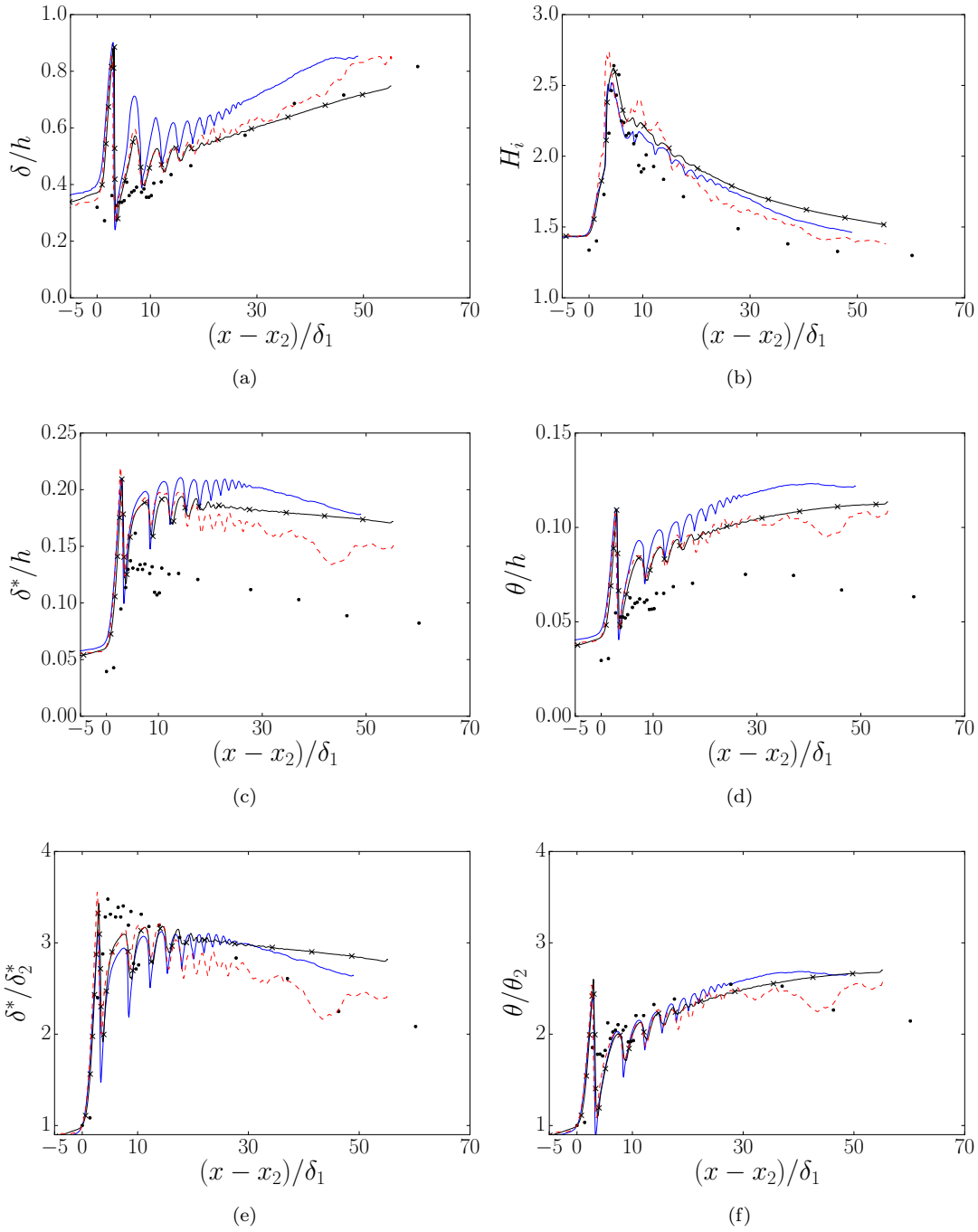

Figure 5.3: Streamwise distribution of the characteristic boundary layer scales for various aspect ratios evaluated at the centerline ($z = Lz/2$). (a) boundary layer thickness scaled by the duct height; (b) incompressible shape factor; (c) displacement thickness scaled by the duct height; (d) momentum thickness scaled by the duct height; (e) displacement thickness scaled by its value at the beginning of the interaction; (f) momentum thickness scaled by its value at the beginning of the interaction. ——, AR=∞ current simulation; – – –, AR=5 current simulation; —×—, AR=∞ LES Ref. [68]; •, exp. Ref. [21], AR=2.257.

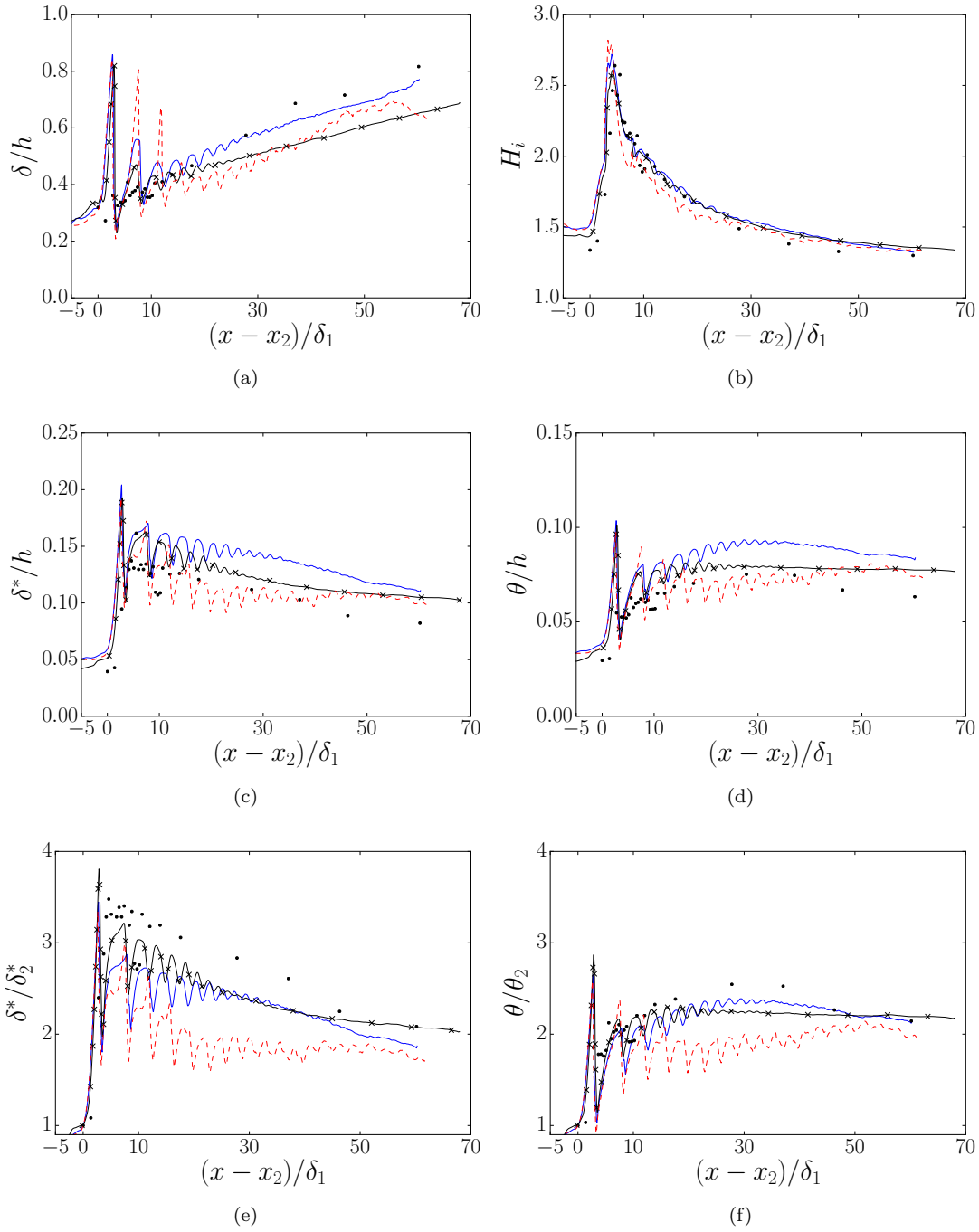

Figure 5.4: Streamwise distribution of the characteristic boundary layer scales for various aspect ratios evaluated at the centerline ($z = Lz/2$). (a) boundary layer thickness scaled by the duct height; (b) incompressible shape factor; (c) displacement thickness scaled by the duct height; (d) momentum thickness scaled by the duct height; (e) displacement thickness scaled by its value at the beginning of the interaction; (f) momentum thickness scaled by its value at the beginning of the interaction. ——— , AR=2.257 current simulation; – – –, AR=1.5 current simulation; —×—, AR=2.257 LES Ref. [68]; •, exp. Ref. [21], AR=2.257.

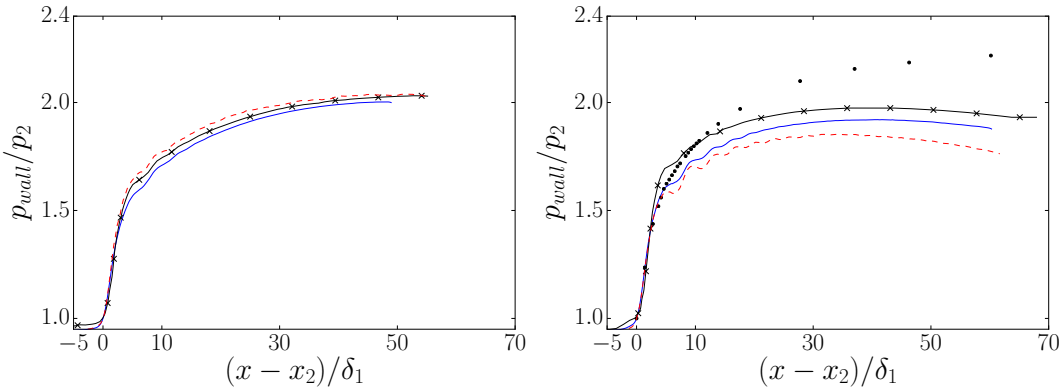

Figure 5.5: Wall pressure distribution along the centerline ($z = L_z/2$) scaled by the wall pressure at the beginning of the interaction p_2 for various shock-train configurations. (a) ——— , AR=∞ current simulation; – – –, AR=5 current simulation; —×—, AR=∞ LES Ref. [68]; (b) ——— , AR=2.257 current simulation; – – –, AR=1.5 current simulation; —×—, AR=2.257 LES Ref. [68]; •, exp. Ref. [21], AR=2.257.

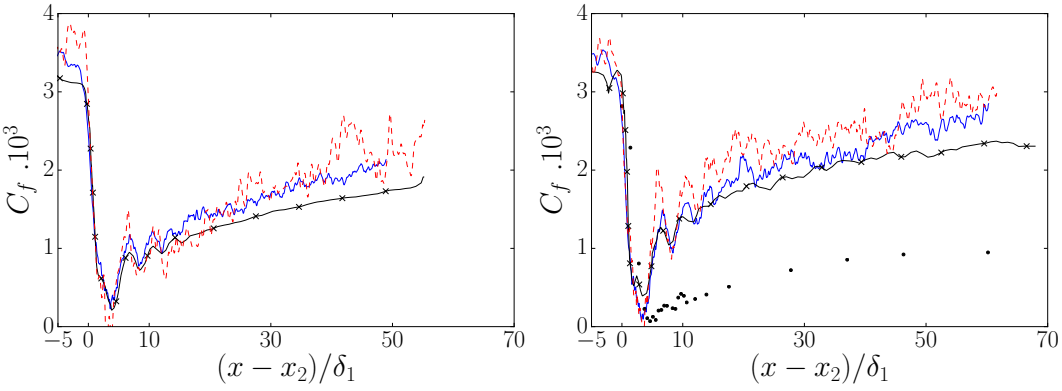

Figure 5.6: Streamwise distribution of the skin friction coefficient evaluated at the centerline ($z = L_z/2$) for various shock-train configurations. Panel a, ——— , AR=∞ current simulation; – – –, AR=5 current simulation; —×—, AR=∞ LES Ref. [68]; Panel b, ——— , AR=2.257 current simulation; – – –, AR=1.5 current simulation; —×—, AR=2.257 LES Ref. [68]; •, exp. Ref. [21], AR=2.257.

5.2.2 Influence of the aspect ratio on the mean flow and turbulence statistical properties

In this subsection we report mean and statistical turbulence properties evaluated at the mid-plane for various aspect ratios and, where appropriate, the results are compared with the LES data of Morgan et al. [68]. In particular we report the contours of the normalized mean streamwise and wall-normal direction (y) velocity components u/u_∞ and v/u_∞, respectively, the local Mach number ($M = \sqrt{\widetilde{u}^2 + \widetilde{v}^2 + \widetilde{w}^2}/\sqrt{\gamma R\bar{T}}$), and the mean total pressure (defined as $p_t = \bar{p}\left(1 + 0.5(\gamma - 1)M^2\right)^{\frac{\gamma}{\gamma-1}}$), as well as their distributions as a function of y at various streamwise locations.

From the contour of the mean velocity components (reported in figures 5.7 and 5.8) we observe similarities in the flow topology independently of the aspect ratio. However, the scales and the intensity of the shocks are affected by AR. The extent of the shock-train increases by reducing the AR, while the length of the pseudo shock decreases (as already mentioned in subsection 5.2.1). The current results compare very well with the LES data of Morgan et al. [68] both in the case of periodic spanwise boundary condition (AR=∞) and in the case corresponding to the conditions of the experiment of Carroll and Dutton [21] (AR=2.257). Similarly, the velocity profiles well compare with the results of Ref. [68] (figures 5.9 and 5.10).

We also observe that reducing the aspect ratio increases the effective aspect ratio parameter (δ^*/W) introduced by Ref. [17] and the "aerodynamic nozzle effect" is enhanced producing stronger expansions of the core flow past the primary, secondary and tertiary shocks (Fig. 5.13). The pressure losses (measured in terms of the local mean total pressure) are also strongly affected by the width-to-height ratio. In particular, a decrease of the total pressure in the core of the flow is observed when reducing the aspect ratio (Fig. 5.14, some doubt remain regarding the results observed in the latter figure). Shown in figure 5.15, is the streamwise distribution of the total pressure at various aspect ratios evaluated at the mid-plane ($z = Lz/2$) and at the duct centerline ($y = Ly/2$). As discussed in a latter section[2] a decrease in the aspect ratio affects the structure of the interaction of the shocks steaming from the upper and the lower walls that changes from regular to irregular thus affecting the pressure losses as observed in figure 5.15.

[2] See section 5.4

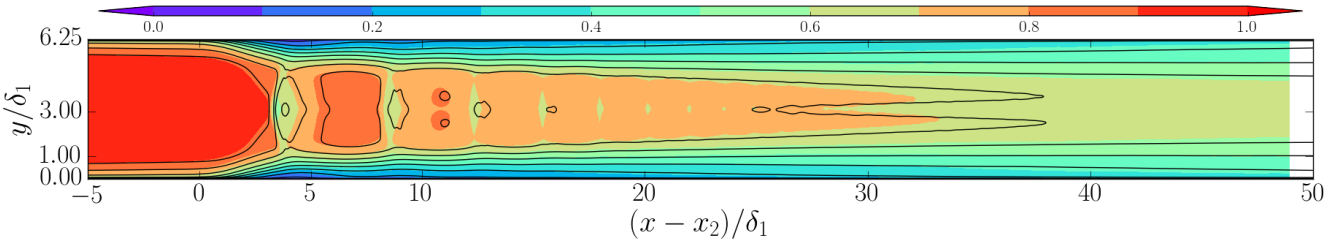

(a)

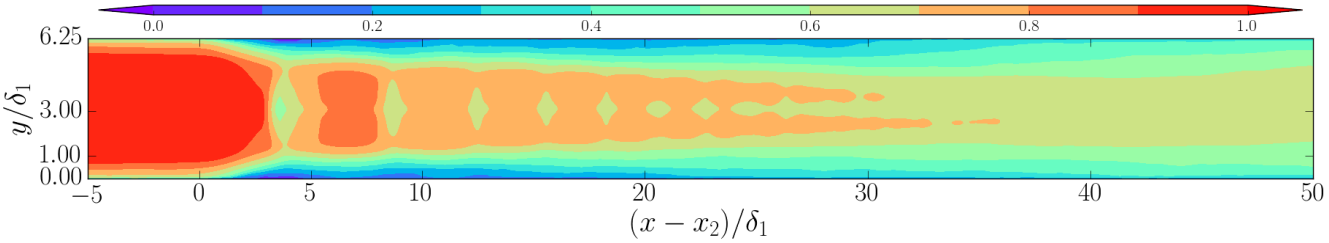

(b)

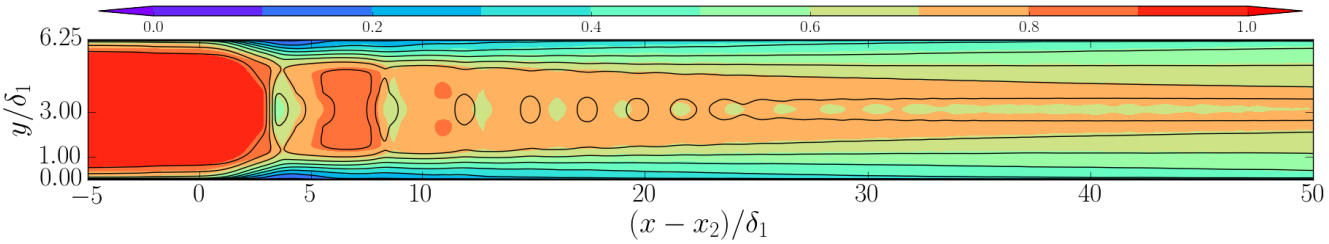

(c)

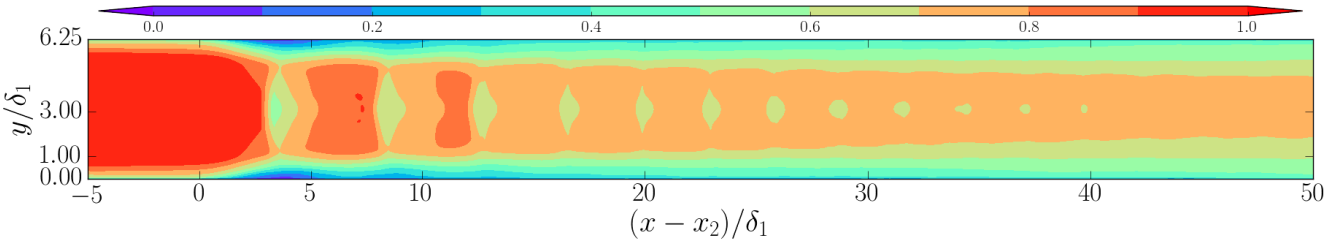

(d)

Figure 5.7: Contours of the streamwise mean velocity component in the longitudinal midplane ($z = Lz/2$). Eleven evenly spaced contours from 0 to 1. Color contours, current simulation; black contour lines, LES data of [68] for the same aspect ratio. Panel a, AR=∞; panel b, AR=5; panel c, AR=2.257; panel d, AR=1.5

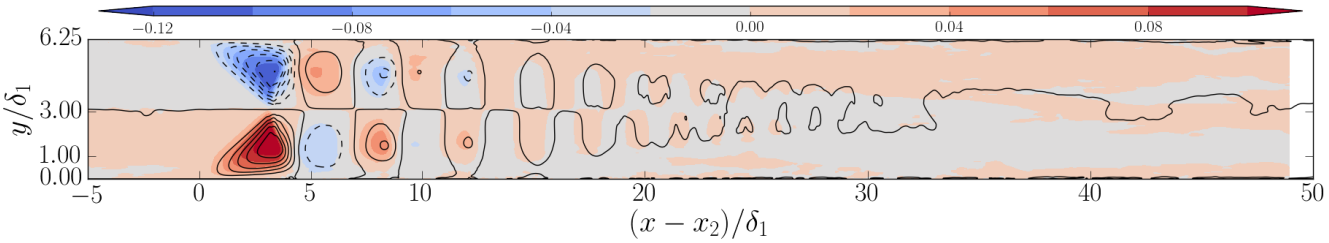

(a)

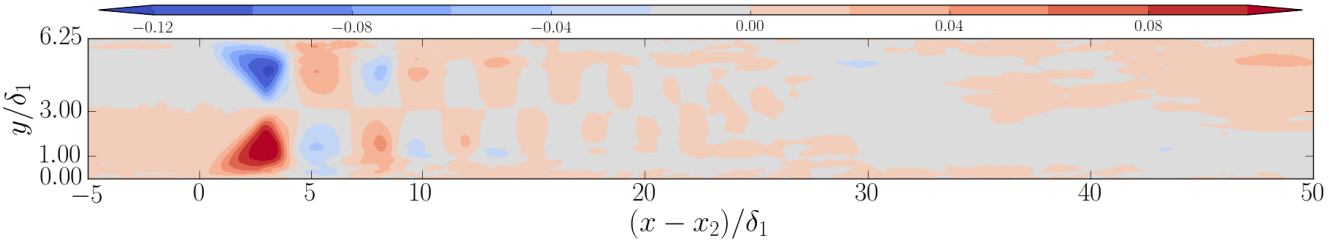

(b)

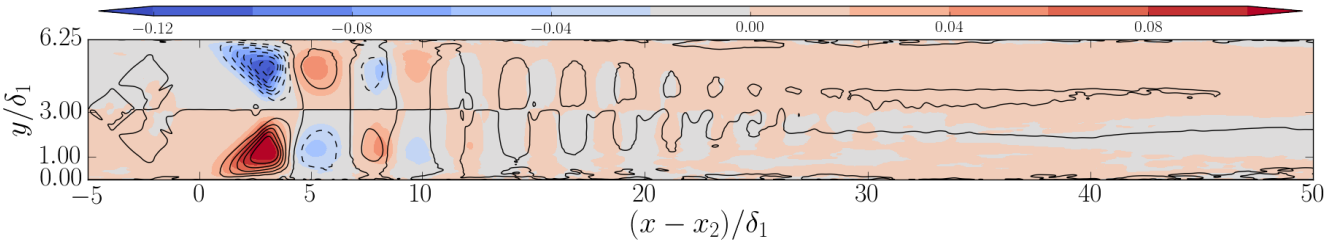

(c)

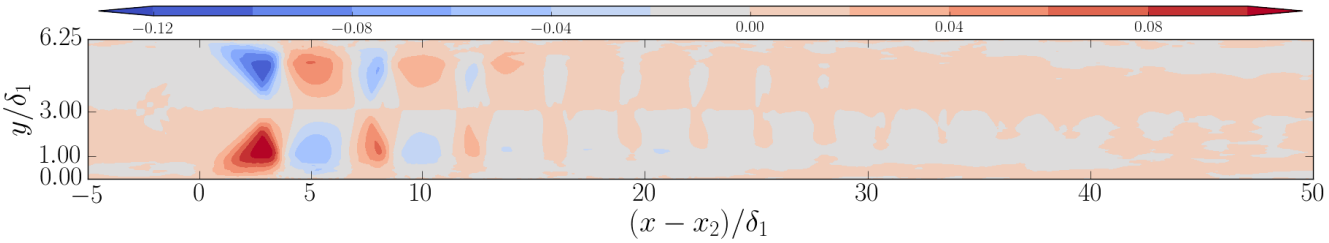

(d)

Figure 5.8: Contours of the mean velocity component in the wall-normal direction (y) in the longitudinal midplane ($z = Lz/2$). Eleven evenly spaced contours from -0.1 to 0.1. Color contours, current simulation; black contour lines, LES data of [68] for the same aspect ratio. Panel a, AR=∞; panel b, AR=5; panel c, AR=2.257; panel d, AR=1.5

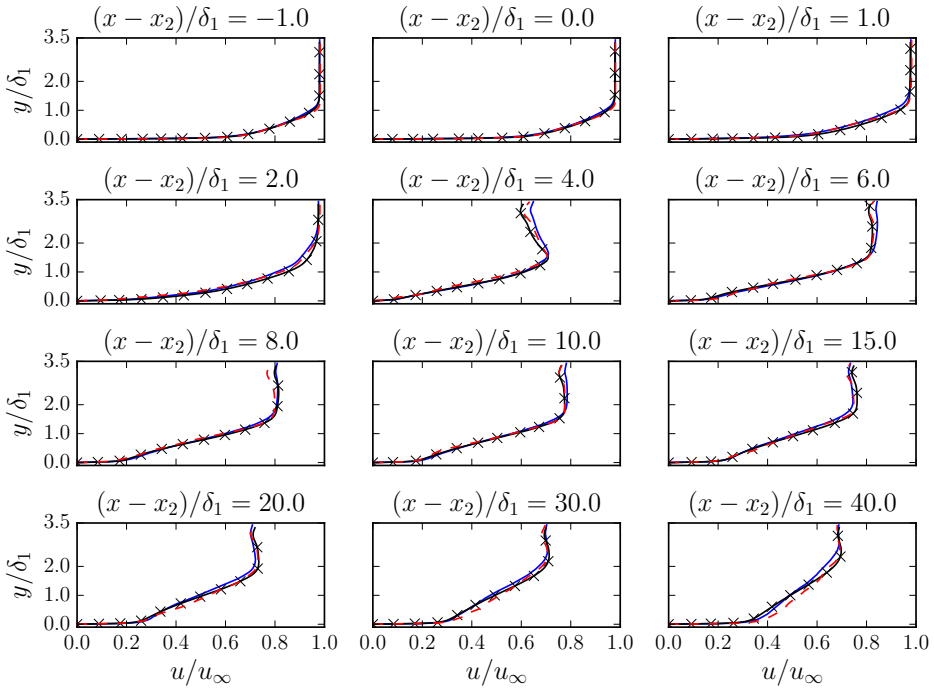

Figure 5.9: Distribution of u/u_∞ in the wall-normal direction (y) at twelve streamwise locations in the longitudinal midplane ($z = Lz/2$). ——— , AR=∞ current simulation; – – –, AR=5 current simulation; —×—, AR=∞ LES Ref. [68]

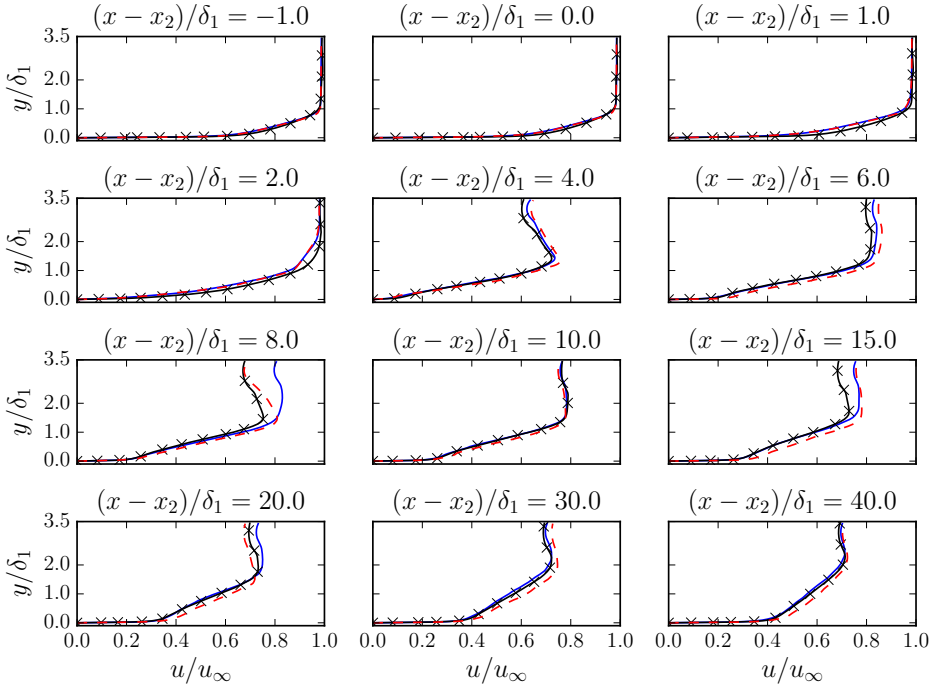

Figure 5.10: Distribution of u/u_∞ in the wall-normal direction (y) at twelve streamwise locations in the longitudinal midplane ($z = Lz/2$). ——— , AR=2.257 current simulation; – – –, AR=1.5 current simulation; —×—, AR=2.257 LES Ref. [68]

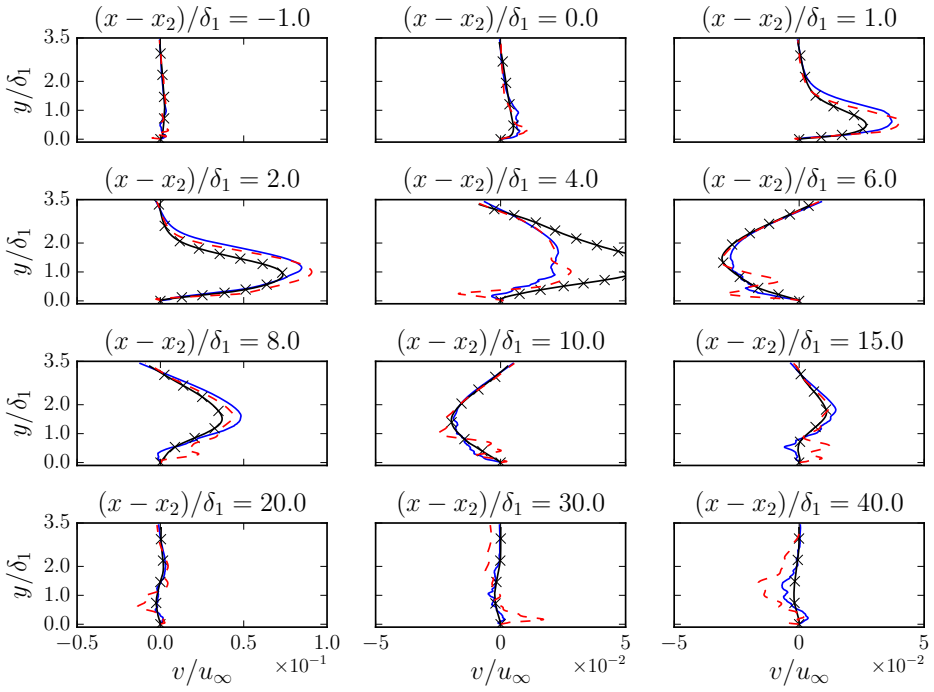

Figure 5.11: Distribution of v/u_∞ in the wall-normal direction (y) at twelve streamwise locations in the longitudinal midplane ($z = Lz/2$). ——— , AR=∞ current simulation; – – –, AR=5 current simulation; —×—, AR=∞ LES Ref. [68]

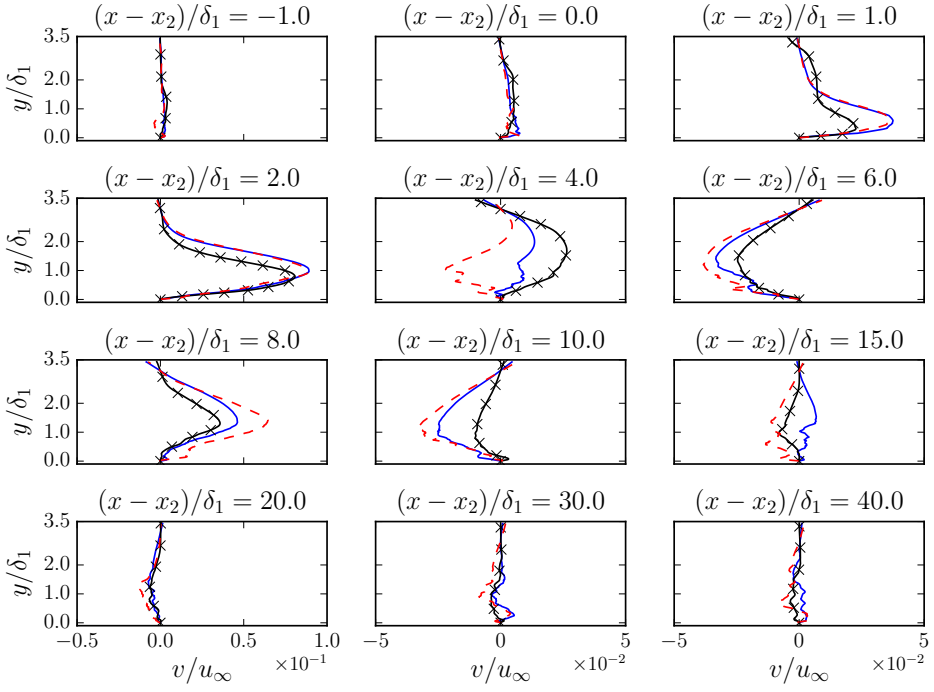

Figure 5.12: Distribution of v/u_∞ in the wall-normal direction (y) at twelve streamwise locations in the longitudinal midplane ($z = Lz/2$). ——— , AR=2.257 current simulation; – – –, AR=1.5 current simulation; —×—, AR=2.257 LES Ref. [68]

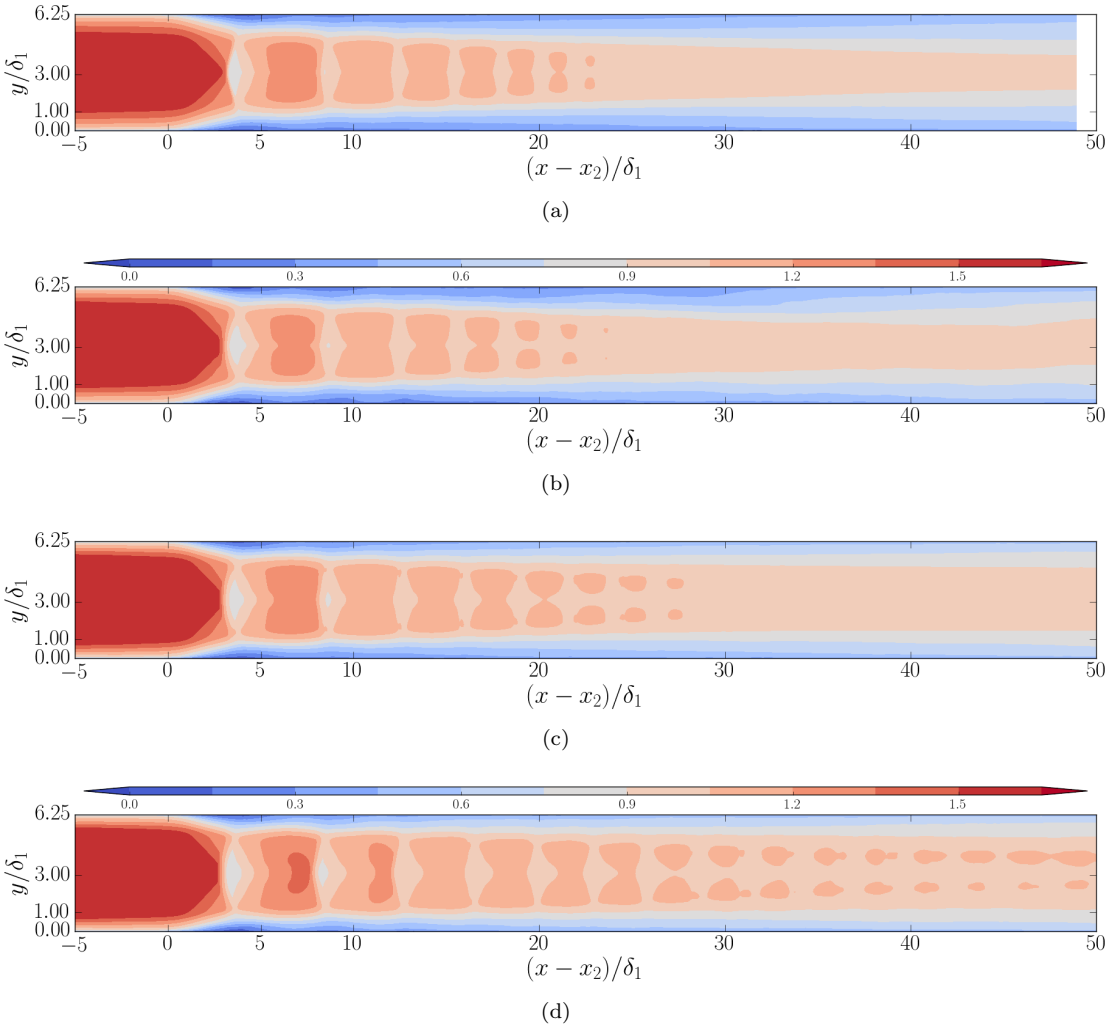

Figure 5.13: Contours of the local Mach number in the longitudinal midplane ($z = Lz/2$). Eleven evenly spaced contours from 0 to 1.61. (a) AR=∞; (b) AR=5; (c) AR=2.257; (d) AR=1.5

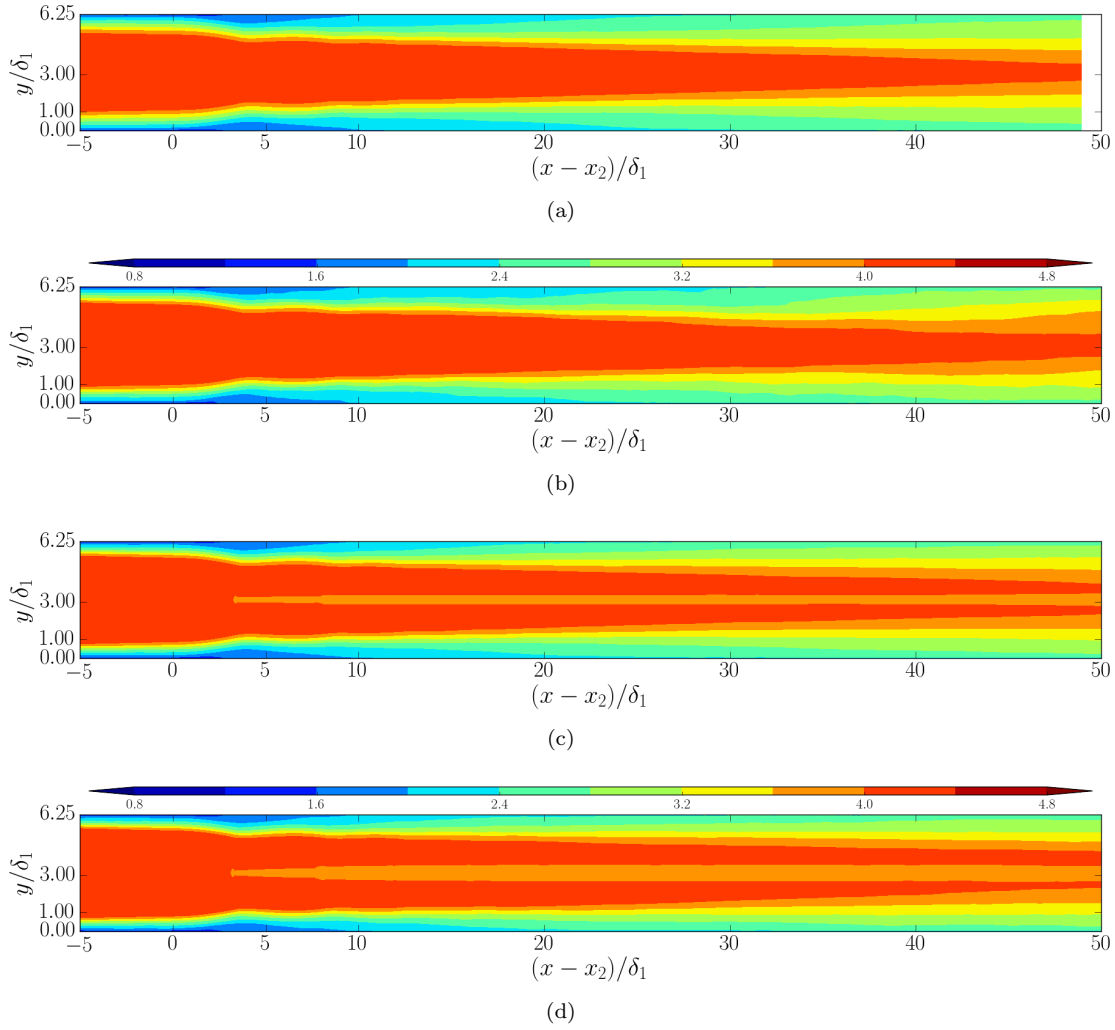

Figure 5.14: Contours of the total pressure in the longitudinal midplane ($z = Lz/2$). Eleven evenly spaced contours from 0.8 to 4.8. (a) AR=∞; (b) AR=5; (c) AR=2.257; (d) AR=1.5

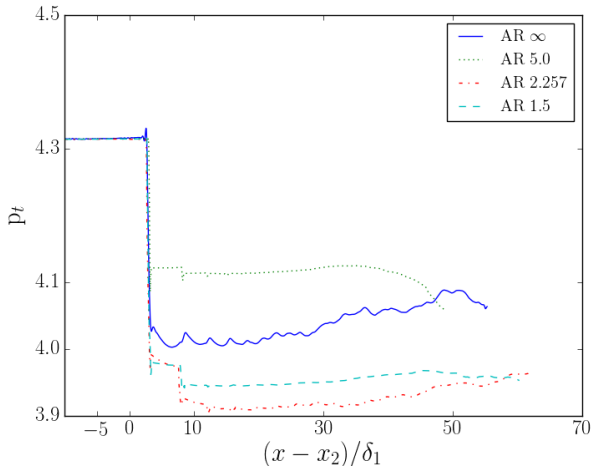

Figure 5.15: Streamwise distribution of the total pressure at various aspect ratios evaluated at the mid-plane ($z = Lz/2$) and at the duct centerline ($y = Ly/2$).

Shown in figure 5.16 to 5.30 are the Reynolds stress components ($\widetilde{u''u''}$, $\widetilde{v''v''}$, $\widetilde{w''w''}$, $\widetilde{u''v''}$), and the turbulent kinetic energy ($k = (\widetilde{u''u''} + \widetilde{v''v''} + \widetilde{w''w''})/2.0$). The results of the 4 different aspect ratio cases are reported in panel a, ,b, c, d (corresponding, respectively to AR=∞;5 ;2.257; 1.5). The AR=∞ and AR=2.257 cases are also compared with the LES data of Morgan et al. [68]. Twelve sections within the pseudo-shock region are selected, corresponding to the rescaled positions $(x - x_2)/\delta_1 = [-1\,, 0\,, 1\,, 2\,, 4.\,, 6\,, 8\,, 10\,, 15\,, 20\,, 30\,, 40]$.

The figures show that the streamwise Reynolds stress component is mostly affected by the primary shock and its interaction with the boundary layer, and the pattern is similar independently of AR (5.16). The wall normal and spanwise component $\widetilde{v''v''}$ and $\widetilde{w''w''}$ are more affected by the shear layer than by the shocks (figures 5.17 and 5.18). Generally very good qualitative and quantitative agreement with the result of Morgan et al. [68] is observed both for the Reynolds stress and the turbulent kinetic energy. Similar generally good comparison is observed for the distributions at the various streamwise locations.

Overall, the mean statistical turbulent properties exhibits similarities in the distributions at the various aspect ratio. The figure also show that the peak of the turbulence kinetic energy moves away from the wall past the shock train in the mixing region.

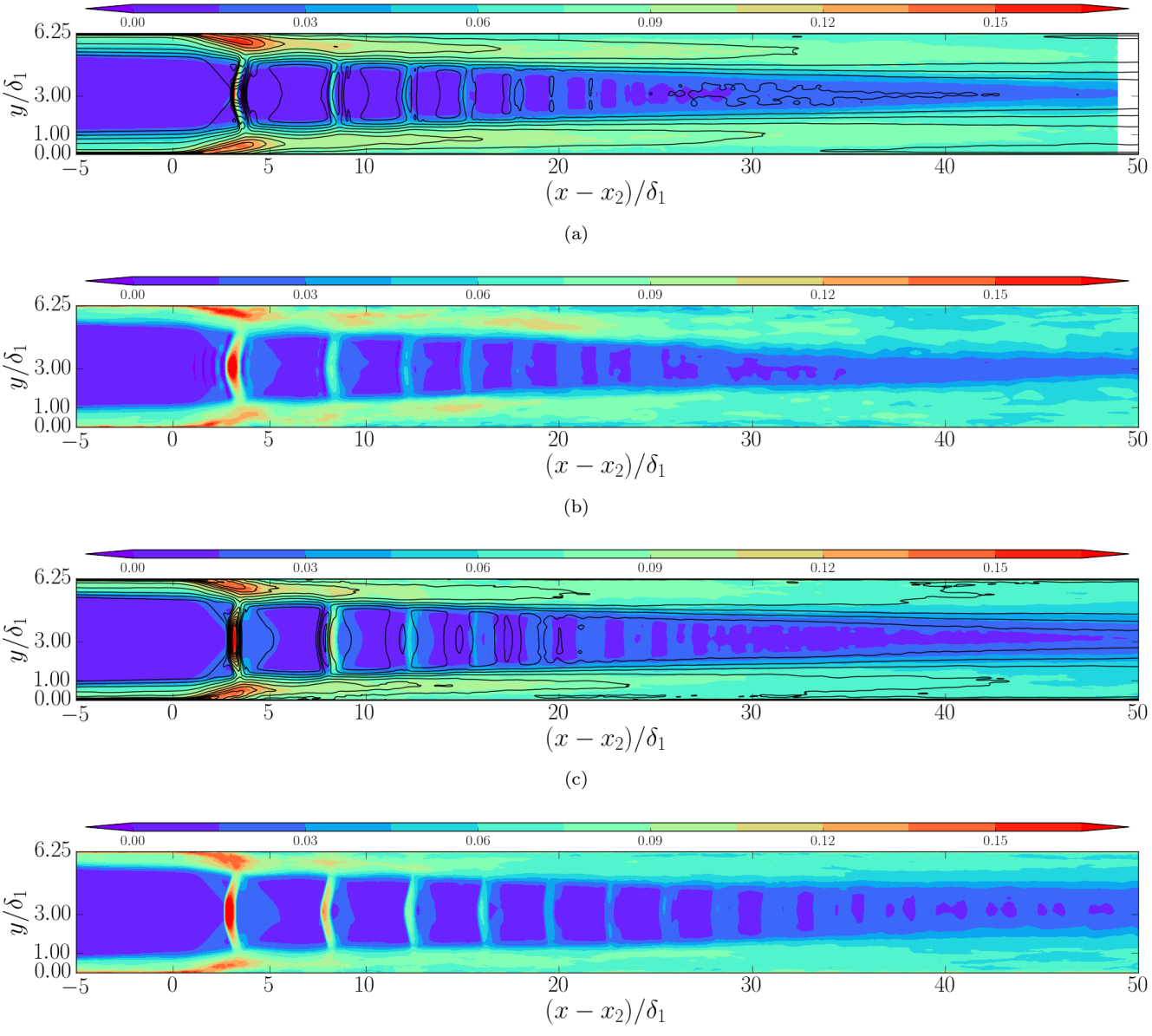

Figure 5.16: Contours of the Reynolds stress $\widetilde{u''u''}/u_\infty^2$ in the longitudinal midplane ($z = Lz/2$). Eleven evenly spaced contours from 0 to 0.016. Color contours, current simulation; black contour lines, LES data of Morgan et al. [68] for the same aspect ratio. (a) AR=∞; (b) AR=5; (c) AR=2.257; (d) AR=1.5

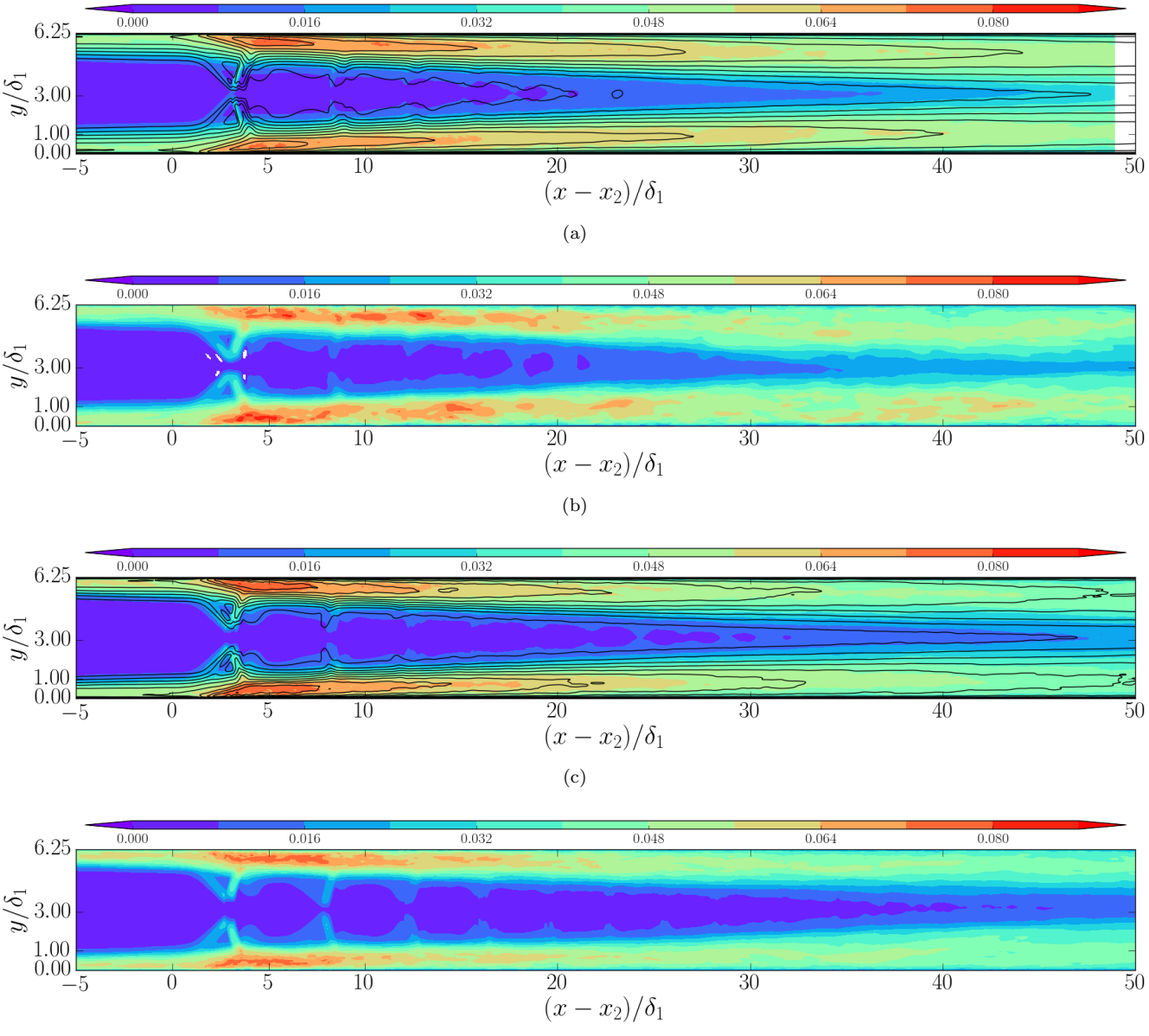

Figure 5.17: Contours of the Reynolds stress $\widetilde{v''v''}/u_\infty^2$ in the longitudinal midplane ($z = Lz/2$). Eleven evenly spaced contours from 0 to 0.08. Color contours, current simulation; black contour lines, LES data of Morgan et al. [68] for the same aspect ratio. (a) AR=∞; (b) AR=5; (c) AR=2.257; (d) AR=1.5

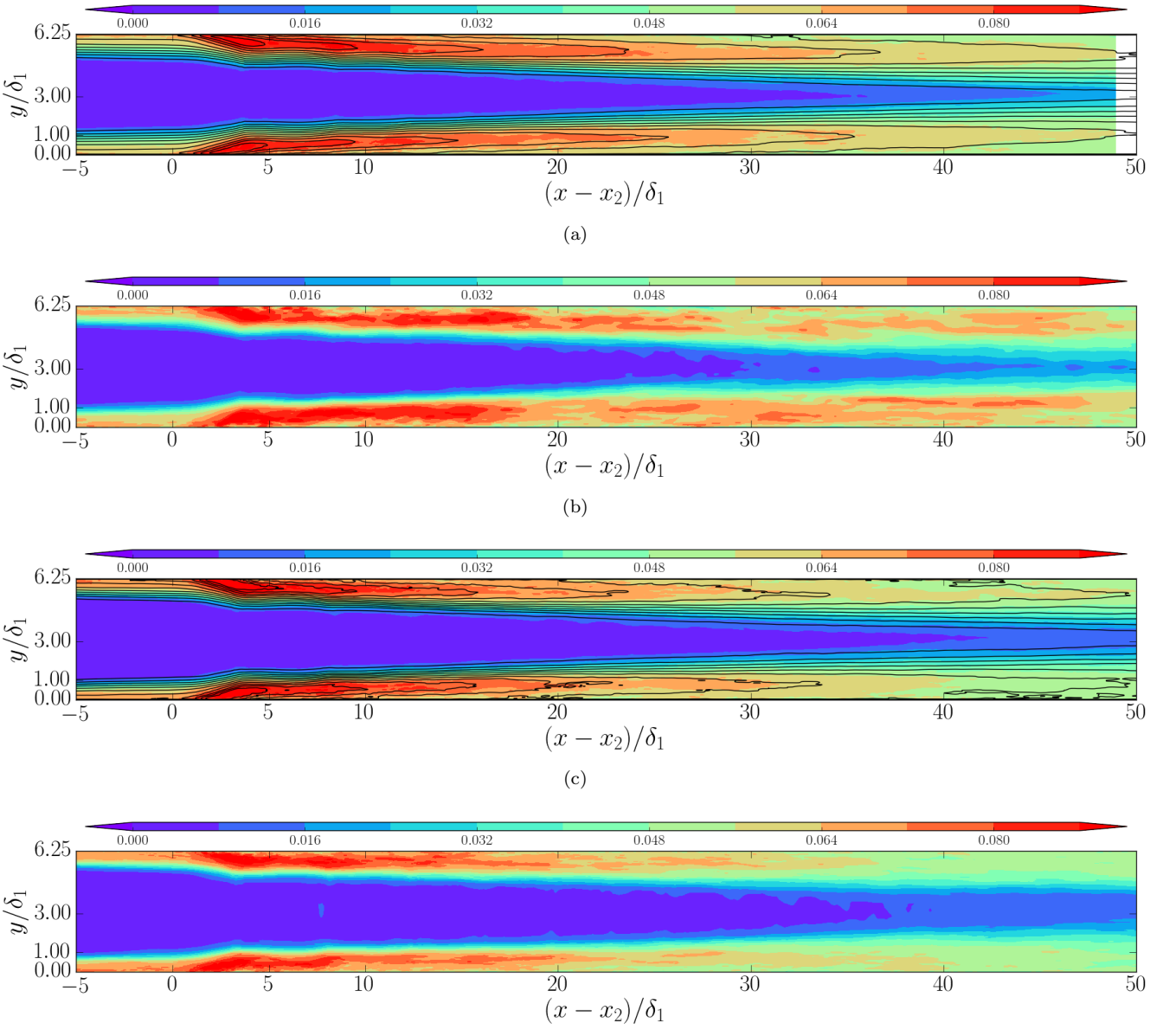

Figure 5.18: Contours of the Reynolds stress $\widetilde{w''w''}/u_\infty^2$ in the longitudinal midplane ($z = Lz/2$). Eleven evenly spaced contours from 0 to 0.08. Color contours, current simulation; black contour lines, LES data of Morgan et al. [68] for the same aspect ratio. (a) AR=∞; (b) AR=5; (c) AR=2.257; (d) AR=1.5

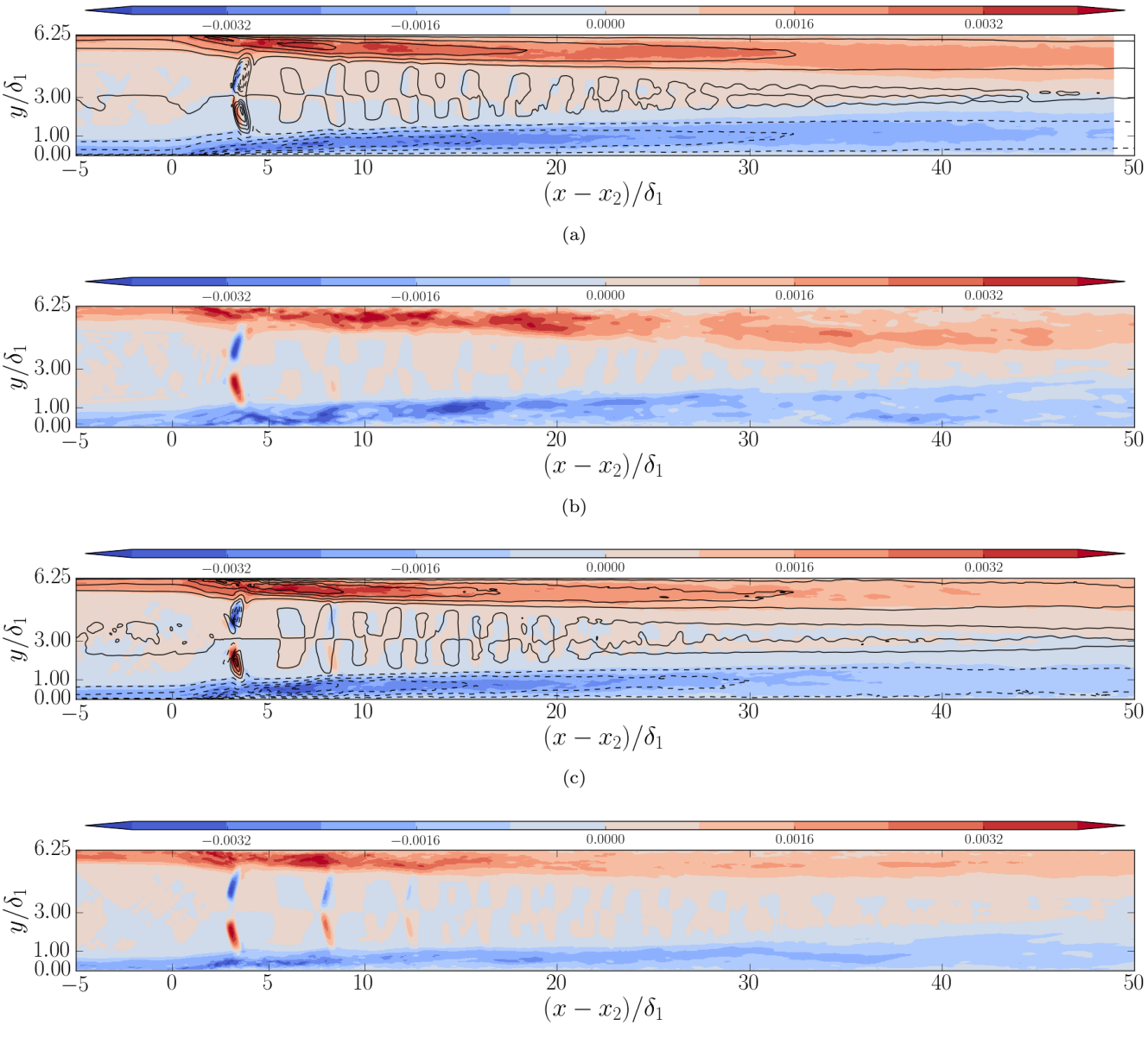

Figure 5.19: Contours of the Reynolds stress $\widetilde{u''v''}/u_\infty^2$ in the longitudinal midplane ($z = Lz/2$). Eleven evenly spaced contours from $-4.0\,10^{-3}$ to $4.0\,10^{-3}$. Color contours, current simulation; black contour lines, LES data of Morgan et al. [68] for the same aspect ratio. (a) AR=∞; (b) AR=5; (c) AR=2.257; (d) AR=1.5

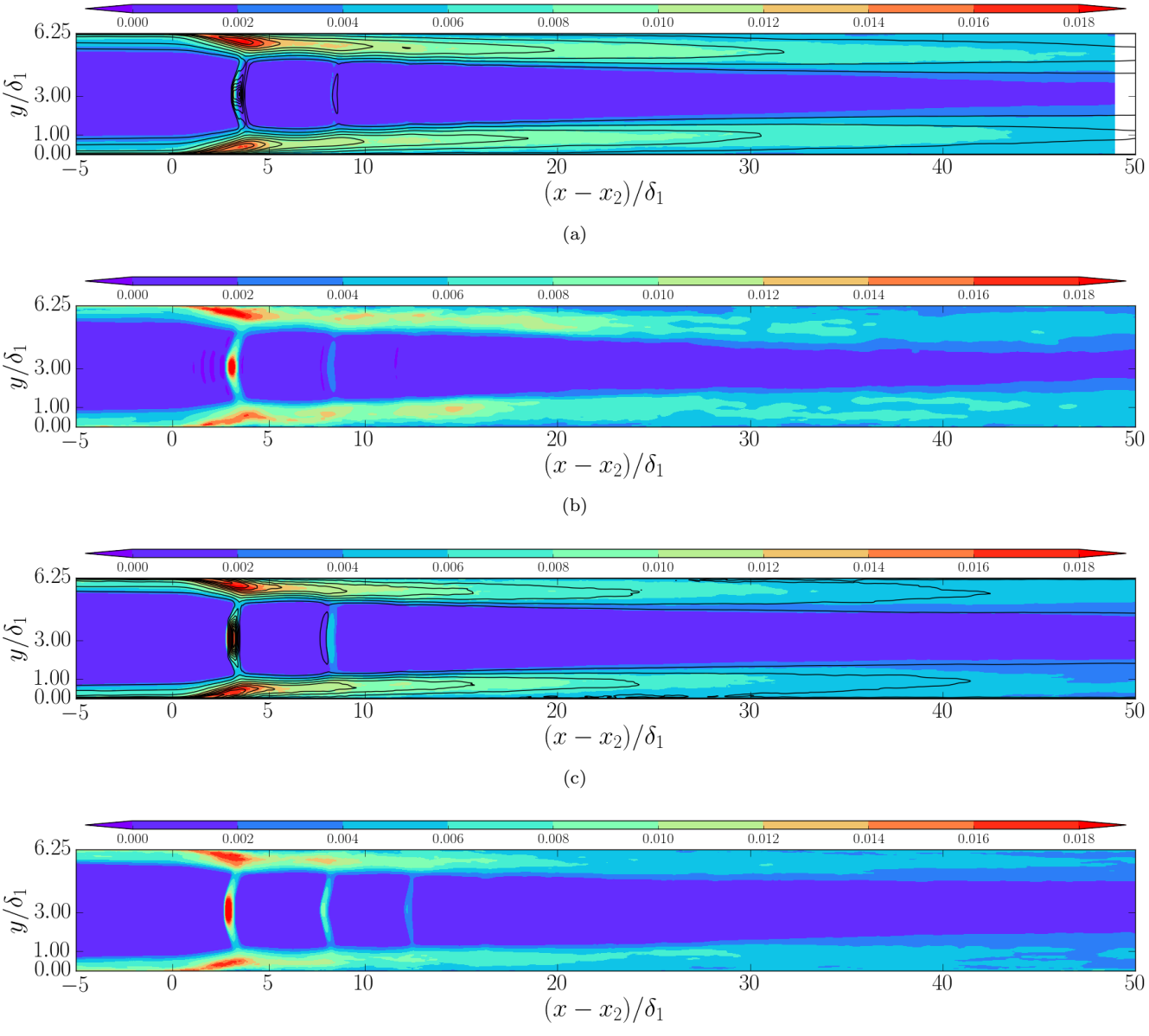

Figure 5.20: Contours of the turbulent kinetic energy k/u_∞^2 in the longitudinal mid-plane ($z = Lz/2$). Eleven evenly spaced contours from 0 to 0.018. Color contours, current simulation; black contour lines, LES data of Morgan et al. [68] for the same aspect ratio. (a) AR=∞; (b) AR=5; (c) AR=2.257; (d) AR=1.5

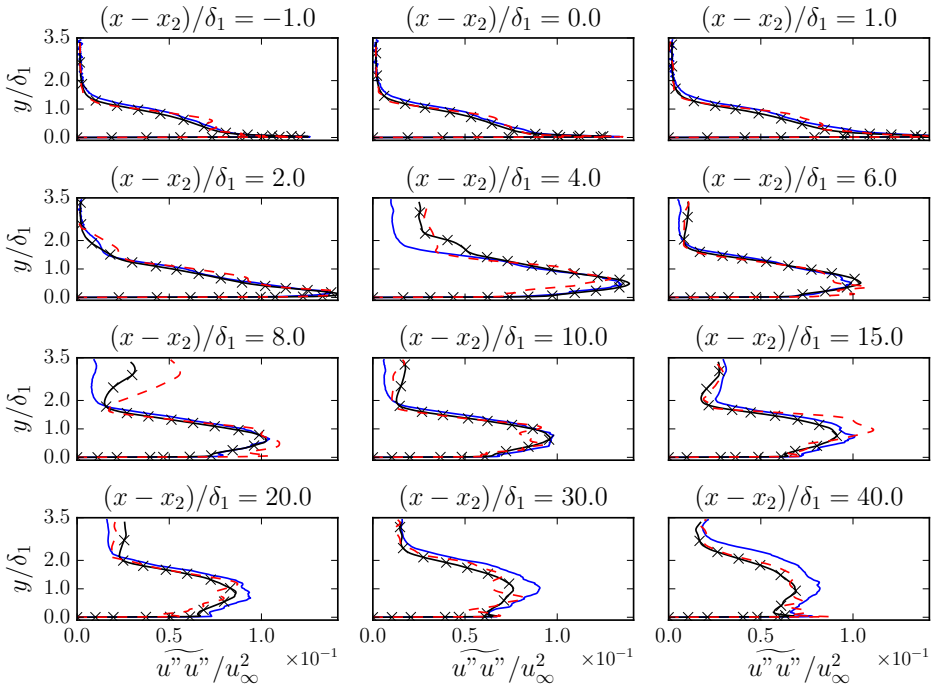

Figure 5.21: Distribution of $\widetilde{u''u''}/u_\infty^2$ in the wall-normal direction (y) at twelve streamwise locations in the longitudinal midplane ($z = Lz/2$). ——— , AR=∞ current simulation; – – –, AR=5 current simulation; —×—, AR=∞ LES Ref. [68]

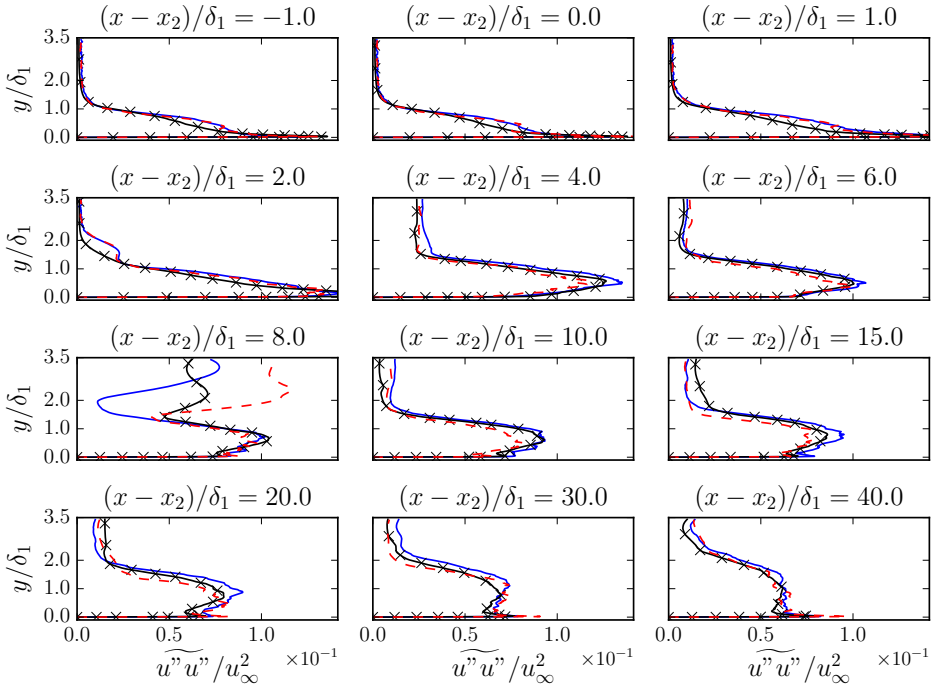

Figure 5.22: Distribution of $\widetilde{u''u''}/u_\infty^2$ in the wall-normal direction (y) at twelve streamwise locations in the longitudinal midplane ($z = Lz/2$). ——— , AR=2.257 current simulation; – – –, AR=1.5 current simulation; —×—, AR=2.257 LES Ref. [68]

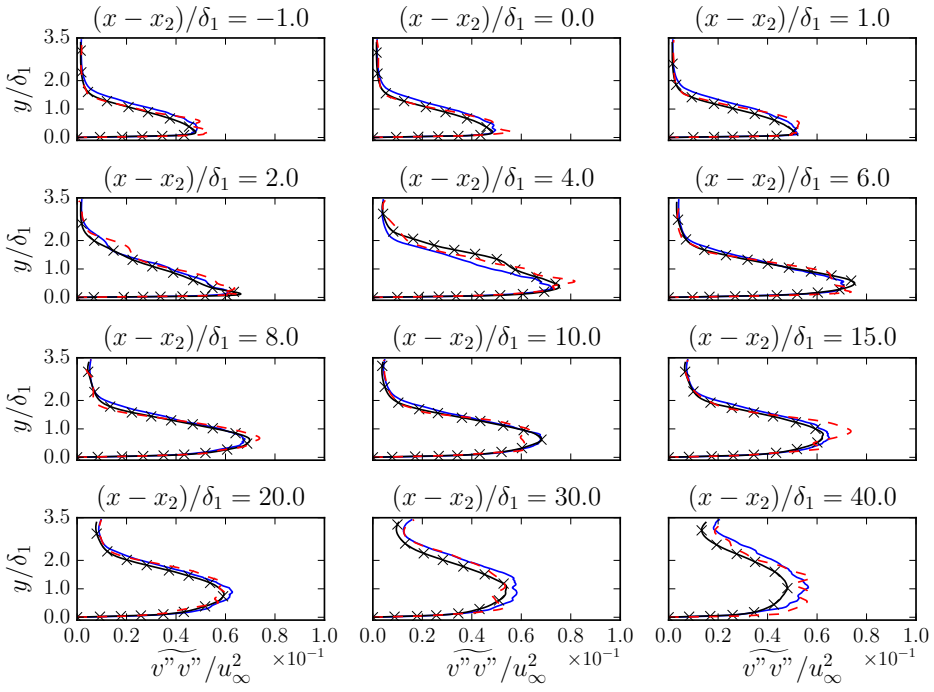

Figure 5.23: Distribution of $\widetilde{v''v''}/u_\infty^2$ in the wall-normal direction (y) at twelve streamwise locations in the longitudinal midplane ($z = Lz/2$). ——— , AR=∞ current simulation; – – –, AR=5 current simulation; —×—, AR=∞ LES Ref. [68]

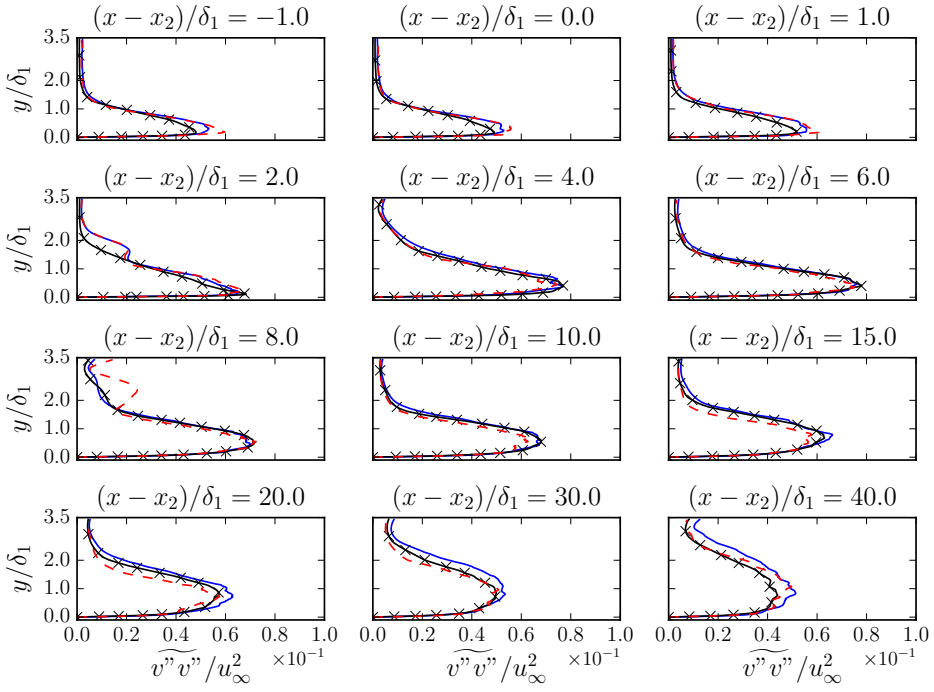

Figure 5.24: Distribution of $\widetilde{v''v''}/u_\infty^2$ in the wall-normal direction (y) at twelve streamwise locations in the longitudinal midplane ($z = Lz/2$). ——— , AR=2.257 current simulation; – – –, AR=1.5 current simulation; —×—, AR=2.257 LES Ref. [68]

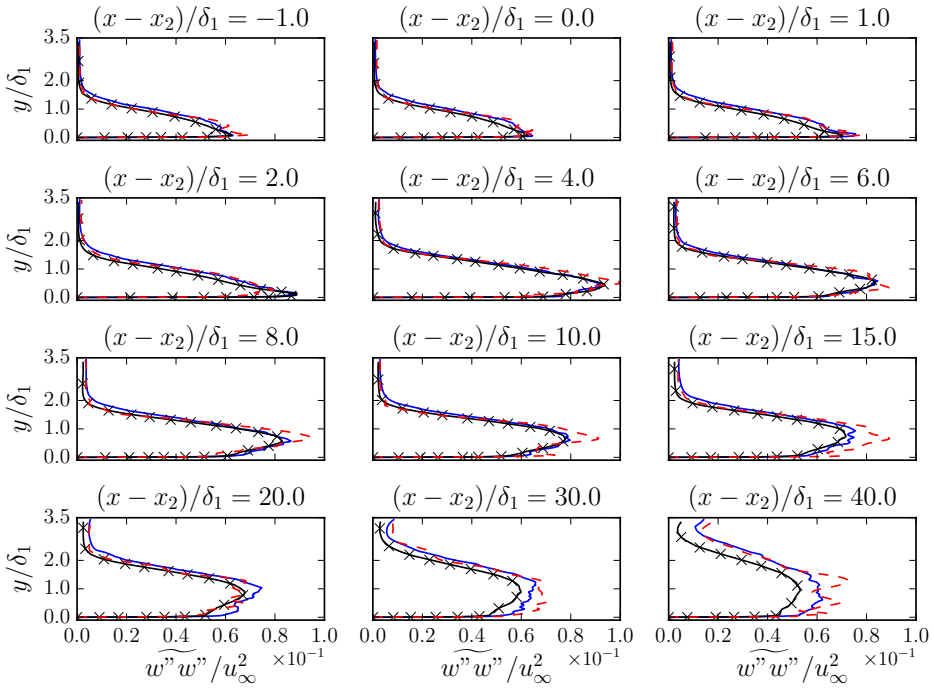

Figure 5.25: Distribution of $\widetilde{w''w''}/u_\infty^2$ in the wall-normal direction (y) at twelve streamwise locations in the longitudinal midplane ($z = Lz/2$). ——— , AR=∞ current simulation; – – –, AR=5 current simulation; —×—, AR=∞ LES Ref. [68]

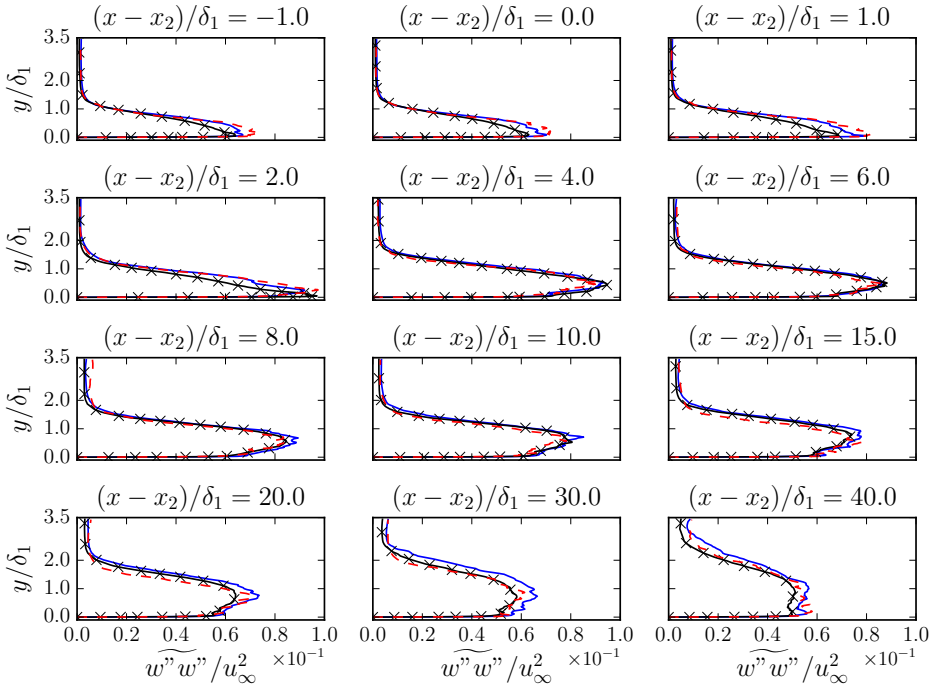

Figure 5.26: Distribution of $\widetilde{w''w''}/u_\infty^2$ in the wall-normal direction (y) at twelve streamwise locations in the longitudinal midplane ($z = Lz/2$). ——— , AR=2.257 current simulation; – – –, AR=1.5 current simulation; —×—, AR=2.257 LES Ref. [68]

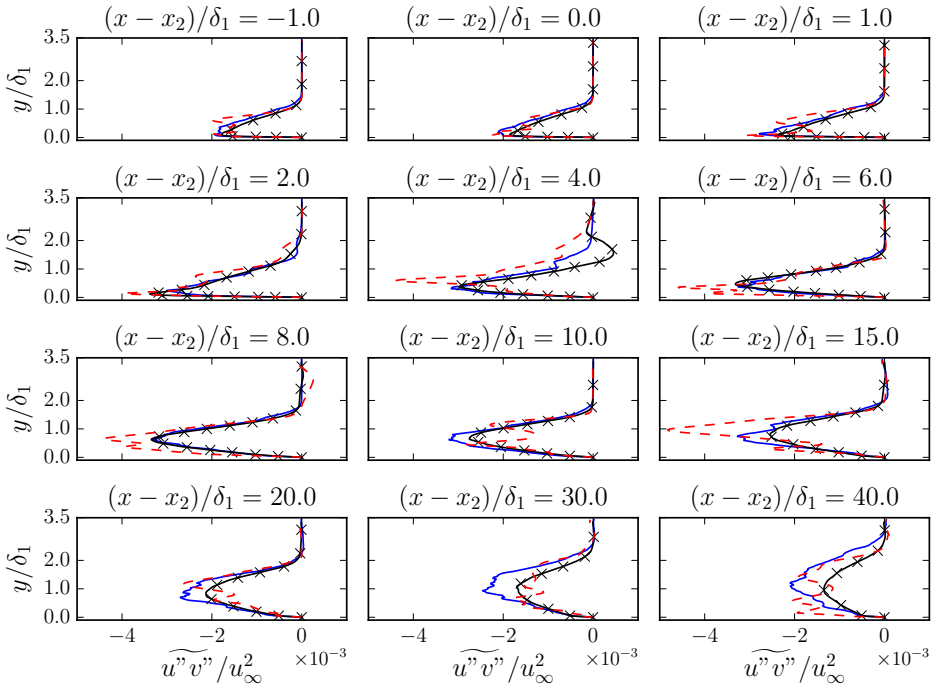

Figure 5.27: Distribution of $\widetilde{u''v''}/u_\infty^2$ in the wall-normal direction (y) at twelve streamwise locations in the longitudinal midplane ($z = Lz/2$). ——— , AR=∞ current simulation; – – –, AR=5 current simulation; —×—, AR=∞ LES Ref. [68]

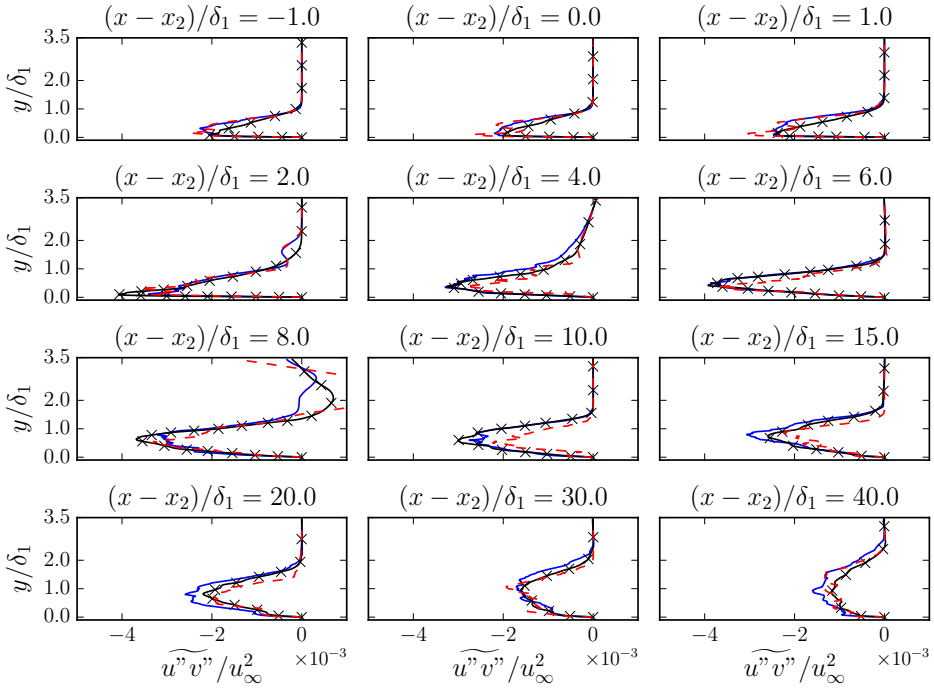

Figure 5.28: Distribution of $\widetilde{u''v''}/u_\infty^2$ in the wall-normal direction (y) at twelve streamwise locations in the longitudinal midplane ($z = Lz/2$). ——— , AR=2.257 current simulation; – – –, AR=1.5 current simulation; —×—, AR=2.257 LES Ref. [68]

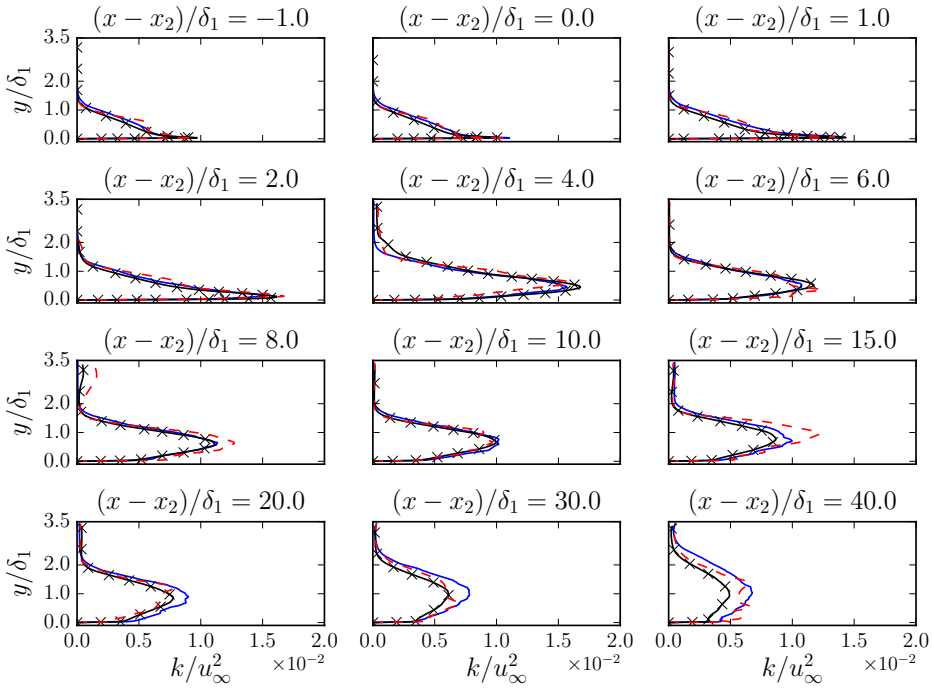

Figure 5.29: Distribution of k/u_∞^2 in the wall-normal direction (y) at twelve streamwise locations in the longitudinal midplane ($z = Lz/2$). ——— , AR=∞ current simulation; – – –, AR=5 current simulation; —×—, AR=∞ LES Ref. [68]

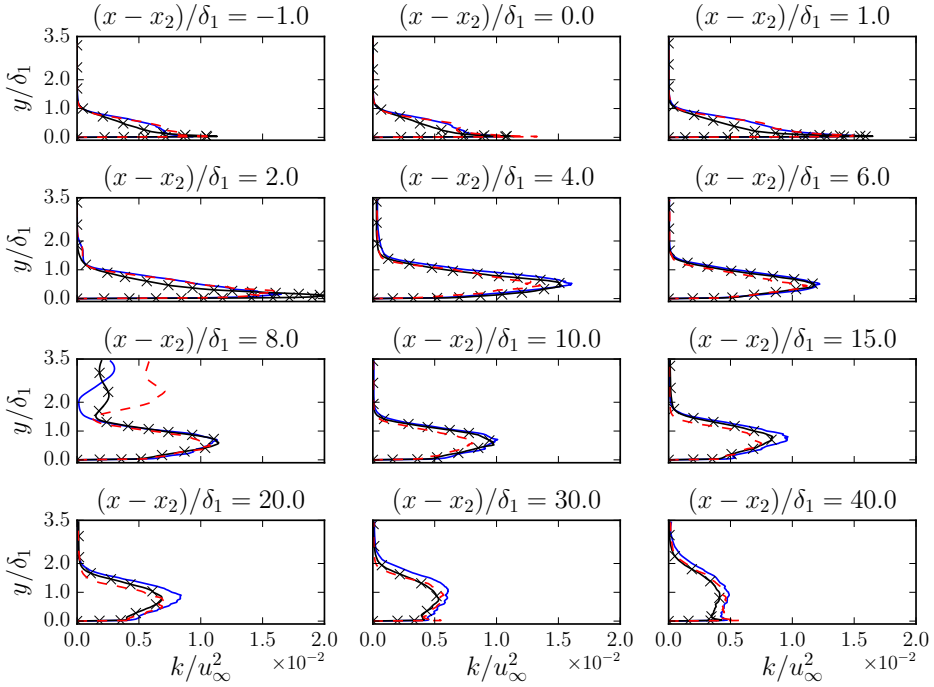

Figure 5.30: Distribution of $k/\rho_\infty u_\infty^2$ in the wall-normal direction (y) at twelve streamwise locations in the longitudinal midplane ($z = Lz/2$). ——— , AR=2.257 current simulation; – – –, AR=1.5 current simulation; —×—, AR=2.257 LES Ref. [68]

5.3 Skin frictions patterns

In figures 5.31, 5.32 and 5.33, we report, respectively, the contours of the skin friction coefficient, the skin friction lines and the contours of the spanwise shear ($\partial w/\partial y$) at various aspect ratios in figures Contour lines of the wall pressure are also overlaid on the figures. The figures show that the flow is not separated in the mean and that strong three dimensionality arise due to the influence of side walls (Fig. 5.33). A deflection of the streamlines on a scale $o(2-3\delta_1)$ is observed and due to corner effects. Good comparison is observed between the AR=2.257 case (figure 5.32, panel c) and the oil flow visualization of Ref. [21] (panel e). As the aspect ratio decreases the expansions strengthen and, consequently, the skin friction exhibits stronger oscillations in the streamwise direction. Due to side walls effects the flow separate in the proximity of the corner.

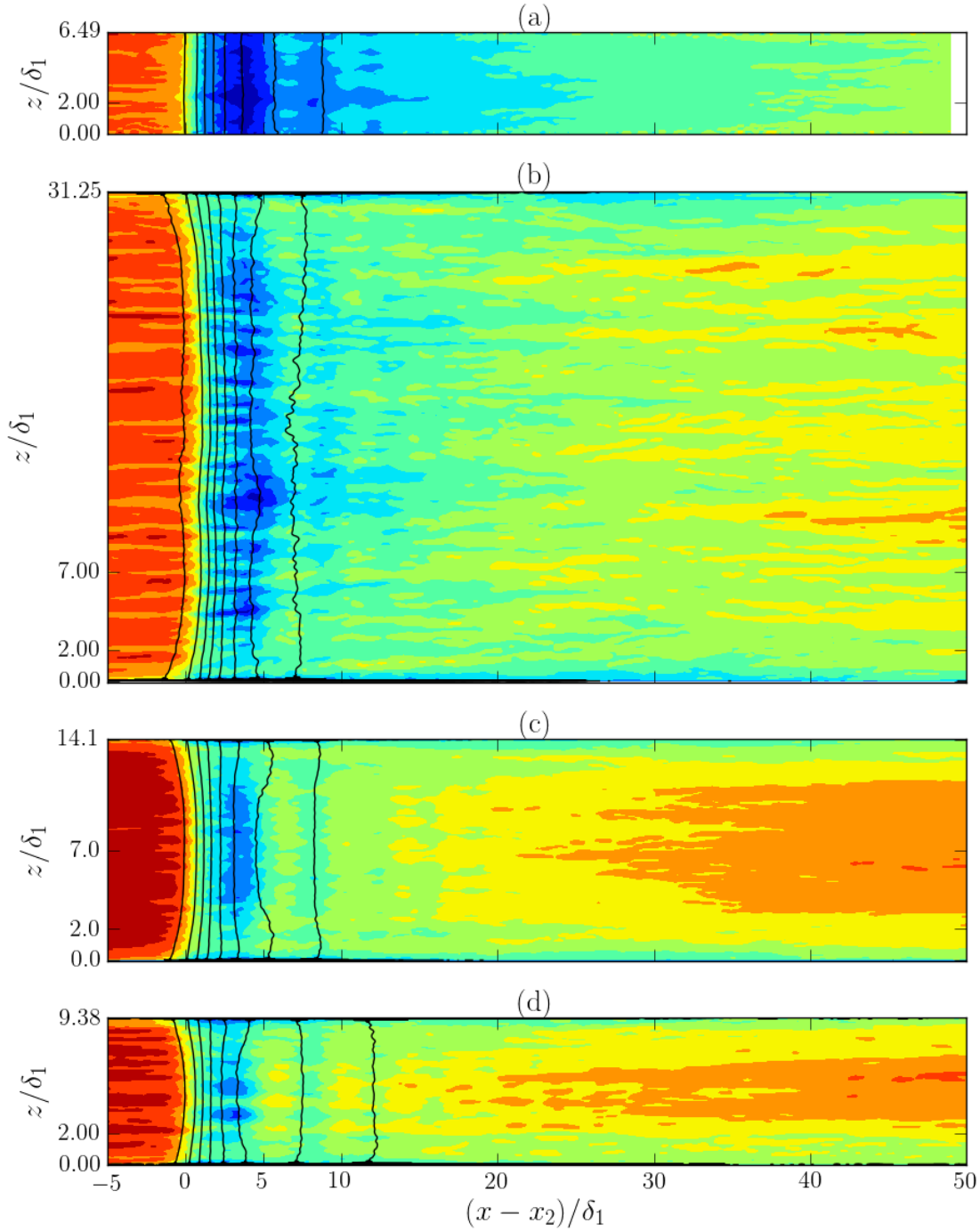

Figure 5.31: Contours of the skin friction coefficient in the plane $y = Ly$ between -0.1 to 3.7 ($\times 10^-3$) overlay with 8 isocontours of the wall pressure scaled by $p2$ (black contour lines) from 1 to 1.7. (a) AR=∞; (b) AR=5; (c) AR=2.257; (d) AR=1.5

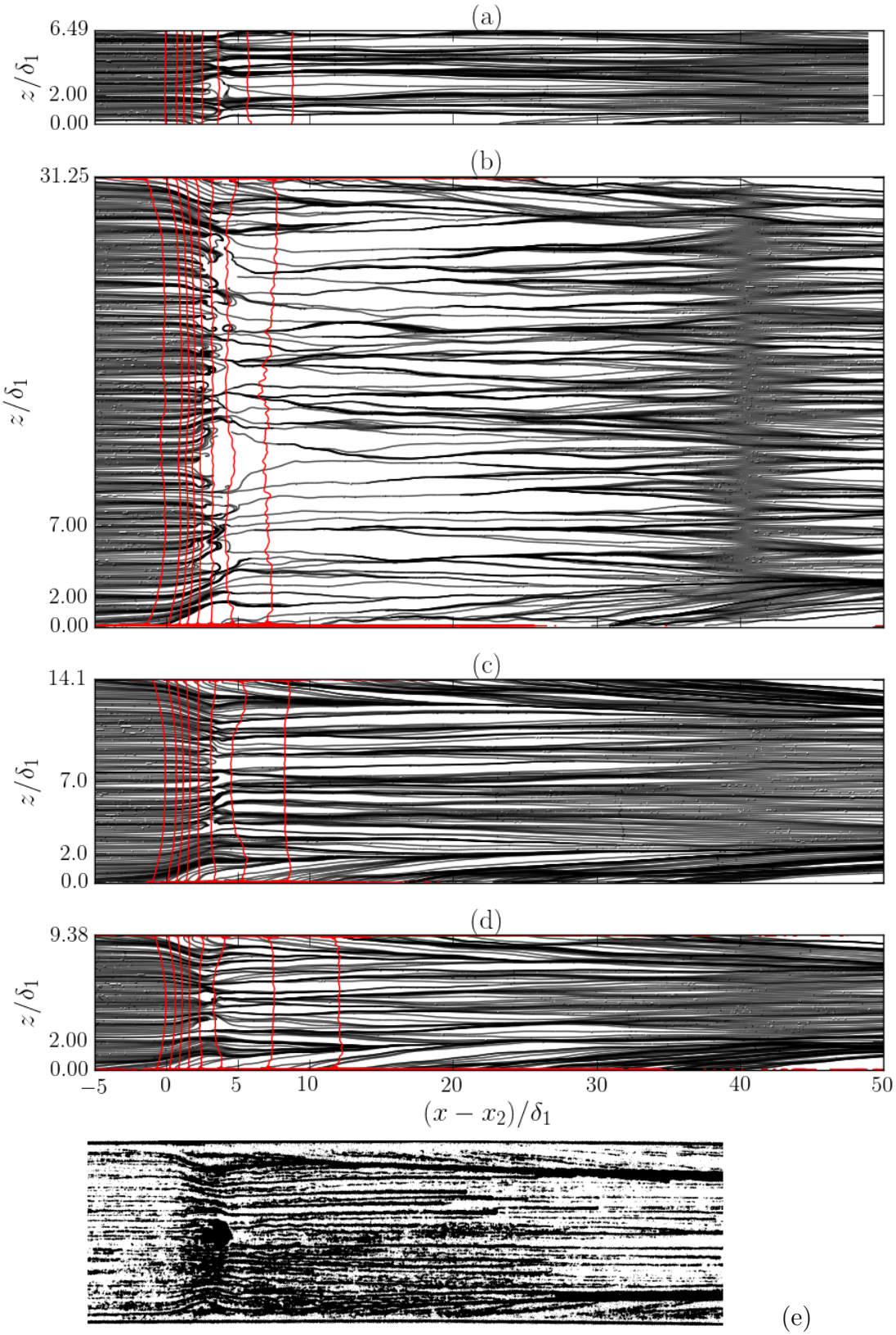

Figure 5.32: Skin friction lines overlay with 8 contours of the wall pressure rescaled by the wall pressure at the beginning of the interaction p_2 (red contour lines) from 1 to 1.7. (a) AR=∞; (b) AR=5; (c) AR=2.257; (d) AR=1.5; (e) AR=2.257, Oil flow visualization Ref. [21]

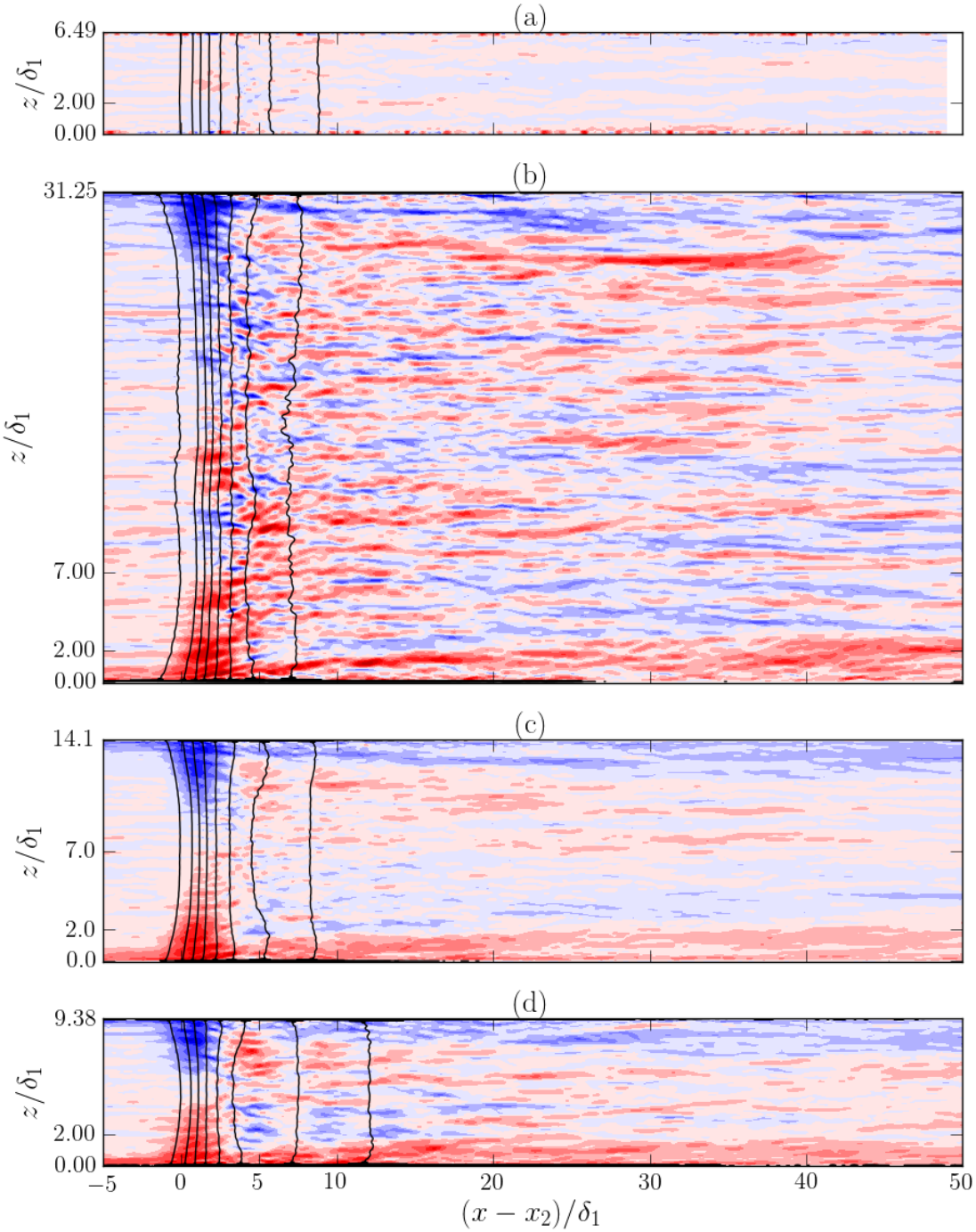

Figure 5.33: Contours of $\partial w/\partial y$ for various shock-train configurations overlay with 8 isocontours of the wall pressure scaled by $p2$ (black contour lines) from 1 to 1.7. (a) AR=∞; (b) AR=5; (c) AR=2.257; (d) AR=1.5

5.4 Flow organization

The instantaneous contours of the density gradient at various aspect ratios at the $y = Ly/2$ plane and at the mid-plane $z = Lz/2$ are reported, respectively, in figures 5.34 and 5.35. The figures show the strong influence of the aspect ratio on the flow topology. The structure of the interaction between the shocks between the left (lower on the figure) and right walls changes from irregular to quasi-regular when decreasing the aspect ratio (Fig. 5.34). The topology of the shock-train in the mid-plane weakly affect by the aspect ratio and it remains similar for all cases. The figure also show that bulgy turbulent structures inclined with respect to the wall (typical of boundary layer under adverse pressure gradient) become stronger as the aspect ratio decreases.

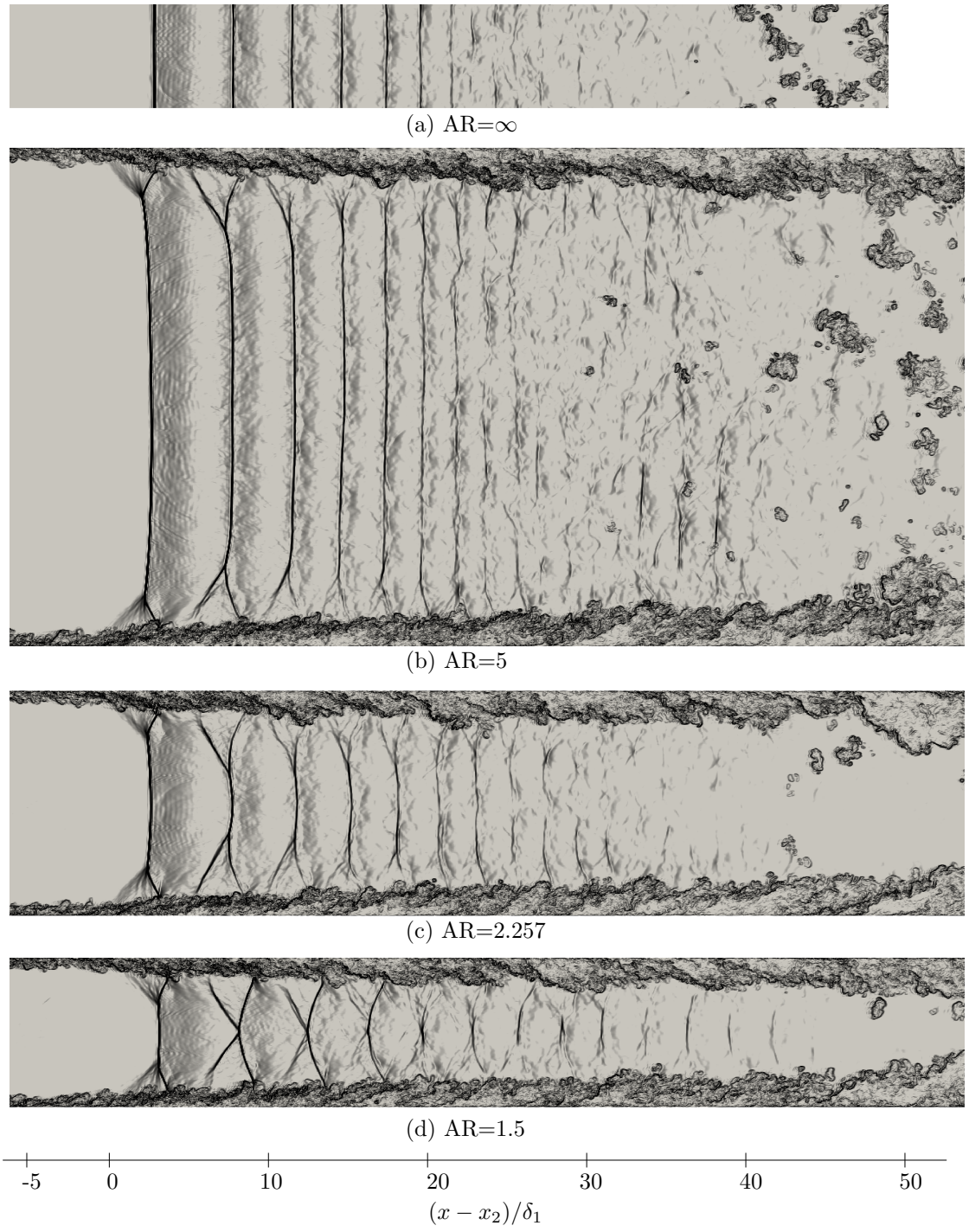

Figure 5.34: Instantaneous contours of the density gradient at various aspect ratios at the $y = Ly/2$ plane as a function of the normalized streamwise variable $x^* = (x - x_2)/\delta_1$. (a) AR=∞. (b) AR=5.0. (c) AR=2.257. (d) AR=1.5

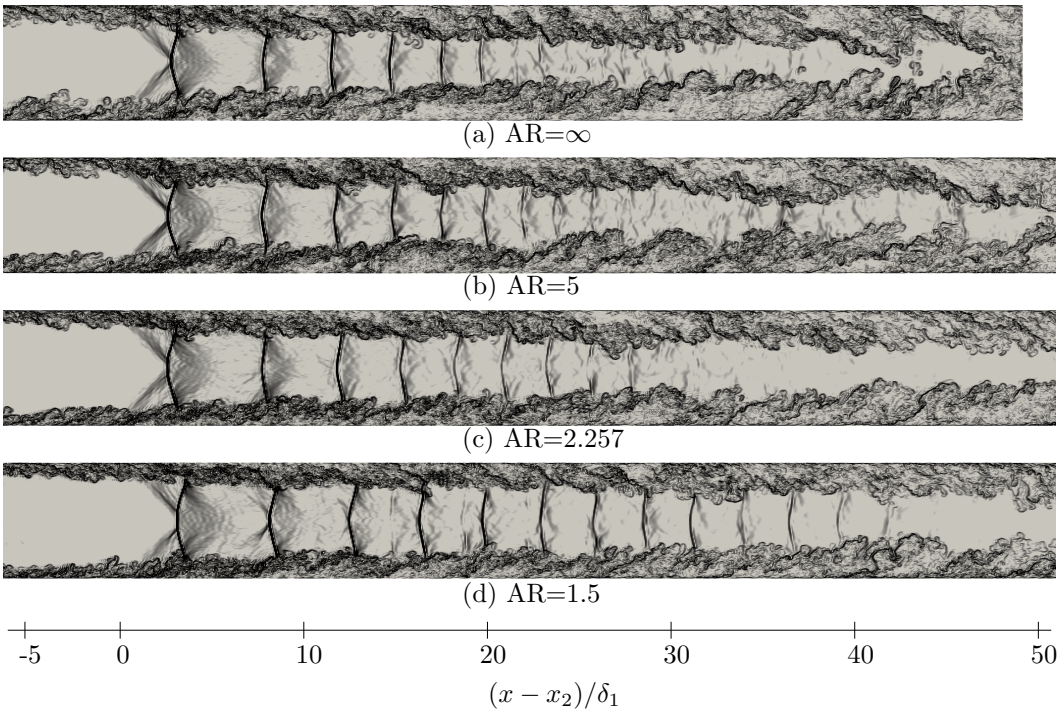

Figure 5.35: Instantaneous contours of the density gradient at various aspect ratios at the $z = Lz/2$ plane as a function of the normalized streamwise variable $x^* = (x - x_2)/\delta_1$. (a) AR=∞. (b) AR=5.0. (c) AR=2.257. (d) AR=1.5

Chapter Summary

- LES of a Mach 1.61 shock-train in constant rectangular duct with various aspect ratios (AR=W/H) have been carried out. We have considered four aspect ratios AR=∞; 5; 2.257; 1.5
- The results are compared with the experiment of Carroll and Dutton [21] (AR=2.257) and the two LES of Morgan et al. [68] (AR=∞ and 2.257).
  - The displacement and momentum thicknesses of AR=2.257 case match the experimental values.
  - Generally very good qualitative and quantitative agreement with the result of Morgan et al. [68] is observed for the mean and turbulent quantities.
  - Different outflow pressure are required to maintain the initial shock at a location where the same confinement is observed
  - We observe a better agreement with the experiment when rescaling δ^* and θ by their values at the beginning of the interaction
- Aspect-ratio and confinement effects
  - The number of secondary shocks increases with confinement [20] and the shock-train becomes shorter [8]. Our studies confirmed this findings except the AR=5 case for which small deviations are observed in the length of the pseudo-shock.
  - Reducing the width, the "aerodynamic nozzle effect" is enhanced producing stronger expansions of the core flow past the primary, secondary and tertiary shocks.
  - The minimum value of the centerline skin friction coefficient is not strongly affected by the distance between side walls. This tends to indicate that the dominant geometric scale to determine the minimum value of the skin friction, and so the onset of separation, is the minimum between the height and the width.
  - Further investigation are required as the vertical confinement δ_2/h is slightly higher for cases with larger width (smaller horizontal confinement). As shown by Dutton and Carroll [36], this variation may change the final downstream pressure.
- Visualisations of the instantaneous density gradient magnitude show that the structure of the shocks in the interaction on the upper and lower walls changes from irregular to quasi-regular structures when decreasing the aspect ratio thus affecting the total pressure losses.

Chapter 6

Unsteady analysis of shock-train interactions

Contents

6.1 Wall pressure dynamics 109
6.2 Dynamic Mode Decomposition 113
6.2.1 Description of the method 113
6.2.2 Flow analysis 115

In the present chapter we focus on the unsteady effects of shock-train interactions. In particular, the interpretation focuses on the interpretation of low-medium frequency dynamics for the AR=2.257 case, corresponding to the experimental conditions. For this test case, 13098 samples are collected over a period of $2495\delta_{in}/u_\infty$ with a sampling frequency of $u_\infty/0.19\delta_{in}$.

6.1 Wall pressure dynamics

In order to estimate the unsteady characteristics of shock-train, we have analysed the wall pressure signatures. For that purpose, we define the Strouhal number in terms of characteristic scales based on the interaction length (L) and the free-stream velocity. In the 2.5D interactions, L is generally defined as the distance between the beginning of the interaction and the streamwise station where isentropic Mach number [1] decreases to unity.

In shock-train interactions, due to aerodynamic nozzle effects that produce compressions and expansions of the flow through the shocks, the isentropic Mach number remains above unit value. As a consequence, the "classical" definition of L is not appropriate for the current analysis. We have the used the empirical definition proposed by Delery and Marvin [28]

$$L \sim 70\delta_2^*(1 - H_{i_2}) \tag{6.1}$$

where subscript 2 indicates the position where the pressure starts rising (and Hi is the incompressible shape factor). This latter definition has also been used by Pirozzoli et al. [76] in transonic interactions at $M = 1.3$. Computing the displacement thickness δ_2^* and momentum one θ_2 at the midplane ($z = Lz/2$) we obtain $L \sim 6.8\delta_1 \sim 10\delta_{in}$. We then introduce the rescaled variables $x^* = (x - x_2)/L$ and the reduced frequency $St_L = fL/u_\infty$. We also used the reduce frequency based on the boundary layer thickness at the beginning of the interaction δ_2 ($St_{\delta_2} = f\delta_2/u_\infty$). Using 4 points per wavelength to resolve the smallest frequencies we obtain the following resolvability limits: $4.10^{-3} < St_L < 13$ and $6.10^{-4} < St_{\delta_2} < 1.9$.

[1] the Mach number corresponding to the local mean wall pressure through the isentropic relations

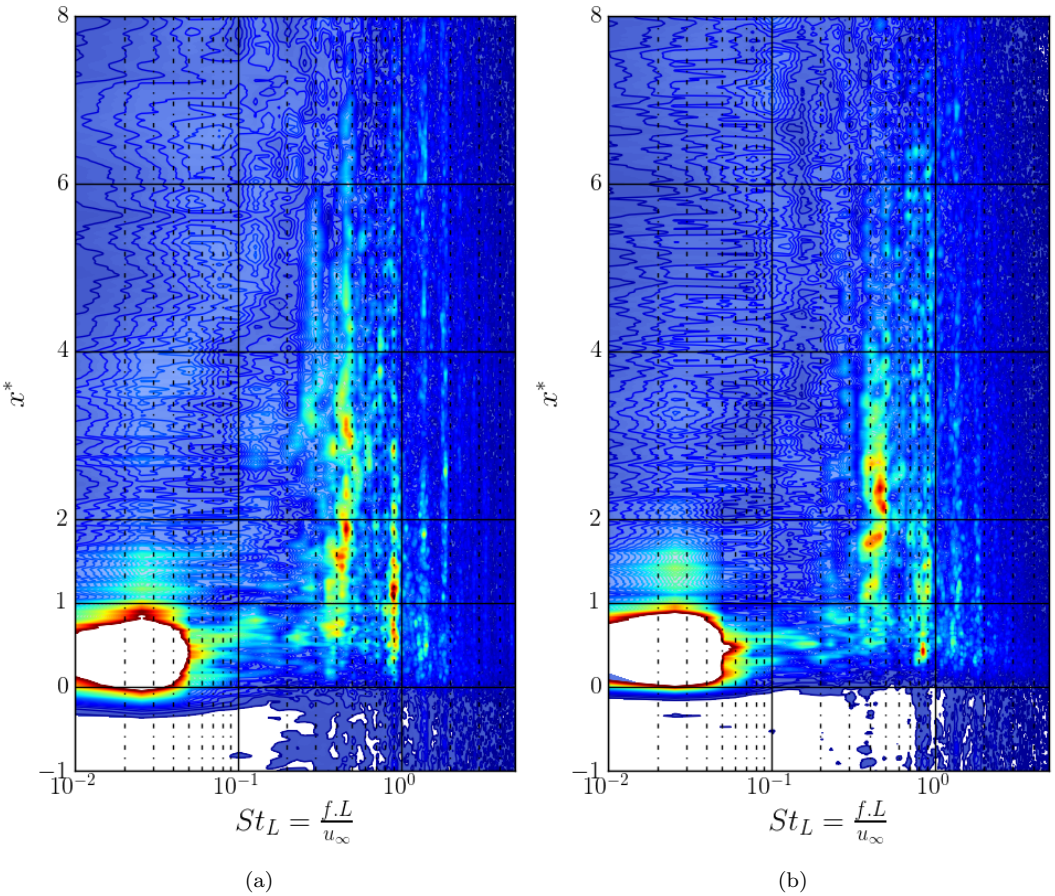

Figure 6.1: Contour of the power spectral density of the wall pressure (PSD(p_w)) on the upper wall $y = L_y$ (a) at a distance of 2 wall units from the lateral wall ($z^+ = 2$); (b) at the mid-plane ($z = Lz/2$). x^* being the rescaled streamwise variable $(x - x_2)/L$ and $St_L = fL/u_\infty$.

In figure 6.1 we report the contour of the power spectral density of the wall pressure (PSD(p_w)) at a distance of 2 wall units from the lateral wall ($z^+ = 2$, panel a) and at the mid-plane ($z = Lz/2$, panel b) on the upper wall $y = L_y$. As in Ref. [4], we have used Welch's method to compute the PSD. The pressure signal is split into in twelve segments with 50% overlap and Hann windows. From the figures, we observe that downstream of the initial shock ($x^* < 1$) the dynamics is mainly of broadband type. Some low-frequency activity seems to occur (both at the sidewall and at the midplane) likely due to a very low motion of the initial shock. From the computed results, we find that the shock displacement over the sampling period T is $o(\delta_2)$, which yields a reduced frequency $o(10^{-2})$.

The shock-train interaction region ($0 < x^* < 4$) is characterised by medium frequency activity of tonal type. Downstream, in the mixing region, broadband dynamics is recovered.

To better characterise the medium frequencies we report the PSD in linear scales (figure 6.2). From the figure two distinct tones at $St_{\delta_2} \sim 0.071$ and 0.142 are observed. Two less intense lines are also visible at $St_{\delta_2} \sim 0.21$ and 0.28. This observation seems to indicate the occurrence of acoustic resonance typical of cavity flows. For a closed box of dimensions $L_x \times Ly \times Lz$, resonant frequencies can be determined through the relation

$$f_{l,m,n} = \frac{c_\infty}{2}\sqrt{\left(\frac{\ell}{L_x}\right)^2 + \left(\frac{m}{L_y}\right)^2 + \left(\frac{n}{L_z}\right)^2} \tag{6.2}$$

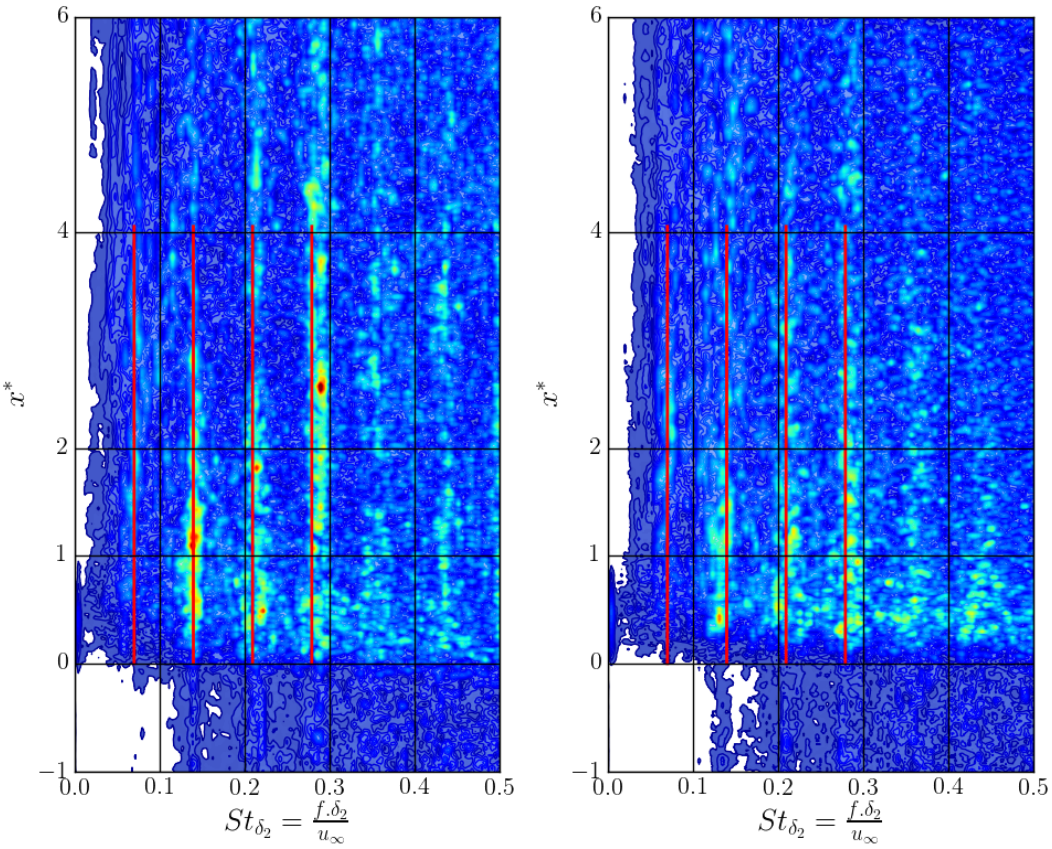

Figure 6.2: Contour of the power spectral density of the wall pressure (PSD(p_w)) on the upper wall $y = L_y$ (a) at a distance of 2 wall units from the lateral wall ($z^+ = 2$); (b) at the mid-plane ($z = Lz/2$). x^* being the rescaled streamwise variable $(x - x_2)/L$ and $St_{\delta_2} = f\delta_2/u_\infty$. Red lines indicate the first four tones given by equation 6.3.

where ℓ, m, n are integer numbers.

For the present case, we then define the frequency of a resonant wave establishing in the y and z directions

$$f_n = n\frac{c_\infty}{2}\sqrt{\left(\frac{1}{L_y}\right)^2 + \left(\frac{2}{L_z}\right)^2} = n\frac{c_\infty}{2W}\sqrt{1 + 2AR^2}. \tag{6.3}$$

The first 4 resonant tones ($St^{(1)}_{\delta_2} = 0.0071$, $St^{(1)}_{\delta_2} = 0.0142$, $St^{(1)}_{\delta_2} = 0.0213$, $St^{(1)}_{\delta_2}0.0284$,) are reported in figure 6.2 (indicated with the red lines). The collapse of the observed tones and the ones computed through equation 6.3 indicates the establishment of an acoustic resonant phenomenon associated with the combined effect due to confinement and shock train interactions.

In figure 6.3 we report the distribution of the amplitude of the wall pressure PSD at a reduced frequency $St_{\delta_2} = 0.071$ as a function of the normalized streamwise variable $x^* = (x - x_2)/L$ at the upper wall ($y = L_y$) and at various spanwise locations ranging between $z/\delta_1 = 0$ and $z/\delta_1 = 7$. The figures show that the amplitude of the PSD obeys a power-law scaling. In the interaction region, between the initial shock and immediately past the tertiary shock, the amplitude approximately grows as ${x^*}^{1/2}$ and it then decays as ${x^*}^{0.7}$ in the proximity of the corner (figure 6.3 panel a). A similar double power-law scaling is observed away from the side walls at various spanwise locations. The amplitude of the PSD increases as ${x^*}^{0.85}$ for $x^* \lesssim 2.5$, and

decreases as $x^{*^{-5/3}}$ afterwards (panels b and c).

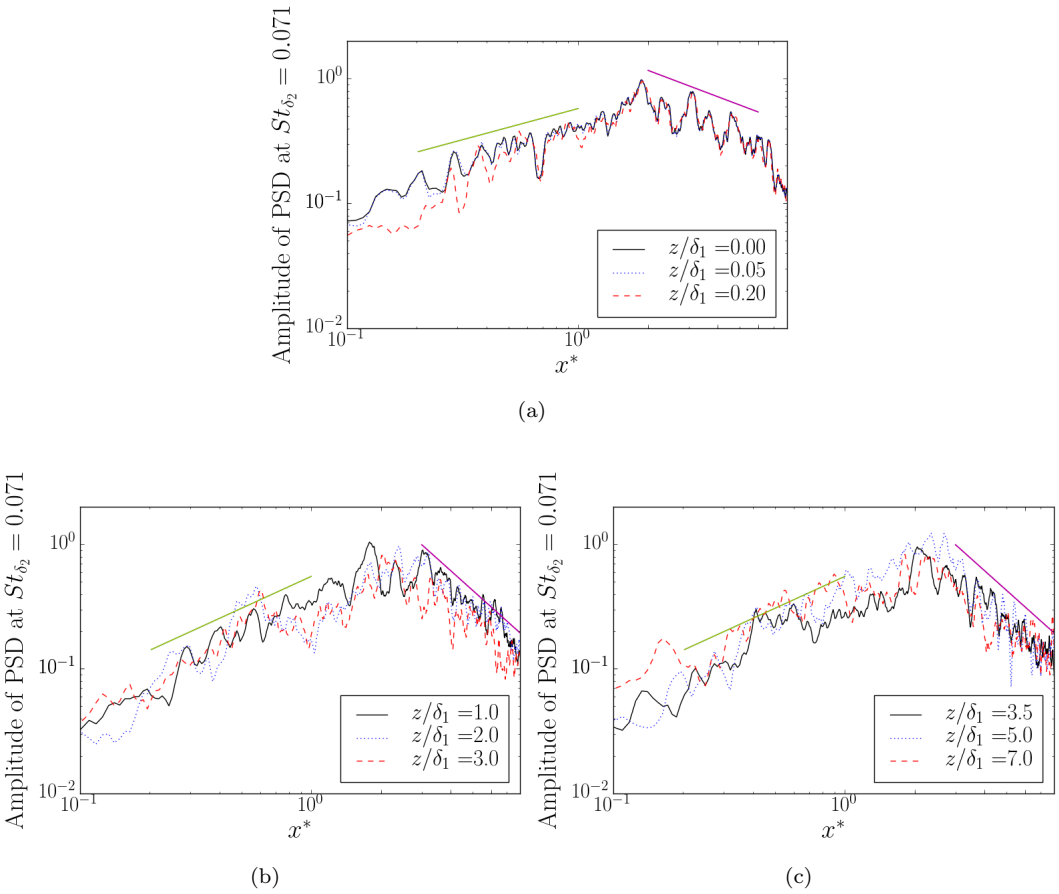

Figure 6.3: Distribution of the amplitude of the wall pressure power spectral density at $St_{\delta_2} = 0.71$ as a function of the normalized streamwise variable $x^* = (x - x_2)/L$ at various spanwise locations and at the upper wall ($y = L_y$). (a) z/δ_1 =0; 0.05; 0.2. (b) z/δ_1 =1; 2; 3. (c) z/δ_1 =3.5; 5; 7.

A second power-law scaling is found for the amplitude of the PSD at the second resonant frequency near the lateral walls, where corner effects are more important. However, no clear power-law scaling is identified away from the lateral wall.

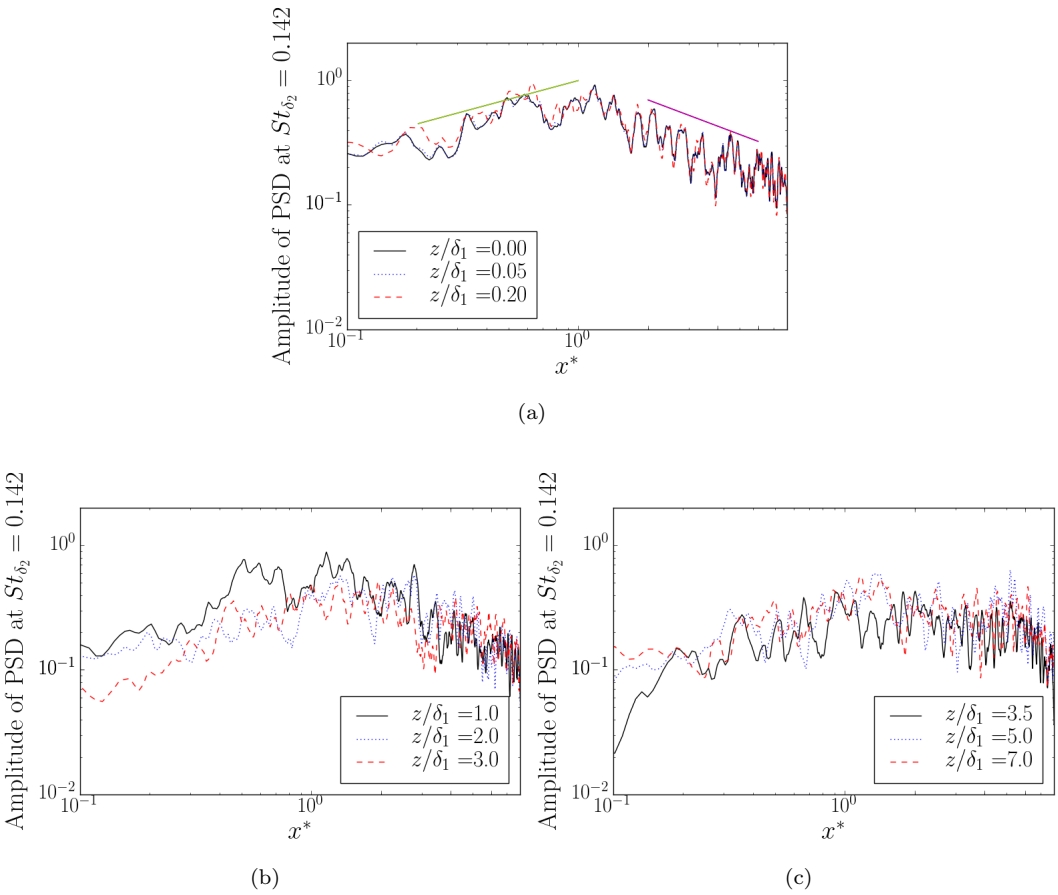

(a)

(b)

(c)

Figure 6.4: Distribution of the amplitude of the wall pressure power spectral density at $St_{\delta_2} = 0.142$ as a function of the normalized streamwise variable $x^* = (x - x_2)/L$ at various spanwise locations and at the upper wall ($y = L_y$). (a) z/δ_1 =0; 0.05; 0.2. (b) z/δ_1 =1; 2; 3. (c) z/δ_1 =3.5; 5; 7.

6.2 Dynamic Mode Decomposition

In order to further characterise the unsteadiness we have also analysed the flow by means of dynamic modes decomposition (DMD). The method is based on a singular value decomposition of the snapshots of the flow following Schmid [94].

6.2.1 Description of the method

Considering a given period T, series of snapshots are extracted every ΔT. Let i identified a generic snapshot u_i composed of a total of m points. We introduce the linear discrete operator A ($A \in \mathcal{M}_{m,m}(\mathbb{R})$) that maps the field u_{i-1} to u_{i-1} according to

$$u_i = Au_{i-1} = A^i u_1 \tag{6.4}$$

The matrix A is not known *a priori* and is supposed to be constant over the period T.

We look for a matrix S, obtained *a posteriori*, that has the same eigenvalues and eigenvectors than A. This data sequence is noted $X_1^{n+1} = [u_1, u_2, \dots u_{n+1}]$ and is stored on disk. The subsequence $X_1^n = [u_1, u_2, \dots u_n]$ is the sequence of observables that are used to determine the approximation of A. The number of dimensions in time is usually lower than the number of

dimensions in space ($n < m$) and consequently the size of S ($n \times n$) is much smaller than the size of A.

From equation 6.4, we can write :

$$X_1^n = \left\{u_1,\, Au_2,\, A^2 \cdots A^{n-1}u_n\right\} \tag{6.5}$$

which is valid under the assumption of a constant mapping between snapshots. The latter equation expresses the sequence of observables as a Krylov sequence [47].

As the number of snapshots increases, the n vectors of X_1^n become linearly dependent leading to

$$u_{n+1} = c_1 u_1 + c_2 u_2 + \cdots + c_n u_n + r \tag{6.6}$$

where c_i are coefficients, r is the residual vector and $i \in \{1, 2, \cdots, n\}$. Let C be the companion matrix (also called the Frobenius matrix) that is defined as:

$$C = \begin{pmatrix} 0 & 0 & \dots & 0 & c_1 \\ 1 & 0 & \dots & 0 & c_2 \\ 0 & 1 & \dots & 0 & c_3 \\ \vdots & \vdots & \vdots & \vdots & \vdots \\ 0 & 0 & \dots & 1 & c_n \end{pmatrix} \tag{6.7}$$

In matrix form, equation 6.6 becomes:

$$AX_1^n = X_2^{n+1} = X_1^n C + re_{n-1}^T \tag{6.8}$$

where $e_{n-1}^T \in \mathbb{R}^{n-1}$ is the (n-1)$^{\text{th}}$ unit vector. The companion matrix C being similar to the discrete propagator operator A, its eigenvalues are approximated by the eigenvalues of C. Some of the eigenvalues of A are approximated by the eigenvalues of C and a first possible choice for S is C. The companion matrix is determined through minimization of the residual (see Rowley et al. [87] for details).

In the present work, we have followed the approach based on the Singular Value Decomposition of X_1^n proposed by Schmid [94]. By definition, the SVD of X_1^n is:

$$X_1^n = U\Sigma W^H \tag{6.9}$$
$$\tag{6.10}$$

where U is the right singular vector of the snapshot sequence and W^H is the transposed-conjugate of the left singular vector, W. Note that U and W are unitary vectors (*i.e.* $UU^H = I$ and $WW^H = I$). Hence we can write:

$$AX_1^n = AU\Sigma W^H \tag{6.11}$$
$$X_2^{n+1} = AU\Sigma W^H \tag{6.12}$$
$$U^H X_2^{n+1} W\Sigma^{-1} = U^H AU\Sigma W^H W\Sigma^{-1} \tag{6.13}$$
$$M = U^H AU \tag{6.14}$$

where $M = U^H X_2^{n+1} W\Sigma^{-1}$ and $M \in \mathcal{M}_{n,n}(\mathbb{C})$. The matrix A and M being similar, the eigenvalues of A are approximated by the eigenvalues of M. According to Schmid [94], the main advantages of this method is its robustness against spurious noise in the data sequence X_1^n and the possibility to account for a rank deficiency in the sequence. This can be done by removing the singular values that are lower than a prescribed threshold and modifying the basis U accordingly.

Let T and Λ be the eigenvectors and eigenvalues of M, by definition we have:

$$\Lambda = T^{-1} M T \tag{6.15}$$

Hence:

$$T^{-1}U^H AUT = T^{-1}MT \tag{6.16}$$
$$(T^{-1}U^H)A(UT) = \Lambda \tag{6.17}$$

The eigenpairs of A are approximated by (Φ, Λ), where $\Phi = UT$ are the dynamic modes.

For a field governed by 1st order, linear ordinary differential equation

$$\frac{du(t)}{dt} = A_c u(t), \tag{6.18}$$

whose solution yields

$$u(t+\Delta t) = e^{A_c \Delta t}\, u(t) = \Psi e^{\Lambda_c \Delta t}\Psi^{-1}\, u(t) \tag{6.19}$$

Where (Ψ, Λ_c) are the eigenpairs of A_c.

In the case of a discrete problem governed by the linear mapping A, we have

$$u_{i+1} = Au_i = \Phi\Lambda\Phi^{-1}u_i \tag{6.20}$$

which shows the analogy between the field reconstructed through DMD and the "continous" problem.

If one then approximate the j^{th} continuous eigenpair by the j^{th} discrete eigenpair, one has

$$\lambda_{c,\,j} = \sigma_{c,\,j} + i\omega_{c,\,j} \tag{6.21}$$
$$\lambda_{c,\,j} \simeq \frac{\log(|\lambda_j|)}{\Delta t} + i\frac{\arg(\lambda_j)}{\Delta t} \tag{6.22}$$

where for the discrete system $\sigma_j + i\omega_j = \log(|\lambda_j|)/\Delta t + i\arg(\lambda_j)/\Delta t$.

Note that the j$^{\text{th}}$ dynamic mode (ϕ_j) is damped if $|\lambda_j| < 1$, and is amplified if $|\lambda_j| > 1$. For statistically stationary flow, $|\lambda_j| = 1$ (and the eigenvalues λ_j are on the unit circle). The discrete eigenpairs are called Ritz eigenpairs and the frequency of the j$^{\text{th}}$ mode is $f_j = \omega_j/2\pi = \arg(\lambda_j)/(2\pi\Delta t)$.

6.2.2 Flow analysis

The flow characteristics are here analysed through the dynamic mode decomposition based on the 1309 snapshots, each ones corresponding to the average of ten samples collected over ten time intervals. The real (λ_r) and imaginary (λ_i) parts of the Ritz eigenvalues are represented in figure 6.5. The figure shows that all eigenvalues fall in the unit circle.

The amplitude and the reduced frequency of the modes are reported in figure 6.6. The red lines indicate the resonant frequencies of the first two resonant tones and the dashed blue lines correspond to the resolvability limits of the DMD assuming 5 points per wavelength. In the following, we analyse the two modes flanking the first resonant tone ($St_{\delta_2} = 0.071$) and having a reduced frequency of $St_{\delta_2}^{\text{left}} = 7.04.10^{-2}$ and $St_{\delta_2}^{\text{right}} = 7.16.10^{-2}$. Their amplitudes are approximately 0.71.

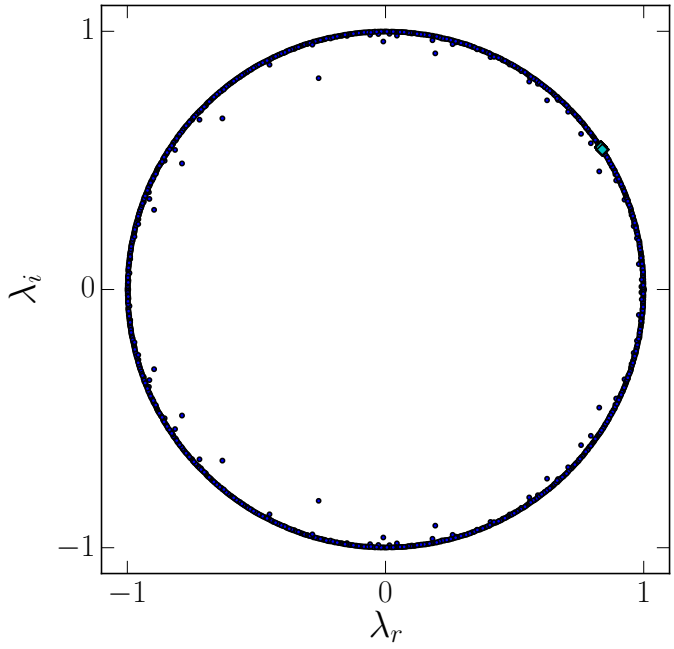

(a)

Figure 6.5: Ritz eigenvalues of the DMD modes where λ_r and λ_i are the real and imaginary parts, respectively. Green diamond symbols indicate that the corresponding modes are plotted.

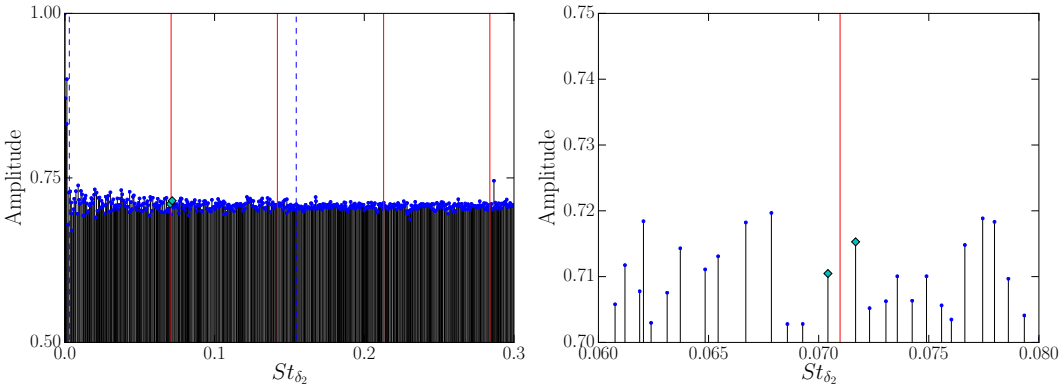

(a) (b)

Figure 6.6: Amplitude of the modes as a function of the reduced frequency ($St_{\delta_2} = fu_\infty/\delta_2$). Red lines indicate the resonant frequencies and dashed blue lines correspond to the resolvability limits of the DMD (assuming 5 points per wavelength). Green diamond symbols indicate the two modes flanking the first resonant tone. (a) Resolved modes (b) zoom between $St_{\delta_2} = 0.06$ and 0.08.

In figure 6.7 we report the contours of the modal quantities to left of the first resonant mode tone. In particular, shown in figure 6.7 (a) is the modal streamwise velocity at mid-plane ($z = Lz/2$). The modal pressure at the upper wall is reported in figure 6.7 (b). The modal y- and z- velocities components (at a location downstream of the beginning of the interaction $x^* = 0.5$) are plotted in figure 6.7 (c) and (d), respectively. The figures 6.7 (a) and (b), show that the streamwise velocity- and the pressure modes exhibit significant coherence within the interaction zone, Further

downstream in the mixing region they become less organized and weaker. The influence of the lateral walls are clearly observed from the contours of the modal velocity components in the cross plane (panel c and d). Similar topology is shown for the modes to the right of the resolved first resonant tones (see figure A.3).

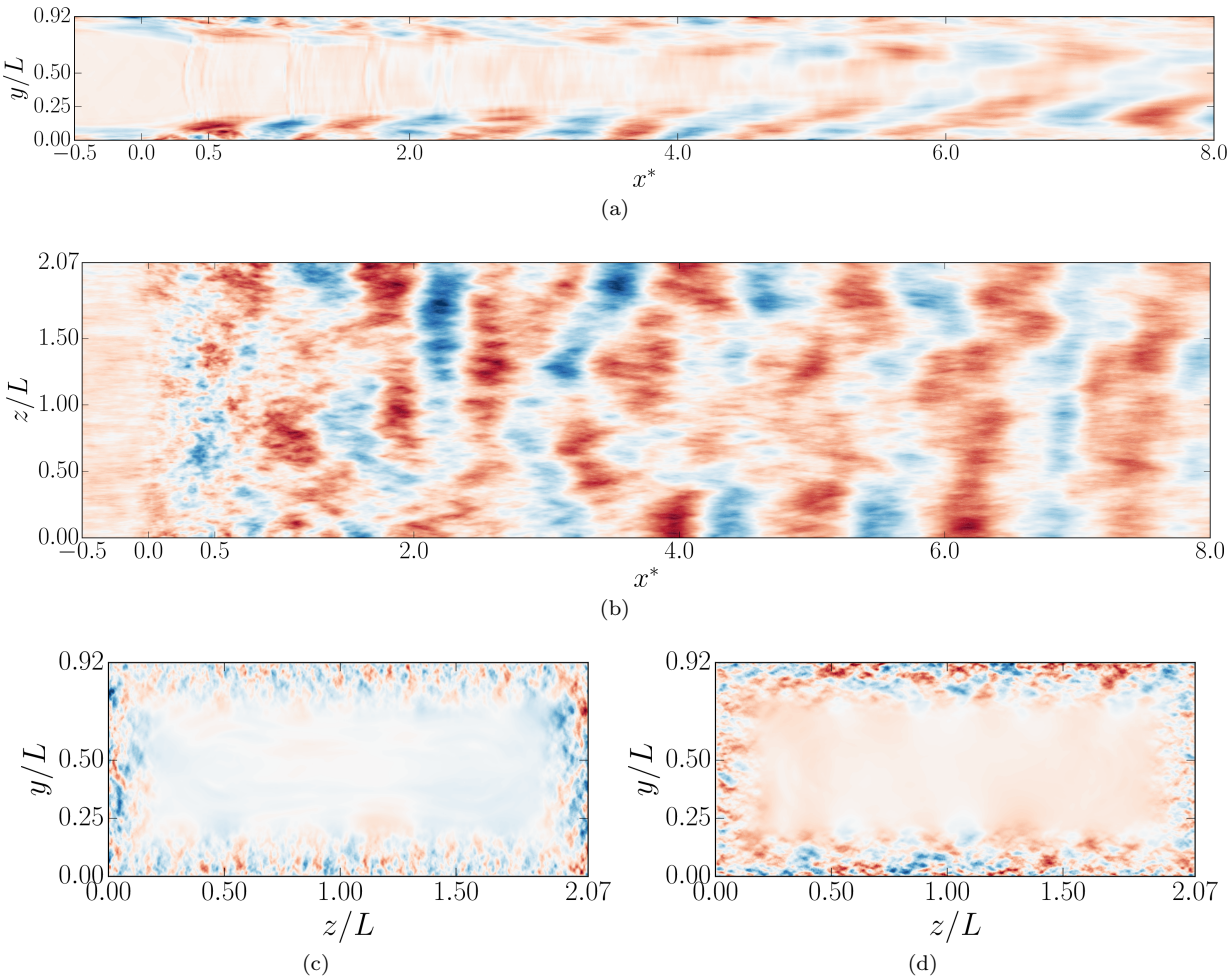

Figure 6.7: Contours of the modal quantities to left of the first resonant mode tone ($St_{\delta_2} = 7.04.10^{-2}$; $St_L = 0.478$) (a) Modal streamwise velocity at mid-plane ($z = Lz/2$). (b) Modal pressure at the upper wall. (c) Modal y-velocity component at $x^* = 0.5$. (d) Modal z-velocity component at $x^* = 0.5$.

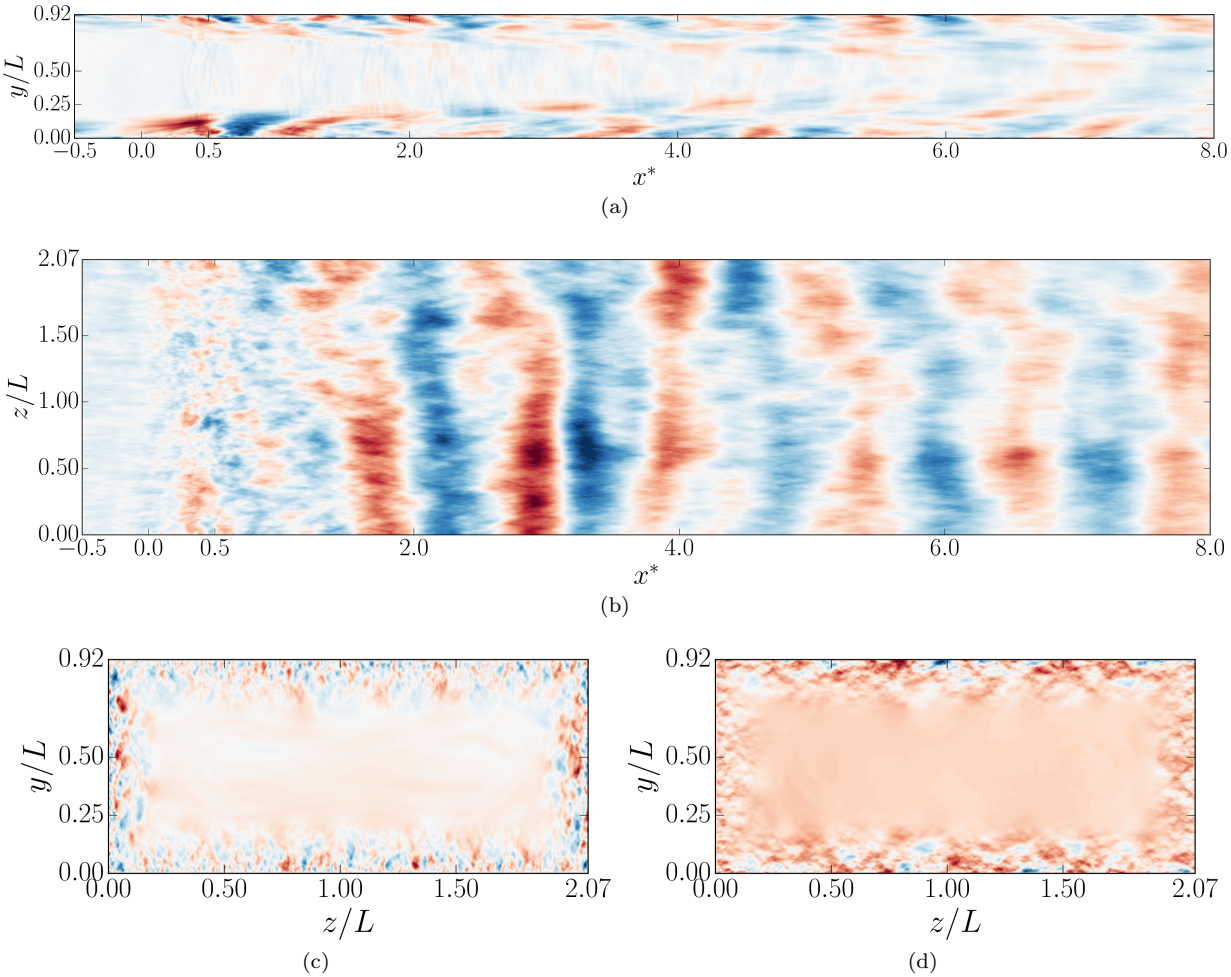

Figure 6.8: Contours of the modal quantities to right of the first resonant mode tone ($St_{\delta_2} = 7.16.10^{-2}$; $St_L = 0.486$) (a) Modal streamwise velocity at mid-plane ($z = Lz/2$). (b) Modal pressure at the upper wall. (c) Modal y-velocity component at $x^* = 0.5$. (d) Modal z-velocity component at $x^* = 0.5$.

In figure 6.9 we report the streamwise distribution (panel a) and the PSD in the streamwise direction (panel b) of the two pressure modes flanking the resolved acoustic tone. The modal pressure exhibits a strong oscillatory pattern with a peak at approximately $x^* \sim 2.5$ and the most significant, reduced wave numbers of the left and right modes varies between $k_x L = 9.5$ and 10, respectively, as inferred from the PSD of these pressure modes. Introducing the phase speed $u_{ph} = 2\pi f / k_x$, and recalling that the reduced frequency of the left and right DMD modes are $St_L^{left} = 0.478$ and $St_L^{left} = 0.489$, we obtain that u_{ph} varies between $0.31u_\infty$ and $0.32u_\infty$ that is nearly equal to the value found by Aubard et al. [4] in shear layer of 2.5D SWBLI. (the value reported by those is approximately $0.35u_\infty$). In appendix A.3, we report the contour of a low frequency dynamic mode.

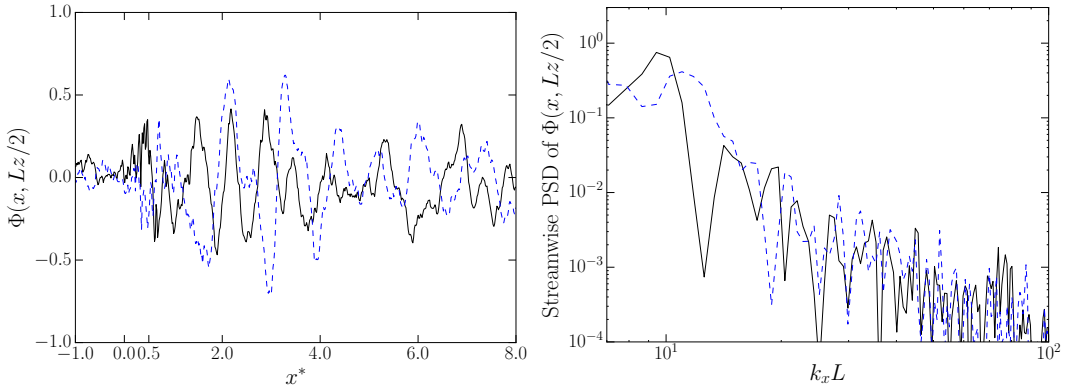

Figure 6.9: (a) Streamwise distribution and (b) PSD in the streamwise direction of the two pressure modes flanking the resolved first acoustic tone

Shown in figure 6.10, are the contours of the modal y- and z-velocity components associated with the mean flow (the zero-frequency dynamic mode) at $x^* = 0.5$. The mode exhibit symmetry at $x^* = 0.5$ in the duct cross section and the effects of the lateral walls and corner are clearly observed.

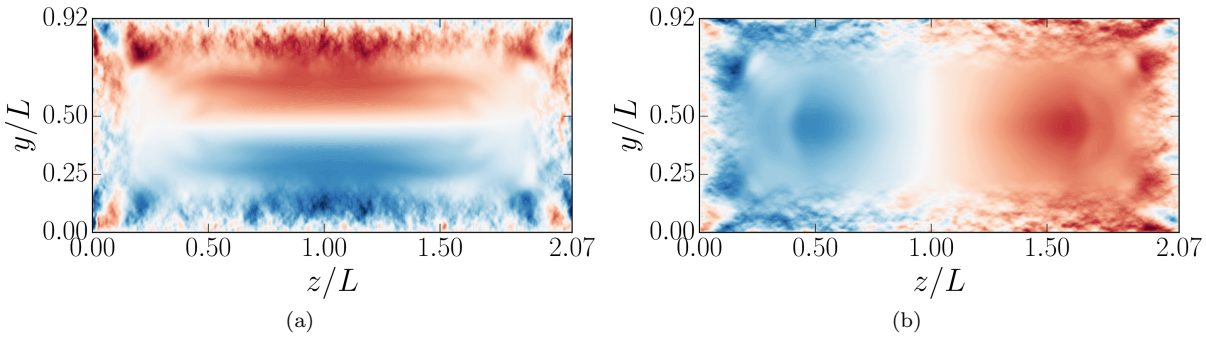

Figure 6.10: Contours of the modal y- and z-velocity components associated with the mean flow (the zero-frequency dynamic mode) at $x^* = 0.5$. (a) y-velocity component (b) z-velocity component

Chapter Summary

- Samples have been collected over a long period and power spectral density of the wall pressure have been computed.
- Low and medium activities are observed.
  - The low frequency is likely due to a very low motion of the initial shock.
  - Tonal activity is observed at St_{δ_2}=0.07,0.14,0.21 and 0.28.
  - The amplitude of the PSD at the first and second tones obeys a power law scaling.
  - The frequency are retrieved with an analytical formula: $f_n = n(c_\infty/2)\sqrt{(1/L_y)^2 + (2/L_z)^2}$.

  → Establishment of an acoustic resonant phenomenon associated with the combined effect due to confinement and shock train interactions.
- Dynamical Mode Decomposition has been used to further characterized the flow.
  - Two modes flanking the first resonant acoustic tone are analysed.
  - A coherent oscillatory pattern is observed.
  - Computing the PSD in the streamwise direction, we observe a peak at $k_x L \sim 10$.
  - A phase velocity of ∼0.32 is found. This value is close to the one found by Aubard et al. [4] in shear layer dynamics associated with 2.5D SWBLI.

Chapter 7

Conclusions and Future Work

Side walls effects in shock-wave boundary layer interaction have a major impact on the flow and only few numerical studies have been carried out in the presence of lateral walls. Strong confinement of transonic shock-wave boundary layer interaction leads to the appearance of additional shocks. This type of interaction is the so-called shock-train interaction that has been investigated in the present thesis by means of large eddy simulations.

A key issue of the simulation of turbulent flow is the generation of the initial turbulent quantities. For a single wall, the mean flow is obtained under the classical turbulent boundary layer assumption and the turbulent quantities are obtained through a recycling-rescaling method. For multiple-walls simulations, the approach of Boles et al. [12] has been used assuming that each wall can be treated separately. The initial turbulent flow is then reconstructed though a combination of each wall contribution (weighted by the inverse square wall distance).

A validation study has been carried out for an undisturbed wall-bounded flow, a transonic 2.5D incipient shock-wave boundary layer interaction, and, on the sensitivity of the flow topology in a rectangular duct by considering two different mean inflow conditions. In particular, we have observed that the topology of the transverse flow is not significantly affected by the turbulent inflow conditions (when scaled in outer units).

LES results of a Mach 1.61 shock-train inside rectangular ducts with various aspect ratios have been reported. The height of the duct is fixed and the influence of the side walls and confinement is analysed for aspect ratios of ∞; 5; 2.257 and 1.5. The ratio δ_2/h is slightly varying between cases and have similar effects than a width variation. Due to the one order of magnitude stronger variation of the duct width the effect of δ_2/h are assumed to be small. AR=2.257 results are in good agreement with the experimental data of Carroll and Dutton [21] and the LES database of Morgan et al. [68]. The results for case AR=5 are likely not fully statistically independent due to shortage in the computational time. We observe that the number of secondary shocks increases with higher confinement and the shock-train becomes shorter as respectively found by Carroll and Dutton [20] and Billig [8]. The minimum value of the centerline skin friction coefficient is not strongly affected by the distance between side walls. From our results it seems that that the dominant geometric scale to determine the minimum value of the skin friction, and so the onset of separation, is the minimum between the height and the width. For the case $AR = 2.257$ our ratio of $\delta_2^*/H = 29$ should be reduced to 7 to have a separated boundary layer on the centerline at $M = 1.61$ (estimated using the representation of separation conditions [17]).

One LES has been run for a (very) long period and a large number of samples has been collected to characterise the unsteadiness of the shock-train. Those samples have been post-treated both with Fourier analysis and the dynamical modes decomposition. The Fourier analysis shows that some low-frequency activity (seems to) occurs both at the sidewall and at the midplane, likely due to a very low motion of the initial shock. We observe that the shock-train interaction region ($0 < x^* < 4$) is characterised by medium frequency activity of tonal type and that

downstream, in the mixing region, a broadband dynamic is recovered. The results may indicate the establishment of an acoustic resonant phenomena associated with the combined effects of confinement and shock-train interaction. For the two DMD modes flanking the first resonant tone, we find that the phase velocity varies between $0.31u_\infty$ and $0.32u_\infty$, a value close to the one obtained by Aubard et al. [4] in shear layer dynamics of 2.5D SWBLI.

7.1 Future Work

Even though still prohibitive for shock-train simulation, assessing the influence of the initial Reynolds number (usually assumed at least one order of magnitude less than the experiment) could be the subject of future work. Similarly, the unsteadiness of stronger shock-train interactions exhibiting large mean separation could further show the influence of confinement and corner flows. Some open issues also remain regarding the possible interaction between the observed tones and the shear layer dynamics.

7.2 Acknowledgement

The authors acknowledge financial support of MBDA missile system, the PhD fellowship from Pres HESAM and the HPC resources of IDRIS and CCRT under the allocation x20152a7151 by GENCI (Grand Equipement National de Calcul Intensif).

The author would like to thank Pr. Dutton and D. Morgan for kindly providing the experimental and numerical database that have been used in this document.

I would like to thank Pr. Bernardini and Pr. Pirozzoli for providing the LES code that was adapted to carry out the simulation of the study.

Part I

Appendix

Appendix A

Uncommented results

In this chapter are gathered additional results. Those results are not shown in the main document and are given here without further indications.

A.1 Contours of the static pressure in the longitudinal midplane (z=Lz/2)

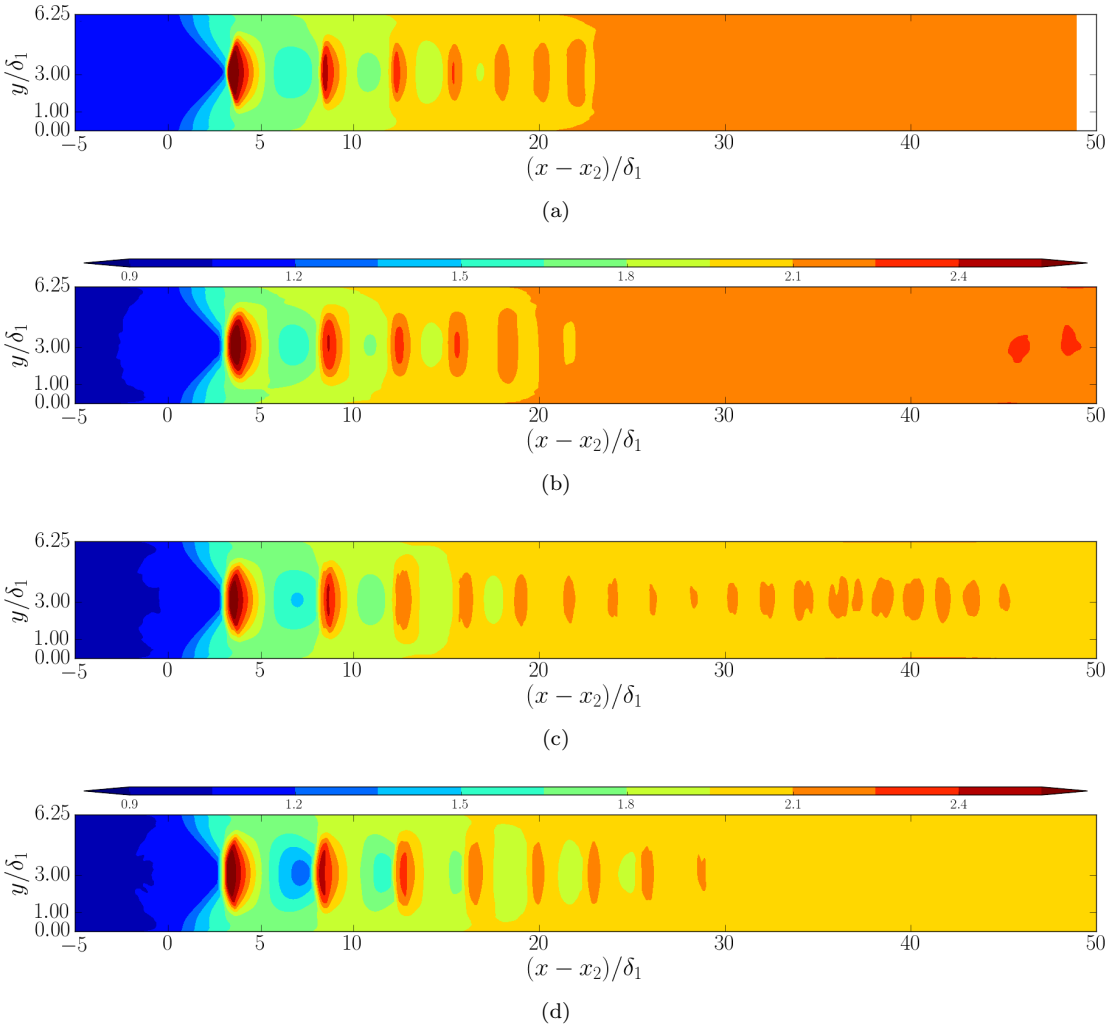

Figure A.1: Contours of static pressure divided by the wall pressure at x_2 in the longitudinal midplane ($z = Lz/2$). Eleven evenly spaced contours from 0.9 to 2.4. (a) AR=∞; (b) AR=5; (c) AR=2.257; (d) AR=1.5

A.2 Instantaneous visualization of the density gradient magnitude

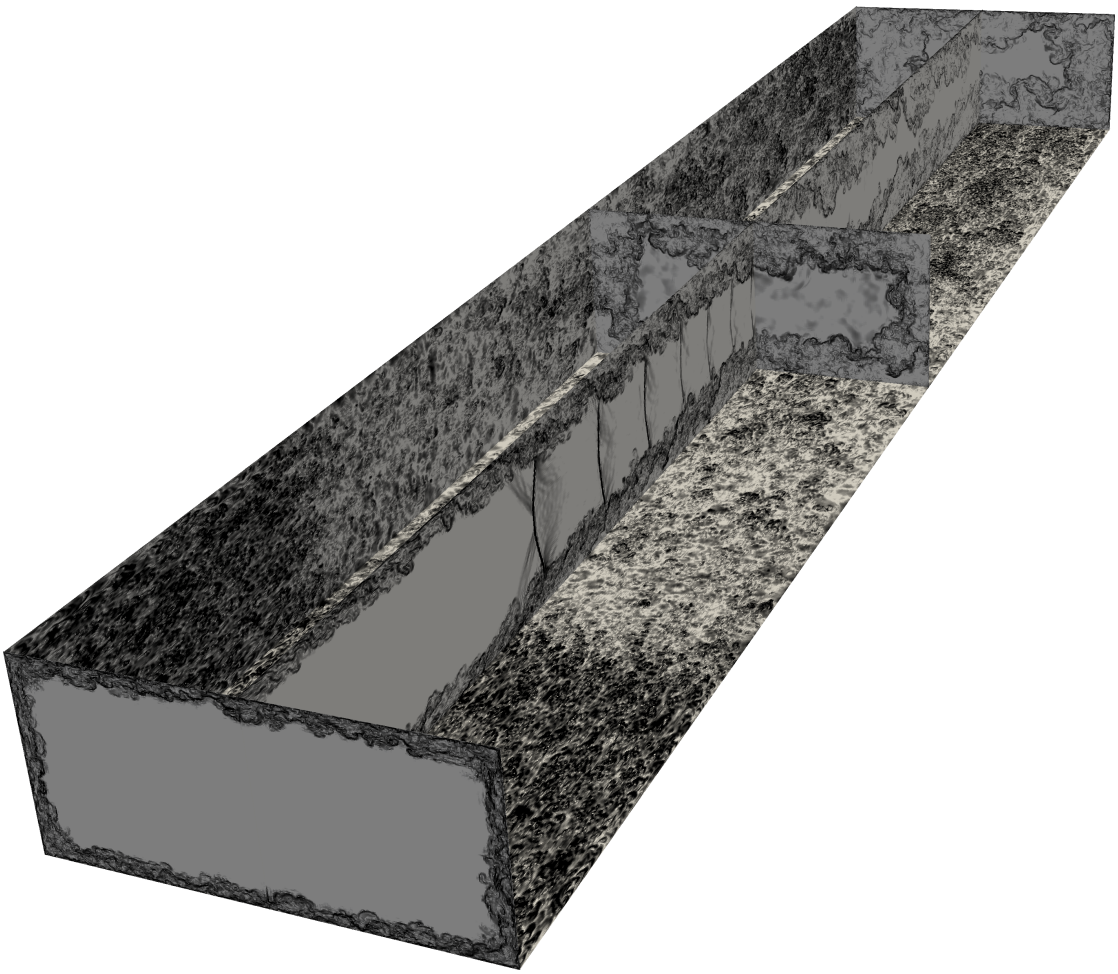

(a)

Figure A.2: Density gradient magnitude for the case AR=2.257.

A.3 Low-frequency DMD mode

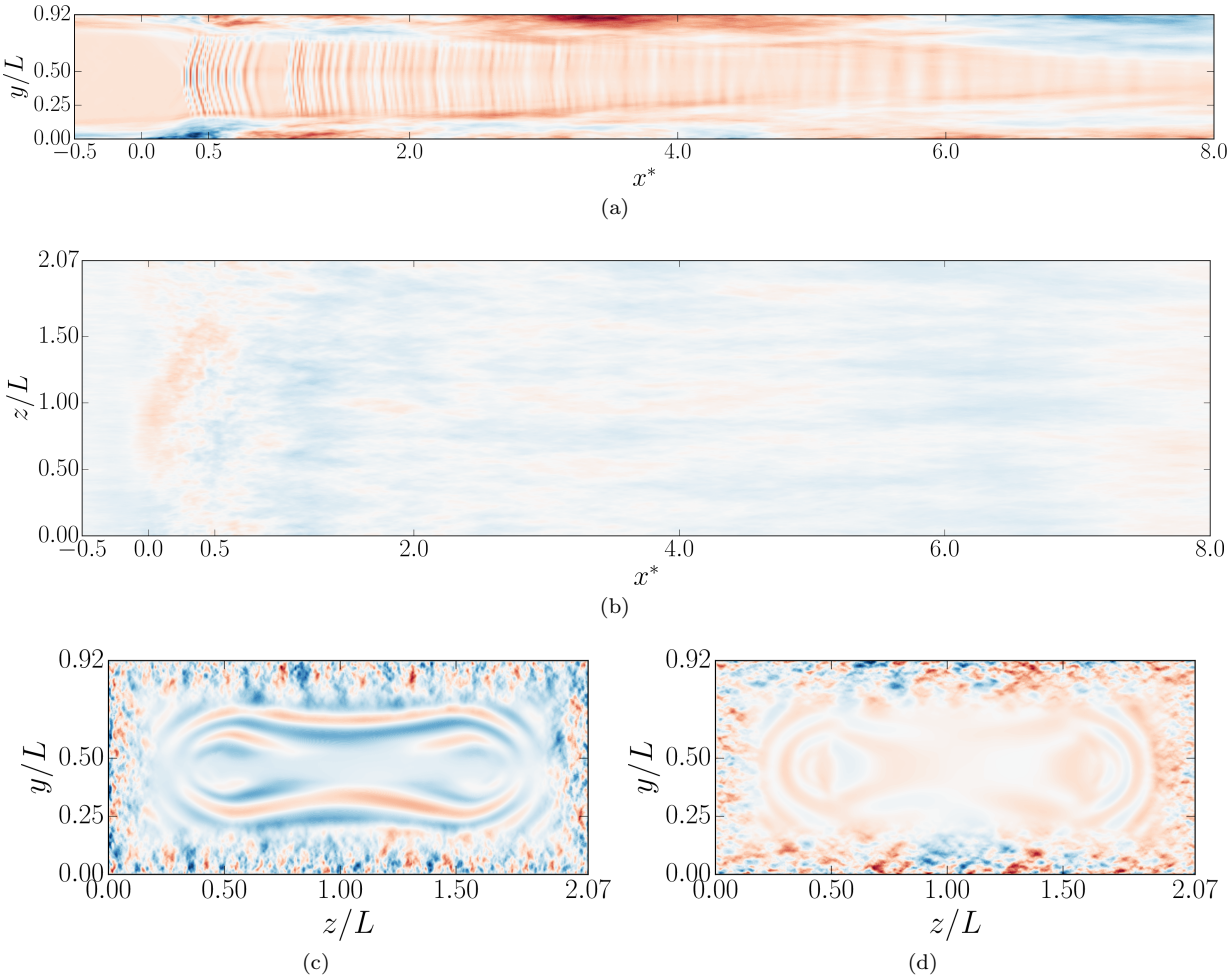

Figure A.3: Contours of the modal quantities to right of the first resonant mode tone ($St_{\delta_2} = 7.4.10^{-3}$; $St_L = 0.05$) (a) Modal streamwise velocity at mid-plane ($z = Lz/2$). (b) Modal pressure at the upper wall. (c) Modal y-velocity component at $x^* = 0.5$. (d) Modal z-velocity component at $x^* = 0.5$.

Appendix B

Details on the post-process

B.1 Measurable budget of the turbulent Kinetic energy equation for LES

In this section of the appendix, we show how to obtain the Favre-average-filtered-turbulent-kinetic energy equation. The final equation contains the contribution from the explicit subgrid model and the filter, where appropriate.

B.1.1 LES momentum equation

The momentum equation or Navier-Stokes equation hold:

$$\frac{\partial \rho u_i}{\partial t} + \frac{\partial \rho u_i u_j}{\partial x_j} + \frac{\partial p}{\partial x_i} = \frac{\partial}{\partial x_j}\left(\mu\left(\frac{\partial u_i}{\partial x_j} + \frac{\partial u_j}{\partial x_i} - \frac{2}{3}\delta_{ij}\frac{\partial u_k}{\partial x_k}\right)\right) \tag{B.1}$$

In order to separate sub-grid scales from larger scales a spatial Favre filtering procedure is used, with:

$$\phi = \phi^* + <\phi>_f \tag{B.2}$$

$$<\rho.\phi> = <\rho> . <\phi>_f \tag{B.3}$$

The filtering procedure is linear but, it does not commute with spatial or temporal derivatives [44]. The error, induced by the lack of commutativity, is supposed to be small enough and is, henceforth, neglected. The LES Favre-filtered equations are then:

$$\frac{\partial <\rho u_i>}{\partial t} + \frac{\partial <\rho u_i u_j>}{\partial x_j} + \frac{\partial <p>}{\partial x_i} = \left\langle \frac{\partial}{\partial x_j}\left(\mu\left(\frac{\partial u_i}{\partial x_j} + \frac{\partial u_j}{\partial x_i} - \frac{2}{3}\delta_{ij}\frac{\partial u_k}{\partial x_k}\right)\right)\right\rangle \tag{B.4}$$

After some manipulation, one obtains:

$$\frac{\partial <\rho><u_i>_f}{\partial t} + \frac{\partial <\rho><u_i u_j>_f}{\partial x_j} + \frac{\partial <p>}{\partial x_i} = \frac{\partial}{\partial x_j}\left(<\mu>\left(\frac{\partial <u_i>}{\partial x_j} + \frac{\partial <u_j>}{\partial x_i} - \frac{2}{3}\delta_{ij}\frac{\partial <u_k>}{\partial x_k}\right)\right) \tag{B.5}$$

Defining $\frac{\partial <\sigma_{ij}>}{\partial x_j}$ to be the right member of this equation and the term:

$$<\rho><u_i u_j>_f = <\rho><(<u_i>_f + u_i^*)(<u_j>_f + u_j^*)>_f = <\rho><u_i>_f <u_j>_f + \tau_{ij} \tag{B.6}$$

With $\tau_{ij} =< \rho > (< u_i u_j >_f - < u_i >_f < u_j >_f)$ containing the sub-grid terms.
We obtain:

$$\underbrace{\frac{\partial < \rho >< u_i >_f}{\partial t}}_{\text{Temporal variation}} + \underbrace{\frac{\partial < \rho >< u_i >_f < u_j >_f}{\partial x_j}}_{\text{Momentum transport}} + \underbrace{\frac{\partial < p >}{\partial x_i}}_{\text{Pressure}} = \underbrace{\frac{\partial \tau_{ij}}{\partial x_j}}_{\text{Sub-Grid terms}} + \underbrace{\frac{\partial < \sigma_{ij} >}{\partial x_j}}_{\text{Viscosity effects}} + \underbrace{\mathcal{F}_2}_{\text{Filter}} - \underbrace{f_2}_{\text{Volume Force}} \tag{B.7}$$

Where $\mathcal{F}_2$ is the measurable contribution of an explicit filter that is applied to the momentum equation. And for the filtered continuity equation we have:

$$\frac{\partial < \rho >}{\partial t} + \frac{\partial < \rho >< u_j >_f}{\partial x_j} = \mathcal{F}_1 + f_1 \tag{B.8}$$

Where $\mathcal{F}_1$ is the measurable contribution of an explicit filter that is applied to the continuity equation.

B.1.2 Kinetic energy

In order to compute the time average value of the turbulent kinetic energy (TKE) we have to take the mean value of: equation B.7 $\times < u_i >''_f$
With the Favre-average (in time) procedure defined as:

$$\phi = \phi'' + \widetilde{\phi} \tag{B.9}$$

$$\overline{\rho.\phi} = \bar{\rho}.\widetilde{\phi} \tag{B.10}$$

The following properties are used:

$$\widetilde{\widetilde{\phi}} = \widetilde{\phi} \tag{B.11}$$

$$\phi'' = \phi - \widetilde{\phi} \tag{B.12}$$

$$\phi'' = \phi' + \bar{\phi} - \widetilde{\phi} \tag{B.13}$$

$$\widetilde{\phi''} = 0 \Leftrightarrow \widetilde{\phi} = \widetilde{\widetilde{\phi}} \tag{B.14}$$

Momentum contributions

Isolating the time derivative and momentum transport contribution we have:
We express those terms in a non-conservative form. Symbol [.] are used when the tilde $\widetilde{.}$ is not long enough.

$$\frac{\partial \rho u_i}{\partial t} + \frac{\partial \rho u_i u_j}{\partial x_j} = \rho \frac{\partial u_i}{\partial t} + u_i \frac{\partial \rho}{\partial t} + u_i \frac{\partial \rho u_j}{\partial x_j} + (\rho u_j) \frac{\partial u_i}{\partial x_j} \tag{B.15}$$

$$= \rho \frac{\partial u_i}{\partial t} + (\rho u_j) \frac{\partial u_i}{\partial x_j} + u_i \underbrace{\left(\frac{\partial \rho}{\partial t} + \frac{\partial \rho u_j}{\partial x_j} \right)}_{\text{eq B.8}} \tag{B.16}$$

$$= \rho \frac{\partial u_i}{\partial t} + (\rho u_j) \frac{\partial u_i}{\partial x_j} + u_i \mathcal{F}_1 \tag{B.17}$$

The time derivative are expressed differently to make $\frac{\partial \bar{\rho} k}{\partial t}$ appear.

$$\overline{\rho \frac{\partial u_i}{\partial t} u_i''} = \overline{\rho . \frac{\partial \widetilde{u_i} + u_i''}{\partial t} u_i''} \tag{B.18}$$

$$= \overline{\rho . \frac{1}{2} . \frac{\partial u_i''^2}{\partial t} + \frac{\partial \widetilde{u_i}}{\partial t} u_i''} \tag{B.19}$$

$$= \frac{1}{2} \overline{\rho . \frac{\partial u_i''^2}{\partial t}} + 0 \text{ (according to eq B.14)} \tag{B.20}$$

$$= \left(\frac{\partial \bar{\rho} . k}{\partial t} \right) - \overline{\frac{u_i''^2}{2} . \frac{\partial \rho}{\partial t}} \tag{B.21}$$

The spatial derivatives are reorganized:

$$\overline{(\rho u_j u_i'') \frac{\partial u_i}{\partial x_j}} = \overline{\rho . (u_j u_i'') \frac{\partial u_i}{\partial x_j}} \tag{B.22}$$

$$= \overline{\rho . (u_j u_i'') \frac{\partial \widetilde{u_i} + u_i''}{\partial x_j}} \tag{B.23}$$

$$= \overline{\rho . u_j \left(u_i'' \frac{\partial \widetilde{u_i}}{\partial x_j} + \frac{1}{2} . \frac{\partial u_i''^2}{\partial x_j} \right)} \tag{B.24}$$

Arguing that $u_j = \widetilde{u_j} + u_j''$ and:

$$\left[\widetilde{u_j} u_i'' \frac{\partial \widetilde{u_i}}{\partial x_j} \right] = \widetilde{u_j} \left[u_i'' \right] \frac{\partial \widetilde{u_i}}{\partial x_j} = 0$$

We then obtain:

$$\begin{aligned} \overline{(\rho u_j u_i'') \frac{\partial u_i}{\partial x_j}} &= \overline{\rho . u_j \left(u_i'' \frac{\partial \widetilde{u_i}}{\partial x_j} + \frac{1}{2} . \frac{\partial u_i''^2}{\partial x_j} \right)} \\ &= \bar{\rho} . \underbrace{\left[u_j'' u_i'' \right] \frac{\partial \widetilde{u_i}}{\partial x_j}}_{Production} + \frac{1}{2} \underbrace{\overline{\rho . u_j . \frac{\partial u_i''^2}{\partial x_j}}}_{Right\, terms} \end{aligned} \tag{B.25}$$

Concerning the terms on the right, we note that:

$$\overline{\rho \widetilde{u_j} \frac{\partial u_i''^2/2}{\partial x_j} + \rho u_j'' \frac{\partial u_i''^2/2}{\partial x_j}} = \underbrace{\frac{\partial \rho \widetilde{u_j} k}{\partial x_j}}_{TKE\, transport} + \underbrace{\frac{1}{2} \overline{\frac{\partial \rho u_j'' u_i''^2}{\partial x_j}}}_{turbulent\, diffusion} - \overline{\frac{u_i''^2}{2} \frac{\partial \rho u_j}{\partial x_j}} \tag{B.26}$$

$$\tag{B.27}$$

Using the second term from the time derivative equation B.21, we can simplify this term as:

$$\overline{\frac{u_i''^2}{2} . \frac{\partial \rho}{\partial t}} + \overline{\frac{u_i''^2}{2} \frac{\partial \rho u_j}{\partial x_j}} = \overline{\mathcal{F}_1 . \frac{u_i''^2}{2}}$$

Others terms: pressure and a passive scalar ϕ

For the others terms:

Pressure:

$$\begin{aligned}
\overline{\frac{\partial p}{\partial x_j}.u_i''} &= \overline{\frac{\partial p}{\partial x_j}.(u_i' - \bar{u}_i + \widetilde{u}_i)} \\
&= \overline{\left(\frac{\partial \bar{p} + p'}{\partial x_j}.u_i'\right)} + \frac{\partial \bar{p}}{\partial x_j}.(-\bar{u}_i + \widetilde{u}_i) \\
&= \overline{\frac{\partial p'}{\partial x_j}.u_i'} + \frac{\partial \bar{p}}{\partial x_j}.(\widetilde{u}_i - \bar{u}_i) \\
&= \frac{\partial \overline{u_i'.p'}}{\partial x_j} - \overline{\frac{\partial u_i'}{\partial x_j}.p'} + \frac{\partial \bar{p}}{\partial x_j}.(\overline{u_i''})
\end{aligned} \tag{B.28}$$

$\overline{\phi_i.u_i''}$:

$$\begin{aligned}
\overline{\phi_i.u_i''} &= \overline{(\bar{\phi}_i + \phi_i').(u_i' - \bar{u}_i + \widetilde{u}_i)} \\
&= \overline{\bar{\phi}_i u_i' + \phi_i' u_i' + \bar{\phi}_i(\widetilde{u}_i - \bar{u}_i)} \\
&= \overline{\phi_i' u_i'} + \bar{\phi}_i(\widetilde{u}_i - \bar{u}_i) \\
&= \overline{(\phi_i - \bar{\phi}_i)u_i'} + \bar{\phi}_i(\widetilde{u}_i - \bar{u}_i)
\end{aligned} \tag{B.29}$$

Replacing ϕ_i with Sub-Grid terms, Viscosity effects, Filter or Volume Force allow a quick computation of all the other component.

TKE equation

$$\begin{aligned}
\frac{\partial \bar{\rho}.k}{\partial t} + \frac{\partial \bar{\rho}\widetilde{u_j}k}{\partial x_j} = \\
&\underbrace{-\bar{\rho}.\widetilde{u_j'' u_i''}\frac{\partial \widetilde{u_i}}{\partial x_j}}_{Production} \\
&\underbrace{-\frac{1}{2}\frac{\partial \bar{\rho}[u_j'' u_i'' u_i'']}{\partial x_j}}_{turbulent\ diffusion} \\
&\underbrace{-\overline{\mathcal{F}_1.\frac{u_i''^2}{2}} - \overline{u_i.u_i''.\mathcal{F}_1}}_{Mass\ Filtering} \\
&\underbrace{-\frac{\partial \overline{u_i'.p'}}{\partial x_i} + \overline{\frac{\partial u_i'}{\partial x_i}.p'} - \frac{\partial \bar{p}}{\partial x_i}.(\overline{u_i''})}_{\text{Pressure}} \\
&\underbrace{\overline{\left(\frac{\partial \tau_{ij}}{\partial x_j} + \frac{\partial \sigma_{ij}}{\partial x_j} + \mathcal{F}_2 + f_i\right).u_i''}}_{Others}
\end{aligned} \tag{B.30}$$

So:

$$\frac{\partial \bar{\rho}.k}{\partial t} + \frac{\partial \bar{\rho}\widetilde{u_j}k}{\partial x_j} =$$

$$\underbrace{-\bar{\rho}.\widetilde{u_j''u_i''}\frac{\partial \widetilde{u_i}}{\partial x_j}}_{\text{Production}}$$

$$\underbrace{-\frac{1}{2}\frac{\partial \bar{\rho}[u_j''u_i''u_i'']}{\partial x_j}}_{\text{turbulent diffusion}}$$

$$\underbrace{-\frac{\partial \overline{u_i''.p'}}{\partial x_i} + \overline{\frac{\partial u_i''}{\partial x_i}.p'} - \frac{\partial \bar{p}}{\partial x_i}.\overline{u_i''}}_{\text{Pressure}}$$

$$\underbrace{-\overline{\frac{\partial u_i''.\sigma_{ij}'}{\partial x_j}} + \overline{\frac{\partial u_i''}{\partial x_j}.\sigma_{ij}'} - \frac{\partial \overline{\sigma_{ij}}}{\partial x_i}.\overline{u_i''}}_{\text{Molecular dissipation}}$$

$$\underbrace{-\overline{\frac{\partial u_i''.\tau_{ij}'}{\partial x_j}} + \overline{\frac{\partial u_i''}{\partial x_j}.\tau_{ij}'} - \frac{\partial \overline{\tau_{ij}}}{\partial x_i}.\overline{u_i''}}_{\text{Turbulence viscosity}}$$

$$\underbrace{-\overline{\mathcal{F}_1.\frac{u_i''^2}{2}} - \overline{u_i.u_i''.\mathcal{F}_1}}_{\text{Explicit filter, Continuity}}$$

$$\underbrace{+\overline{\mathcal{F}_2.u_i''}}_{\text{Explicit filter, Momentum}}$$

$$\underbrace{-\overline{f_1.\frac{u_i''^2}{2}} - \overline{u_i.u_i''.f_1}}_{\text{Forcing in the Continuity equation}}$$

$$\underbrace{+\overline{f_{2\,i}.u_i''}}_{\text{Forcing in the Momentum equation}} \tag{B.31}$$

Bibliography

[1] Adams, N. (2000). Direct simulation of the turbulent boundary layer along a compression ramp at $m = 3$ and $re_\theta = 1685$. *Journal of Fluid Mechanics*, 420:47–83.

[2] Adamson, T. and Messiter, A. (1980). Analysis of two-dimensional interactions between shock waves and boundary layers. *Annual Review of Fluid Mechanics*, 12:103–138.

[3] Anderson, J. D. (1999). *History of Aerodynamics: And its impacts on flying machines.* Cambridge University Press, USA.

[4] Aubard, G., Gloerfelt, X., and Robinet, J.-C. (2013). Large-eddy simulation of broadband unsteadiness in a shock/boundary-layer interaction. *AIAA journal*, 51(10):2395–2409.

[5] Babinsky, H. and Harvey, J. K., editors (2011). *Shock Wave–Boundary-Layer Interactions.* Cambridge Univ Press.

[6] Babinsky, H., Oorebeek, J., and Cottingham, T. G. (2013). Corner effects in reflecting oblique shock-wave/boundary-layer interactions. In *51st AIAA Aerospace Sciences Meeting including the New Horizons Forum and Aerospace Exposition.*

[7] Bermejo-Moreno, I., Campo, L., Larsson, J., Bodart, J., Helmer, D., and Eaton, J. K. (2014). Confinement effects in shock wave/turbulent boundary layer interactions through wall-modelled large-eddy simulations. *Journal of Fluid Mechanics*, 758:5–62.

[8] Billig, F. (1993). Research on supersonic combustion. *Journal of Propulsion and Power*, 9(4):499–514.

[9] Bogey, C. and Bailly, C. (2004). A family of low dispersive and low dissipative explicit schemes for flow and noise computations. *Journal of Computational Physics*, 194:194–214.

[10] Bogey, C., de Cacqueray, N., and Bailly, C. (2008). Self-adjusting shock-capturing spatial filtering for high-order non-linear computations. *14th AIAA/CEAS Aeroacoustics Conference,* 5-7 May, Vancouver, Canada, AIAA Paper 2008-2968.

[11] Bogey, C., de Cacqueray, N., and Bailly, C. (2009). A shock-capturing methodology based on adaptative spatial filtering for high-order non-linear computations. *Journal of Computational Physics*, 228(5):1447–146.

[12] Boles, J. A., Choi, J.-I., Edwards, J. R., and Baurle, R. A. (2010). Multi-wall recycling/rescaling method for inflow turbulence generation. In *48th AIAA Aerospace Sciences Meeting Including the New Horizons Frum and Aerospace Exposition.*

[13] Bookey, P., Wyckham, C., and Smits, A. (2005). Experimental investigations of mach 3 shock-wave turbulent boundary layer interactions. *AIAA Paper*, (2005-4899).

[14] Bourgoing, A. (2002). *Instationnarité et dissymétrie d'un écoulement supersonique d'écollé dans une tuyère plane.* PhD thesis, Universite Pierre et Marie Curie - Paris VI.

[15] Bradshaw, P. (1987). Turbulent secondary flows. *Annual Review of Fluid Mechanics*, 19(1):53–74.

[16] Bruce, P. J. K. and Babinksy, H. (2008). Unsteady shock wave dynamics. *Journal of Fluid Mechanics*, 603:463–473.

[17] Bruce, P. J. K., Burton, D. M. F., Titchener, N. A., and Babinksy, H. (2011). Corner effect and separation in transonic channel flows. *Journal of Fluid Mechanics*, 679:247–262.

[18] Brundrett, E. and Baines, W. D. (1964). The production and diffusion of vorticity in duct flow. *Journal of Fluid Mechanics*, 19:375–394.

[19] Burton, D. M. F. and Babinksy, H. (2012). Corner separation effects for normal shock wave/-turbulent boundary layer interactions in rectangular channels. *Journal of Fluid Mechanics*, 707:287–306.

[20] Carroll, B. and Dutton, J. (1990). Characteristics of multiple shock wave/turbulent boundary-layer interactions in rectangular ducts. *Journal of Propulsion and Power*, 6(2):186 – 193.

[21] Carroll, B. F. and Dutton, J. C. (1992). Multiple normal shock wave/turbulent boundary-layer interactions. *Journal of Propulsion and Power*, 8(2):441–448.

[22] Chapman, D. R. Kuehn, D. M. and K., L. H. (1957). Investigation of separated flows in supersonic and subsonic streams with emphasis on the effect of transition. Technical report, Technical Note 3869 NACA.

[23] Clemens, N. T. and Narayanaswamy, V. (2014). Low-frequency unsteadiness of shock wave/-turbulent boundary layer interactions. *Annual Review of Fluid Mechanics*, 46:469–492.

[24] Cocks, P. A., Bruno, C., Donohue, J. M., and Haas, M. (2013). Iddes of a dual-mode ethylene fueled cavity flameholder with an isolator shock train. *AIAA Paper*, 116:2013. 51st AIAA Aerospace Sciences Meeting including the New Horizons Forum and Aerospace Exposition.

[25] Cousteix, J. (1989). *Aerodynamique, Turbulence et couche limite*. Cepadues-Editions, la chevêche edition.

[26] Deck, S. (2002). *Simulation numérique des charges latérales instantionnaires sur des configurations de lanceur*. PhD thesis, Université d'Orléans. p34.

[27] Délery, J. and Dussauge, J. (2009). Some physical aspects of shock wave/boundary layer interactions. *Shock Waves*, 19(6):453–468.

[28] Delery, J. and Marvin, J. G. (1986). Shock-wave boundary layer interactions. *AGARDograph*, 280.

[29] Dolling, D. S. (2001). Fifty years of shock-wave/boundary-layer interaction research: what next? *AIAA journal*, 39(8):1517–1531.

[30] Donaldson, C. D. (1944). Effects of interaction between normal shock and boundary layer. Technical Report CB–4A27 NACA.

[31] Ducros, F., Ferrand, V., Nicoud, F., Weber, C., Darracq, D., Gacherieu, C., and Poinsot, T. (1999). Large-eddy simulation of the shock/turbulence interaction. *Journal of Computational Physics*, 152(2):517–549.

[32] Ducros, F., Laporte, T., Soul/'eres, Y., Guinot, V., Moinat, P., and Caruelle, B. (2000). High-order fluxes for conservative skew-symmetric-like schemes in structured meshes: Application to compressible flows. *Journal of Computational Physics*, 161:114–139.

[33] Dupont, P., Haddad, C., and Debieve, J. (2006). Space and time organization in a shock induced boundary layer. *Journal of Fluid Mechanics*, 559:255–277.

[34] Dussauge, J. (2009). Compressible turbulence in interactions of supersonic flows. *Turbulence and interactions*, pages 35–54.

[35] Dussauge, J., Piponniau, S., Sidorenko, A., and Debieve, J. (2008). Investigation of an oblique shock reflection with separation by piv measurements. *American Institute of Aeronautics and Astronautics*, 46:1365–1370.

[36] Dutton, J. C. and Carroll, B. F. (1988). Numerical and experimental investigation of multiple shock wave/turbulent boundary layer interactions in a rectangular duct. Urbana, IL 61801 ADA190772, University of Illinois at Urbana-Champaign.

[37] Délery, J. (2008). *Traité d'aérodynamique compressible. Ecoulements monodimensionnels stationnaires et surfaces de discontinuité, vol. 2. Collection mécaniques des fluides.*

[38] Edwards, J. R. (2008). Numerical simulations of shock/boundary layer interactions using time-dependent modelling techniques: A survey of recent results. *Progress in Aerospace Sciences*, 44(6):447–465.

[39] Fage, A. and Sargent, R. F. (1947). Shock wave and boundary layer phenomena near a flat surface. In *Proceedings of the Royal Society of London, serie A: Mathematical and Physical Sciences*, volume 190, pages 1–20.

[40] Ferri, A. (1940). Experimental results with airfoils tested in the high speed tunnel at guidonia. Technical Report TM–946 NACA.

[41] Ganapathisubramani, B., Clemens, N. T., and Dolling, D. S. (2007). Effects of upstream boundary layer on the unsteadiness of shock-induced separation. *Journal of Fluid Mechanics*, 585:369–394.

[42] Ganapathisubramani, B., Clemens, N. T., and Dolling, D. S. (2009). Low-frequency dynamics of shock-induced separation in a compression ramp interaction. *Journal of Fluid Mechanics*, 636:397–425.

[43] Garnier, E. (2009). Stimulated detached eddy simulation of three-dimensional shock/boundary layer interaction. *Shock waves*, 19(6):479–486.

[44] Garnier, E., Adams, N., and Sagaut, P. (2009). *Large Eddy Simulation for Compressible Flows.* Springer.

[45] Garnier, E., Sagaut, P., and Deville, M. (2002). Large eddy simulation of shock/boundary-layer interaction. *AIAA journal*, 40(10):1935–1944.

[46] Germano, M., Piomelli, U., Moin, P., and Cabot, W. H. (1991). A dynamic subgrid-scale eddy viscosity model. *Physics of Fluids*, 3:1760.

[47] Greenbaum, A. (1997). *Iterative Methods for Solving Linear Systems.*

[48] Guiho, F., Alizard, F., and Robinet, J.-C. (2016). Instabilities in oblique shock wave/laminar boundary-layer interactions. *Journal of Fluid Mechanics*, 789:1–35.

[49] Hadjadj, A. (2012). Large-eddy simulation of shock/boundary-layer interaction. *AIAA Journal*, 50(12):2919–2927.

[50] Handa, T., Masuda, M., and Matsuo, K. (2005). Three-dimensional normal shock-wave/boundary-layer interaction in a rectangular duct. *AIAA Journal*, 43(10):2182—-2187.

[51] Helmer, D., Campo, L., and Eaton, J. (2012). Three-dimensional features of a mach 2.1 shock/boundary layer interaction. *Experiments in fluids*, 53(5):1347–1368.

[52] Huang, P. G., Bradshaw, P., and Coakley, T. J. (1993). Skin friction and velocity profile family for compressible turbulentboundary layers. *AIAA Journal*, 31(9):1600–1604.

[53] Hunt, D. L. and Nixon, D. (1995). A very large eddy simulation of an unsteady shock wave/turbulent boundary layer interaction. In *Fluid Dynamics Conference*, volume 95-2212.

[54] Ingenito, A., Bruno, C., and Cecere, D. (2010). Les of the hyshot scramjet combustor. In *48th AIAA Aerospace Sciences Meeting Including the New Horizons Forum and Aerospace Exposition. Orlando, Florida.*, number 2010-758.

[55] Jayaprakash Narayan, M. and Govardhan, R. N. (2015). *29th International Symposium on Shock Waves 2: Volume 2*, chapter Experimental Study of Supersonic Flow over a forward Facing Step, pages 1211–1216. Springer International Publishing, Cham.

[56] Jiang, G.-S. and Shu, C.-W. (1996). Efficient implementation of Weighted ENO schemes. *Journal of Computational Physics*, 126:202–228.

[57] Kennedy, C. A. and Gruber, A. (2008). Reduced aliasing formulations of the convective terms within the navier–stokes equations for a compressible fluid. *Journal of Computational Physics*, 227(3):1676–1700.

[58] Knight, D., Yan, H., Panaras, A. G., and Zheltovodov, A. (2003). Advances in {CFD} prediction of shock wave turbulent boundary layer interactions. *Progress in Aerospace Sciences*, 39(2–3):121 – 184.

[59] Koo, H. and Raman, V. (2009). Detailed numerical simulations of a supersonic inlet-isolator. In *Sixth International Symposium on Turbulence and Shear Flow Phenomena*, pages 1528–1542.

[60] Lele, S. K. (1992). Compact finite difference schemes with spectral-like resolution. *Journal of Computational Physics*, 103(1):16–42.

[61] Li, Q. and Coleman, G. N. (2003). Dns of an oblique shock wave impinging upon a turbulent boundary layer. In R. Friedrich, B. J. G. . O. M., editor, *In Direct and Large-Eddy Simulation V*, volume ERCOFTAC of *9*, page 387–396.

[62] Liepmann, H. W. (1946). The interaction between boundary layer and shock waves in transonic flow. *Journal of Aerospace Sciences*, 13(12):623–638.

[63] Lighthill, M. J. (1953). On boundary layers and upstream influence. ii. supersonic flows without separation. *Proceedings of the Royal Society of London A: Mathematical, Physical and Engineering Sciences*, 217(1131):478–507.

[64] Liu, X.-D., Osher, S., and Chan, t. (1994). Weighted essentially non-oscillatory schemes. *Journal of Computational Physics*, 115:200–212.

[65] Lund, T. S., Wu, X., and Squires, K. D. (1998). Generation of turbulent inflow data for spatially-developing boundary layer simulations. *Journal of Computational Physics*, 140(2):233–258.

[66] Matsuo, K., Miyazato, Y., and Kim, H.-D. (1999). Shock train and pseudo-shock phenomena in internal gas flows. *Progress in Aerospace Sciences*, pages 33–100.

[67] Morgan, B. (2012). *Large-eddy simulation of shock/turbulence interactions in hypersonic vehicle isolator systems*. PhD thesis, Stanford University.

[68] Morgan, B., Duraisamy, K., and Lele, S. K. (2014). Large-eddy simulations of a normal shock train in a constant-area isolator. *AIAA Journal*, 52(3):539–558.

[69] Morgan, B., Duraisamy, K., Nguyen, N., Kawai, S., and Lele, S. (2013). Flow physics and rans modelling of oblique shock/turbulent boundary layer interaction. *Journal of Fluid Mechanics*, 729:231–284.

[70] Morkovin, M. (1961). Effects of compressibility on turbulent flows. *Mecanique de la Turbulence*, pages 367–380.

[71] Piponniau, S., Dussauge, J., Debieve, J., and Dupont, P. (2009). A simple model for low-frequency unsteadiness in shock-induced separation. *Journal of Fluid Mechanics*, 629(87–108).

[72] Pirozzoli, S. (2010). Generalized conservative approximations of split convective derivative operators. *Journal of Computational Physics*, 229(19):7180–7190.

[73] Pirozzoli, S. (2011). Numerical methods for high-speed flows. *Annual Review of Fluid Mechanics*, 43:163–194.

[74] Pirozzoli, S. and Bernardini, M. (2011). Turbulence in supersonic boundary layers at moderate reynolds number. *Journal of Fluid Mechanics*, 688(1):120–168.

[75] Pirozzoli, S., Bernardini, M., and Grasso, F. (2008). Characterization of coherent vortical structures in a supersonic turbulent boundary layer. *Journal of Fluid Mechanics*, 613:205.

[76] Pirozzoli, S., Bernardini, M., and Grasso, F. (2010). Direct numerical simulation of transonic shock/boundary layer interaction under conditions of incipient separation. *Journal of Fluid Mechanics*, 657:361–393.

[77] Pirozzoli, S. and Grasso, F. (2006). Direct numerical simulation of impinging shock wave/-turbulent boundary layer interaction at m = 2.25. *Physics of Fluids*, 18:065113.

[78] Plotkin, K. J. (1975). Shock wave oscillation driven by turbulent boundary-layer fluctuations. *AIAA Journal*, 13(8):1036–1040.

[79] Poinsot, T. J. A. and Lele, S. K. (1992). Journal of computational physics. *Journal of computational physics*, 101(1):104–129.

[80] Prandtl, L. (1926). Über die ausgebildete turbulenz. *Verh. 2nd Int. Kong. Tech. Mech*, page 62–75. (translation in NACA Tech. Memo. no. 435).

[81] Priebe, S. and Martin, P. (2012). Low-frequency unsteadiness in shock wave–turbulent boundary layer interaction. *Journal of Fluid Mechanics*, 699:1–49.

[82] Ringuette, M., Wu, M., and Martin, M. (2008). Low reynolds number effects in a mach 3 shock/turbulent-boundary-layer interaction. *AIAA Journal*, 46:1884–1887.

[83] Robinet, J.-C. and Casalis, G. (1999). Shock oscillations in diffuser modeled by a selective noise amplification. *AIAA journal*, 37(4):453–459.

[84] Robinet, J.-C. and Casalis, G. (2001). Critical interaction of a shock wave with an acoustic wave. *Physics of Fluids*, 13(4):1047–1059.

[85] Roe, P. (1981). Approximate riemann solvers, parameter vectors, and difference schemes. *Journal of Computational Physics*, 43:357–372.

[86] Roussel, C., Alizard, F., and Grasso, F. (2015). Turbulent inflow generation in square duct at supersonic mach number. In *22nd AIAA Computational Fluid Dynamics Conference*, number 2015-2618.

[87] Rowley, C. W., Mezić, I., Bagheri, S., Schlatter, P., and Henningson, D. S. (2009). Spectral analysis of nonlinear flows. *Journal of Fluid Mechanics*, 641:115–127.

[88] Sagaut, P. (2006). Large eddy simulation for incompressible flows.

[89] Sagaut, P., Garnier, E., Labourasse, E., Larcheveque, L., and Tromeur, E. (2004). Turbulent inflow conditions for large-eddy-simulation of compressible wall-bounded flows. *AIAA Journal*, 42:469–477.

[90] Sajben, M., Morris, M., Bogar, T., and Kroutil, J. (1991). Confined normal-shock/turbulent-boundary-layer interaction followed by an adverse pressure gradient. *AIAA journal*, 29(12):2115–2123.

[91] Sandham, N. D., Yao, Y. F., and Lawal, A. A. (2003). Large-eddy simulation of transonic flow over a bump. *International Journal of Heat and Fluid Flow*, 24:584–595.

[92] Sartor, F., Mettot, C., Bur, R., and Sipp, D. (2015). Unsteadiness in transonic shock-wave/boundary-layer interactions: experimental investigation and global stability analysis. *Journal of Fluid Mechanics*, 781:550–577.

[93] Schlatter, P. and Örlü, R. (2010). Assessment of direct numerical simulation data of turbulent boundary layers. *Journal of Fluid Mechanics*, 659:116–126.

[94] Schmid, P. J. (2010). Dynamic mode decomposition of numerical and experimental data. *Journal of Fluid Mechanics*, 656:5–28.

[95] Shahab, M. (2011). *Numerica investigation of the influence of an impinging shock-wave and heat transfer on developing turbulent boundary layer.* PhD thesis, Institut P'prime.

[96] Smagorinsky, J. (1963). General circulation experiments with the primitive equations: I. the basic experiment. *Monthly weather review*, 91(3):99–164.

[97] Smits, A. J. and Dussauge, J.-P. (1996a). *Turbulent shear layers in supersonic flow.* American Institute of Physics (Woodbury, NY).

[98] Smits, A. J. and Dussauge, J.-P. (1996b). *Turbulent shear layers in supersonic flow.* American Institute of Physics (Woodbury, NY).

[99] Spalart, P. R. (2009). Detached-eddy simulation. *Annual Review of Fluid Mechanics*, 41:181–202.

[100] Stewartson, K. and Williams, P. G. (1969). Self-induced separation. *Proceedings of the Royal Society of London A: Mathematical, Physical and Engineering Sciences*, 312(1509):181–206.

[101] Touber, E. and Sandham, N. (2009). Large-eddy simulation of low-frequency unsteadiness in a turbulent shock-induced separation bubble. *Theoretical and Computational Fluid Dynamics*, 23(2):79–107.

[102] Touber, E. and Sandham, N. D. (2011). Low-order stochastic modelling of low-frequency motions in reflected shock-wave/boundary-layer interactions. *Journal of Fluid Mechanics*, 671:417–465.

[103] Urbin, G., Knight, D., and Zheltovodov, A. (2000). Large eddy simulation of a supersonic compression corner. In *38th Aerospace Sciences Meeting and Exhibit.*

[104] Vinuesa, R., Bartrons, E., Chiu, D., Dressler, K. M., Rüedi, J.-D., Suzuki, Y., and Nagib, H. M. (2014). New insight into flow development and two dimensionality of turbulent channel flows. *Experiments in fluids*, 55(6):1–14.

[105] Vinuesa, R., Schlatter, P., and Nagib, H. M. (2015). On minimum aspect ratio for duct flow facilities and the role of side walls in generating secondary flows. *Journal of Turbulence*, 16(6):588–606.

[106] Vreman, B., Geurts, B., and Kuerten, H. (1995). A priori test of the large eddy simulation of the compressible plane mixing layer. *Journal of Engineering Mathematics*, 29:299–327.

[107] Wang, B., Liu, W., Zhao, Y., Fan, X., and Wang, C. (2012). Experimental investigation of the micro-ramp based shock wave and turbulent boundary layer interaction control. *Physics of Fluids*, 24(5).

[108] Wang, B., Sandham, N. D., Hu, Z., and Liu, W. (2015). Numerical study of oblique shock-wave/boundary-layer interaction considering sidewall effects. *Journal of Fluid Mechanics*, 767:526–561.

[109] Xu, S. and Martin, M. P. (2004). Assessment of inflow boundary conditions for compressible turbulent boundary layers. *Physics of fluids*, 16(7):2623–2639.

MODELISATION ET SIMULATION DE L'INTERACTION ONDE DE CHOC – COUCHE LIMITE TURBULENTE EN ÉCOULEMENT INTERNE AVEC EFFETS DE COINS

RÉSUMÉ : Afin de concevoir des systèmes de propulsion innovants, l'amélioration des performances des prises d'air supersonique constitue un enjeu majeur. En particulier, les écoulements intervenant au sein des entrées d'air et/ou de diffuseurs supersoniques mettent en jeu des phénomènes complexes associés aux diverses échelles spatiales et temporelles: dynamique de la turbulence pariétale, interaction entre une onde de choc et une couche limite turbulente, décollements tridimensionnels et effets de coins. Malgré les contributions significatives et récentes des simulations numériques de haute fidélité sur les instationnarités de l'interaction onde de choc/couche limite sans paroi latérales, peu d'études numériques ont été menées sur l'influence des coins dans la dynamique de l'écoulement. En présence de parois latérales et à des nombres de Mach suffisamment élevés, l'interaction se modifie et un train de choc se forme dans le diffuseur. Dans le cadre de cette thèse, les équations de Navier-Stokes en régime compressible sont résolues à l'aide de schémas d'ordre élevé. Des simulations en régime supersonique de l'écoulement dans des diffuseurs rectangulaires de largeurs différentes sont effectuées. L'étude permet la mise en évidence de l'influence du confinement et des effets de coins. Une deuxième partie de l'étude est consacrée à la compréhension des instationnarités générées par un train de choc dans un diffuseur rectangulaire à l'aide d'outils de post-traitement avancés: décomposition modale dynamique et périodogramme. Les résultats montrent la présence d'un possible phénomène de résonance du diffuseur à des fréquences proches de celles émises par l'écoulement.

Mots clés : écoulement transsonique, interaction onde de choc/couche limite turbulente, LES, confinement, écoulement de coin, DMD.

MODELISATION AND SIMULATION OF SHOCK-WAVE TURBULENT BOUNDARY LAYER INTERACTION IN INTERNAL FLOW WITH CORNER EFFECTS

ABSTRACT : To design innovative propulsion systems, improving the performance of supersonic air intakes is a major issue. In particular, the flows through the air intakes and/or supersonic diffusers involve complex unsteady phenomena associated with various spatial and temporal scales such as: wall-bounded turbulence dynamics, interaction between a shock-wave and a turbulent boundary layer, three-dimensional separated flows and corners effects. Despite the significant contributions from recent high-fidelity simulations of unsteady shock-wave boundary layer interaction in the absence of side walls, few numerical studies were conducted with secondary flows due to corner effects. In the presence of side walls and at Mach numbers large enough, the topology of the interaction is modified and a shock-train forms in the diffuser. In this thesis, the Navier-Stokes compressible equations are solved using high-order schemes. Simulations of supersonic flows in rectangular diffusers of different widths are carried out. The study allows to highlight the influence of confinement and corners effects on the mean flow. A second part of the study is devoted to the understanding of the unsteadiness associated with a shock-train in a rectangular supersonic diffuser. For that purpose, advanced post-processing tools have been developed such as: dynamic mode decomposition and Fourier analysis. The results show the presence of a possible resonance phenomenon in the diffuser at frequencies close to those associated with the flow.

Keywords : transonic flow, shock wave/turbulent boundary layer interaction, LES, confinement, corner flows, DMD.

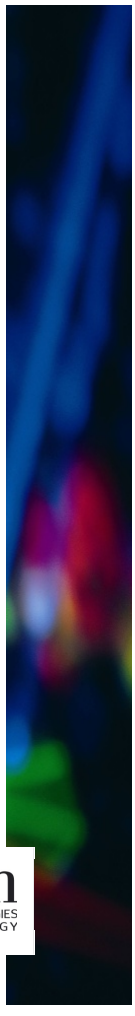

ARTS ET MÉTIERS ParisTech

ParisTech INSTITUT DES SCIENCES ET TECHNOLOGIES PARIS INSTITUTE OF TECHNOLOGY